THÈSE

Pour l'obtention du Grade de

DOCTEUR DE L'UNIVERSITE DE POITIERS

(Faculté des Sciences Fondamentales et Appliquées)
(Diplôme National - Arrêté du 25 mai 2016)

Ecole Doctorale : Science et ingénierie des matériaux, mécanique énergétique,

Secteur de Recherche : Génie Mécanique, Productique et Transports

Présentée par:

Mihail RĂDOI

****

ÉTUDE EXPÉRIMENTALE ET THÉORIQUE DES PALIERS DE TÊTE DE BIELLE

EXPERIMENTAL AND THEORETICAL STUDY OF CONNECTING ROD BIG END BEARINGS

****

Directeur de Thèse : Aurelian FATU ; Co-directeur : Yann HENRY

****

Soutenue le 08/11/2022

devant la Commission d'Examen

****

JURY

M. WODTKE	Professor, Gdansk Université of Technologie, Pologne	Rapporteur
T. DA SILVA BOTELHO	Professor, ISAE-Supméca - Institut supérieur de mécanique de Paris	Rapporteur
O. EL GANAOUI MOURLAN	Professor, IFP School, Paris	Examinateur
T. CICONE	Professor, Université « Politehnica » de Bucarest	Examinateur
M. ARGHIR	Professor, Université de Poitiers	Examinateur
Y. HENRY	Maître de conférences, Université de Poitiers	Examinateur
A. FATU	Professor, Université de Poitiers	Examinateur
B. CARRE	Ingénieur, AKIRA	Invité

(this page intentionally left blank)

ABSTRACT

Key words: dynamically loaded journal bearing, conrod big-end bearing, elastohydrodynamic, calibration, oil-supply flow, oil film thickness, lubrication, journal orbit, clearance, metrology

The main objective of the current thesis is to validate, reconfigure and reinforce a *simulation software* (ACCEL), developed in the laboratory in order to predict the tribological phenomena inside a journal bearing. The thesis is built around a campaign of experiments performed on a special test bench called MEGAPASCALE. Throughout the experiments, two types of connecting rods are used: a Renault RS and a Kawasaki ZX10. For both connecting rods, different oil supplies positions are evaluated. For the case of the Kawasaki connecting rod, multiple clearances are tested. Furthermore, eddy current gap sensors are installed to measure the journal position, and the voltage drop technique is utilised to qualitatively describe the lubrication conditions of the bearing. Additionally, the temperature, supply pressure, speed and load are monitored. The sensor calibration, as well as to the metrological measurements of the geometric characteristics of the bearings were attentively performed, in order to ensure a high accuracy of the measured physical quantities. It was proven that the ACCEL simulations match experimental measurements, which speaks not only for the accuracy of the results, but also for the quality of the calibration method. Furthermore, the software and know-how are envisioned to be transferred and used in industrial applications, within the AKIRA enterprise.

RESUME

Mots clé : palier lisse chargé dynamiquement, palier de bielle, élastohydrodynamique, calibrage, débitd'alimentation en huile, épaisseur du film d'huile, lubrification, orbite du palier, jeu radial, métrologie

L'objectif principal de la présente thèse est de valider un logiciel de simulation numérique (ACCEL), développé au laboratoire pour prédire les phénomènes tribologiques à l'intérieur d'un palier lisse. La thèse est construite autour d'un programme expérimental réalisé sur un banc d'essai spécial appelé MEGAPASCALE. Deux types de bielles ont été utilisés. La première est une Renault RS et la seconde une Kawasaki ZX10. Pour les deux bielles, différentes positions circonférentielles d'alimentation en lubrifiant ont été testées. Dans le cas de la bielle Kawasaki, plusieurs jeux sont essayés. De plus, des capteurs de déplacement à courants de Foucault sont installés pour mesurer la position de l'arbre en régime dynamique. La technique de différence du potentiel est utilisée pour décrire qualitativement le régime de fonctionnement du palier. La température, la pression d'alimentation, la vitesse et la charge ont été contrôlées. Une attention particulière est accordée à l'étalonnage des capteurs ainsi qu'aux mesures métrologiques des caractéristiques géométriques des paliers. Les simulations avec ACCEL correspondent aux mesures expérimentales, ce qui témoigne non seulement de la précision des résultats, mais aussi de la qualité de la méthode d'étalonnage. Le logiciel et le savoir-faire seront transférés et utilisés dans l'industrie - AKIRA.

(this page intentionally left blank)

ACKNOWLEDGEMENTS

To professor **Traian CICONE** at University "Politehnica" of Bucharest

My sincerest gratitude goes to Traian CICONE who guided me through my studies and showed to me the beautiful world of research.

To professor **Aurelian FATU** and Lecturer **Yann HENRY** at University of Poitiers

I would like to thank my directors for their brilliance, guidance, patience and their insightful comments and suggestions.

To **Bertrand CARRE** and **Thomas QUIRANTE** my supervisors from AKIRA

I would like to thank my supervisors from AKIRA for their moral and technical support.

To **Bastien LETOWSKI** and **Remi LABORDE** engineers at AKIRA

A special thanks for their advice on the subjects of electronics and computational mechanics. As well I would like to thank all the engineers and technicians from AKIRA which helped and supported me during the engine testing.

To **Cédric DELIAS** technician at IUT Angouleme

I am thankful for his technical advice and his support in parts machining.

To **Coutellerie RENOUX**

For their moral support and the machining performed on the connecting rods.

To my **parents**, my **sister** and my **niece**

My sincerest thank you for supporting me through my life and especially throughout my journey during the PhD.

To all my **friends**

Thank you for all the beautiful moments that you offered to me: for your sincerest moral support.

TABLE OF CONTENTS

General introduction

The Internal Combustion Engines (ICE) are usually selected for propulsion of ground and water vehicles due to their favourable energy density. The ICE transforms the chemical energy to mechanical energy through a reciprocating mechanism. The mechanism is composed of a piston, connecting rod and crankshaft. The piston supports the combustion pressure and transfers the work to the connecting rod. The connecting rod function is to transform the linear motion of the piston into rotation motion and transfer the work to the crankshaft.

All those components, which are in contact with each other, move. On the contact surfaces occurs the phenomenon called friction which causes wear. Wear is defined as the degradation process between interacting bodies. In order to reduce wear, along with the implied waste and friction, it is required to implement the usage of lubricants. Especially for the big-end connecting rod bearings, which is one of the most critical bearings in terms of applied load, due to the reciprocated nature of the mechanism (dynamically loaded journal bearing).

Even though the ICE exists for decades, the big-end bearing lubrication process still remains a field with lots of unknowns. The friction power loss represents a big issue for cars, which affects the fuel economy and pollutants emission. From the total chemical energy generated by combustion, about 50 % is already lost through exhaust and cooling. The remaining 50 % is converted to mechanical power. From this remaining 50 %, a large part of about 33 % is used to overcome the engine and driving frictional resistance that includes the tires and brakes [1]. This issue can be overcome with better lubrication, bearing design and materials.

(this page intentionally left blank)

Chapter 1 Background

1.1. Aim of the work

The aim of the present work is to reconfigure and reinforce an already existing simulation software - ACCEL (created within the laboratory of the Pprime Institute in Angoulême) - which is able to reproduce the tribological phenomena inside a journal bearing. Furthermore, the software and know-how are envisioned to be transferred and used in industrial applications, within the AKIRA[1] enterprise. The current thesis targets mainly the bearing performance. The procedure requires performing experimental measurements on a dedicated test rig. The experimental data is furthermore compared with numerical predictions, in order to validate the theoretical models. The dedicated test rig has the tremendous advantage – which is a rare feature within most testing configurations – to clearly isolate a specific measurement and observe its evolution, but at the cost of a less realistic loading condition. The simulation software consists in a set of algorithms, based on Thermo-Elasto-Hydro-Dynamic (TEHD) equations, solved using the finite elements method.

1.2. Introduction

What is Tribology? Tribology is the science of lubrication, friction and wear of moving or stationary parts. The word comes from the Greek τρίβω, [tribo], which means to rub. The first time when this field was introduced as a science was in 1966, when Peter Jost (a British mechanical engineer) baptized this field. Even though tribology is not a very popular science, it uses knowledge from chemistry, physics, fluid dynamics, structural mechanics, surface topology, etc.

[1] AKIRA 6 Rue Joseph Szydlowski, 64100 Bayonne, France. Official website: https://www.akira.pro/

Tribology can be found in almost every aspect of our mundane lives. As an example, think about you as walking on the street. The shoe sole is made of rubber which helps you to move forward due to the friction force. On the other hand, friction leads to frequent changes of shoes due to wear. If you walk on a wet surface, for instance, you start sliding due to water acting as a lubricant, which leads to the decrease in the frictional force.

To sum up, tribology can be informally split into two parts: *"friction friend"* and *"friction enemy"*. The present work is focused on the latter, namely lubrication, and more specifically, dynamically loaded journal bearing lubrication.

1.3. What is a journal bearing?

In order to respond to the subsection question: "*what is a journal bearing*" let us start by looking at the lexicon definitions in different languages. Therefore:

ENG: bearing (n.): mid-13c., *"a carrying of oneself, deportment,"* verbal noun from bear (v.). The meaning *"direction or point of the compass in which an object is seen or is moving"* dates from 1630s; to take (one's) bearings dates from 1711. The mechanical sense of *"part of a machine that 'bears' the friction"* dates from 1791.

FR: palier xiii^{e} siècle, paelier. Dérivé de paele, forme ancienne de poêle, « ustensile de cuisine », par analogie de forme.

GER: lager from Lager *"storehouse"* (From Proto-Germanic *legraz, from PIE root *legh- *"to lie down, lay"*)

From the above-mentioned definitions, a bearing is nothing but a device (*"house")* which bears the shaft and constrains the relative motion to the desired motion. Their duty is to enable two parts to move freely relative to each other, in either one or two directions, while constraining them in the remaining ones – with the less amount of friction.

There are many types of bearings, and their classification is plentiful. For the readers ease, and to understand where the current work locates, a brief list of the most relevant types of bearings is further presented. A more holistic bearing classification please check [2] .

Bearings can be classified by the type of motion they are subjected to: rotation, linear, trust, etc. Depending on the friction reduction methods, bearings can be: rolling, sliding, magnetic, dry.

For example, a rolling bearing utilizes rolling elements (spherical, cylindrical or conical) to reduce friction for the desired motion. Sliding bearings relate only on the bulk physical properties of the fluid film (oil, water, air) between the two surfaces. Positive pressure is generated inside the fluid film to support the load.

Depending on the pressure source, sliding bearings are divided into two categories: hydrostatic and hydrodynamic. For a hydrostatic bearing, the pressure is provided by an external pump. For a hydrodynamic bearing, the pressure develops mainly due to the relative speed and the wedge region between the two sliding surfaces, as shown in Figure 1.1.

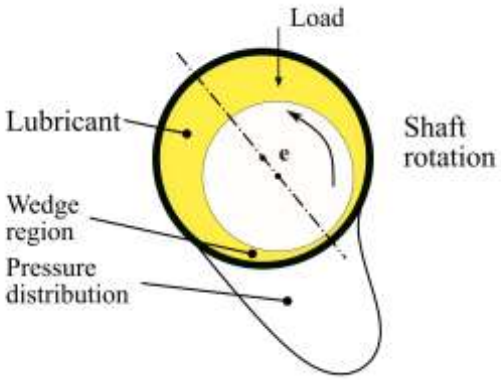

Figure 1.1 Journal bearing pressure distribution

Lubrication is the process of introducing a lubricant between sliding surfaces to reduce friction. The friction reduction is achieved due to the lubricant low shear strength within a fluid film. The fluid film thickness depends on: load, speed, viscosity, viscosity temperature dependence, viscosity-pressure dependence, surface topology, material, and so on. Therefore, the next natural subject following up to be discussed is related to lubrication regimes. A conceptual representation of the lubrication regimes is the Stribeck diagram [2] .

The Stribeck diagram presented in Figure 1.2 plots the friction coefficient (μ) under steady state conditions. The abscissa is the dimensionless Hersey number, which is the product of the dynamic viscosity (η) and the rotational frequency (ω) over the specific pressure (p), computed as the ratio between the applied load W and the bearing projected surface. Basically, this number is an image of the bearing state (running condition). A higher Hersey number means a thick fluid film, while a small one means that the surfaces are in contact. The pictograms above the plot show the fluid film thickness status for each of the four lubrication regimes. W stands for the normal load and U is the linear velocity.

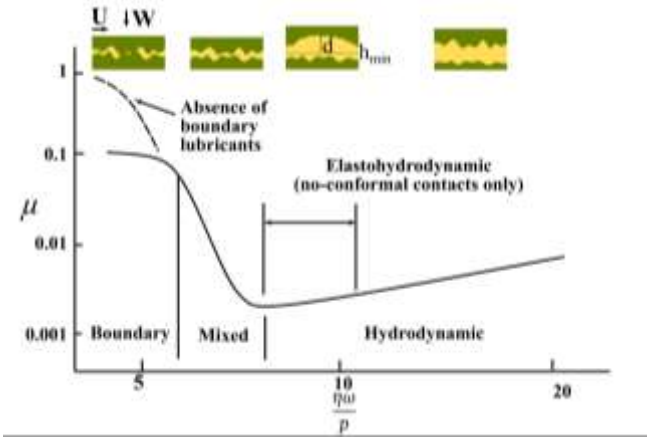

Figure 1.2 Adapted Stribek curve describing the lubrication regimes (Adapted from [2])

Starting from the righthand side of the diagram, the following lubrication regimes are depicted:

Hydrodynamic (HD) – It is characterized by conformal surfaces. The surfaces are separated by a bulk lubricant film. The positive pressure (usually less than 5 MPa) is not sufficient to cause a significant elastic deformation of the surfaces. The film layer is thick enough to prevent the surfaces to enter in contact: *"ideal lubrication"*. The gradually growth of the curve is mainly due to the increase of the linear velocity leading to an increase in redundant work in the lubricant or shear strength.

Elastohydrodynamic (EHD). It is a particular case of hydrodynamic lubrication. It is usually associated with non-conformal surfaces. The elastic deformation becomes important due to the hydrodynamic pressure and may exceeds several times the fluid film thickness. The pressure is between 0.5 to 3 GPa, and the fluid film thickness does not exceed 0.1µm. Also, the lubricant viscosity changes due do pressure (piezo viscosity). For both HD and EHD, the fluid film is thick enough to prevent solid contact.

Mixed or partial lubrication – The load is supported by both the bulk lubricant and the direct contact of asperities. On the Stribeck curve, it is depicted as the region of the steep descending section of the friction coefficient. Here, the friction coefficient is the smallest due to very thin fluid film, therefore a small amount of shear force exists between the fluid layers.

Boundary – The surfaces are in contact or separated by a molecular lubricant layer. The friction coefficient has a weak dependency on the bulk physical properties of the lubricant and hardly depends on the solid properties. The fluid film thickness varies between 1 to 10 nm.

Another important aspect of the bearing classification is the type of load. Bearings can support either static or dynamic load. For the particular case of a big-end connecting rod bearing, the

load is dynamic. Even though the rotational speed of the crankshaft is continuous, the loads vary with the crankshaft position, depending on the engine operation point (load - cylinder pressure and speed - inertial forces) and changes the lubrication regime.

For a connecting rod big-end bearing, the lubrication regime is predominantly elastohydrodynamic, and in some cases, transitions to mixed lubrication – where most of the wear process occurs. Boundary lubrication happens as well during the start-stop cycles. That is why after one starts an engine, it is recommended to wait for a few minutes in order to let the oil travel and feed all the bearings and lubricated contacts (bearings, cams, piston rings), and not rattle the engine in idle position. For my particular case the bearing is a rotational – sliding – elasto - hydrodynamic-dynamically loaded - bearing.

1.4. Connecting rod and bearing shell

The connecting rod connects the piston to the crankshaft and consists of three main regions: big-end, small end and shank (see Figure 1.3). The small end transmits the combustion pressure from the piston to the shank, while the big-end pushes the crankpin imposing rotation motion to the crankshaft.

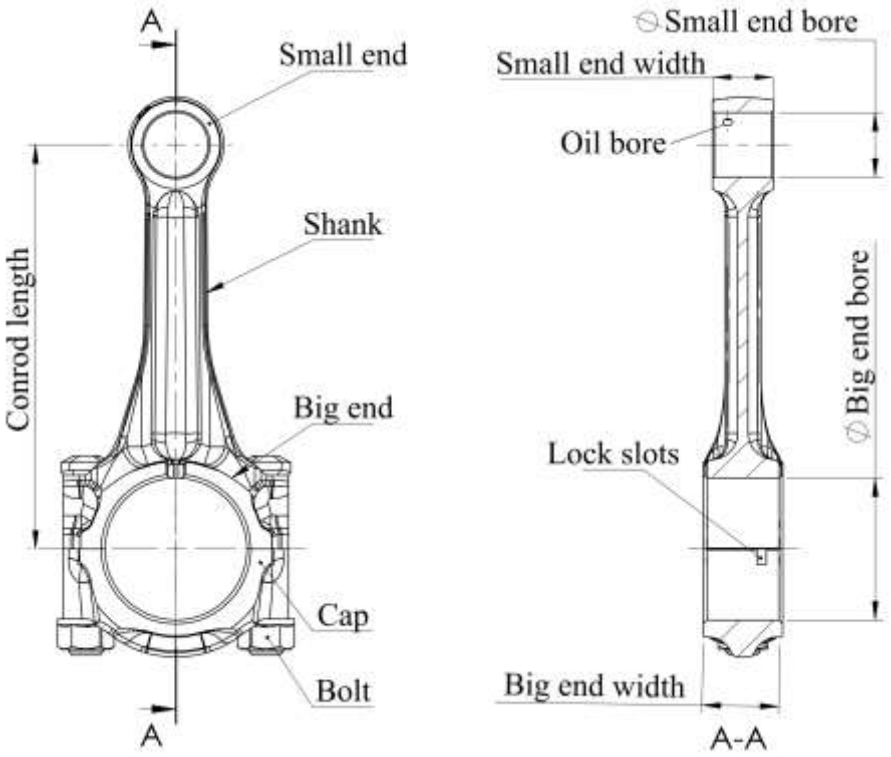

Figure 1.3 Terms and major dimensions of a connecting rod

Under cylinder pressure and inertial forces, the connecting rod is mainly subjected to compression/tensile dynamical loads. The transition of power in an ICE from the piston to the crankshaft is achieved by lubrication in bearings. The inertial forces are held in equilibrium by the fluid film hydrodynamic pression formed on the cap side. The joint integrity is provided by the bolts. Under maximum cylinder pressure, the shank pushes on the crankshaft pin via the lubrication hydrodynamic pressure. The reason that the connecting rod big-end is cut in two parts is to ensure the assembly on the crankshaft pin: therefore, the bearing is also divided in two half bearing shells.

1.5. Load diagram for a connecting rod big end bearing

Depending on the type of engine, the load diagram of a connecting rod big end bearing can differ considerably. For example, in the case of a passenger car, the rotational speeds rarely overpass 5000 rpm, thus the predominant loads on the big end bearings come from gas pressure. On the opposite spectrum are the F1 cars or motorcycles engines, which can reach higher speeds, for example Kawasaki Ninja outputs the maximum torque of 113 Nm at 11500 rpm, therefore, the inertial loads become more important than the combustion loads.

Figure 1.4 and Figure 1.5 represent the load diagram for a connecting rod big end bearing for two different rotational speeds at full load. At lower speeds, for example 5000 rpm, the inertial forces are relatively small, compared to the gas pressure loads. The connecting rod is mainly subjected to tensile stress during the compression and power stroke, which corresponds to crankshaft angles varying from 180° to 540°.

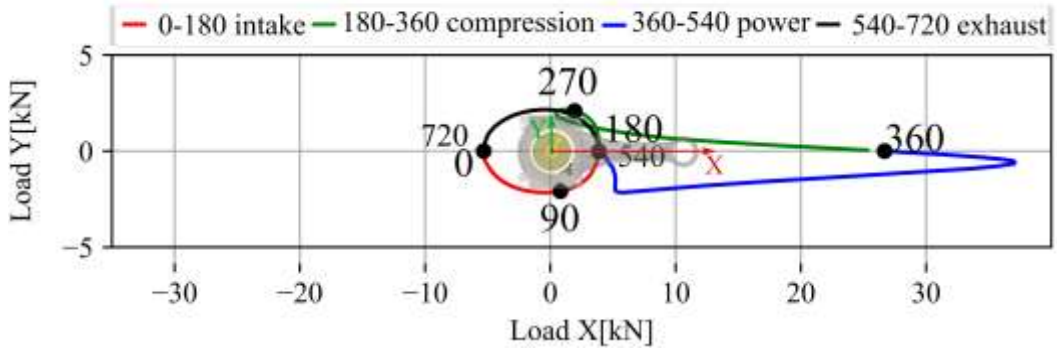

Figure 1.4 Load diagram of a connecting rod big end bearing at a speed of 5000rpm

At higher rotational speeds, for example 11500 rpm, the inertial forces become dominant. The traction at the top dead centre (TDC), which represents the 0° crankshaft angle, is higher than the compression at the end of the power stroke, at 540° crankshaft angle. At the bottom dead centre (BDC - 180° crankshaft angle), the compression is purely due to the inertial forces.

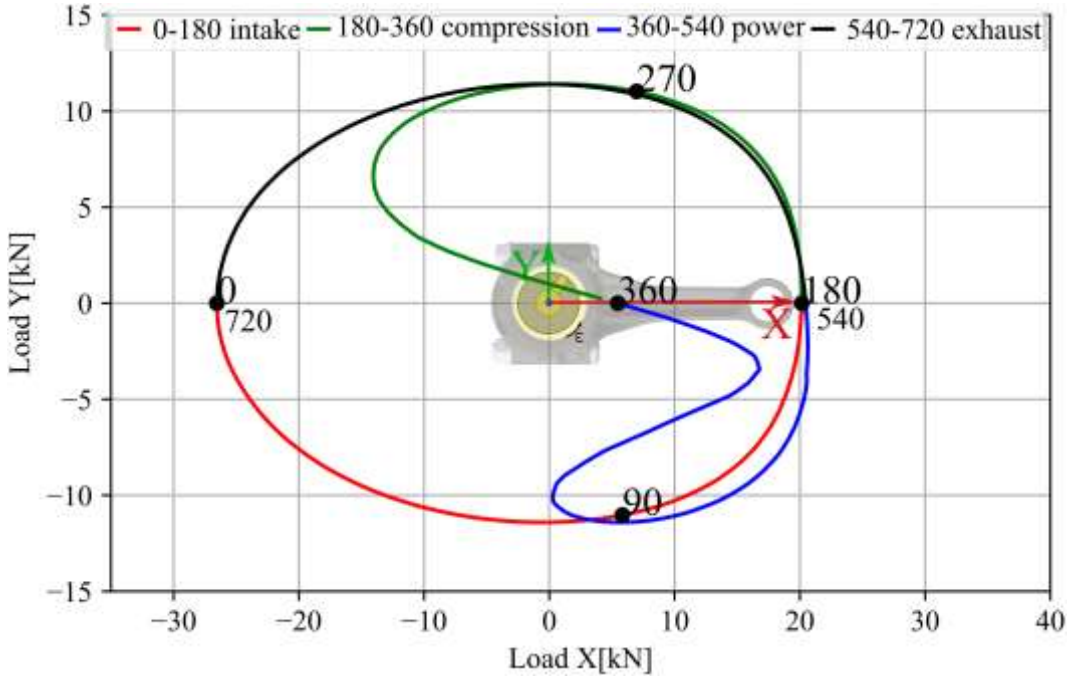

Figure 1.5 Load diagram of a connecting rod big end bearing at a speed of 11500rpm

1.6. Bearing Shell

The half bearing shell has a specific construction, shown in Figure 1.6 a. The free spread (3), which represents the difference in diameter between housing and bearing in free condition, provides good seat and good heat transfer. The locating lug (1) ensures the axial location. The crush relief (5) provides a smooth transition from one shell to the other.

Another important design feature is the bearing profile, presented in Figure 1.6 b. This profile is known in the French literature as *"forme citron"* (lemon shape), and it is depicted in Figure 1.7. This form is achieved by a circumferential variation of the shell thickness.

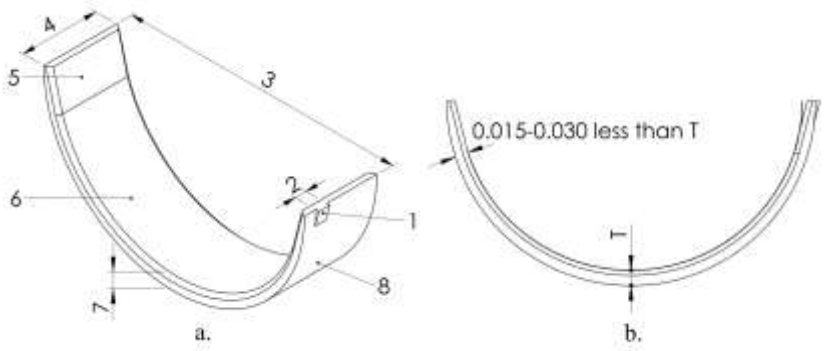

Figure 1.6 Terms and major dimensions of a big-end bearing: 1 Locating lug; 2 Locating lug width; 3 Free spread; 4 Bearing length; 5 Crush relief; 6 Bearing surface; 7 Bearing wall thickness; 8 Bearing back

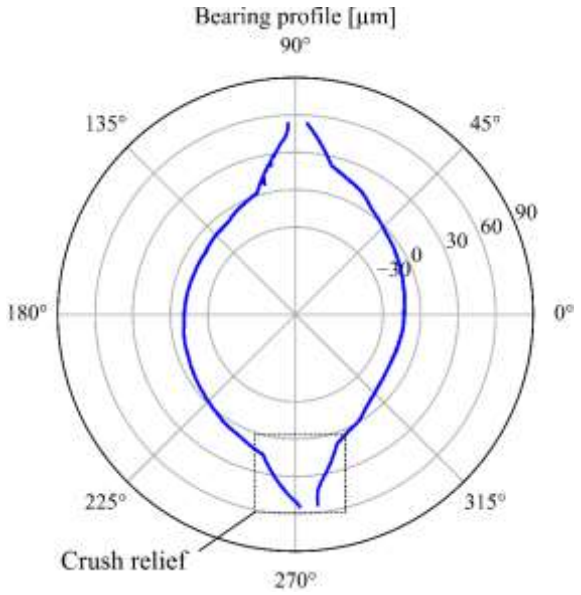

Figure 1.7 Bearing *"forme citron"* and crush relief

1.7. Experimental investigations on dynamically loaded journal bearings

This section describes the experimental work on dynamically loaded journal bearings. The descriptions are classified by the type of test benches: special and engine test benches. Along with the description of the experimental devices, the characteristics of the tested bearings, the measured quantities, and the used sensors are presented.

1.7.1. Special Test Benches

In **1968,** W.L. Cooke [3] designed a machine at the National Engine Laboratory (NEL) with the aim to study dynamically loaded journal bearings. In the cited work, the author does not mention what kind of journal bearing is subjected to study, as the paper aims to present the bench in a general manner. Only an example of a possible dynamically loaded journal bearing is given, that is, a turbine bearing where the load is composed of a synchronous rotating load generated by the unbalanced rotor and a steady load due to the gravity mass of the rotor. The tested bearing is loaded through four hydraulic rams, two horizontal and two verticals (see Figure 1.8). The rams are controlled via electrohydraulic pistons, achieving loads of 5 kN and speeds up to 5000 rpm. An interesting feature of this set-up is that the dynamic load can be around the journal. This feature facilitates an oil hole radial position study without machining new parts. The oil supply can be achieved through the journal or through the bush.

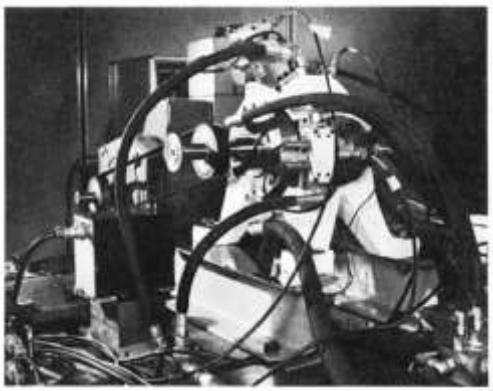

Figure 1.8 NEL machine [3]

SAPPHIRE is a specialized test rig used for the study of bearing materials whose design has been established. Its first mention was in 1973, when Pratt proposed a new machine to test materials for dynamically loaded bearings [4].

Figure 1.9 shows a schematic of the SAPPHIRE machine. The test bearings are mounted inside a rigid connecting rod. The dynamic load is generated using a journal which has a small, controlled eccentricity, with respect to the shaft. The induced reciprocating motion of the connecting rod encounters resistance induced by a hydraulic ram. The magnitude of the maximum bearing load is controlled by a relief valve on the hydraulic cylinder. The bearing is fed with oil through a hole drilled in the connecting rod cap and not by the journal as in an internal combustion engine.

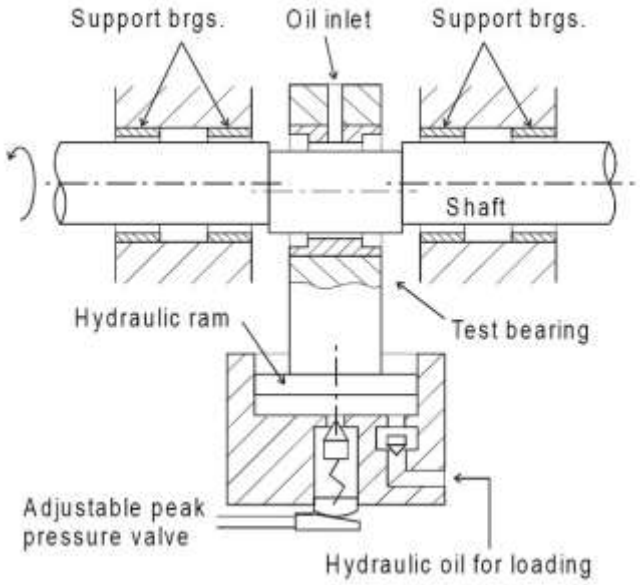

Figure 1.9 SAPPHIRE test bench schematic. [5]

In **1988,** Tripp and Berker [6] measured the minimum oil film thickness (MOFT) on the SAPHIRE test bench. The authors used eight eddy current gap sensors mounted in two orthogonal pairs at each end of the bearing. The tests were performed at a constant speed of 2000 rpm. The dynamic load was up to 20 kN (12 MPa specific load). The bearing bore and width are 64 mm and 25 mm, respectively. The authors calculated the MOFT by comparing the measured clearance with stationary measurements taken with the shaft pressed at the top, bottom, and sides of the bearing. No information about the temperature compensation for the sensors was mentioned. The experimentally obtained MOFT were in good agreement with the MOFT calculated using the Goenka model [7]. It must be pointed out that the maximum eccentricity ratios reached is 0.8. Even though their specific load values were very weak, compared to modern, real combustion engines, their work remains an important milestone of measuring MOFT.

In **1999,** Xu [5] in collaboration with Daido Metal Co. Ltd investigated the influence of wear on the performance of hydrodynamically lubricated bearings. The test was performed at a speed of 3250 rpm with a specific load of 78.4 MPa for a period of 10 hours. The bearing diameter and width were of 35 mm and 17 mm, respectively. A good agreement with a simple simulation wear model, based on minimum film thickness and roughness, was obtained. No clear information regarding the metrological technique measurements were specified.

In **2011,** Kataoka [8] measured the local oil film thickness using the capacitance variation between the shaft and bearing shell. They developed a thin film electrode, embedded inside the

bearing layers, which measures the local capacitance. The authors performed two tests: low speed - low load: 1000 rpm with a load pick amplitude of 20 kN, and high-speed - high load: 3000 rpm with a 40 kN load pick amplitude. The bearing diameter and width were of 42 mm and17 mm, respectively, with a radial clearance of 35 μm. The measurements were compared with an EHD simulation. For the tests performed in low speed-low load conditions, the results matched perfectly. On the other hand, for high speed - high load, the measured thickness was 25% lower than the calculated one. The authors supposed that the difference came from the cavitation phenomenon, which would interfere with the measurement of film thicknesses. Because the air has a relative dielectric constant, approximately half of that of an oil, this led to overestimations in the oil film thickness.

In **2015,** Sander [9] investigated the importance of considering in simulation models. Their work compared experimental results and numerical simulations in terms of frictional torque and power loss due to friction. The tests were performed at speeds ranging from 1000 to 7000 rpm. Two dynamic charges were considered: a moderate charge of 50MPa pick pressure, which corresponds to a 40kN pick load, and a severe one, having a 100MPa pick load (80kN pick load). As lubricant, they used a multi-grade 0W20 oil. The bearing diameter and width were 47.8 mm and 17.2 mm, respectively, with a radial clearance of 30 μm. Four thermocouples measured the bearing shell temperature. A torque sensor measured the friction torque. The authors examined, by comparing with experimental results, the importance of the afore-mentioned parameters in modelling and simulation processes. They concluded that, for an accurate prediction of the behaviour of bearings lubricated with modern multi-grade oils, a model must take all three effects (temperature, pressure and shear rate) into account, especially at high speeds.

Another specialized test bench is the JBM (Journal Bearing test Machine), manufactured by PCS Instruments. The machine was used in **2018** at Imperial College London to study the impact of temporary shear thinning of Visco Modifiers (VM) blends on the friction in a plain journal bearing [10]. The study was an in vitro extension of the work done by Spikes and Marx [11], [12]. The machine was used to measure the hydrodynamic friction of a steadily-loaded engine bearing, lubricated by some of the same VM blends characterised previously. Figure 1.10 shows a schematic of the JBM machine. The journal bearing was mounted inside a big-end connecting rod-like stem. The load was applied via an amplifying system involving a lever arm, either statically, or dynamically, with the use of a cam. Then the load was transferred via a coupling from which strain and load were measured, and the friction force could thus be

approximated. The coupling had also the ability to ensure (but not perfectly), the isolation of the nominal applied force from the lateral load. To compensate this imperfection, the user averaged two measurements with the shaft rotating in opposite directions. Temperatures were measured in the bearing shell proximity. The bearing was fed with oil through a hole drilled in the connecting rod cap, and not by the journal, as in an internal combustion engine. In the published paper, the author applied different static *loads* (10kN, 7kN, 3kN) at 1000 rpm to 3500 rpm shaft speeds. The oil supply temperatures were 60°C, 80°C, 100°C, 120°C, and the oil supply pressure was 150 kPa. The aim of their study was to assess the impact on friction of factors modifying the viscosity in engine bearings. The study was conducted on six different oils, all having the same base oil and same High Temperature - High Shear viscosity (HTHS) of 3.7 mPa·s, and involved using different viscosity modifiers. Furthermore, the authors specified that the viscosity - shear rate dependency at a given temperature was described by a Carreau-Yasuda equation [13]. The authors compared the experimental results with an isothermal model and with a thermodynamic model. They concluded that an isothermal model with a constant temperature equal to that measured at the bearing - housing interface led to satisfactory results.

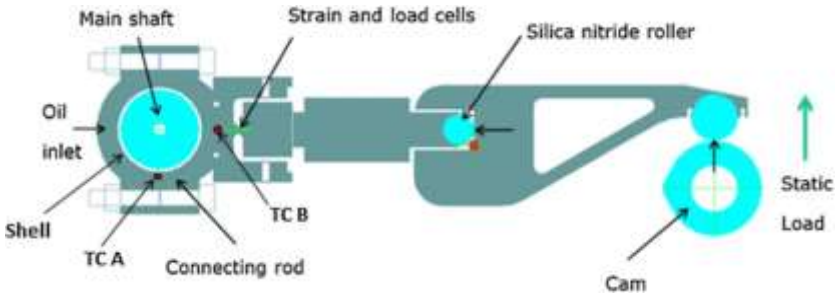

Figure 1.10 Journal Bearing Machine (JBM). [10]

1.7.2. Engine test benches

Due to the complex movement of the connecting rod, one of the greatest issues for the experimental testing is the data acquisition. Several solutions to this challenge stood out over the years.

The first one, which can be called *"direct method"* is the grasshopper linkage. This method carries the sensor cables out of the engine crankshaft through a mechanical linkage which follows the connecting rod path (see Figure 1.11).

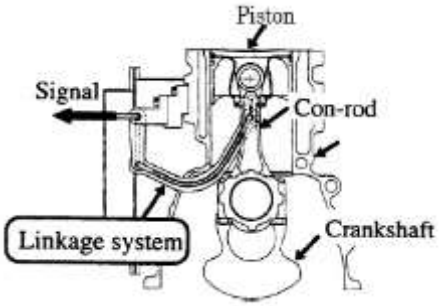

Figure 1.11 Grasshopper linkage [14]

The second method is the wireless telemetry method. In general, a radio or Bluetooth communication protocol sends the data from the engine [15]–[18] .

The third solution is to mount the sensors inside the crank pin. In this manner, the sensor cables are carried out through the crankshaft and the data is acquired by using slip rings.

In **1977,** Goodwin [19] measured the connecting rod big-end bearing temperature inside a medium sized diesel marine engine. Through this paper, the authors established the proof of concept for the grasshopper linkage.

In **1992,** Masuda [20] measured the oil film pressure distribution. The authors performed the tests on a highly modified internal combustion engine. The concept was based on the idea of transferring the load of an internal combustion engine to another connection rod, statically mounted outside the engine (see Figure 1.12). The gas pressure from the combustion engine was transferred through a mechanical linkage to the external connecting rod small-end. The pressure sensor was installed inside the shaft. Slip rings were used for data transfer. The tests were performed at speeds of 4000 rpm and 6000 rpm corresponding to 9.8 kN and 21.6 kN loads, respectively. The bearing diameter and width were 45 mm and 18 mm, respectively, with a diametral clearance of 60 µm. The authors observed a 25% decrease in the maximum pressure and a wider pressure angle on the cap side, compared to the shank side, in circumferential direction. Moreover, for the axial direction of the bearing, it has been noticed that, on the cap side, the pressure distribution deviated from a parabolic curve; these phenomena were due to the bearing housing elasticity. Another important remark of their work is that, as the inertial load increased (i.e. speed increased) the pressure distribution on the cap side increased, and changed from a single hump Gauss distribution to a double hump pressure distribution. This phenomenon was mainly due to the bearing elasticity. As the maximum pressure values, the authors measured 60MPa (tensile – cap side) and 80MPa (compression – shank side) at 4000 rpm and a 9.8 kN load. For the second running point (6000 rpm and 21.6 kN load), they

observed a higher oil film pressure distribution and a wider pressure angle due to the larger load input.

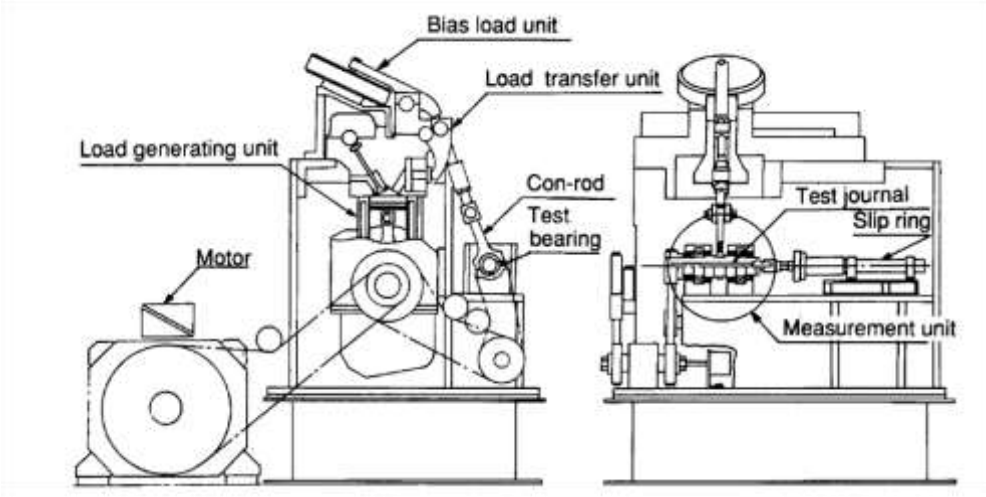

Figure 1.12 Masuda test bench schematic [20]

In **1995** and **1997,** Ozasa et al. [21] [22] measured the journal orbit on a diesel engine. The maximum rotational speed was 5000 rpm. The bearing diameter and width were 50.4 mm and 18.8 mm, respectively, with the diametral clearance of 75 µm.

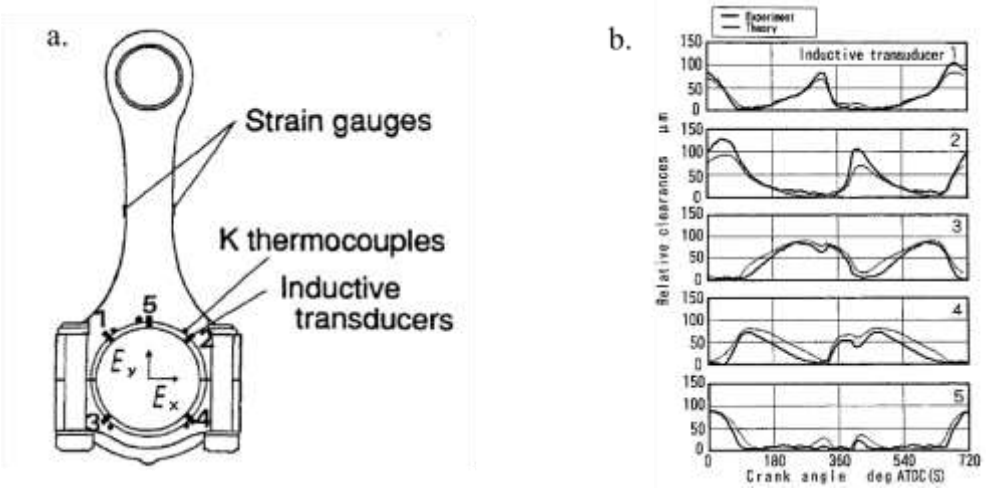

Figure 1.13 Ozasa a. sensor location, b. eddy current cap sensors measurements comparison with numerical results [21] [22]

Four eddy current gap sensors were orthogonally mounted, with a 45° rotation from the shank axis. A fifth sensor was mounted on the shank side, colinear with its axis, to measure the distortion of the bearing cap (see Figure 1.13 a.). Additionally, the authors used strain gauges for measuring the tensile force and bending moment of the shank. They observed that, when the rotation speeds increase (2000, 3000, 4000 rpm), the measured journal orbit was larger than the clearance. This observation was attributed to the bearing deformation under high inertial

loads and proved the need of EHL modelling for such bearings. The authors pointed out a good agreement of the experimental data and EHL simulation in terms of journal orbit (see Figure 1.13 b.).

In **1998,** Suzuki et al. [14] analysed the big-end bearing lubrication under oil starvation inside a real engine. Bearing temperature, journal orbit, contact, oil supply pressure, and oil supply flow were measured (see Figure 1.14).

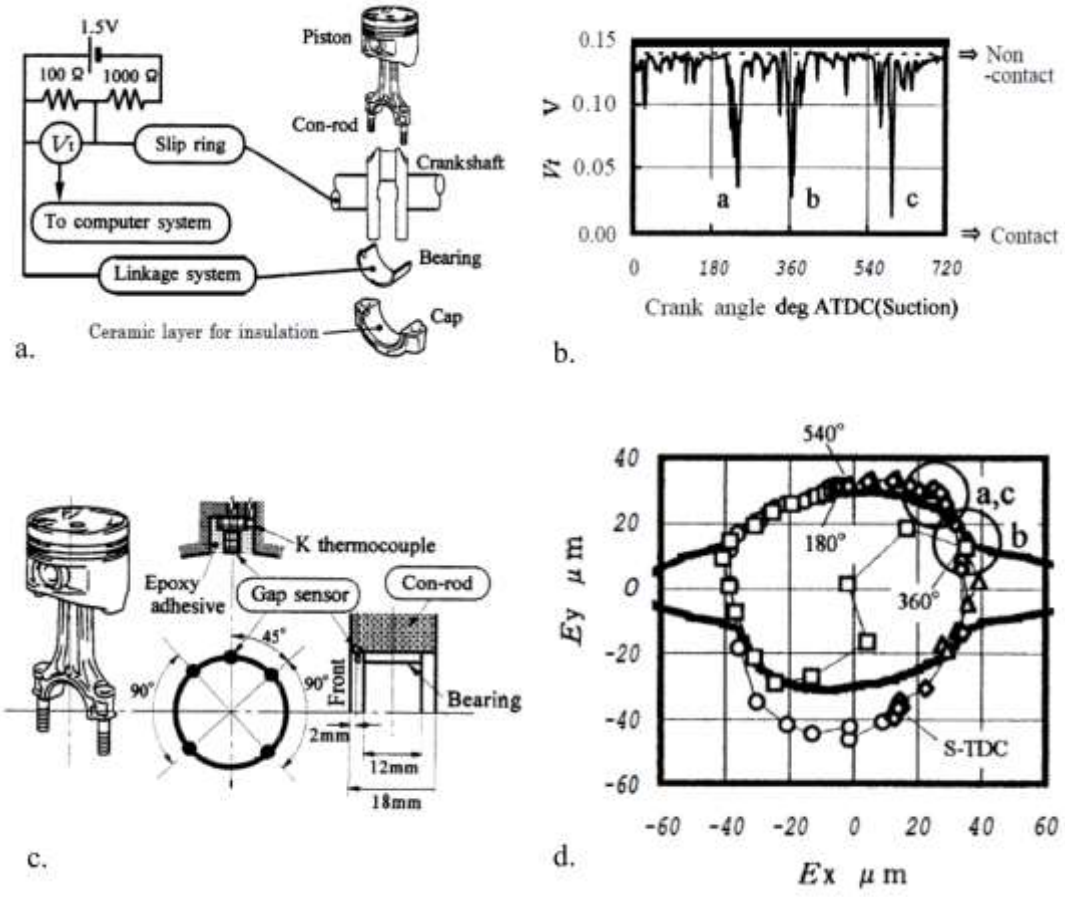

Figure 1.14 Suzuki a. Contact measurement schema; b. Contact measurements results; c. eddy current gap sensors schema; d. results eddy current gap sensors schema [14]

The sensor cables were carried out from the engine via a linkage system. The journal orbit was measured via eddy current gap sensors, while the contact was measured via the voltage drop method. The bearing diameter and width were 40 mm and 12 mm, respectively, with a diametral clearance of 51 μm. The authors performed tests at speeds of 3000 rpm, 4000 rpm and 5000 rpm. They showed that the contact of the journal-bearing shell was found on both the eddy current gap sensors measurement and the contact voltage. Additionally, the authors observed that the voltage decent ratio tends to decrease with speed. Also, the voltage decent ratio was found to be hardly affected by the increase of the oil supply flow rate.

In **2000,** Goodwin et al. [23] measured the big-end bearing journal orbit. For this study, the author installed two eddy current gap sensors inside the crankpin of an internal combustion engine. The sensors were mounted inside the crankpin at an 90° with respect to each other, while the cables were carried out of the engine through the crankshaft. Slip rings were used for both power supply and data transaction. Furthermore, the paper put great emphasis on the sensor thermal calibration. The author performed a calibration at 20°C, 40°C and 60°C, used further to extrapolate the measurements. The measurements were performed at a speed of 3000 rpm. No direct information was given about the load. The author mentioned the engine output power: 1.2 kW, 4.5 kW, 12 kW and 17 kW. The bearing bore and width were 44 mm and 22 mm, respectively. The measured orbits were compared with measured bearing clearance spaces. Goodwin pointed out through his work that for a connecting rod big-end bearing, the eccentricity ratio can be greater than 1. The author observed that the journal eccentricity overpassed by 20% the available bearing clearance space on the cap region for the higher power outputs test. He supposed that the difference came from the bearing shell deformation under high loads.

In **2000,** Mian et al. [24] measured the oil flow rate and bearing temperature for grooved bearings. For this study, the oil supply system of a commercial engine was modified in order to isolate the studied bearing (see Figure 1.15).

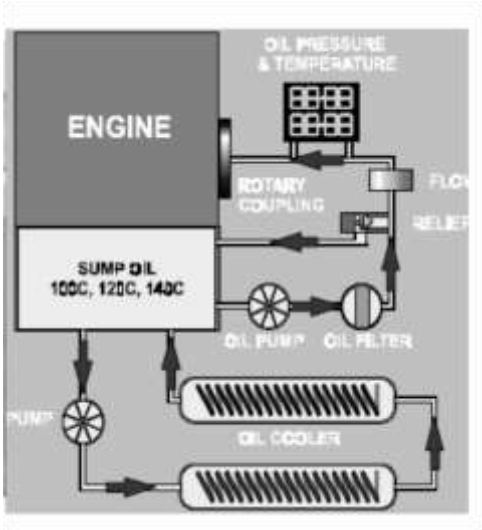

Figure 1.15 Mian test bench schematics [24]

The authors have used the same linkage in order to log the measured data. The speed of the studied engine was 6500 rpm. The diameter and width of the bearing were 49.6 mm and 19.1 mm, respectively, while the diametral clearance was 40 µm. Two types of bearings were

studied: a full groove and a half groove. They concluded that a full groove improves the thermal and oil flow of the bearing.

In **2002** Moreau et al. [25] measured the fluid film thickness of a connecting rod big-end bearing inside an internal combustion engine through eddy current gap sensors. Four sensors were placed inside the centre of the connecting rod, their axes been located at 40° with respect to the connecting rod axis (see Figure 1.16 b.). The sensors signal was carried out of the engine crankshaft through a mechanical linkage (see Figure 1.16 a). The measurement was performed at speeds of 1250 rpm, 2000 rpm and 2500 rpm. The tests were stopped due to mechanical linkage breakage at higher speeds. The diameter and width of the bearing were 50 mm and 19.2 mm, respectively, with the diametral clearance of 50 µm. A good agreement between the experimental measurements and the simulation was found. As previous works on the journal orbit, Moreau concluded that the inertial loads generate elastic deformations of the bearing, as the journal orbit increases about 50% of the actual clearance.

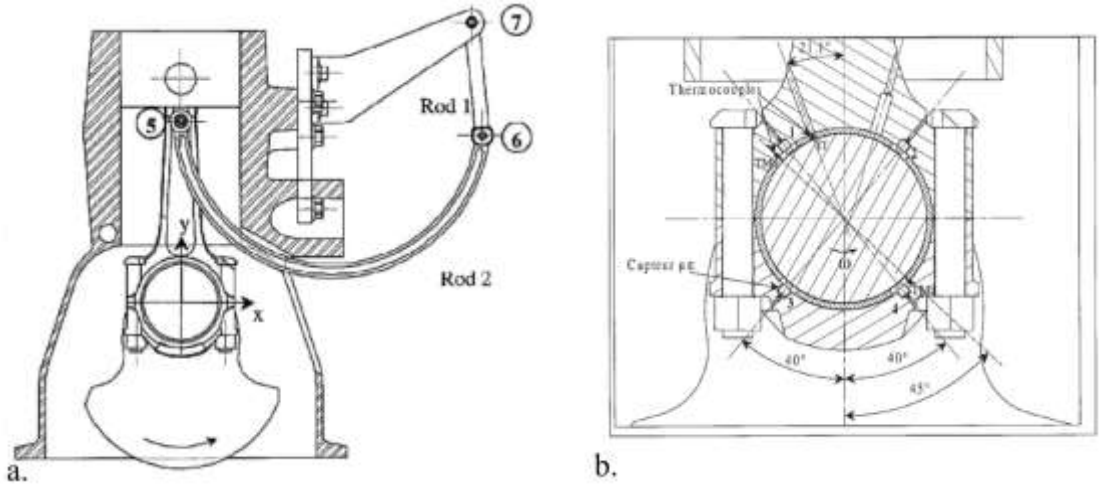

Figure 1.16 Moreau: a. test rig, b. sensor location [25]

In **2007,** Merritt et al. [26] used a 2.0L gasoline engine to study the effects of inertia on the fluid film thickness and pressure. The connecting rod was equipped with four strain gauges (see Figure 1.17). Two of them were placed opposite in the connecting rod shank, and were used to measure the bending moment. The third strain gauge was placed on the big-end side, while the fourth one was placed on the cap side. The sensor cables were carried out of the engine using the grasshopper linkage. The bearing bore deformation was calculated through a commercial finite element (FE) software; furthermore, the deformations were introduced into an EHD algorithm (SABRE-EHL). The strain gauges measurements served as a validation

means for the FE analysis. The authors concluded that the inertia effect on the oil film thickness became important for rotational speeds greater than 3000 rpm.

Figure 1.17 Merrit connecting rod grass hopper linkage [26]

In **2007,** Wang et al. [27] measured the oil flow rate and bearing temperature on a 2.0L gasoline engine. Four thermocouples were installed within the bearing shell. The oil supply was modified in order to isolate and measure only the oil flow rate of the studied bearing. The oil flow rate measurements were compared with theoretical results obtained for the isothermal elastohydrodynamic and thermo-elastohydrodynamic models. A good agreement was found between the experimental measurements for oil flow rate and the EHL and TEHL calculations. Lastly, a better oil flow rate prediction for higher speeds (6000-7000 rpm) was given using the THEL model.

During recent years, thanks to the improvement and miniaturisation of electronic components, wireless telemetry systems became more and more accessible to be created and implemented on connecting rods. All the studies presented hereafter use in house electronic telemetry models.

In **2008,** Isarai et al.[18] developed a new telemeter system, capable of multipoint measurements. The module was tested on a gasoline engine at speeds up to 6000 rpm. The authors did not detail the wireless communication protocol, neither did they offer information on the electronic circuits details. Robust measurements of the piston skirt and connecting rod strain were performed.

In **2019** and **2021,** Fang et al. [17], [28] developed a new telemetry system (see Figure 1.18). The authors fully described the communication protocol used for logging the data (ZigBee). The transducer was mounted on the connecting rod, while the receiver antenna was placed inside the engine crankcase. As power source, the authors used rechargeable batteries. A magnetic charge port was used for charging the batteries while testing. In order to synchronise the measurements, an infrared trigger was installed. As sensors, the authors installed strain

gauges to measure the tensile and compression forces on the shank. Their goal was to investigate the friction at the piston ring-liner interface.

Figure 1.18 Fang telemetry system on a connecting rod [17], [28]

This section presented the most relevant experimental work on connecting rod journal bearings. Two types of test rigs stand out, the firs one being the special test rig, which is meant to simplify and ease the bearing instrumentation at the cost of real testing conditions, while the second category is the engine test bench, which has the advantage of real testing condition, but which makes the implementation of measurements techniques difficult. From the upended presented background work, several measurement techniques stands out. For the measurement of the orbits and distance between shaft and journal, eddy current gap sensors have been employed by the authors. Concerning the mounting solution, several authors included the sensors inside the shaft, while others mounted them on the connecting rod big-end. In the same realm of measuring film thickness, the capacitance (local or global) and voltage drop techniques gave good results.

Based on this background study, the present work focuses on the eddy current gap sensors and voltage drop techniques. In addition, the bearing-housing interface temperatures are monitored on several points, and the oil supply flow rate, temperature, and pressure are monitored as well.

1.8. Numerical simulation on conformal EHD

The Elasto-Hydro-Dynamic (EHD) lubrication applies to a situation where the elastic deformation is of the same order of magnitude as the fluid film thickness, and therefore, it cannot be ignored. Two types of EHD models arise, based on the type of contact, namely the non - conformal model (see Figure 1.19 b.) and the conformal model (see Figure 1.19 a.), respectively. In non-conformal EHD, the elastic deformation is due to the local compression, while for the non-conformal case, is caused by bending.

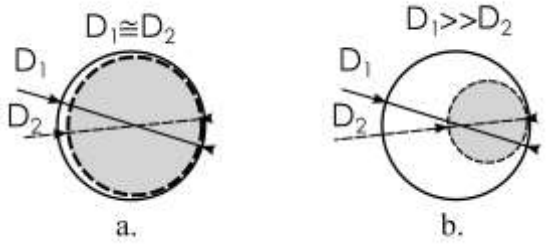

Figure 1.19 Types of contacts: a. conformal; b. non-conformal

Several review papers [29], [30] presented numerical solutions for the conformal contact EHD lubrication model. The following section will present through a critical point of view several papers dealing with the conformal EHD modelling of connecting rods big end bearings.

According to Allmaier and Offner [29], the beginning of the modern methods for conformal EHD simulation begins in 1973, with the work of Oh and Huebner [31]. The elasticity equation of the 3D bearing housing is solved simultaneously with the hydrodynamic equations, in order to predict the deformation of the housing and the film pressure distribution. The EHL analysis relies mainly on the coupling between the structural dynamics and fluid dynamics.

1.8.1. Structural Dynamics

The representation of the solid components requires a finite element or finite differences discretisation for both the lubricant and the elastic structures. For EHL problems, one of the unknowns is the solid deformation generated by the hydrodynamic pressure within the lubricant. Therefore, the solution requires information about the solid compliance (stiffness).

Several authors [32]–[45] used precalculated compliance matrices at the bearing surface nodes. The matrices are often obtained through commercial finite element analysis software and matrix operations. According to Bonneau [46, pp. 163–180], the method is based on computing the elementary solutions obtained by loading the structural mesh by a unitary force, which is normal to the bearing surface. Once calculated, the elementary solutions are re-introduced within the computing algorithm. The nodal elastic deformation vector of the solids is then computed directly from the discreate nodal load vector and the solid compliance matrix. This technique is also referred in the literature as being quasi-static [29], [30], [47].

Recent publications (from 2013 to 2019 [48]–[51]) integrated lubricated contact models into multi-body system commercial softwares (MBS). From a mathematical point of view, the software couples the first order Differential Algebraic Equation systems (DAEs) for each component present in the studied mechanism with mixed lubricated contacts. The DAEs are used to compute the interactions between the parts, for example, bearing shell - crankpin. The required structural matrices are pre-processed using a commercial software.

1.8.2. Fluid Dynamics

Automotive oils are complex mixtures of base oils and additives. Therefore, their rheological properties become complex. New emission targets and fuel economy drives the automotive manufacturers to increase the engine efficiency. One of the solutions is the usage of lower viscosity lubricants [52] in order to reduce the power loss through viscous shear. According to [53], the new multi-grade oil standards demand a drastically viscosity decrease. The new formulation of multi-grade lubricants is standardized for one set of conditions, which are defined as High Temperature High Shear (HTHS) viscosities. It is widely known that the new HTHS oils have a non-Newtonian behaviour [54]. On the other hand, researchers as Macián and Tormos [55], [56] noticed a decrease of hardware durability by using ultra low viscosity oils. Bair [57], [58] pointed out the importance of the viscosity dependence on pressure and temperature. Moreover, pure hydrodynamic lubrication regimes were replaced by mixed lubrication. In addition to the change of the lubrication regime, the simulation methods must inherit also the robust rheological properties of the lubricants, such as the viscosity dependency on pressure, temperature, and shear rate.

This next section is structured around the fluid dynamics simulations. All the presented works are based on the Reynolds equation, which is modified depending on the complexity of the required analysis. For this work, the rheological properties of the lubricant and cavitation models are analysed.

Regarding the rheological behaviour of the lubricant, several models are proposed and used within the literature. For the temperature dependency on the viscosity, the Vogel model [59] is widely used. The pressure dependency is often modelled with the Barus model [60], while the shear rate dependency follows the Cross law [61]. These models are generally referred to using the following notations $\eta(T)$, $\eta(T,p)$ and $\eta(T,p,\dot{\gamma})$. Even more, the interdependency of the piezoviscous effect and non-Newtonian behaviour makes the measurements very difficult [30].

Allmaier et al. et al. [62] accounted for pressure dependent behaviour using the Barus law. Four different monograde oils are tested: SAE10, SAE20, SAE30 and SAE40. Their viscosity oil-model was derived from the measured temperature dependency, and the pressure dependency by applying the Barus coefficients measured by Bukovnik and Offner [63]. Their work compared two simulation models, one accounting just for temperature dependency (base oil-model), and the second accounting for the pressure dependency with experimental data, in terms of friction loss. The authors concluded that the base oil-model was able to predict well the friction power loss for pure hydrodynamic lubrication. On the other hand, for more severe running conditions, (70 MPa and 120 MPa specific pressure) the model largely overestimates (with 30%) the experimental results. The base oil - model underpredicts the average friction torque, which clearly shows the importance of pressure dependency on viscosity. In the case of extended model, the results well agree with the experimental friction loss measurements.

Sander [9],[64] accounted for temperature, pressure and shear influence on the viscosity. Their study compared the experimental and numerical results in terms of friction power loss. For numerical reasons the authors used the exponential Vogel law for viscosity-temperature dependency. The viscosity pressure dependency was measured using a quartz viscosimeter and then fitted using the Barus law.The viscosity shear rate dependency was also measured and described by Cross law. Finally, the authors measured the density for different pressures and temperatures. They calculated the friction torque by integrating the shear stress over the bearing surface. The authors concluded that by using only the pressure or non-Newtonian behaviour the simulation accuracy increases only in certain operating conditions. Therefore, the combination of both pressure and non-Newtonian oil behaviour must be considered. For example, if only the

pressure dependency is considered, the friction torque is overestimated especially at high rotation speeds.

Fatu et al. [65] performed numerical analysis using a global thermo-elastohydrodinamic model taking into account the effects of viscosity dependence on temperature. Their computation considered the Gecim non-Newtonian model and Barus law for pressure dependency. Concluded that the non-Newtonian effect cannot be neglected for high speeds engines, but the pressure dependency is more important than the non-Newtonian effect.

1.8.3. Cavitation models

In its simplest formulation, the Reynolds equations assumes that the fluid film domain is fully occupied by lubricant. This is not always the case: negative pressures in the diverging clearance can lead to high tensile stresses and cavitation or film rupture may occurs [66]. Several algorithms are available in the literature to predict those effects.

Two types of cavitation models are intensively used. The first one is Murty's algorithm [67]. The concept is based on the idea of searching active and inactive zones based on pressure threshold. The models do not consider continuity equation, therefore no mass flow continuity at the reformation film boundaries. In 1984, Oh [68] applied Murphy's algorithm for a EHD study. Through his work, Oh, simultaneously solved the Reynolds equation and the load balance. The pressure and eccentricity are computed in the same time by the use of Newton - Raphson method.

The second model is described by the Jakobsson, Floberg[69] and Olsson[70] and is known in the literature as JFO algorithm. The algorithm takes into consideration the continuity equation. For numerical computation ease, Elrod [71] modified the JFO algorithm and used finite differences method. Their results agreed with experimental observations.

In 2001 Bonneau and Hajjam [72] purposed a new method based on the JFO algorithm. In order to find the active and inactive zones, the authors introduced a modified Reynolds equation. The finite element method allowed to take into consideration all the boundaries condition needed to be satisfied by the new purposed algorithm. Other authors treated the cavitation with the JFO models [48], [51], [73]–[75].

1.8.4. Coupling: between the structure dynamics and fluid dynamics

At its core, the EHL solution relays on the coupling between the fluid and structural dynamics. Traditionally, the coupling is addressed by using the nodal or modal approach [29].

The modal approach is less used in the literature. According to this method, the solid displacements are computed from linear combinations of modal shapes. The nodal method is more used by authors. The displacement in this case is computed directly with the use of linear compliance matrices of the elastic structures. According to Profito [76] two nodal sub-methods are identified. The first one is called the nodal indirect (or monolithic), this method implies sophisticated Newton-Raphson solutions schemes. All equations are solved simultaneously. The second sub-model is referred as nodal direct (or partitioned): the hydrodynamic and structural problems are addressed and computed separately. The main advantage of this method is the ability to use optimised codes for each of the problems (structural and fluid). owever, when the deformations of the solids are important, this method does not converge

1.8.5. Commercial simulation codes

Over the years, researchers developed simulation codes with the purpose to predict the phenomenon inside journal bearings. Some of their work evolved into polished software either commercials or just internal tools for bearing manufactures. In the following section are listed and briefly presented the most published ones.

AVL EXCITE™ is a rigid and flexible multi-body dynamics software (MBS) for power train analysis. Initially was developed for rotor dynamic analysis. Furthermore, the software was updated with elastohydrodynamics models, enabling tribological simulations. The software's theory basis can be found in [50], [74].

From a mathematical point of view, the software is coupling first order Differential Algebraic Equation system (DAEs) for each body present in the studied mechanism with mixed lubricated contacts.

The DAEs are used to compute the global and local vibration motions. The required structural matrices are pre-proceed using a commercial software. Then the DOF are condensed in order to reduce computational time for the MBS simulation.

The mixed lubricated contacts are represented by oil film lubricated contact and dry contact models. The oil film lubricated contact is an averaged Reynolds equation solved using the Newton – Raphson method. Also, the equation includes the surface roughness influence introduced by Patir and Cheng model [77].

The average Reynolds equation is extended with a cavitation algorithm by Jacobson - Floberg - Olsson. As well aware model based on Archard's law is considered.

SABRE (Software for Analysis of Bearing Reciprocating Engine) is a computer program, which has been developed by Glacier Vandervell R&D as detailed by H.Xu et al in [5]. This software was based on the ELAN software code which was originally developed by McIvor Fenner at Kings College, London [78]. In 2007 Glacier Vandervell R&D becomes property of MAHLE. SABRE will become an internal lubrication software for the bearing manufacturer.

The modern software is divided into two modules an analytical and a numerical one. The first one is SABRE-M, a routine simulation, which utilises the mobility method proposed by Booker [79]. This tool is based on the mobility method curve fitting from the finite bearing theory to simulate the hydrodynamic lubrication in steady-state conditions. As results, the software can predict specific load, minimum oil film thickness, operating temperature, oil flow rate and power losses [80]. The advantage of this approach is that the computational time is shorter in comparison to a finite element analysis method, giving the manufacturer a fast and raw idea at the kick off stage of a new bearing design project. A limitation of code comes from the assumption of rigid body and fully folded conditions.

The second module, called SABRE-TEHD is a simulation package used for performing Thermo-Elasto-Hydrodynamic Lubrication (TEHL) analysis of bearing systems. The tool utilises finite difference numerical method to solve the non-linear Reynolds equation in bearing clearance space. In comparison with the above-mentioned approach, this one takes in consideration more complex details such as the full bearing geometry: clearance, crush relief, etc. The code requires the structure stiffness i.e. connecting rod, bearing, crankshaft, information provided by a commercial structural finite element analysis software. As output the software is able to predict oil film pressure, oil film thickness, power loss, oil flow rate, distributed temperature and wear.

The above-mentioned codes have been subject of several scientific papers tacking subjects as: wear [5], oil flow rate [24], [27], [81] oil viscosity [80].

1.9. ACCEL software

All numerical calculations presented in chapter 3 of the thesis were performed with the ACCEL software. ACCEL stands for *L'**A**nalyse et le **C**alcul des **C**ontacts **E**lastique **L**ubrifies or the analyse and computation for lubricated elastic contacts*. It is a TEHD tool based on the finite element method designed for the numerical simulation of all types of bearings whose operation can be considered alone. The connecting rod big end bearing is a representative example. A detailed description of the theoretical and numerical models implemented in the software can be found in the references [46], [82]–[84].

ACCEL can take into account all rheological, geometrical, physical or operating parameters that may influence the operation of ICE bearings: dynamic load, thermo-viscous, piezo-viscous or non-Newtonian lubricant behaviours, geometrical features such as the crush relief, the lemon shape or other shape defects, mixed lubrication conditions, wear, cavitation phenomenon, etc. In order to efficiently consider, the elasticity of the housing and/or the shaft, it is coupled with commercial finite element software such as Abaqus or Ansys. Accel solver is based on a modified Newton-Raphson algorithm, which allows it to achieve a fast convergence rate even for highly nonlinear problems.

1.10. Conclusions

This chapter described the experimental and simulation work on big-end connecting rod journal bearings. From the experimental point of view, it has been noticed that two types of testing rigs stand out. The first type are the special testing rigs. Their purpose is mainly to ease the connecting rod instrumentation while keeping as close as possible the real ICE conditions. The second category is the real engine test rigs. The main advantage are the real testing conditions, but the data logging is difficult to perform due to the complex motion of the connecting rod. Two methods for data logging stand out. The first one is a mechanical linkage which carries out the sensor cables. The biggest disadvantage of this methods is the mechanical reliability. The second data logging technique is the wireless telemetry which become to be more and more accessible due to electronics component miniaturization and availability.

Furthermore, several measurement techniques for different tribological quantities have been noted. The first one is the eddy current gap sensors which are installed on both, engine and special testing rigs. Authors using these techniques claimed to measure the journal orbit or fluid film thickness. All the authors pointed out the complexity of the calibration for those types of measurements. A second measurement technique is the local and global capacitance. Authors treated the journal bearing as a capacitor in order to measure the global or local film thickness. In their work they related the film thickness with the measured capacitance. The conclusion was that the measurements give quantitative and qualitative information about the fluid film height. Another technique, similar to capacitance is the voltage drop which is easier to implement. On the other hand, the measurements tend to have a qualitative information rather than a quantitative one.

From a numerical point of view, it has been noticed the increase complexity of the EHL models over the years. The drastically demand on fuel consumption efficiency and pollution thresholds drives new oil blends formulations. Complex viscosities dependencies with temperature, pressure and shear rate must be considered in order to improve the accuracy of the simulations.

The next chapter, Chapter 2, will tackle the experimental methods and calibrations performed along this study. The chapter begins with a description of the used testbench. Furthermore, the metrology technique used to measure the bearings is described. The chapter ends by presenting the method and calibration for the eddy current gap sensors and voltage drop.

(this page intentionally left blank)

Chapter 2 Experimental methods and calibration

This chapter is dedicated to the description of the developed experimental methods and calibration. The thesis is built around an experimental core which will serve as comparison basis for the simulation. Several new features are added to the bench during the thesis. The first one is to develop the transversal loading of the MEGAPASCALE. Second is the improvement of the LabView software of the control and data acquisition PCs. New measuring methods are added as well. All of the improvements are described in the sections to come.

Firstly, the description of the test bench (MEGAPASCALE) is made, then the design of experiments on which the tests are based, the techniques and the calibrations for each measurement technique. All recorded experimental results analysis and simulation comparison are delayed until Chapter 3.

2.1. Test rig description

The experimental apparatus used for this research is known under the acronym of MEGAPASCALE (**M**achine d'**E**ssais pour **G**uidage d'**A**rbre par **PA**liers **S**ous **C**harges **AL**ternativées **E**levees) and is operated by the researchers of the Pprime Institute located in Angoulême. The purpose of MEGAPASCALE is to performed experimental tests on connecting rod bearings where the inertial effects are predominant. As performance characteristics, the machine is designed to reach rotational speeds up to 20.000 rpm, 90 kN of traction - compression charge and 20 kN transversal charge.

2.1.1. Bench overview

A schematic representation of the experimental setup is shown in the Figure 2.1 through an isometric view. As a general description, inside MEGAPASCALE are mounted two connecting rods which are immobile, so that the scientific instrumentation is easier to install than in an internal combustion engine, where the connecting rod has a complex motion.

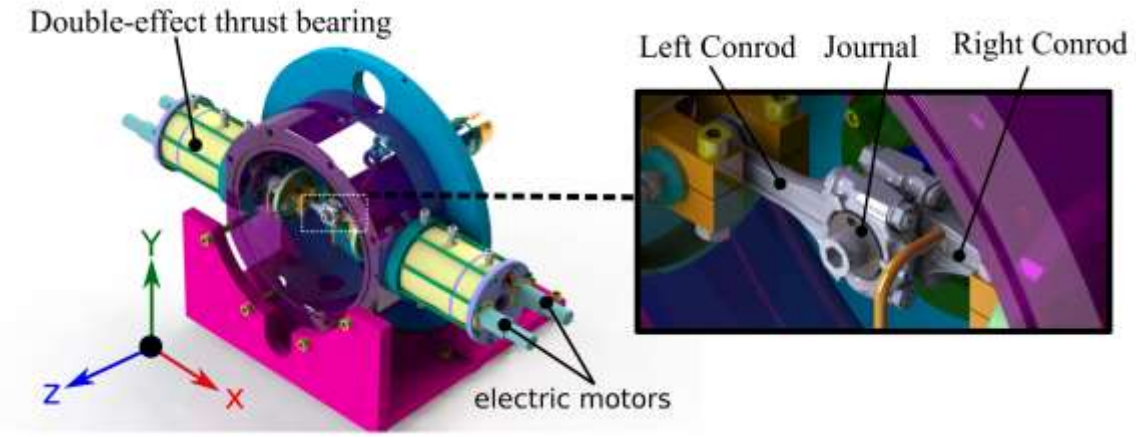

Figure 2.1 MEGAPASCALE isometric view and connecting rods location detail

The connecting rods are placed opposite to each other as shown in Figure 2.1 and Figure 2.2. The so-called right connecting rod (marked as “1” in Figure 2.2.) serves as study dummy and has all the sensors attached on it. The left connecting rod (2), the opposite one, ensures the balance of the charges inside the machine. A journal (3) with a particular geometry (described in section 2.1.3) is installed inside the connecting rod bore. This piece is tightened with a hollow bolt (4) to the main shaft, which is spun by an electric motor and supplies with oil the line for the bearings. Both connecting rods are held by the small end through a stem (5) which is connected through a rod to a hydrostatic double-effect thrust bearing. The dynamic charge is applied to the connecting rod by the variable displacement of the journal and generates, therefore, a sinusoidal shaped force. At the same time, the amplitude is controlled by adjusting the stiffness behind the small end stem through the double-effect thrust bearing.

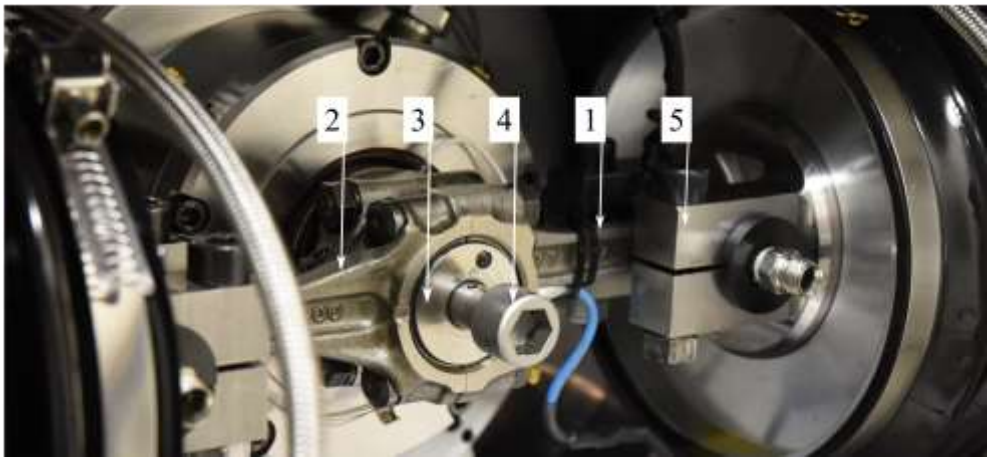

Figure 2.2 MEGAPASCALE load system

2.1.2. Loading system

The charge on MEGAPASCALE is composed of two components. The first one is the so-called traction - compression load, which is the X axis component (see Figure 2.3) generating traction and compression load. The second one is the transversal load, in the Y direction. Both loads are controlled based on the same mechanical principle (see Figure 2.4) but using different design approaches which are further explained.

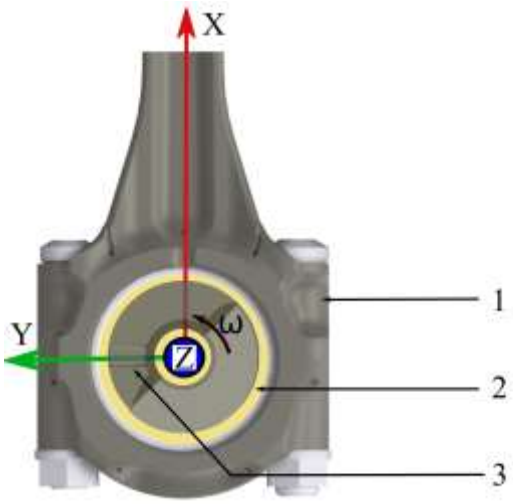

Figure 2.3 Coordinate System: 1. Connecting rod; 2. Journal; 3. Oil Supply Hole

The dynamic load amplitude depends on three controlling factors. The first one is the journal right (e_R) and left (e_L) eccentricities, the second is the connecting rod stiffness (K_c) and the third is the adjustable stiffens (K_f) of the locking system. All of three factors are schematically presented in Figure 2.4.

The first two are established in the predesign phase along with other custom parts needed to accommodate the tested connecting rod and they will remain fixed for the testing campaign.

The journal eccentricities are computed through an algorithm which aims for the wanted charge amplitude and depends on the connecting rod and machine stiffness (including the hybrid bearings which held the shaft) and takes in account the dynamic effect of the hydrostatic double effect thrust bearings. The detailed algorithm is presented in reference [85].

The connecting rod bearing stiffness (K_c) is calculated by using a CAE software.

The last controlling factor, the adjustable stiffness K_f, is controlled during the actual tests and allows the user to easily charge the system.

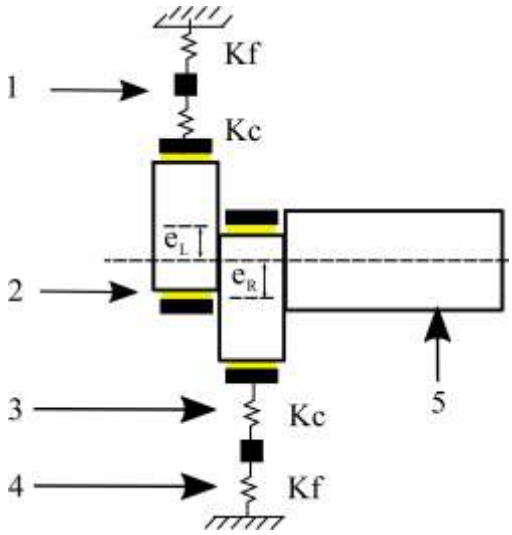

Figure 2.4 MEGAPASCALE loading principle: 1. Force Sensor; 2. Journal, 3. Connecting rod; 4. Double-Effect Thrust Bearing; 5. Shaft

In the case of the traction - compression load, the locking system is a double-effect thrust bearing. The displacement imposed by the journal eccentricity (10 in Figure 2.5) to the connecting rod (9) is transmitted via a beam (6) to the floating piston (2). The adjustable stiffens K_f is modulated by the controlling valves (1 and 3) which regulates the oil outlet flow and therefore the charge amplitude (as seen in the close-up in Figure 2.5). The valves opened/closed by means of a gear system (5) moved by independently controlled electric motors (4). An advantage of this set up is that it allows to adjust the average value of the journal sinusoidal charge (shift the zero) to realistic ICE charge values.

The load is measured using a strain gauge force sensor (7) mounted between the small end stem (8) and the floating piston (2).

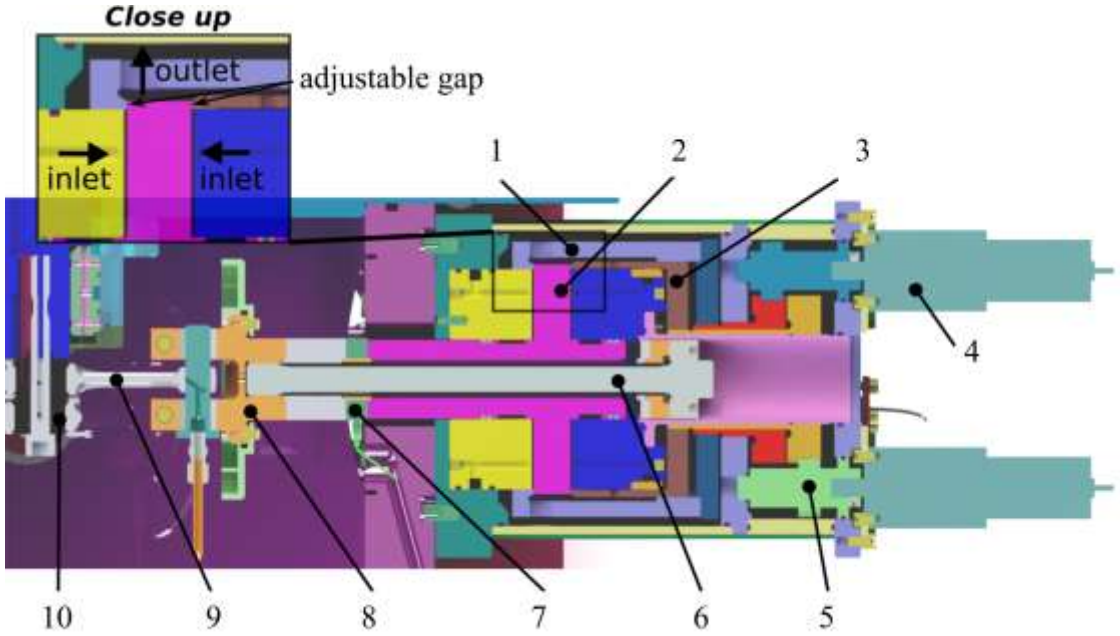

Figure 2.5 MEGAPASCALE axial locking system: 1. Traction Control Valve; 2. Floating Piston 3. Compression Control Valve; 4. Electric Motors; 5. Gearing; 6. Beam; 7. Force Sensor; 8. Stem; 9. Connecting rod; 10. Journal

In the case of the transversal load, the working principle is the same as for traction°-°compression loading (see Figure 2.6) but instead of using a double effect thrust bearing to control the load amplitude it uses a variable length beam.

As in the case of axial looking system, the journal (1) pushes the connecting rod (2) towards a rod (4) which is clamped to the connecting rod by the clamp (3). At the opposite end, the rod is connected to a steal beam (6) which is located inside of two brass bushings (7). The bushes are connected to electric motors (8) through a trapezoidal screw (9).

In order to control the transversal load amplitude, the motors push the bushings back and forth and changes the embedded sections of the steel beam. In such manner, the adjustable bending stiffness K_f and therefore the transversal load amplitude is controlled.

It has to be mentioned that the presented study uses for the first time the transversal load system of MEAGAPASCALE. An intensive labour during the beginning of the thesis was done. Despite effort, the transversal load cannot reach up to 2800 N pick to pick amplitude due to the mechanical clearance between different parts. The transversal loading was carried out only for a connecting rod of an engine used in a gasoline car (mentioned in the text as the Renault RS connecting rod). A second test campaign was conducted on a connecting rod used by Kawasaki motorcycles (mentioned in the text as the Kawasaki ZX10 connecting rods). Due to the reduced dimensions of the last one, the transverse component of the load could not be achieved.

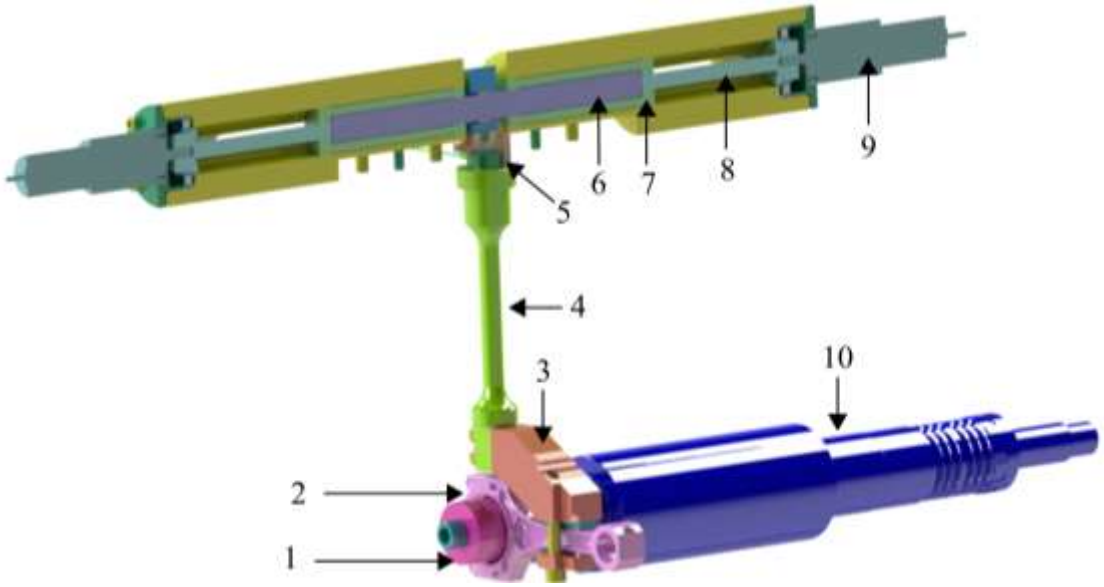

Figure 2.6 MEGAPASCALE transversal locking system 1. Journal; 2. Connecting rod; 3. Clamp; 4. Rigid rod; 5. Force sensor; 6. Beam; 7 Brass Bushing; 8. Screw; 9. Motor; 10. Shaft

An example of traction - compression measured charge is showed in the Figure 2.7. The positive charge is compression, while negative is tensile. It should be noticed that the cycle completes after 360° and not 720° as in an ICE.

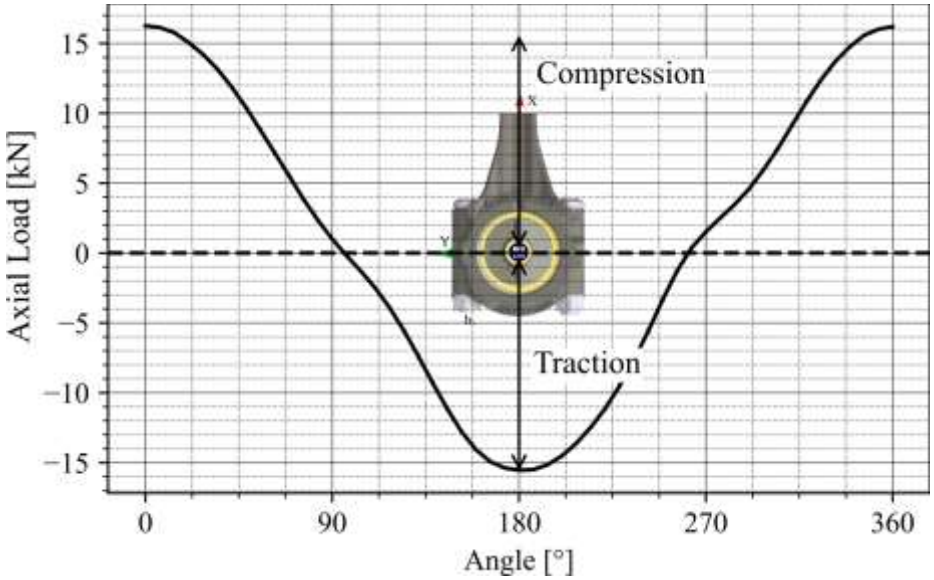

Figure 2.7 MEGAPASCALE traction - compression load example

2.1.3. Journal and Connecting rod Oil supply

Figure 2.8 shows the MEGAPASCALE's journal. The journal is composed of two cylinders machined from the same chunk on metal. Each cylinder is shifted from the rotation axis with a

specific calculated eccentricity (e_R-right connecting rod, e_L -left connecting rod). The bearing oil feed is provided through drilled holes as in an ICE (yellow arrows in Figure 2.8).

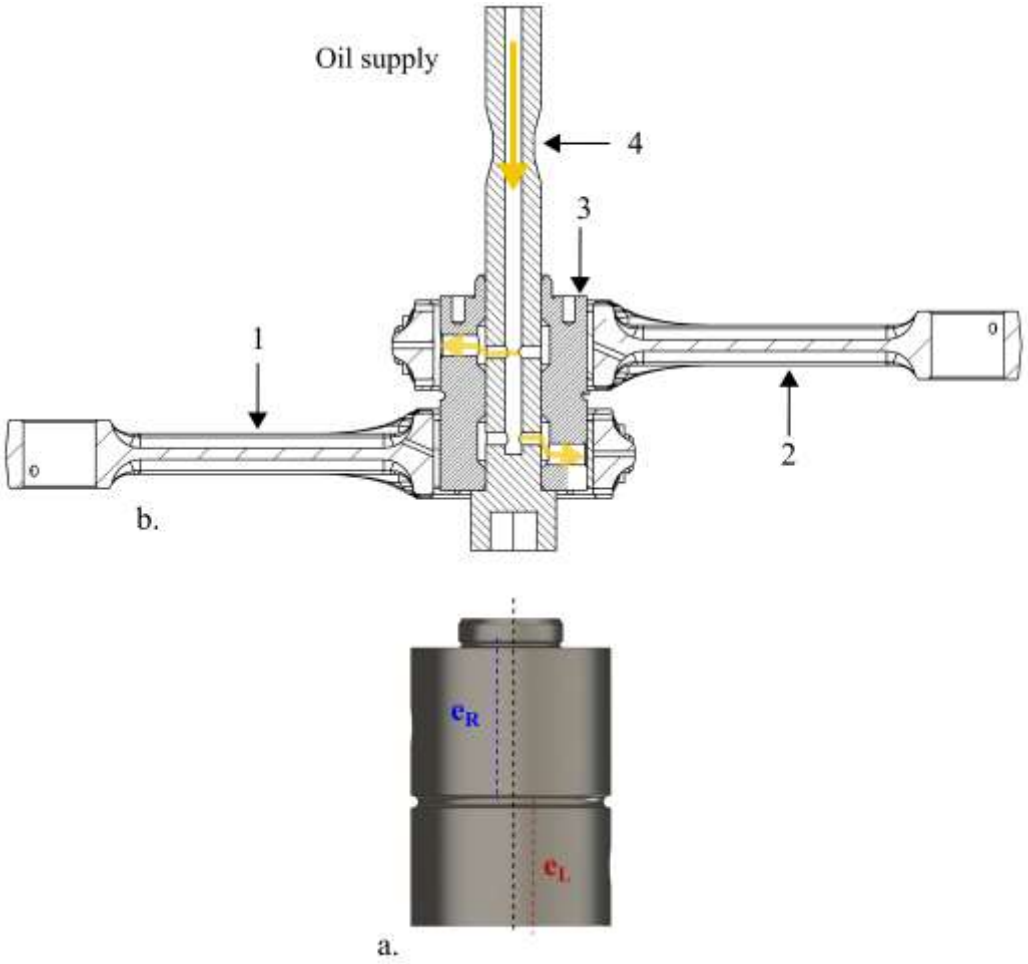

Figure 2.8 MEGAPASCALE oil feed and journal: a. Eccentricity; b. Oil supply path: 1. Left Connecting rod; 2. Right connecting rod; 3. Journal; 4. Hollow Bolt

2.1.4. Control desk and Data Acquisition

The testing cell control system (see Figure 2.9) is composed of two computers. The first one is used for the control and the supervision of the testing device. The second one serves as data acquisition system. The bench uses National Instrument PXI rigs to control and acquire data.

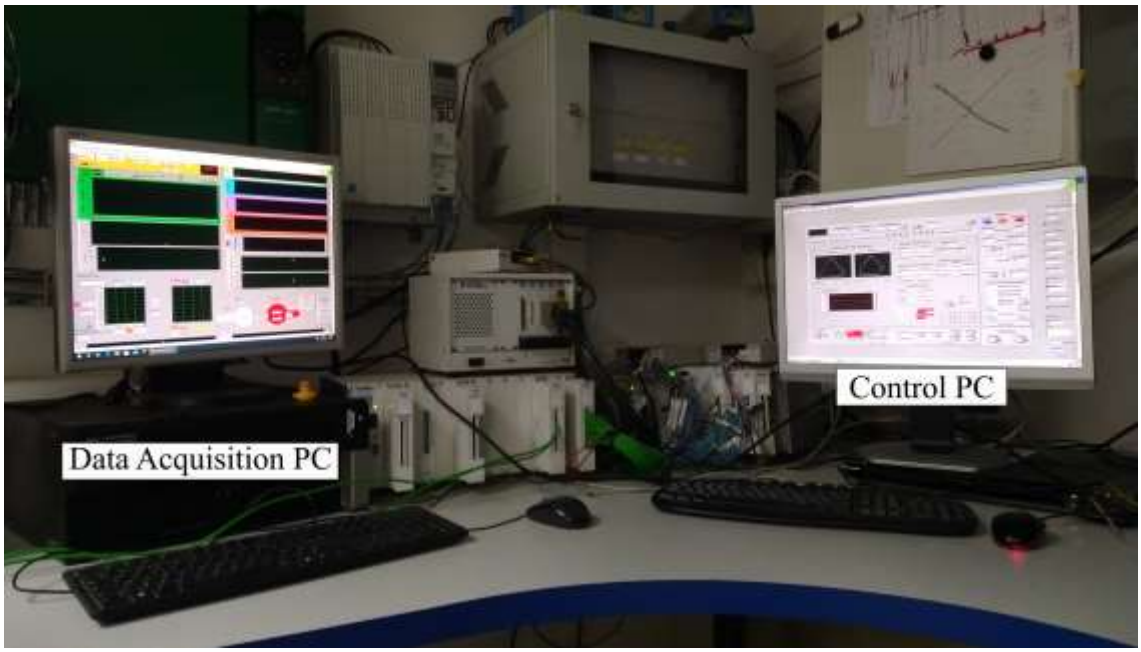

Figure 2.9 MEGAPASCALE Control Desk

The data logging files are divided into two categories: High frequency and Low frequency. The High frequency logging (an example is given in Figure 2.10) is triggered by the user through a push button. The acquisition frequency is 10 kHz and contains different data such as load amplitude, bearing temperature, eddy current gap sensors. The file contains as well a header with Time, Speed, Flow rate, Pressure and other parameters of the load control system.

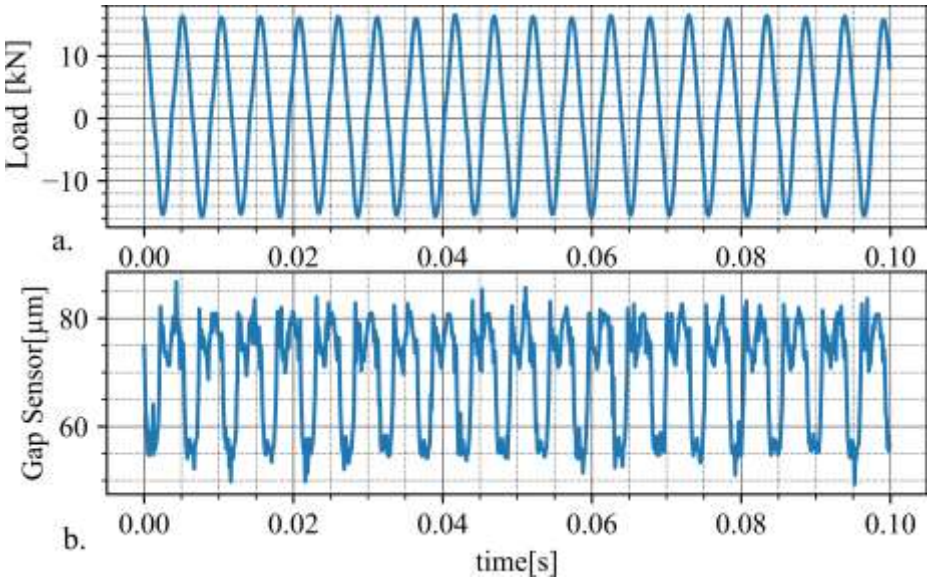

Figure 2.10 MEGAPASCALE high frequency data acquisition detail: a. Traction - compression Load and b. Eddy current gap sensor

The Low frequency data acquisition files (an example is given in Figure 2.11) are continuously recorded during the test. The acquisition frequency is 1 Hz. The monitored data are Time, Load, Speed, Oil Supply Temperature, Oil Supply Flow rate, Oil Supply Pressure. Moreover, bench

control parameters such as: position of the motors controlling the load, main shaft bearing temperature and hydrostatic double-effect thrust bearing oil supply temperature and pressure are also tracked and recorded.

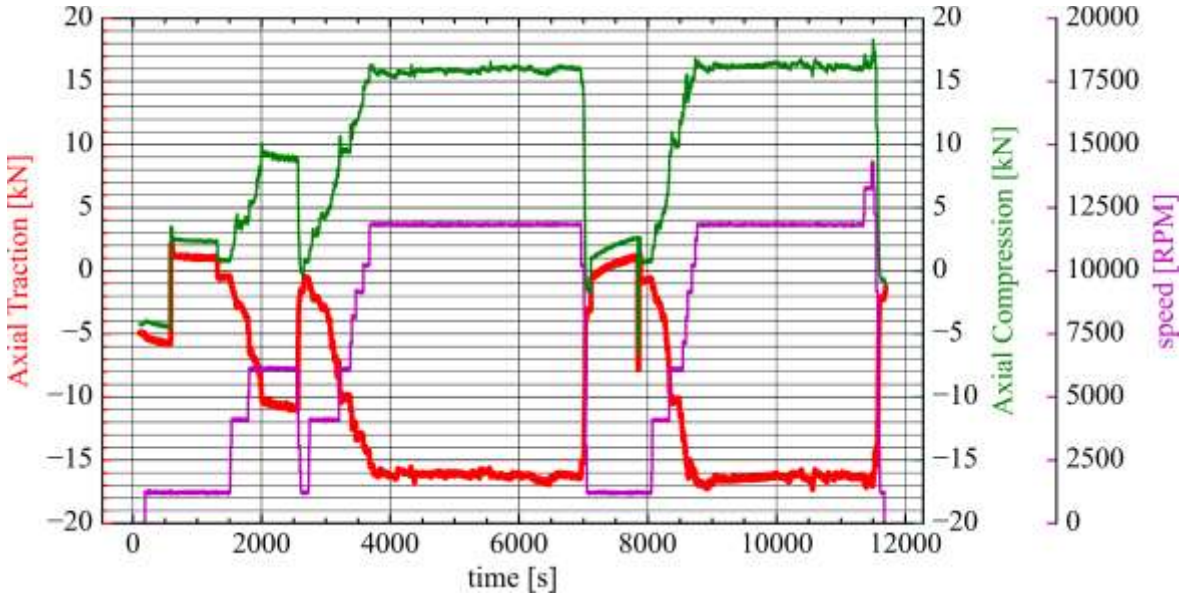

Figure 2.11 MEGAPASCALE low frequency data acquisition detail

2.2. Design of Experiments

The experimental tests were carried out on two different connecting rods. The first one is a Renault RS connecting rod. This connecting rod firstly served to performed preliminary tests, check the bench functionality, debug and improve the control system. A first testing campaign was carried out. The goal was to study various oil supply positions and holes as well as the transversal load influence on the bearing performances.

For the second testing campaign the bench was modified to accommodate a Kawasaki ZX10 connecting rod, which is the connecting rod provided by AKIRA, a mechanical engineering society based in Bayonne, France. The list and the drawing of the modified parts are available in the Appendix D.

Table 2.1 sums up the general testing conditions in terms of Load, Speed, Oil Supply Pressure and Oil Supply Temperature. Those values are chosen based on the real engine operating conditions. For the case of ZX10 load, the pick to pick amplitude was limited at 32 kN (instead of 46 kN in real engines). On MEGAPASCALE, the load transmitted to the small end has same magnitude as that imposed on the big end. In a high-speed ICE, inertia effects cause the load

applied to the big end to be significantly higher and therefore, for optimization reasons, the connecting rod has a smaller mechanical failure limit on the small end.

Table 2.1 General testing parameters

Parameters	Renault RS	Kawasaki ZX10
Transversal Load [kN]	2.8 (pick-to-pick)	-
Axial Load [kN]	Traction: 10 Compression: 20	Traction: 16 Compression: 16
Speed [rpm]	2000; 3000; 4000	11500
Supply pressure [bar]	20; 25; 30	10; 15; 20
Supply Temperature [°C]	70	80; 100

Table 2.2 sums up the tested hardware and sensors for both connecting rods. Multiple journals with different oil supply positions and diameters are tested.

Table 2.2 Tested hardware and sensors

	Renault RS	Kawasaki ZX10
Journal	RS_J60_3	ZX10_J90_5
	RS_J60_4	ZX10_J135_5
	RS_J160_3	
Sensors		3 Eddy current gap sensors
		Voltage drop
	Bearing Temperature	Bearing Temperature
	Pressure oil supply	Pressure oil supply
	Temperature oil supply	Temperature oil supply
	Oil supply flow rate	Oil supply flow rate
Oil	5W30	HTX 860
Connecting rod length [mm]	120	106.6
Crank pin diameter [mm]	48	34.5
Bearing width [mm]	18.3	15

For the RS connecting rod, three different eccentrics were used. The index J60 and J160 refers to the position of the feed hole in relation to the pick load (60° and respectively 160° before the maximum eccentricity), followed by the value of the feed hole diameter (3 mm or 4 mm). For the ZX10 connecting rod, only two eccentrics were used, having feed holes of the same diameter (5mm) but positioned circumferentially differently with respect to the load pick

For the ZX10 connecting rod, a clearance sensitivity study was also performed. For both connecting rods the bearing temperature at multiple points, oil supply pressure, oil supply temperature, oil supply flow rate are investigated. In the case of ZX10 two new types of sensors are added: eddy current gap sensors and Voltage Drop.

The eddy current gap sensors are used to measure the relative position of the journal in respect with the bearing. The Voltage Drop is used to measure the bearing-journal contact.

The Kawasaki ZW10 bearings are manufactured in thickness classes. The bearing shell thickness "T" is depicted in Figure 1.6 (chapter 1 section 1.6). Table 2.3 depicts the colour code and thickness values from the manufacturer manual [86]. Along this thesis and due to numerous clearance values, the bearings will be referred to as the colour code. As explained in the further sections, the clearances are defined as the single pair journal-bearing shells. For the Renault connecting rod, only one bearing shell dimension was available.

Table 2.3 Bearing shell thickness

Connecting rod	**Colour**	**Thickness**
Kawasaki ZX10	BLUE	1.488 ~1.493 mm
	BROWN	1.478 ~ 1.483 mm
	PINK	1.473 ~ 1.478 mm
Renault RS	-	1.77 mm

2.3. Surface Metrology

Surface metrology is a branch of metrology which measures features on a surface such as surface primary form, roughness, etc. The surface measurement can be obtained either by contact or non-contact methods. The contact method relays on 2D profiles measured by a stylus which are stacked up to form a 3D image of the surface. The non-contact method relays on optical techniques, having the advantage of grader resolution.

In this study, the surface metrology will serve to define the radial clearance and investigate any wear evolution for the tested bearings shells.

The bearing profiles are measured using Taylor-Hobson Talyrond 356 (see Figure 2.12 b.) which is a contact profilometer. The measurements were performed with a 2 mm stylus ball radius at a table rotation speed of 2 rpm. The recorded data are raw, no filtration was used. The

bearing surface topology was investigated using Taylor-Hobson Talysurf CCI 6000 (see Figure 2.12 a.) which uses optical methods (interferometry). A X20 magnification lends giving a 0.9ºmm x 0.9ºmm measure area at a resolution of 0.9ºµm.

Figure 2.12 Surface topology measurement machines: a.: Talysurf CCI 6000; b. Talyrond 356

2.3.1. Contact profilometer method

This section describes the contact profilometer measurements performed during the thesis and checks the robustness of the collected data.

The connecting rod big-end journal bearing features a specific complex shape and have been described in chapter 1 section 1.6. Therefore, defining the clearance by a number: radial or diametral clearance is not sufficient enough to performed pertinent analysis. On the other hand, it is sufficient enough and simple to refer to a bearing while discussing about. Even tough, the clearance is unique for a pair journal-bearing shell. Therefore, a new concept of clearance may be defined: clearance space. In order to obtain the clearance space, measurements of the journal and bearing shells surfaces are needed. More precisely, the surface metrology techniques used is: roundness. The bearing surface is reconstructed from multiple roundness profiles measured at multiple bearing cross section planes heights which are later stacked in order to obtain the final surface topology.

Roundness measuring can be performed in two ways. First, implies that the workpiece is stationary, while a sensing instrument, called stylus, rotates around the workpiece. Second, the workpiece is fixed on a turning table, while the stylus remains stationary during the measurement. Talyrond 356, the instrument used in this study, is a Roundness Measuring Machine (RMM) and belongs to the second category. The instrument has a high precision turning table which rotates the workpiece against a sensitive indicator (stylus) which is held stationary by a horizontal arm. The output of Talyrond is a polar graph which represents the roundness profile of the workpiece.

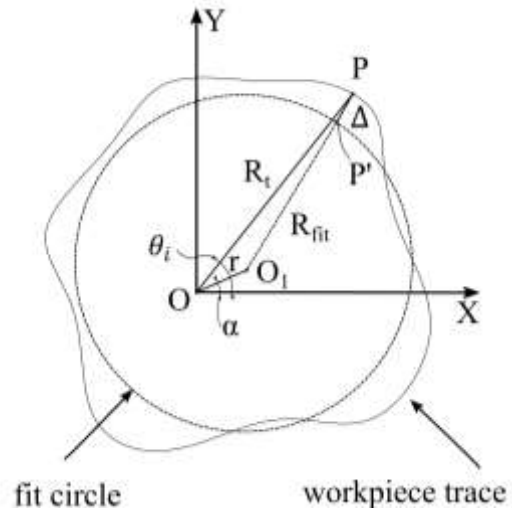

Figure 2.13 Roundness Vocabulary [87]

Figure 2.13 depicts the vocabulary of a roundness measurement. The roundness profile deviation ($\vec{\Delta}$) of a workpiece represents a calculated value and is defined by ISO 12181-1 as being the "*extracted circumferential line intentionally modified by a filter*". Basically, it represents the deviation from a reference circle. ISO defines the reference circle as being "*associated circle fitting the roundness profile in accordance with specified conventions, to which the deviations*". With other words, the reference circle is the fitted circle of the trace.

$\left|\overrightarrow{O_1P'}\right| = R_{fit}$ represents the radius of the reference circle. In this particular case the fitting technique is least mean squares (LSC); $\left|\overrightarrow{OO_1}\right| = r$. and α represents the deviation of the centre of the reference circle from the datum (spindle) and is called eccentricity

The RMM records the workpiece trace, or shorter trace, which represents the radial deviation ($\left|\overrightarrow{OP}\right| = R_t$) of the workpiece from the centre of rotation of the spindle (O). Included in the trace are the horizontal arm position ($\overrightarrow{H_p}$) and the stylus deflection ($\overrightarrow{S_d}$).

Concluding from the upper definition the general formulas for Trace and Roundness profile are:

$$\text{Trace}(\overrightarrow{OP}) = \text{horizontal arm position}(\overrightarrow{H_p}) + \text{stylus deflection}(\overrightarrow{S_d}) \quad (2.1)$$

$$\text{Roundness profile}(\vec{\Delta}) = \text{Trace}(\overrightarrow{\text{OP}}) - \text{Reference circle } (\overrightarrow{\text{OP}'}) - \text{eccentricity } (\overrightarrow{\text{OO}_1}) \quad (2.2)$$

The purpose of this section is to understand the output files of Talyrond 356 and to develop a method for wear and clearance quantification of the big end connecting rod bearing. The types of measurement files that can be created by the Talyrond are: *.STR, *.PFR, *.MDR.

The *.STR file is the straightness measurement output and it contains the straightness values and the stylus height. This file will be used further to verify the alignment methods.

The *.PRF contains the only stylus deflection (roundness profile $(\vec{\Delta})$ relative to the datum) expressed in mm as a function of the angular position of the turning table in degrees (For 3600 different angular positions of the turning table). No information about the fitted radius is given. And the fitted radius is needed for the clearance space calculation.

The *.MDR contains the roundness profile $(\vec{\Delta})$ expressed in mm and the angular position of the turning table in degrees. Along those information, additional data are exported, such as: reference circle radius, eccentricity, horizontal arm position, vertical arm position**.** Information which will be useful for clearance space and wear measurements.

The disadvantage of the *.MDR files is that it contains only the roundness profile. By this mean each the roundness measurement at one cross section plane loses its spatial location relative to the others cross section planes which is an inconvenient for the clearance space definition wear monitoring. Therefore, an algorithm that computes the stylus deflection from *.MDR data is needed. The proposed algorithm is explained and proved in the following sections.

2.3.2. Stylus deflection from *.MDR data - Proposed algorithm

The goal of this section is to describe the algorithm used to compute the stylus deflection from the *.MDR data files.

The traces of both files (PRF and MDR) should be equal. Therefore:

$$\vec{S}_{d\_PRF} + \vec{H}_p = \vec{\Delta}_{MDR} + \vec{R}_{fit\_MDR} + \vec{r} \tag{2.3}$$

Translating all the data from polar to Cartesian coordinates, the eccentricity becomes:

$$x_{ecc} = |\vec{r}| * \cos\alpha \tag{2.4}$$

$$y_{ecc} = |\vec{r}| * \sin\alpha \tag{2.5}$$

Where r, α are the *eccentricity radius* and *angle* from the *.MDR file.

The roundness profile is added to the fitted radius

$$\vec{R}_{\_MDR(i)} = \vec{\Delta}_{MDR(i)} + \vec{R}_{fit\_MDR} \tag{2.6}$$

where i is the index of a circumferential position

The **trace** cartesian coordinates are computed as follow:

$$x_{MDR(i)} = \left|\vec{R}_{\_MDR(i)}\right| * \cos\theta_i + x_{ecc} \tag{2.7}$$

$$y_{MDR(i)} = \left|\vec{R}_{\_MDR(i)}\right| * \sin\theta_i + y_{ecc} \tag{2.8}$$

The trace of the *.MDR file in polar coordinates is:

$$\left|\vec{R}_{t\_MDR\_ecc(i)}\right| = \sqrt{{x_{MDR(i)}}^2 + {y_{MDR(i)}}^2} \tag{2.9}$$

As explained in the equation (2.1), the stylus deflection of the *.MDR file is equal to the difference between the trace and horizontal arm position.

$$\vec{S}_{d\_MDR} = \vec{R}_{t\_MDR\_ecc(i)} - \overrightarrow{H_p} \tag{2.10}$$

This section established the components and the mathematical equation of the profiles measured by Talyrond and proposed an algorithm to append the eccentricity to the MDR files output by the machine in the need of data details provides by this specific fie. The next sections will tackle the special support used to fix the connecting rod on the Talyrond's turning table, as well the testing of the proposed algorithm following by the encountered errors.

2.3.3. Connecting rod support for the contact profilometer (Talyrond)

In order to obtained accurate measurements a new and improved support was developed. The support (see Figure 2.14) is mounted on the RMM turning table (6) via a Maxwell kinematic coupling (the principle of exact coupling) in order to ensure precision and certainty of location. This type of coupling is frequently used in multi tool machining robots [88]. In this apparatus, three ball bearings spheres (7) are mounted through interface fitting with the turning table v - grooves and three drilled holes on the support plate. This method provides six contact points, enough to constrain all the six degrees of freedom with minimal amount of residual force. Furthermore, a centring sleeve (5) ensures the location of the connecting rod's big end bore relative to the plate (4). The sleeve is shrink fitted to the plate. The connecting rod (1) is fixed to the plate (4) via two flexible lamella clamps (3). 5 degrees of freedom are constrained through the cantering sleeve (5), while the sixth one (rotation around bearing axis) is constrained via the pin (2).

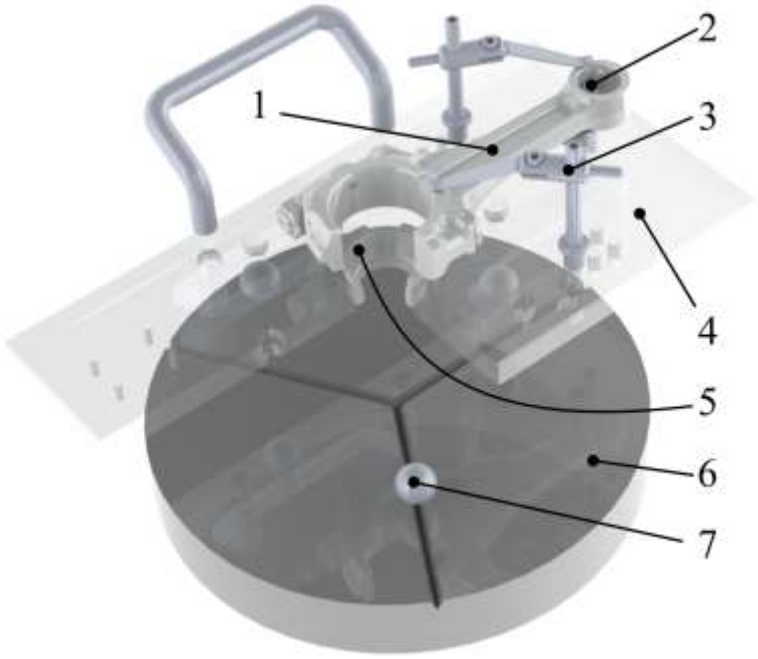

Figure 2.14 Talyrond support: 1. Connecting rod; 2. Pin; 3. Flexible Lamella Clamp; 4. Plate; 5. Centring sleeve; 6. Turning Table; 7. Ball Bearing Sphere

2.3.4. Stylus deflection from *.MDR data - Proof of Method for one cross plane

The following section is meant to proof the algorithm proposed in section 2.3.2 . Let's take the same measured profile which was exported in three different files by Talyrond365 and plotted in Figure 2.15 a.:

1. PRF (red line) is the stylus trace from PRF file
2. MDR (BLUE line) is the roundness profile form MDR file

After applying the algorithm mentioned in sections 2.3.2 we obtained a fourth profile:

3. MDR with eccentricity (green line) is the stylus trace – calculated through the proposed algorithm

The goal is to compare the calculated stylus deflection from MDR (3) data with the PRF (1) data in order to validate the algorithm.

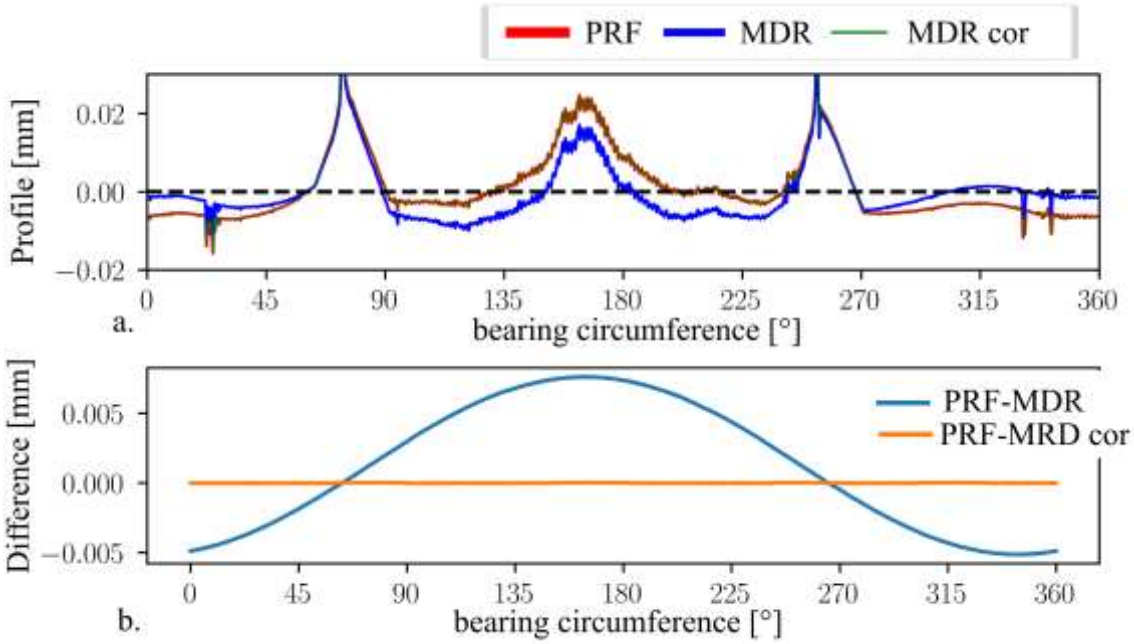

Figure 2.15 Roundness profile file comparison: a. Raw measurements; b. Profile difference

As shown in the profile difference plot (see Figure 2.15 b.), the *.MDR stylus deflection obtained by applying the algorithm is identical with the *PRF stylus deflection (orange line). Another strong proof of the method is the straightness of the workpiece. Straightness measurements of the same bearings were performed and compared to the straightness values

extracted from the roundness values at the same angle. The Figure 2.16 compares the straightness measurement on four generatrix around the bearing. It can be observed that the green line which represents the stylus deflection after applying the algorithm follows the red (straightness measurement) and black lines (extracted straightness from PRF file).

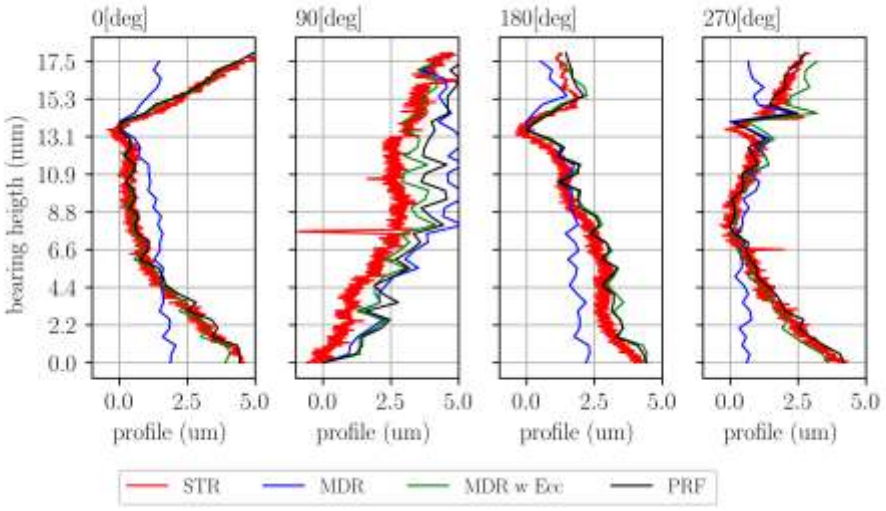

Figure 2.16 Straightness comparison along different bearing generatrix

This section proofs the success of appending the eccentricity to the MDR files. All the further analysis is performed using the corrected MDR files due to convenience of useful data contradictory to PRF files.

2.3.5. Measurements comparison and improvements for multiple cross planes over the bearing height

This section is intended to emphasise the difficulty of measuring such an irregular shape and to comprehend the errors source and encounter them. In order to investigate the robustness of the data we have developed the following method.

Two measurements of the same bearing are performed in the same day, at the same temperature, with the same stylus angle, but one is done first and the second one is done after bringing back to zero the RMM machine and after a new calibration was performed. The only variable in the method is the centring and levelling of the connecting rod. The method steps are presented in the Table 2.4.

It should be mentioned that the utilised data comes from ZX10 connecting rod bearing measurements.

Table 2.4 Method steps

Index	Step description
1	Horizontal arm calibration is performed using a calibration workpiece of 17.25 mm radius.
2	The connecting rod is placed on the turning table via the support and a Z straightness is performed in order to detect the bearing height position. Such manner, ensures that all the roundness profiles are measured at the same height for any bearing.
2.1	A double level centre is performed, first with a tolerance of 1 µm, then the tolerance is reduced to 0.5 µm. This allows the machine algorithm to converge
2.2	Roundness measurements of 30 plane sections along the bearing generatrix are performed
2.3	*MDR files are exported
3	The machine is set to zero
4	The second measurement is perform following the above steps

For each measurement 30 planes at a 0.5 mm step over the total bearing width of 15 mm are measured along the bearing axis. Figure 2.17 depicts three roundness profiles along the bearing axis. Three relevant planes have been chosen, corresponding to the top outer edge (h = 1 mm), centre ($h^o=^o8$ mm) and lower outer edge (h = 13.5 mm). The connecting rod is located on the same face for each measurement. The lower edge is the edge facing the turning table (see **7** inFigure 2.14).

The left-hand side column of the Figure 2.17 represents the measured roundness profiles. In black (I) is the first measurement, in red (II) is the second measurement after re-centring and re-levelling (see Table 2.4). Both roundness profiles are the corrected MDR (algorithm in section 2.3.2).

The right-hand side of the Figure 2.17 represents the roundness profile differences. The red line is the difference between the raw profiles I and II. As it can be seen, for all three planes, the difference between the raw profiles (d, e, f: I-II) does not converge to Zero and it is not a flat line, even though the measured bearing and conditions are the same. Looking closer at the shape of the difference curve, one can observe that it is an offset sinusoidal curve, especially at the outer edges. This is not surprising and was already observed by multiple authors describing the weakness of an RMM machine [89], [90]. This shape tells us two things and it can be decomposed into two deviations.

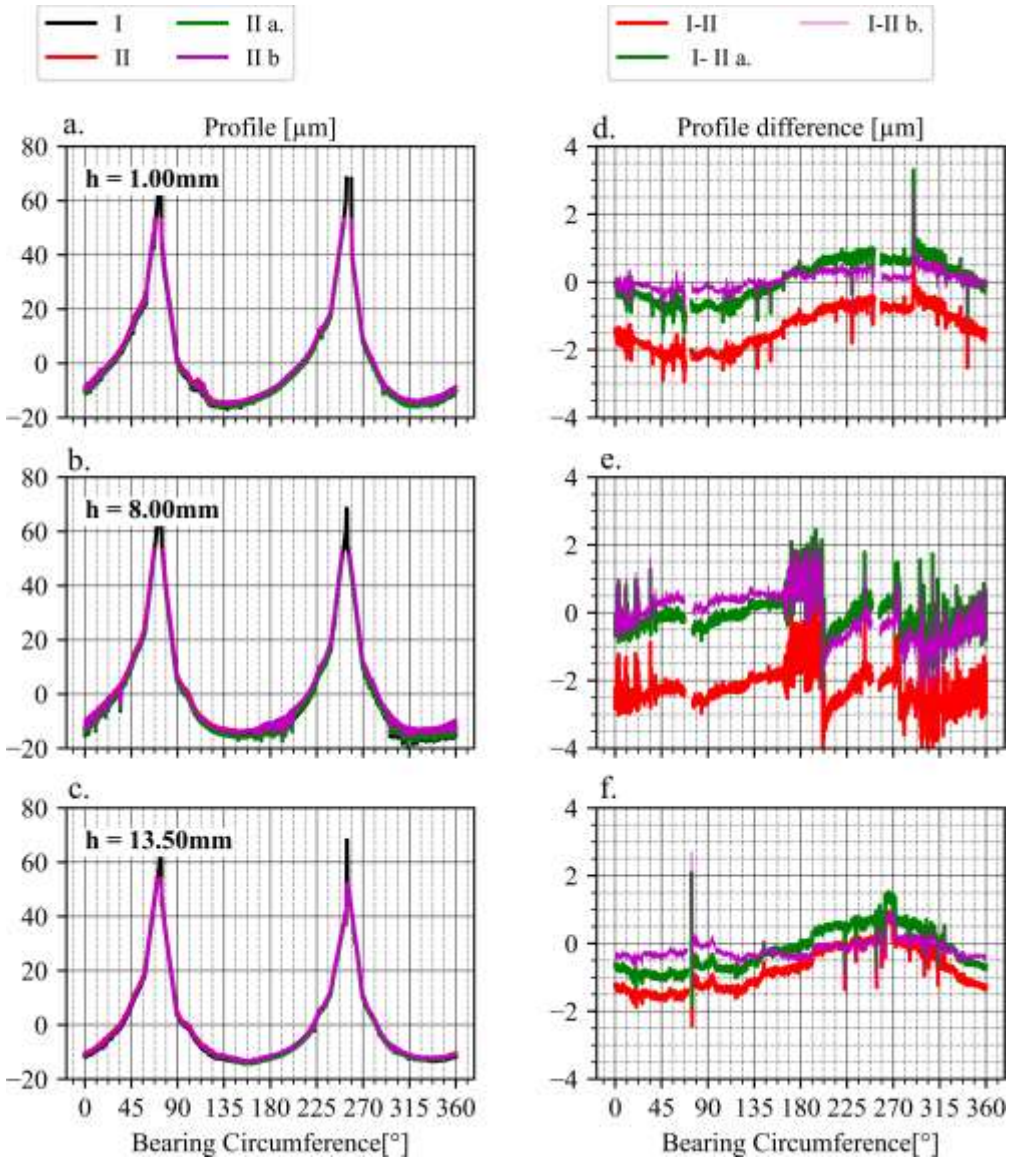

Figure 2.17 Centring and levelling compensation: a,b,c: measured profiles at different heights: I- First measurement raw profile; II – Second measurement raw profile; IIa DC compensation: ; IIb DC and AC compensation; d,e,f profile differences: I-II: raw profiles difference, I-IIa: difference of raw and DC compensation; I-IIb difference between raw and DC-AC compensation

The first is the offset from zero, here expressed as DC deviation. This deviation suggests that the calculated LSC radius is not the same for the two sets of measurements. This is firstly due to the deviation introduced by the points in the bearings joint plane. And secondly by the precision of the horizontal arm. As explained in section 2.3.2, this value influences the LSC.

The second component is the sinusoid, here referred as, the AC deviation. This deviation suggests that the centres of the two LSC do not coincide.

A solution to compensate the DC deviation is to searches for minimal offset diameter in the crush relief [2]and append the difference to one of the two profiles. This method supposes that the crush relief is the unchanged region of the bearing. The investigation of the solution is captured by the green line (II a.) in Figure 2.17. As expected, the profile differences now have only the AC deviation.

In order to compensate for the AC deviation, the axis difference from the levelling of I to II is added to the II. As expected, the profile difference is level out: magenta line (IIb).

This section points out that even measuring the same bearing at the same conditions the centring and levelling errors influences the results. To account for these errors, DC and AC compensations are proposed. Furthermore, the method is proofed by comparing the raw measurement with the corrected one. After all the compensations, the difference between the profiles tends towards zero.

2.3.6. Different bearings states measurements

This section tests the algorithm for two different bearing states measurements. By this means the presented profiles come from two measurements, one performed before usage, the second one performed after usage, therefore some change of profile shape may be suspected. On the other hand, as mentioned previously, the crush relief region (45°-90° and 225°-270°) is considered to be undamaged, therefore it is considered as common reference for both profiles. Consequently, the roundness profiles difference in this region should be zero. This section is meant just to verify the algorithm proposed in section 2.3.5 and highlights error sources.

Figure 2.18 represents the profiles comparison of the same bearing before and after usage. In black [I] is the roundness profile of the first measurement (new bearing). In magenta are represented the roundness profile after usage. For this particular measurement, the null difference in the crush relief region assures the robustness of the measurements algorithm. Therefore, the difference of the profiles can be considered as wear.

[2] Crush relief: Bearing shell chafer on the active zone ensuring the bearings shells assembly

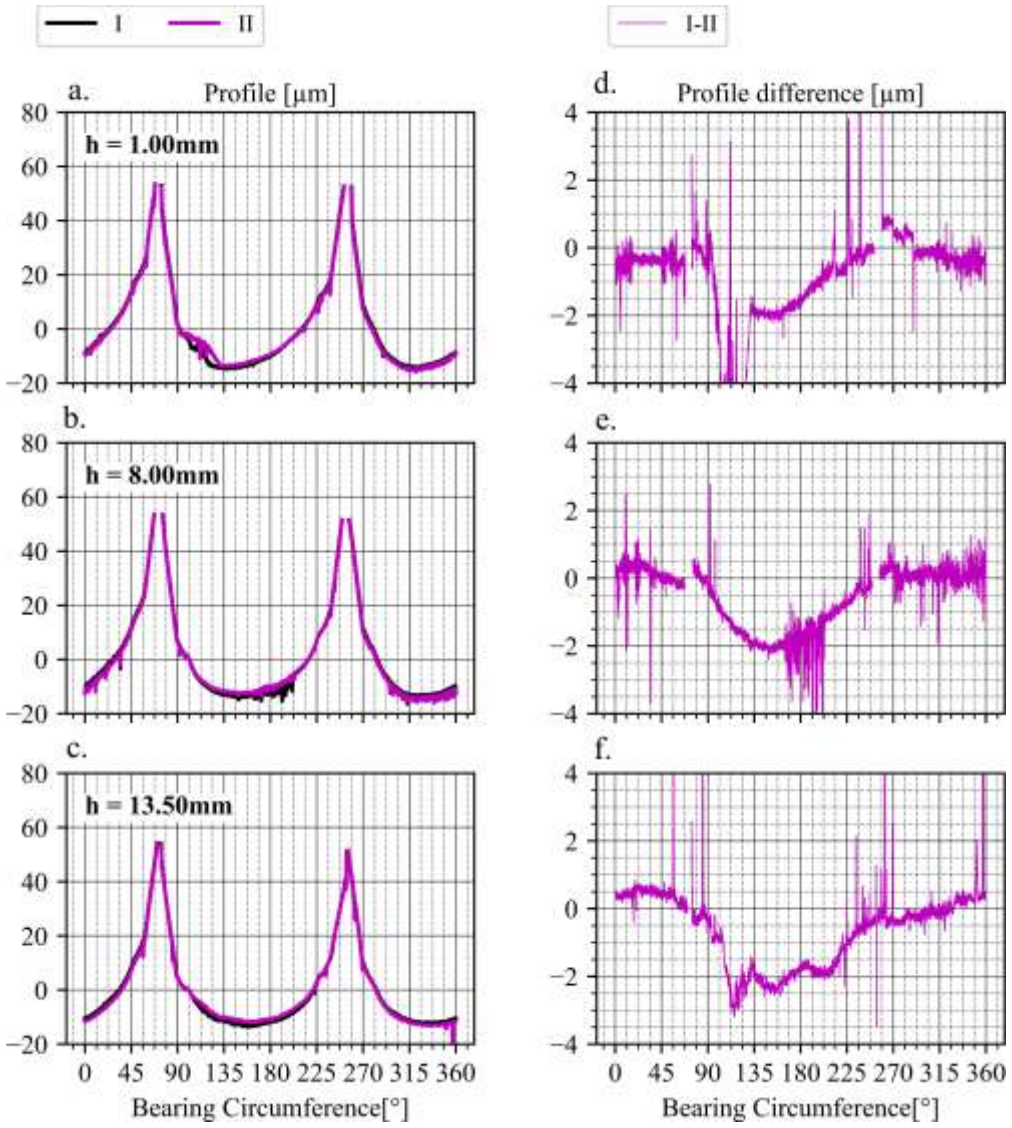

Figure 2.18 Roundness measurements comparison at different bearing cross sections between new (I) and used (II) states after profile correction

For a further set of measurements, the null difference in the region of crush relief is not observed. For example, Figure 2.19 and Figure 2.20 depicts two different axial roundness plane bearing heights: 1 mm and 4 mm respectively. Those profiles come from a different bearing than the one presented hereabove. The error responsible for this difference is the stylus jump. Figure 2.19 and Figure 2.20 shows a zoom plot on the region where the trace is alternated due to stylus jump. A solution to this problem is multiple roundness measurements at the same height and choose the one that is continuous.

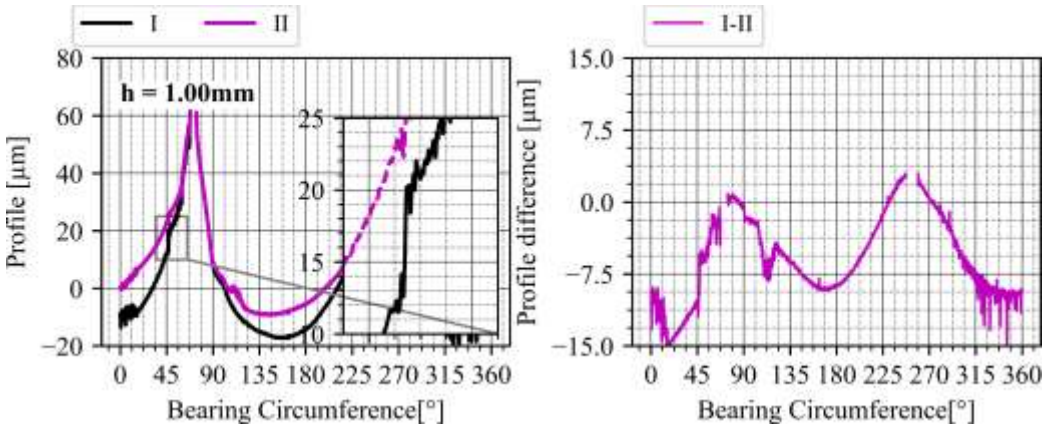

Figure 2.19 Roundness profile error source at 1 mm bearing cross section plane

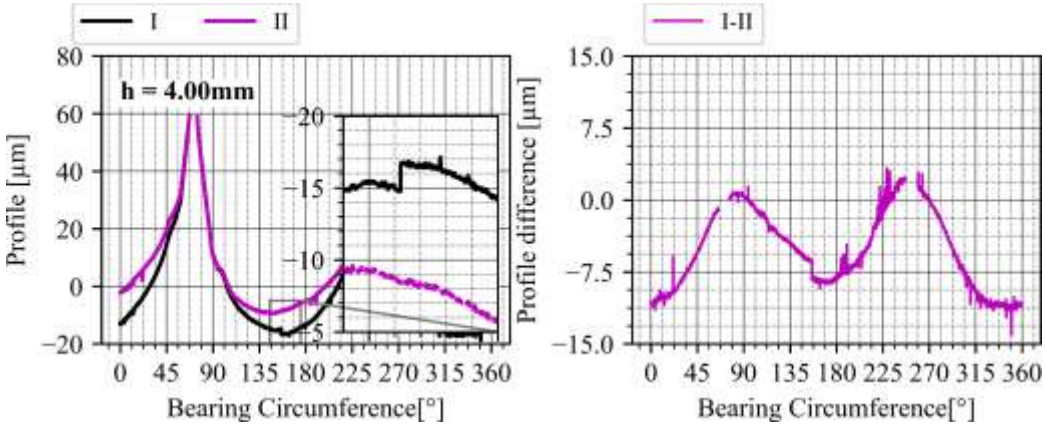

Figure 2.20 Roundness profile error source at 4mm bearing cross section plane

2.4. Bearing Temperature measurement

This section describes the bearing temperature measurement location. As previously explained, two different connecting rods were tested. One is a passenger car connecting rod from a Renault RS and the other is a smaller motorcycle high speed Kawasaki ZX10. For both types of connecting rods, a pair of two is always used on the MEGAPASCALE test bench. Those two connecting rods are always referred as left and right, where the left connecting rods purpose is to balance the load and the right is the tested one, equipped with various sensors.

For the Renault RS connecting rods 20 thermocouples are installed on tree cross planes around the bearing shell: front, mid and back (see Figure 2.21). All the thermocouples are installed inside drilled holes. The mid plane thermocouples are measuring the temperature at the back of the bearing shell, while the front and back plane thermocouples are measuring the temperature of the axial oil leak. The circumferential location of all the front and back plane thermocouples

is the same for all connecting rods and it is shown in Figure 2.23 a and b, while c depicts the MEGAPASCALE set up equipped with the instrumented Renault RS connecting rods.

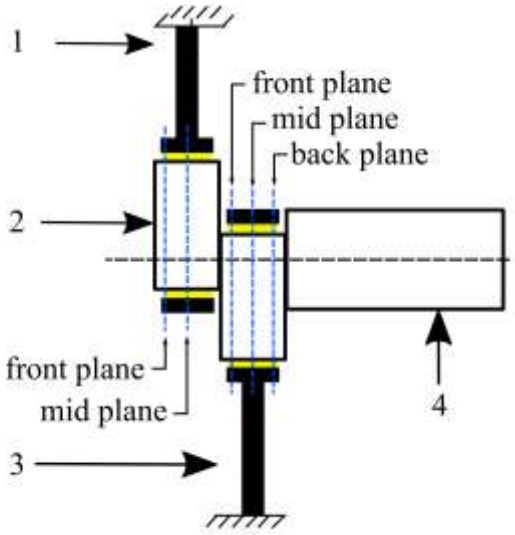

Figure 2.21 Renault RS connecting rod thermocouples planes locations: 1. Left Connecting rod; 2. Journal, 3. Right Connecting rod; 4. Shaft

On the left connecting rod, six thermocouples are installed. Four of them are placed on the front plane and 2 on the mid plane. The Right Connecting rod is equipped with 14 thermocouples, 8 are installed on the front and back plane, while the last 6 are installed in the mid plane (see Figure 2.22).

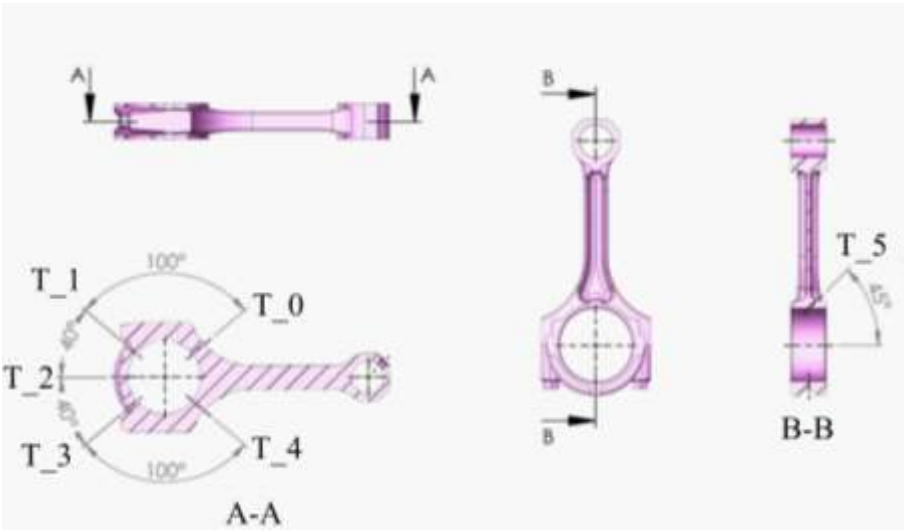

Figure 2.22 Renault RS right connecting rod mid-plane bearing thermocouples location

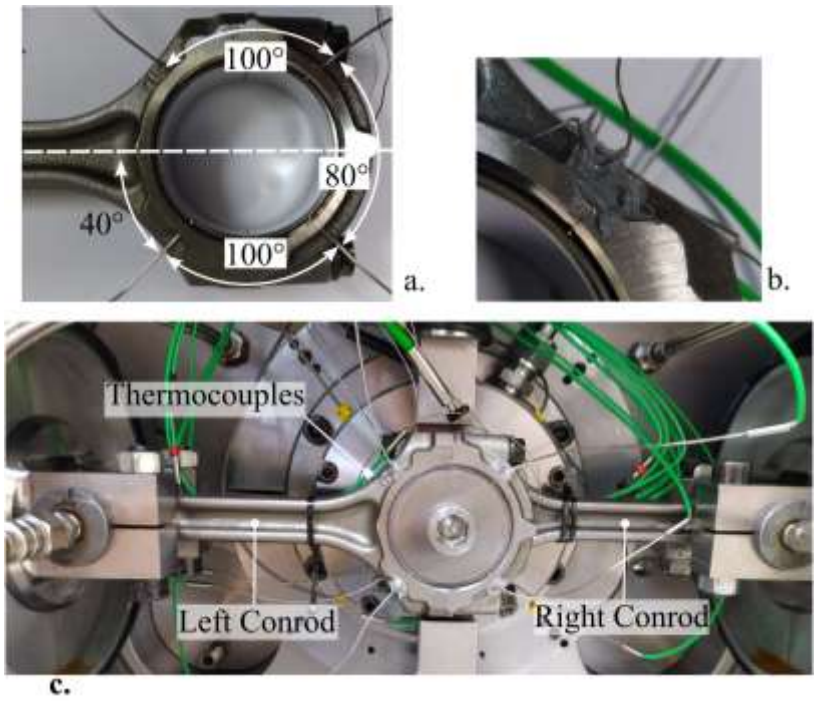

Figure 2.23 Renault RS thermocouples a. outer planes; b. close up; c. MEGAPASCALE test preparation

Figure 2.24 shows the thermocouples location for the ZX10 connecting rod. Five thermocouples are installed on the right connecting rod: three of them (T0, T1 and T2) are measuring the back-bearing shell temperature at mid plane, while other two (T3 and T4) measures the temperature of the exiting flow bulk in the shank region on both sides. For the left connecting rod, only two thermocouples are used (see Figure 2.25) to measure the temperature of the axial flow bulk exiting the bearing.

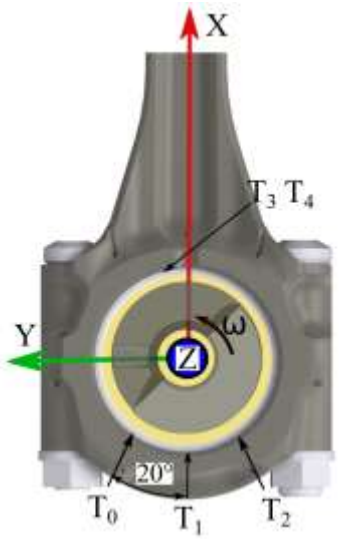

Figure 2.24 Kawasaki ZX10 right connecting rod thermocouple location

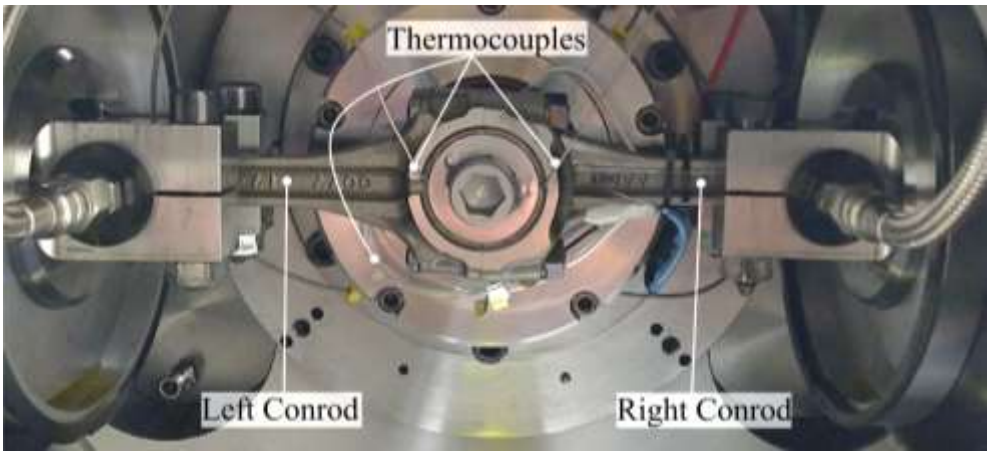

Figure 2.25 MEGAPASCALE test preparation with Kawasaki ZX10 connecting rod

2.5. Eddy Current Gap sensors

Eddy current gap sensors are a type of measurement instruments that performs non-contact distance measurements. For this thesis, the sensors are used to track the journal position relative to the bearing.

The selected sensors are Kamman 2up. They have been chosen for their reduced dimensions (3 mm diameter) and convenient measuring range (500 µm). The sensors are placed around the bearing's circumference. One of them, P2, was placed on the connecting rod cap, collinear with the shank axis. The other two (P1 and P3) were placed on the shank side at 65º respectively 293 º (see Figure 2.26).

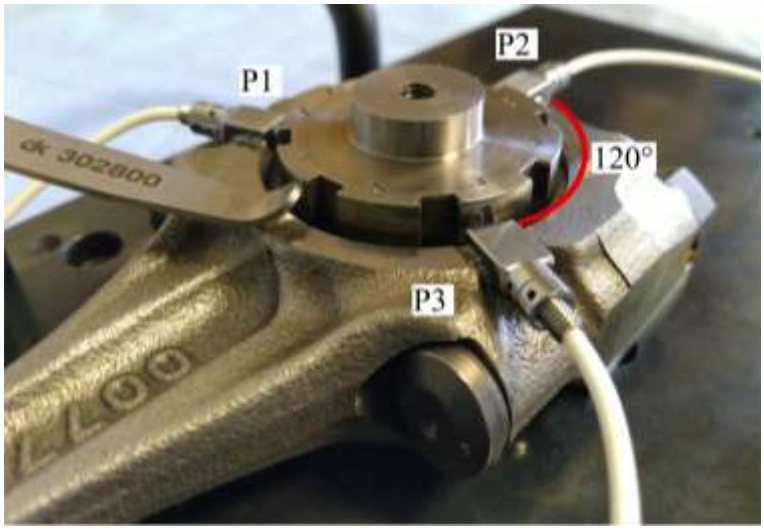

Figure 2.26 Eddy current gap sensors location

The sensors are mounted on 3 additionally supports (see Figure 2.27). The supports consist of three small steel blocks placed inside milled slots and laser welded to the connecting rod itself. Other similar measurements placed the sensors in the centre of the bearing [25] or on the outer edge, drilled the bearing shell and filled the gap with epoxy resin [14], [21]. We customized our mounting method in order to achieve a minimal impact on the connecting rod big end stiffness and not to alter the bearing shell shape and, with it, the pressure distribution.

Figure 2.27 Eddy current gap sensors mounts

The calibration was first performed at 20º C using a calibration cylinder (target) (see Figure 2.28 b.). In order to achieve the most accurate measurements and reduce the risk that the presence of the calibration target impacts the collected data, its design has been adjusted by choosing a certain material and shape/geometry. The target is manufactured from the same material and with the same roughness as the tested journals (32CDV13 steel alloy and mean roughness R_a = 0.05 µm). By choosing identical materials and surface finish, the influence of the shape and of the ferromagnetic properties on the behaviour of the sensor has been reduced. The geometry of the target was also customized: instead of a continuous elliptical shape, eight concentric lobes, each of them corresponding to a different diameter, have been designed.

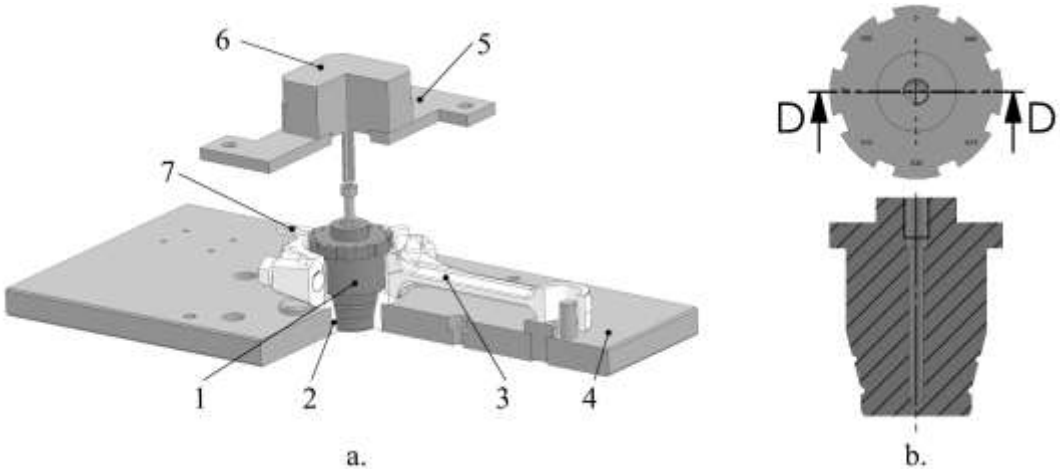

Figure 2.28 Eddy current gap sensors calibration a. stand 1-target; 2-center sleeve; 3-conrod;4-support; 5,6-stepper assembly; 7-sensor; b. target

One lobe has a 17.25 mm radius same as the journal, four of them increase with a +25 µm step; the other three lobes decrease with -25 µm step. The total calibration range is 150 µm and ensures 2.5 times coverage over the maximum diametral clearance (60 µm) indicated by the bearing manufacturer. Although more difficult to manufacture, this geometry was chosen in the aim to faithfully reproduce the real journal and increase the accuracy of the measurements, by eliminating, or at least reducing, the loss of data which happens when operating a mediated measurement. The target design is shown in Appendix D.

Additionally, a RMM (Talyrond 365) has been used in order to obtain a better position accuracy and to determine the voltage-distance calibration functions for each eddy current sensor. Figure 2.28 a. depicts the support used for eddy current gap sensor calibration, which is the same support used for bearing roundness measurements presented in section 2.3.3. The only differences are the addition of the calibration cylinder and stepper motor. The calibration cylinder (1) interference with the centring sleeve via a conical coupling with 30º inclination. This angle ensures centring and eliminates the risk of galling while rotation. The calibration cylinder is then rotated by a stepper motor (6). The stepper motor is mounted on a floating plate (5) to allow the calibration target to self-centre in its location.

2.5.1. Calibration method

With all the above-mentioned parts placed on the RMM turning table, each sensor is calibrated one at a time by the following method.

The Zero lobe is positioned in front of the desired sensor. Then, the stylus of the RMM contacts the lobe in the near vicinity of the sensor; the RMM sets this position as reference value. The stepper motor then rotates the target, bringing each lobe in front of the sensor. The live stylus value is logged along with the sensor voltage for each step/lobe. We repeated each calibrating cycle 5 times for each sensor.

Goodwin et al., [23] state that the eddy current sensor is influenced by the change in environment temperature. Therefore, a voltage - temperature sensitivity investigation must be performed. For this verification, the RMM is excluded from the setting. Four temperature steps, each at 50, 70, 90 and 110º C are performed.

This entire setup is placed inside an oven. The connecting rod temperature is monitored through the connecting rod thermocouples to ensure the thermal equilibrium for each step. The stepper motor offers the possibility to turn the target inside the oven without opening the door.

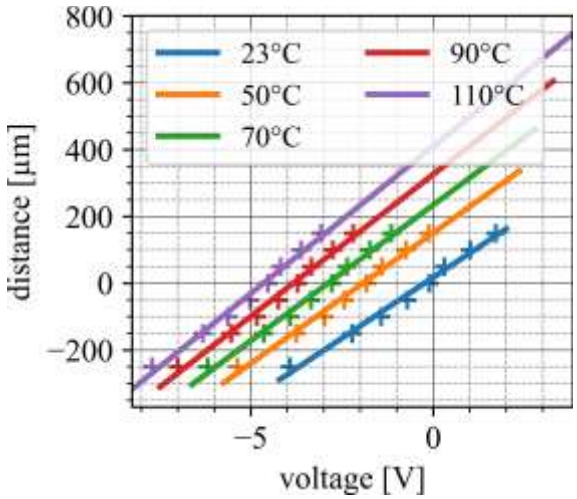

Figure 2.29 Eddy current gap sensors temperature influence

Two conclusions can be drawn from the verification curves shown in the Figure 2.29. First, for this particular sensors and the particular temperature increments, a zero offset happens. Second, the sensor linearity does not change much: 4%*full scale/20ºC, from one temperature to another. This verification guarantees the validity of relative measurement, as the temperature is within the above-mentioned range.

2.6. Voltage Drop

The voltage drop measurement belongs to the greater category of electrical measurements of fluid film status. Those methods are giving important insights of the fluid film history. Both, quantitative and qualitative measurements have been investigated by multiple authors: voltage drop – discussed in [91] or [92] – and the capacitance, which can be global [93], [94] or local [11], [95].

This thesis focuses mainly on the qualitative investigation of the voltage drop in a journal bearing. Related to these methods, Crook [94], in an comparative work between the capacitive and voltage drop methods, concluded from a disk machine test that: "*A weakness of the method lies in the attribution to the oil in the gap of an electrical behaviour observed under the vastly different physical conditions of static calibration experiments*". Therefore, the voltage drop measurement for disk machines can be flawed by calibration conditions. In contrast, the

capacitance method, which relies on the dielectric constant of the fluid is less impacted by calibration because the dielectric constant remains constant with the pressure variance within some percentage (20%). Nevertheless, fluid film thickness / voltage drop ratio remains linear for relative thicker (1 μm) films [92]. The methods were intensively tested on conformal EHD where the fluid film thickness tends to be under 1 μm and hydrodynamic pressures are in the range of few GPa, in contrast to non-conformal EHD where the fluid film thickness is mainly over micron and hydrodynamic pressure are in the range on hundreds of MPa or less. Even though, most of the above-mentioned authors prefer the capacitance method that provides the best trade-off between accessibility and measurement quality. The voltage drop has been successfully utilized by Suzuki [14] for qualitative study purposes on a nonconformal EHD.

In the present study, the contact between the bearing shell and journal was measured by voltage discharge method in which the two acts as electrodes. A constant current of 1mA is applied by a current power source while the voltage drop is monitored (see Figure 2.30 and Figure 2.31). The used instrument is a National Instruments digital mustimeter (DMM). The contact measurement is performed simultaneously with the temperature and eddy current measurement. Electrical insulation between the connecting rod and the rest of the bench is ensured by diamond-like carbon (DLC) coating on the small end pin.

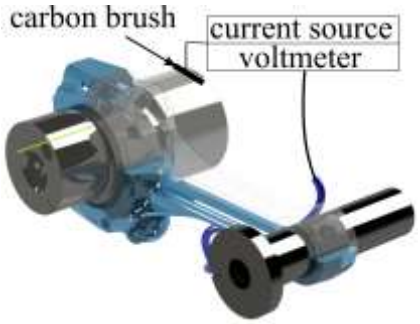

Figure 2.30 Voltage drop measurement schematics

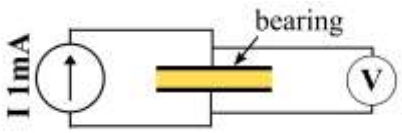

Figure 2.31 Electrical schema for the voltage drop measurement

2.7. Conclusions

This chapter discussed the experimental methods and calibrations used along this thesis. First, MEGAPASCALE working principle have been elaborated. Furthermore, it has been pointed out the importance of clearance space calculation and the problems and solution for obtaining accurate measurements.

A special calibration support has been developed which serves firstly as calibration support for eddy current gap sensors but also for metrological measurements. Particular attention was paid to adapting the location of the support on the Talyrond turning table. The proposed solution enabled robust location for each measurement and thus improved the accuracy of the results.

Furthermore, it has been shown the placement of the thermocouples for both connecting rods. Those thermocouples measures at once the back-bearing temperature and the temperature the bulk flow exiting the bearing.

It has been presented the eddy current gap sensors mounting solution and calibration. A special attention has been paid to the calibration method. The original contribution to calibrating the sensors is the back to back checking. By this mean, the Talyrond RMM machine has been used to check the real distance between the sensor and calibration target. Another original approach, is the temperature calibration of the sensors. For this method, a stepper motor has been employed to rotate the target. In such manner the robustness of the angular position of the target cylinder has been ensured.

The chapter ends by presenting a simple, but handy method to qualitatively measure the contact between the journal and the bearing. This method is called the voltage drop method and consists in measuring the voltage drop between the journal and the connecting rod. The next chapter will show that this measurement does not give binary information such as ON/OFF states, but rather a variation depending on the running condition.

After the detailed description of the test device and the different measurement techniques employed, the reader will now be able to understand the elements that will be presented in chapter 3, which will deal with the analysis of the experimental results and the comparison with the numerical calculations.

(this page intentionally left blank)

Chapter 3 Experimental results and numerical comparison

This chapter describes the experimental results performed individually on two different connecting rods. The first connecting rod belongs to a passenger car: Renault RS. This connecting rod mainly served to performed preliminary tests, check the bench functionality, debug and improve the control system. The second connecting rod belongs to a high-speed motorcycle: Kawasaki ZX 10. Experimental running point tests are systematically doubled by numerical calculation performed with ACCEL software. Results interpretation and comparison are performed in a sequential manner.

The experimental tests are governed by the control parameters and the indicator parameters. The control parameters represent the predefined testing conditions. An individual set of control parameters defines the test running point. The set of control parameters are common for both Renault RS and Kawasaki ZX 10 connecting rods.

Test Running Point = [Speed, Traction - compression Load, Transversal Load, Oil Supply Temperature, Oil supply Pressure, Oil Hole Angle, Oil Hole Diameter, Clearance, Oil]

A control parameter can be either a scalar or a vector. By this mean, for example in the case of Renault RS conrod, only a bearing clearance is available and therefore the clearance for this test is a scalar. In the case of Kawasaki ZX10, two different bearing shells thicknesses are available, therefore the clearance control parameter is a vector and a clearance sensitivity are performed.

The Indicator Parameter represents the observed measurements obtained through installed sensors

Indicators Parameters Renault RS= [Oil Supply Flow rate, Bearing Temperature]

In the case of the Kawasaki ZX 10, as my experience and understanding of the bench increased, a more complex indicator parameters has been added.

Indicators Parameters Kawasaki ZX10 = [Oil Supply Flow rate, Bearing Temperature, Eddy Current Gap Sensors, Voltage Drop, Telemetry]

The numerical calculation methodology is based on the experimental set of control parameters. By this means, the set of the control parameters of the experimental is the input data of the ACCEL software.

The results interpretations and discussions are first discussed on the experimental side and then numerical results are next presented.

For the particular case of the Kawasaki ZX10 connecting rod, since the indicator parameters are sensors, they are complementary and can be analysed together. Back-to-back pure experimental comparison are performed in order to understand the bearing specific behaviour. The numerical computation firstly serves as basis for the ACCEL code validation, but in the same time reinforces the particularities observed through the experimental results.

3.1. RENAULT RS connecting-rod campaign tests

This section describes the result of the Renault RS connecting rod testing campaign. Firstly, a description of the design of experiments is performed, the control parameters and indicators are set; furthermore, the numerical simulations are performed, compared and analysed.

3.1.1. Description of the performed tests

This section describes the design of experiments for the Renault RS connecting rod. As already defined in the introduction of this chapter, the set of control parameters defines the tests running points. For the particular case of the Renault RS connecting rod the control parameters are:

Test Running Point = [Speed, Traction - compression Load, Transversal Load, Oil Supply Temperature, Oil supply Pressure, Oil Hole Angle, Oil Hole Diameter, Clearance, Oil]

As the Renault RS connecting rod belongs to a passenger car, the speed is set to 2000 rpm, 3000 rpm and 4000 rpm. The traction - compression load is kept constant for all the running point at the values of 20 kN compression, respectively 10 kN traction. The transversal load is tested for the first time on the MEGAPASCALE and the maximum achieved load through this bench configuration is 2.8 kN pick-to-pick.

The oil supply temperature is set to 70°C. The oil supply pressure is set to 20, 25 and 30 bars. The oil hole angle and oil hole diameters are varied through the construction of the journals. By this means, three different journals, having two angles and two diameters are studied. The first journal called RS_J160_3 has an angle of 160° before the maximum load and a 3 mm diameter hole. The second journal, called RS_J60_4, has an angle of 60° before the maximum load and a 4 mm diameter hole. The third one is RS_J60_3 and has an angle of 60° before the maximum load and a 3mm diameter hole. The journal schemas are depicted in Figure 3.1 while the technical drawing can be found in Appendix D. The testing conditions are summed up in the Table 3.1. The indicator parameters for the Renault RS Connecting rod are the oil supply flow rate and the bearing temperature.

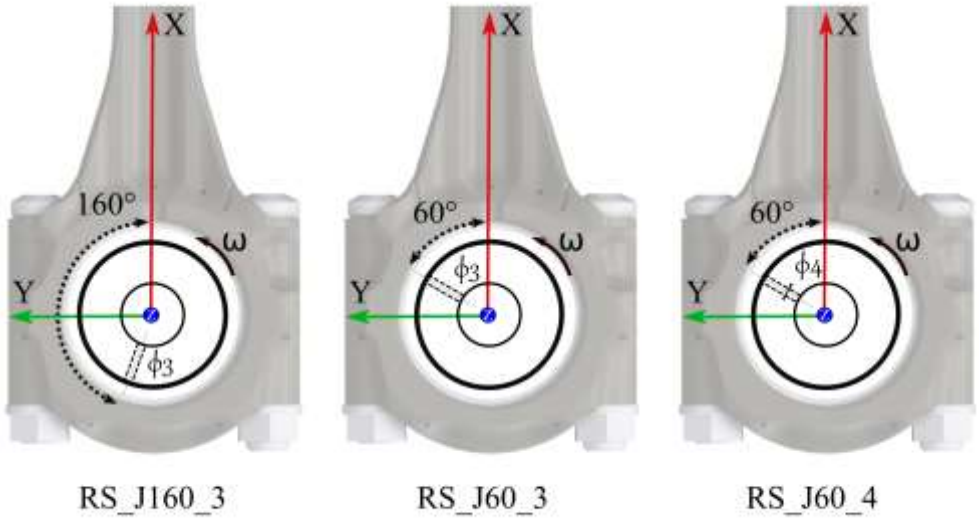

Figure 3.1 Renault RS journals, oil supply angle and diameter

Table 3.1 Testing conditions

Category	Name	Values
Control parameters	Speed (rpm)	2000; 3000; 4000
	Load [kN]	Transversal: 2.8 – pick-to-pick
		Traction: 20 kN Compression: 10 kN
	Oil Supply Temperature [°C]	70
	Supply pressure [bar]	20, 25, 30
	Journals	RS_J60_3; RS_J60_4; RS_J160_3
	Oil	5W30
	Nominal Radial Clearance [µm]	30
Bearing dimensions	Crank pin diameter [mm]	48
	Bearing width [mm]	18.3
	Conrod length [mm]	120
Indicator parameters	Oil Supply Flow rate	
	Bearing Temperature	

3.1.2. Description of the numerical simulations

The numerical simulations have been performed in the ACCEL software. It has been chosen to only take into account the elasticity of the housing. The modelling is isothermal, considering that the fluid temperature is the average of the measured bearing temperature. The oil viscosity, as a function of the bearing temperature, is interpolated through Mc Coull and Walther law described in the equations: (3.1); (3.2); (3.3). The parameters are shown in Table 3.2. The viscosity temperature dependency law is plotted in the Appendix C

Table 3.2 Oil 5w30 Viscosity parameters

Parameter	Value
Coefficient a	0.650 cSt
Viscosity at 40°C	58.4 cSt
Viscosity at 100°C	9.450 cSt

$$log_{10}[log_{10}(\nu + a)] = -m log_{10}T + n \quad (3.1)$$

$$m = \frac{-log_{10}[log_{10}(v_2 + a)] - log_{10}[log_{10}(v_1 + a)]}{log_{10}(T_{v_2}) - log_{10}(T_{v_1})} \quad (3.2)$$

$$n = m * log_{10}(T_{v_1}) + log_{10}[log_{10}(v_1 + a)] \quad (3.3)$$

The numerical simulation uses as loading parameter the measured traction - compression and transversal loads on the MEGAPASCALE. An example of a load diagram is shown in Figure 3.2. If for the compression/tension loading the test rig allows to control the load levels precisely, the same cannot be said for the lateral loading. Indeed, because of the clearances in the system, we could not reproduce the lateral load levels identically. A variation of up to 500 N of the pick-to-pick value was measured. Also, a zero offset was measured but could not be controlled. However, during the simulations carried out with Accel, we always use the measured load which corresponds to the analysed case.

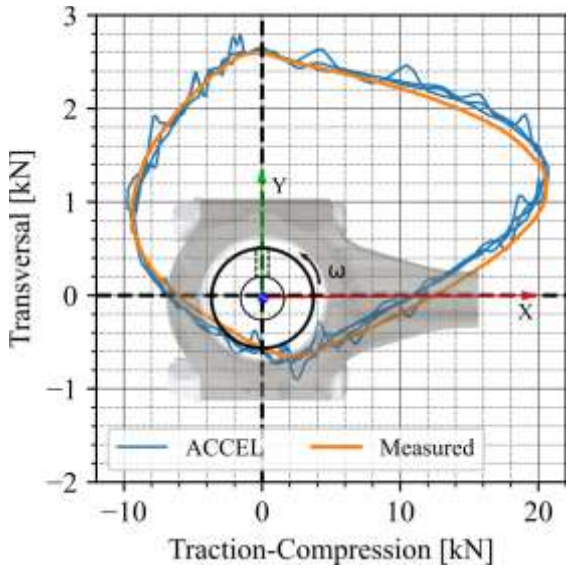

Figure 3.2 Example of Renault RS complete load

As explained in chapter 1, section 1.6, a conrod big-end bearing enhances a complex shape. Therefore, an accurate definition of the clearance space must be performed. For one bearing shell, the clearance space used for the computations is defined for this particular case through seven points. Three of them describes the clearance height (clearance height left, clearance height central, clearance height right) and the remaining four describes the crush relief (crush relief height left, crush relief width left, crush relief height right, crush relief width right). The values of those points come from metrological measurement, technique described in the chapter 2, section 2.3.

The Figure 3.3 represent the general parameters of the 2D clearance space. In continuous line is the measured profiles which are the mean of 30 roundness profiles along the bearing height. Those values are calculated relative to a base radius which is the mean journal radius on the bearing sector. In dashed line is the interpolated profile used in ACCEL calculations. The ACCEL profile is defined individually for each bearing shell by three clearance points and four crush relief points, therefore a tola of fourteen points for the entire bearing (upper and lower bearing shells). The dimensions are graphically described in Figure 3.3, while the nomenclature of the terms is summed up in Table 3.3.

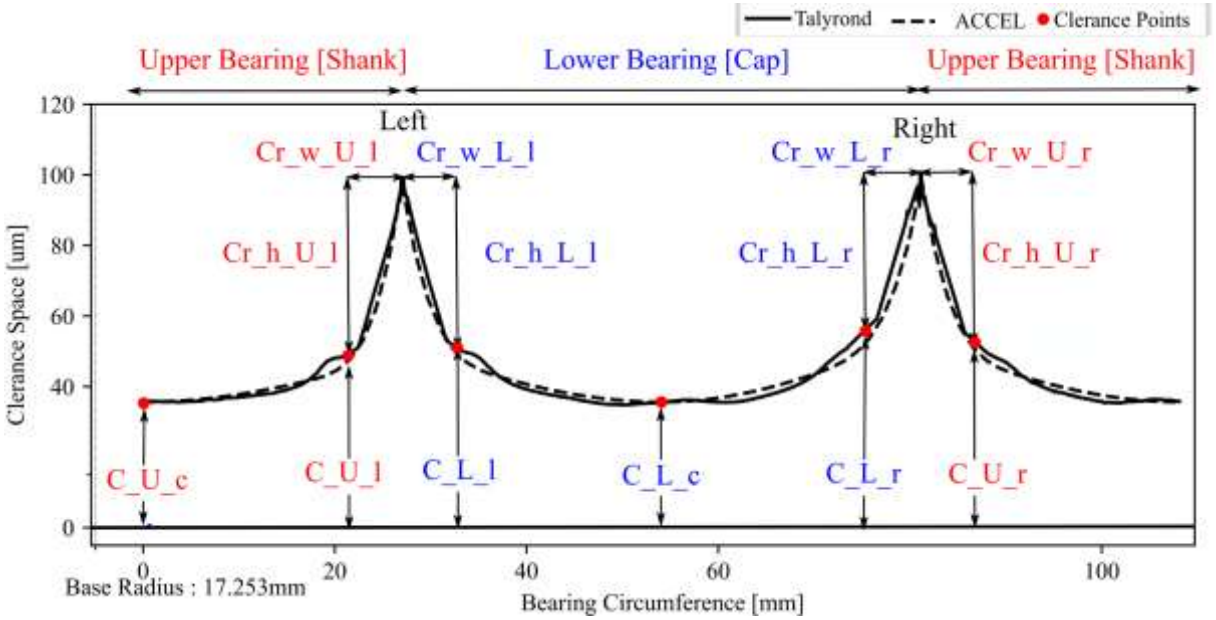

Figure 3.3 Example Description of Clearance points for Accel

Table 3.3 Clearance points nomenclature

Position	Location		Upper bearing shell	Lower bearing shell
Clearance Height	Left		C_U_l	C_L_l
	Centre		C_U_c	C_L_c
	Right		C_U_r	C_L_r
Crush Relief	Height	Left	Cr_h_U_l	Cr_h_L_l
		Right	Cr_h_U_r	Cr_h_L_r
	Width	Left	Cr_w_U_l	Cr_w_L_l
		Right	Cr_w_U_r	Cr_w_L_r

Figure 3.4 depicts the Renault RS clearance space. The measured bearing profile is represented in continuous black line. The red dots are the clearance heights extracted from the measured profile and serves as interpolation points for the ACCEL clearance space. The doted black line represents the interpolated ACCEL clearance space used for calculation. The mean radial

clearance for this study is 30 µm and is defined by being the mean value of the upper and lower bearing central clearance height (C_U_c and C_L_c). The measurements show a bump of 7 µm at 50° to 125°. These surface default may come from extra bearing shell crushing during bolt tightening or due to the presence of an impurity at the cap-bearing interface. The bolts were tightened to the manufacturer requirements which is: an angle of 110°, after applying an initial torque of about 20 Nm.

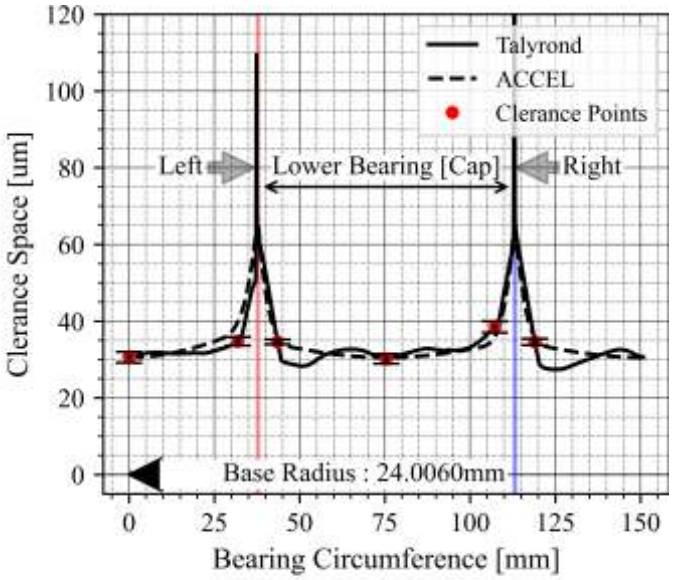

	C_U_c	C_U_l	C_L_l	C_L_c	C_L_l	C_U_r
cl[µm]	30.6	34.7	34.6	30.2	38.5	34.6
disp[µm]	1.4	1.1	0.6	1.3	1.5	0.8

Figure 3.4 Renault RS Clearance space

Table 3.4 RS Journals radius

	Journal Radius [mm]	
Connecting Rod	**Left**	**Right**
RS J160 3	24.007	24.006
RS J60 4	24.008	24.006
RS J60 3	24.006	24.005

3.1.3. Oil supply flow rate and bearing temperature measurements

The following section is dedicated to the interpretation of the Renault RS conrod experimental results in terms oil supply flow rate and bearing temperature in relation to load (traction - compression and transversal), speed, oil hole position and diameter, pressure supply and temperature oil supply. Each running point was performed on steady-state condition and

repeated at 3 times. As a reminder, the oil supply pressure and flow rate supply measurement are common for both connecting rods. For this specific test campaign, the oil supply flow rate is considered to be equally distributed between the two connecting rods. Therefore, the experimental results are compared with the double of the numerical oil supply flow rate results.

3.1.3.1 Experimental results

Figure 3.5 depicts oil supply flow rate in function of oil supply pressure for each tested. The oil supply temperature has been set to 70°C. The error bars represent the standard deviation of the recorded values. In red line is plotted the journal RS_J160_3, with an angle of 160° and a diameter of 3 mm, in green is the RS_J60_4 with an angle of 60° and a diameter of 4 mm and in BLUE is RS_J60_3 with an angle of 60° and a diameter of 3 mm.

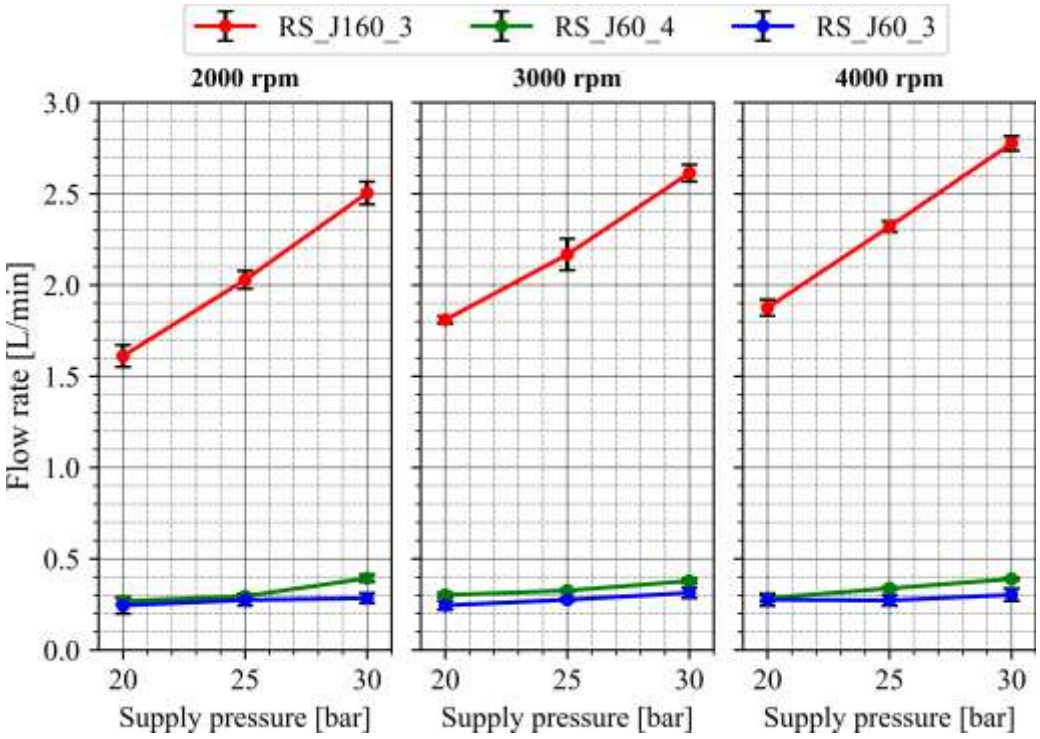

Figure 3.5 Pressure influence on flow rate at iso speed. Testing conditions: 20 kN compression, respectively 10 kN traction; 2.8kN transversal load; oil supply temperature at 70°C

As expected, for the case of RS_J160_3 journal, it can be clearly seen that the oil supply flow rate increases with the increase of the oil supply pressure. On the other hand, for RS_J60_3 and RS_J60_4 journals which have a 60° oil supply hole angle, the flow rate increases slightly with the supply pressure. This shows that the circumferential position of the supply hole has a great

influence on the flow rate and also shows the change in behaviour of the flow rate sensitivity to the pressure supply variation. For the geometries used in this study, a decrease in the diameter of the feed hole does not have a significant influence on the flow rate. Another reading of Figure 3.5 shows that the increase of the speed leads to an increase of the flow rate for a circumferential position of 160° but, has no real influence for a circumferential position at 60°.

Figure 3.6 depicts the mean bearing temperature[3] evolution with oil supply pressure. Once again, it is noted that, compared to the variation in the diameter of the supply hole, the circumferential position has a more significant influence on the operating temperature of the bearing. However, it can be mentioned that for the 3 mm oil hole (RS_J160_3 and RS_J60_3) the bearing temperature remains quasi constant (considering the error bars) with the variation of the oil supply pressure when for the larger hole of 4 mm (RS_J60_4 - green line), the increase of the oil supply pressure slightly cools down the bearing.

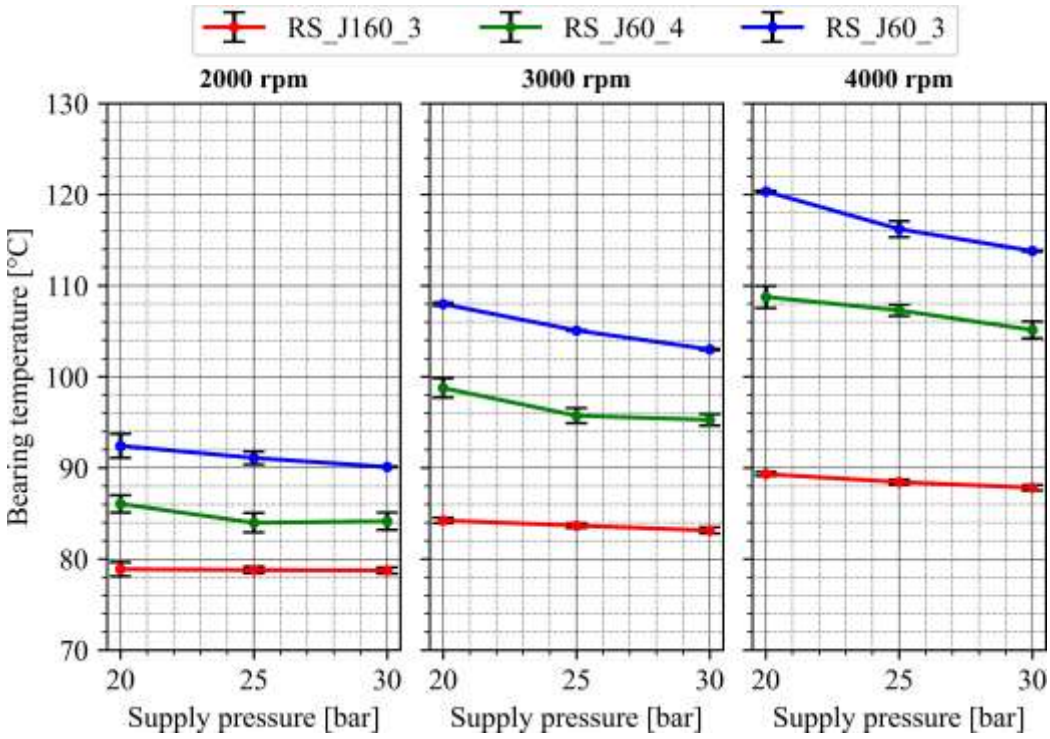

Figure 3.6 Pressure influence on bearing temperature at iso speed. Testing conditions: 20 kN compression, respectively 10 kN traction; 2.8kN transversal load; oil supply temperature at 70°C

Figure 3.7 presents the same information given in Figure 3.6 but highlights the influence of the speed on the average temperature of the bearing. As expected, the bearing temperature increases with speed, due to the viscous shear in the lubricant. An interesting note to be made is the

[3] Thermocouples T0, T1, T2, T3, T4 in figure 2.22 Chapter 2

influence of the oil hole diameter on bearing global temperature. Looking at the RS_J60_4 and RS_J60_3 it can be seen that the rate of temperature increase with speed is the same. It is also notice that an increase of the supply pressure from 20 to 25 bar leads to an increase of about 6°C of the temperature difference between the two cases: the decrease of the average temperature with the increase of the supply pressure is more important for the case RS_J60_4. The transition to 30 bar has no real influence on the temperature difference which remains constant around 6°C.

The oil hole angle has an important influence on the increase of the bearing temperature with the speed. Comparing RS_J160_3 and RS_J60_3, it is observed that the rate of temperature increase with speed is much lower for a position at 160°. If at 2000 rpm, the difference between the bearing temperatures is only 10°C, at 4000 rpm this difference is double.

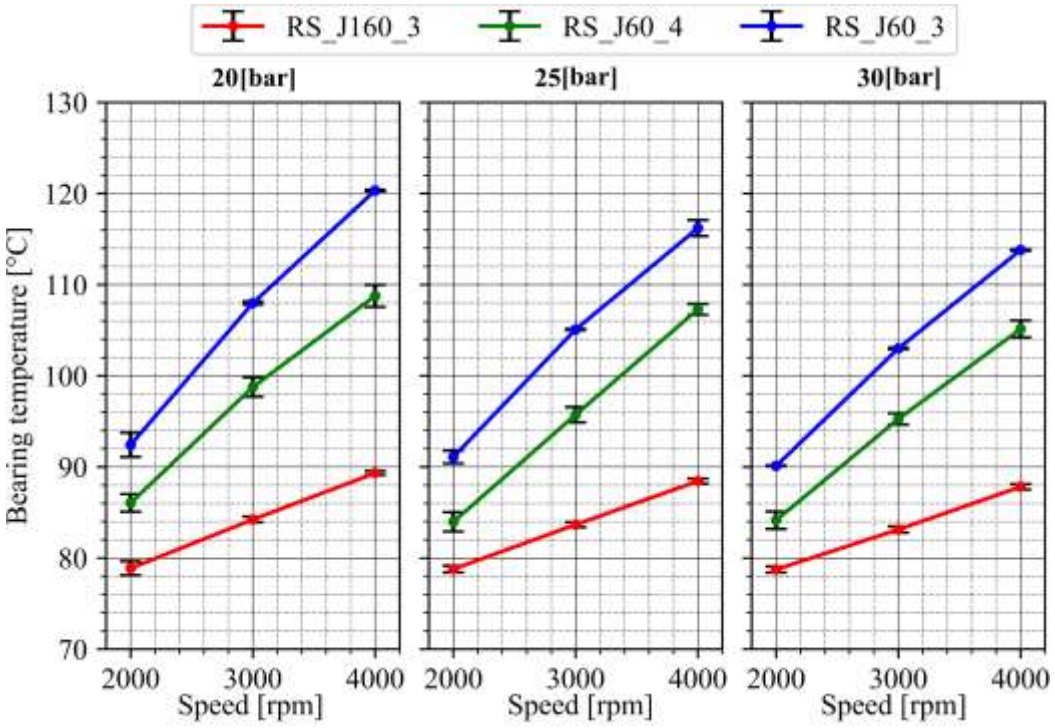

Figure 3.7 Journal Speed influence and pressure supply on average bearing temperature. Testing conditions: 20 kN compression, respectively 10 kN traction, oil supply at: 70°C oil temperature

The set of results presented in Figure 3.7 shows that the circumferential position of the supply hole in relation to the load diagram has a very strong influence on the flow rate and operating temperature of the bearing. The supply hole diameter also influences the flow rate and operating temperature.). For a circumferential position of the supply hole at 160°, the increase of the rotational speed as well as the supply pressure leads to a significant increase of the operating temperature and the leakage flow rate. For a circumferential position at 60°, the influence of

the speed and the supply pressure over both bearing temperature and flow rate is much smaller and, in some cases, not even measurable.

3.1.3.2 Interpretation and comparison with numerical results

The following analysis compares the numerical with the experimental results of the RS_J160_4 and RS_J60_3[4] in terms of oil supply flow rate dependence on pressure supply and speed. The measured feed rate is common for both connecting rods mounted on the test bench. Considering that the test rod and the service rod have the same operating conditions, the measurement is compared to twice the calculated flow rate for one rod.

It is important to note that the oil supply flow rate is calculated by computing the difference between the flow rate exiting the bearing and the flow rate entering the bearing through the bearings edges. Indeed, in the areas where the pressure inside the bearing near the edge is higher than the ambient pressure, the oil flow exists the bearing. Meanwhile, in areas where the pressure inside the bearing near the edge is lower than the ambient pressure and, at the same time, no film rupture occurs, the oil present in the vicinity of the bearing edge can feed the bearing. For the film rupture zones which reaches the edges of the bearing, the outflow or inflow is approximated by an algorithm described in reference [96].

First, a comparison will be made of the measured feed rate values with those predicted by the numerical model. As the algorithm computes the bearing supply flow rate taking into account the presence of oil in the vicinity of the bearing, two extreme cases are considered. The first one is: bearing fully submerged into oil (expressed in the plot as f1), and the second case being no oil around the bearing (F0), therefore for this last case no entering oil flow will be possible.

Figure 3.8 compares the flow rate measurements to the calculated flow rate for the RS_J160_3 journal. We note that the sensitivity of the rate of the flow with the pressure is different between the measured values and those calculated numerically. A maximum difference of approximately 24.1% can be observed at 4000 rpm and a supply pressure of 25 bar while a minimum difference of 0.4% can be calculated at 2000 rpm and a supply pressure of 30 bar. Those values are obtain

[4] In terms of the dependence of the flow rate on pressure supply and speed, the results obtained for the RS_J60_4 journal are quite similar to the results obtained for the RS_J60_3 journal and will therefore not be presented.

considering the bearing fully submerged in oil (F1). On the other hand, considering the other extreme case, no presence of oil around the bearing (F0), it can be seen a logical increase of the supply flow rate, even though, is hard to physically quantify the amount of oil in the vicinity of the bearing due to the connecting rods positioning inside the test bench (chapter 2, section 2.1, Figure 2.1). Considering the different hypotheses formulated to carry out the simulations (perfectly aligned bearing, right and left connecting rod considered as identical, isothermal model, not considering the possible thermal deformations) but also uncertainties on the values defining the clearance space[5], the comparison can be considered as relatively good.

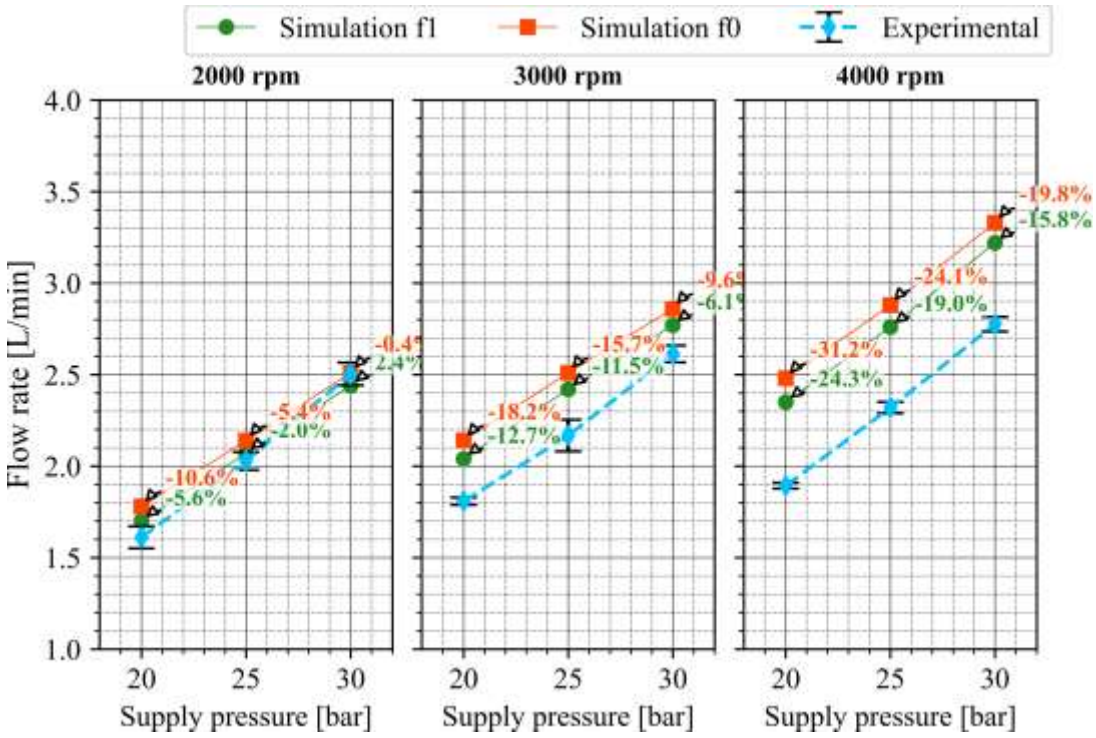

Figure 3.8 Oil supply flow rate variation with oil supply pressure numerical and experimental comparison. RS_J160_3 journal

Figure 3.9 compares the flow rate measurements and the calculated flow rate for the RS J60 4 journal. While experimentally no real variation in the measured flow rates with speed, numerically there is a significant increase in flow rate with increasing the journal rotational frequency. Overall, the differences between the measurements and the predictions increase with the increase of the speed. Even if the comparisons between the numerical calculations and the

[5] the metrology of these bearings was carried out at the beginning of the thesis; the rigorous methodology described in chapter 2 as well as the support allowing very precise measurements were developed later and the measurements for the RS connecting rod were not able to be repeated.

experimental results are far from perfect, both show a drastic decrease of the flow rate between a supply hole positioned at 160° compared to a supply hole positioned at 60°.

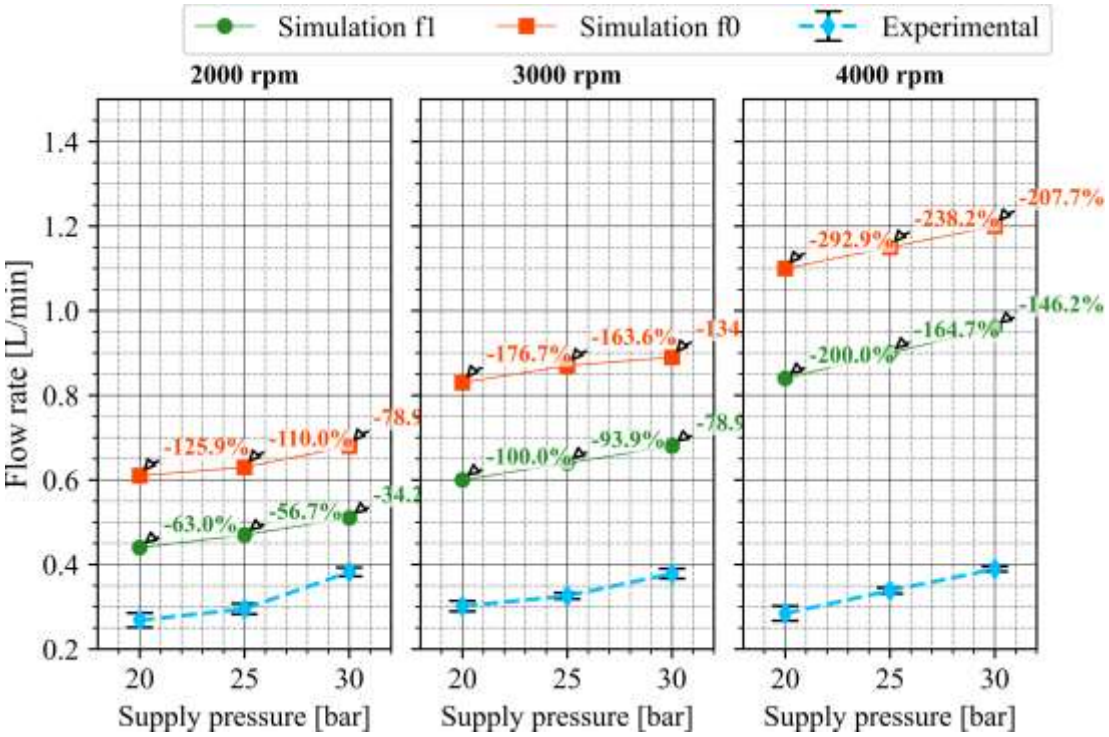

Figure 3.9 Oil supply flow rate variation with oil supply pressure numerical and experimental comparison. RS_J60_4 journal

In order to understand this behaviour, Figure 3.10 depicts the variation of the oil flow rate as a function of the cycle angle, for both journals, at 2000 rpm and 20 bar supply pressure. In BLUE line is drawn the 60° oil hole angle case (RS_J60_4 journal), while in BROWN is represented the 160° oil hole angle case (RS_J160_3 journal). The variation during the cycle can be divided into three regions: the first region from 0° to 150°, the second region from 150° to 250° and the third region from 250° to 360°. For the first and the third regions, it can be observed that the flow rate variation follows the same trend with a quasi-constant difference. For the second region, the flow rate of RS_J60_4 journal does not encounter the hump encountered by the RS_J160_3 journal.

The comparisons shown in Figure 3.9 reveal the limitations of numerical modelling in this particular case, which can be related to the boundary conditions used to model the supply hole. The pressure supply for the simulation is imposed as constant throughout the simulation, therefore back flow phenomena through the oil supply hole is not considered.

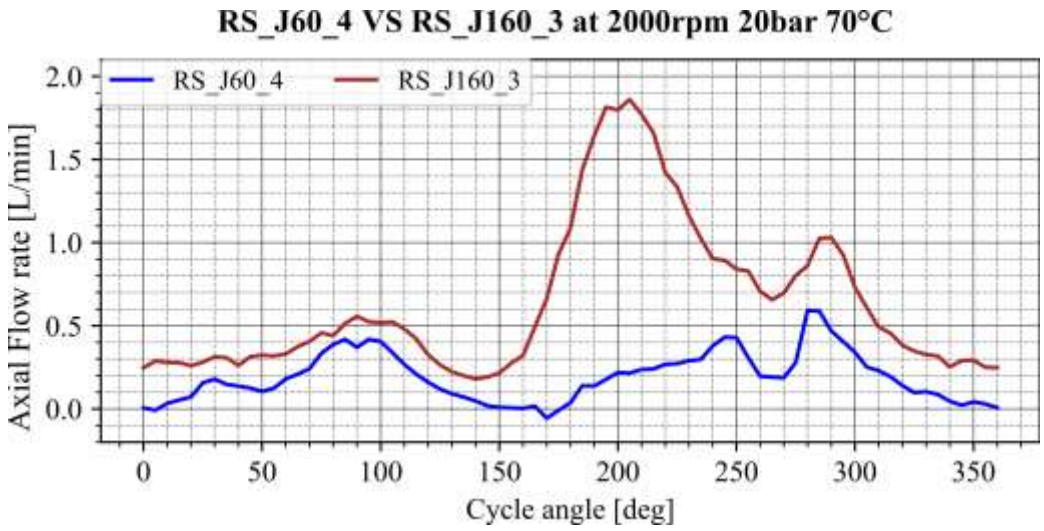

Figure 3.10 Numerically predicted oil flow rate at 2000 rpm and 20 bar oil supply pressure

Figure 3.11 shows the oil hole position in relation with the hydrodynamic pressure and the film thickness for both studied journals and for several cycle angles. On each plot, the *x* axis represents the journal angle, while the *y* axis represents the cycle angle. It can be noted that for the RS_160_3 journal, the supply hole is always positioned in a thick film region, which favours the bearing feed and contributes to the cooling of the bearing (the temperatures measured for both journals, systematically shows lower values for the RS_160_3). For the RS_J60-4 journal, the supply hole is often positioned in areas of thinner film thickness and even, between 100° and 200° of the cycle, it interferes with regions of high-pressure. It should also be noted that in these situations, the supply pressure may be considerably lower than the hydrodynamic pressure inside the bearing and, as a result, the oil may flow out of the contact, back through the supply hole. This particular situation is not modelled by the numerical model which imposes a constant supply pressure. This is one of the reasons for the poor predictions of the oil flow rate in the case of RS J60 4, where the supply oil hole faces most of the cycle the thin film regions.

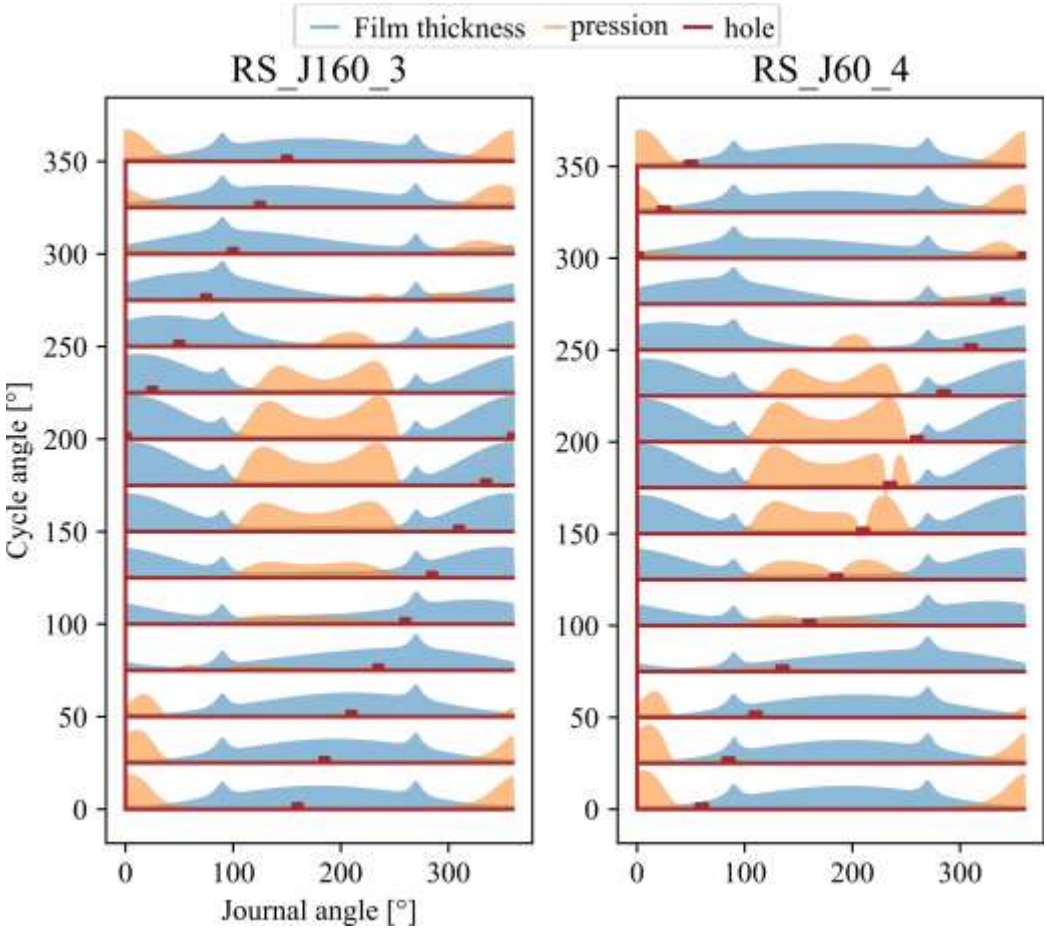

Figure 3.11 Film thickness, pressure and oil supply hole positioning versus cycle angle at 2000 rpm and 20 bar oil supply pressure and 70°C supply temperature

Summing up the tests and calculation performed, the importance of the circumferential position of the feed hole on the feed rate as well as the operating temperature of the bearing has been proven. The numerical-experimental comparisons are much less accurate for cases where the oil hole penetrates the hydrodynamic pressure field.

3.1.4. Conclusions on Renault RS conrod campaign test

This test campaign, carried out at the beginning of the thesis, allowed us to highlight the importance of the position of the feed hole on the flow rate and the operating temperature of a connecting rod bearing.

Furthermore, the transversal load has been tested for the first time on MEGAPASCALE. It has been noticed that due to the clearances, the transversal loading conditions are difficult to be identically reproduced. A dispersion of 500 N pick-to-pick has been observed.

The numerical predictions helped to understand the measured parameters and, at the same time, showed some limitations of the modelling.

From a technical point of view, this campaign also allowed us to define new measurements necessary to better characterize the behaviour of the connecting rod bearings, measurements which were implemented for the second test campaign presented in the following paragraphs.

3.2. KAWASAKI ZX10 Conrod campaign tests

For the second testing campaign the MEGAPASCALE bench was modified to accommodate a Kawasaki ZX10 conrod, which is the one provided by AKIRA. Taking advantage of the experience gained with the RS connecting rods, it was decided to introduce new measuring systems. The list and the drawing of the modified parts are available in the Appendix D.

3.2.1. Description of the performed tests

This section describes the design of experiments for the Kawasaki ZX10 connecting rod. The particularities of the Kawasaki ZX10 connecting rod compared to the Renault RS connecting rod are firstly the high speeds (up to 11 500 rpm instead of 4000 rpm) and secondly, installation of new sensors such as eddy current gap sensors and voltage drop. Furthermore, a sensibility of the clearance is performed.

As already defined in the introduction of this chapter, the set of control parameters defines the tests running points. For the particular case of the Kawasaki ZX10 connecting rod the control parameters are:

Test Running Point = [Speed, Traction - compression Load, Oil Supply Temperature, Oil supply Pressure, Oil Hole Angle, Oil Hole Diameter, Clearance, Oil]

For this test campaign, the speed was kept constant at 11500 rpm. Also, the traction - compression load was identical for all the running points and has a pick-to-pick amplitude of 32 kN (16 kN traction and 16 kN compression). Even though the traction - compression load inside the engine can reach 25 kN traction and 20 kN compression, on MEGAPASCALE the load was limited due to connection rod small end structural

limitations. Applying a transversal load for this particular connecting rod was not possible, due to its small dimensions and clamping issues.

The oil supply temperature was set to 80°C and 100°C. The oil supply pressure was set to 10, 15 and 20 bars.

For the Kawasaki ZX10 only the oil hole angle is varied; the oil hole diameter is kept constant at 5 mm. The journals are called J90 for the one having the angle of 90° before the maximum load and J135 for the journal having the angle of 135° before the maximum load. The journal schematics are depicted in Figure 3.12, while the technical drawing can be found in Appendix D. For this connecting rod, the clearance is varied through two bearing shells thicknesses; therefore, the clearances are called: BLUE-Cxx, where xx is the average radial clearance value.

The indicator parameters for the Kawasaki ZX10 Connecting rod are: The Oil Supply Flow rate, Bearing Temperature, Eddy Current Gap Sensors, Voltage Drop, Telemetry, Wear. Since the results of the tests performed with telemetry system did not give satisfactory results from a tribological point of view, but did validate the proof of concept of the telemetry system, they are only presented in the Appendix A.

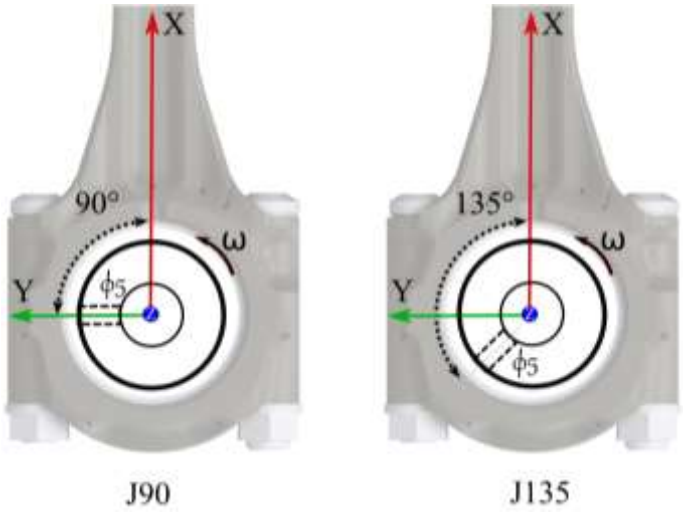

Figure 3.12 Kawasaki ZX10 journals oil hole position.

3.2.2. Description of the numerical simulations

As previously, ACCEL software is used for numerically predict the bearing behaviours. Isothermal model is considering with the mean fluid temperature[6] measured on bearing during tests. The viscosity temperature dependence is interpolated through Mc Coull and Walther model, while the piezoviscous behaviour is modelled by the Barus model. The used parameters are shown in Table 3.5. The viscosity temperature dependency law is plotted in the Appendix C.

Table 3.5 HTX 860 Viscosity parameters

Law	Coefficient	Value
Mc Coull and Walther	Coefficient a	0.700 cSt
	Viscosity at 40°C	150.6 cSt
	Viscosity at 100°C	23.590 cSt
Barus	Coefficient α	0.009 MPa-1

Figure 3.13 depicts the load applied on the Kawasaki ZX10 test (right) connecting rod. For this test campaign, it was not possible to apply an identical load on the second connecting rod. Indeed, as the diameter of the journal is relatively small (34.5 mm), this would have led to a misaligned operating mode for both connecting rods, generated by the bending of the journal under the applied load. Consequently, to ensure aligned operating conditions for the test (right) connecting rod, it was decided to apply only half of the load on the left connecting rod.

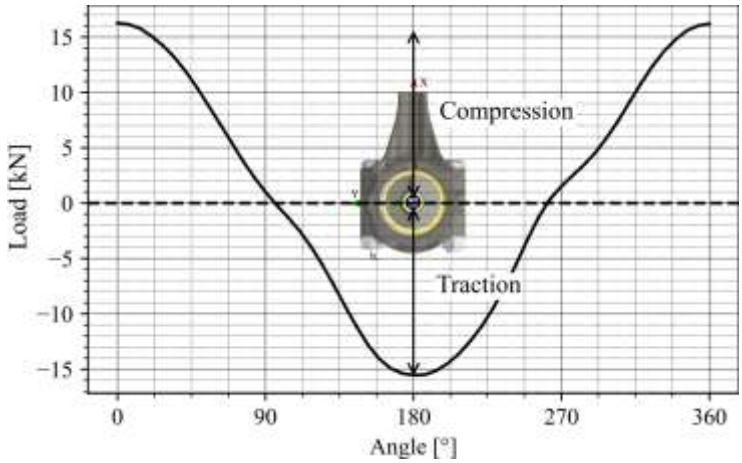

Figure 3.13 Kawasaki ZX10 load

[6] Thermocouples T0, T1, T2 figure 2.25 in chapter 2

3.2.3. Oil flow rate supply and temperature bearings

This section presents the experimental and numerical interpretation and comparison of oil flow rate and temperature. A special attention is payed to the clearance interpretation because the measurements for the KAWASAKI ZX10 connecting rod are performed on an improved rig and with an improved measuring method than the Renault RS connecting rod. Multiple observations have been noticed during the testing campaign. The clearance is an important input to the oil flow rate computation, therefore special attention should be paid to this parameter. Moreover, it was possible to investigate the influence of a modification of the bearing clearance, by using bearing shells with different thicknesses.

3.2.3.1 Clearance space and surface metrology results – interpretation and discussions

As for the Renault RS connecting rod, the numerical clearance space for one bearing shell is defined by 7 interpolation points three of them for clearance height and four for the crush relief. The points are taken from metrological measurements and their profiles are depicted in Figure 3.14 and Figure 3.15. Table 3.7 sums up the central radial clearance of new bearing shells for each bearing-journal pair. The radial central clearance is the average of the upper bearing central (C_U_c) and lower bearing central (C_L_c) clearance. Along this manuscript, the clearances will be referred as: BLUE-CXX, where XX represents the value of the average initial clearance. Table 3-6 represents the mean radius of the journals which are used to calculate the clearance space. The bolts have been tightening to the manufacturer requirements which is 320 µm elongation and checking torque of 50 Nm torque ±1%.

Table 3.6 Journals radius

	Journal Side Radius [mm]	
Connecting rod	**Left**	**Right**
J90 Journal	17.252	17.253
J135 Journal	17.254	17.254

Table 3.7 Central radial clearance values – New Bearings (C1)

	Central Radial Clearance [µm]		
Connecting rod	**Left**	**Tight**	
Bearing name	**PINK**	**BLUE**	**BROWN**
J90 Journal	39.35	14.95	25.85
J135 Journal	37.1	13.45	24.35

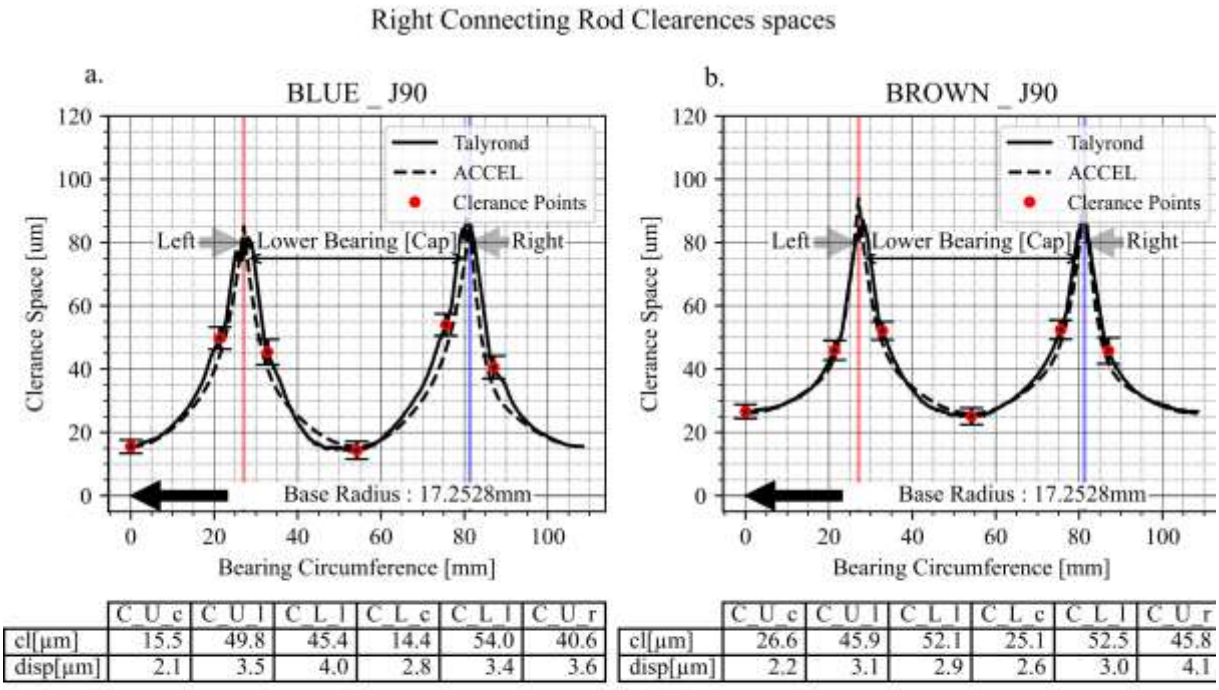

	C_U_e	C_U_l	C_L_l	C_L_e	C_L_l	C_U_r
cl[µm]	15.5	49.8	45.4	14.4	54.0	40.6
disp[µm]	2.1	3.5	4.0	2.8	3.4	3.6

	C_U_e	C_U_l	C_L_l	C_L_e	C_L_l	C_U_r
cl[µm]	26.6	45.9	52.1	25.1	52.5	45.8
disp[µm]	2.2	3.1	2.9	2.6	3.0	4.1

	C_U_e	C_U_l	C_L_l	C_L_e	C_L_l	C_U_r
cl[µm]	14.0	48.3	43.9	12.9	52.5	39.1
disp[µm]	2.1	3.5	4.0	2.8	3.4	3.6

	C_U_e	C_U_l	C_L_l	C_L_e	C_L_l	C_U_r
cl[µm]	25.1	44.4	50.6	23.6	51.0	44.3
disp[µm]	2.2	3.1	2.9	2.6	3.0	4.1

Figure 3.14 New Bearing Right Connecting Rod Clearance Spaces: a. and b. BLUE and BROWN bearing with J90 journal; c. and d. BLUE and BROWN bearing with J135 journal

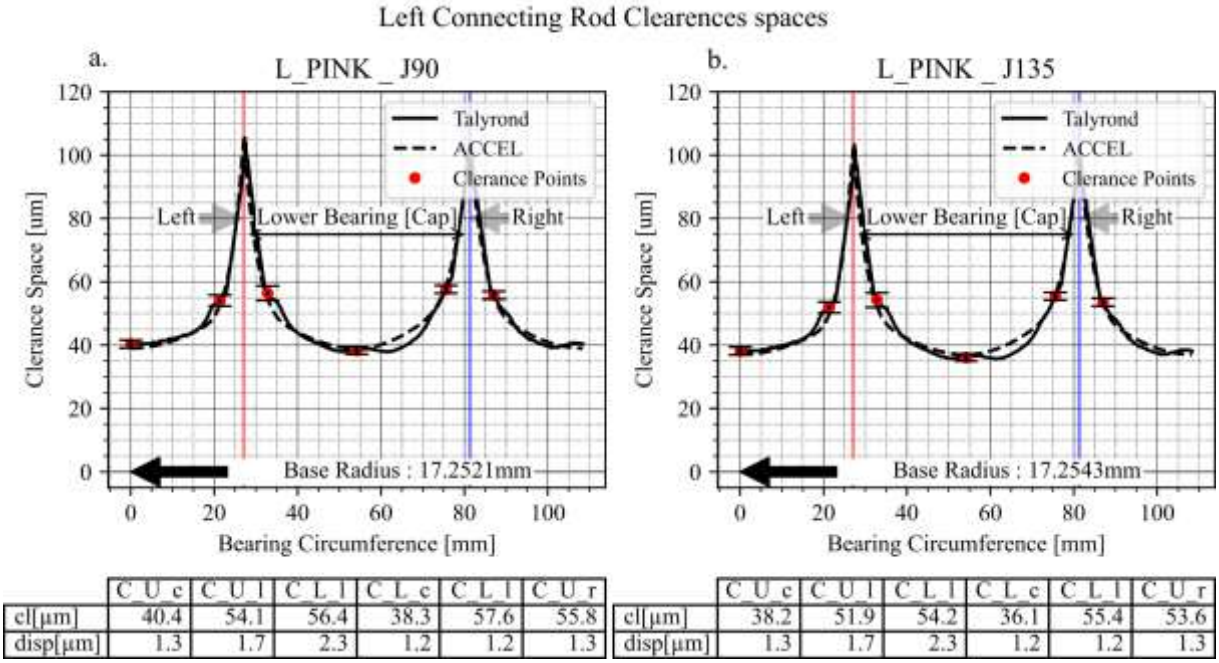

	C_U_c	C_U_l	C_L_l	C_L_c	C_L_l	C_U_r
cl[µm]	40.4	54.1	56.4	38.3	57.6	55.8
disp[µm]	1.3	1.7	2.3	1.2	1.2	1.3

	C_U_c	C_U_l	C_L_l	C_L_c	C_L_l	C_U_r
cl[µm]	38.2	51.9	54.2	36.1	55.4	53.6
disp[µm]	1.3	1.7	2.3	1.2	1.2	1.3

Figure 3.15 New Bearing Left Connecting Rod Clearance Space: a. Pink bearing with J90 journal; b. Pink bearing with J135 journal

3.2.3.2 Experimental Results

The following section first shows the oil flow rate measurements for the tests performed with the Kawasaki ZX10 connecting rod. Furthermore, the bearing temperatures are analysed. The tests are carried out with a left connecting rod equipped with a PINK bearing. The same connecting rod is used for all the test campaign.

Figure 3.16 shows the experimental measurements of the oil supply flow rate as a function of the supply pressure, the supply hole angle position and the average bearing clearance.

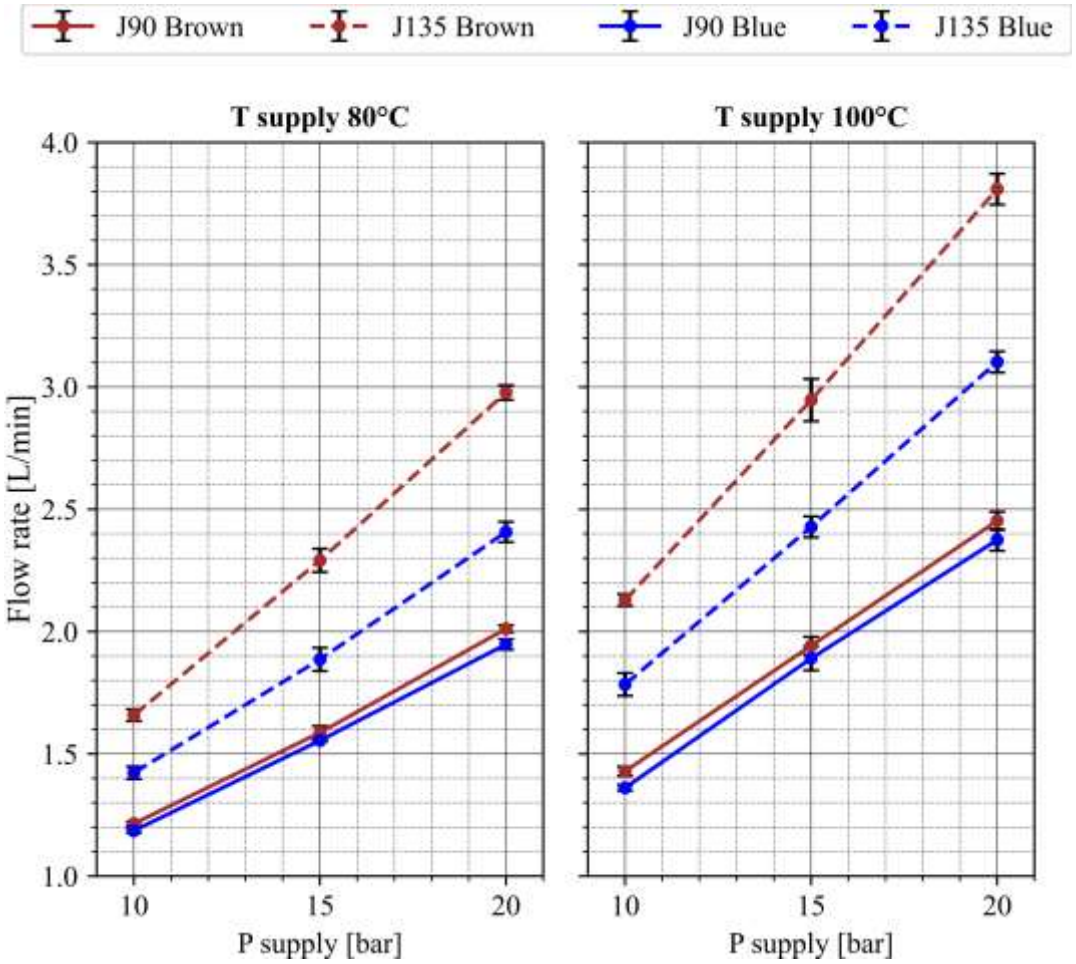

Figure 3.16 Oil supply Flow rate sensitivity analysis for Kawasaki ZX 10 experimental results

The left plot are the measurements for a supply oil temperature of 80°C, while the right one is a supply oil temperature of 100°C. In dashed line are plotted the measurements for the J135 journal, while in continuous line are plotted the measurements for the J90 journal. In blue colour are the BLUE bearings while in brown colour line is the BROWN bearings. The flow rate values are expressed in l/min and represents the total measured flow rate on both connecting rods (left

and right). The reason of choosing to plot the total flow rate is that the flow rate distribution over each conrod is unknown. In order to compare the experimental flow rate with the ACCEL results, computations for both right and left connecting rods will be performed.

Table 3.8 Linear regression coefficients

Journal-bearing pair	a_T80	b_T80	Cor.Coef.	a_T100	b_T100	Cor.Coef.
J90 BROWN	0.080	0.409	0.99	0.102	0.405	0.99
J135 BROWN	0.132	0.330	0.99	0.168	0.441	0.99
J90 BLUE	0.076	0.420	0.99	0.101	0.355	0.99
J135 BLUE	0.098	0.429	0.99	0.132	0.460	0.99

For all the running points oil supply flow rate increases linearly with the increase of the oil pressure supply. By looking at the Table 3.8, which represents the linear regression coefficients, it can be noticed that the flow rate for J135 journal increases faster with pressure at the same oil supply temperature when compared with J90 journal. A similar observation was made during the test campaign for Renault connecting rods where a feed hole far from the maximum load allows a better feeding of the bearing.

When analysing the flow rate for the J135 journal, it can be seen that it clearly increases with the increase of the clearance. For example, at a supply pressure of 10 bar and a supply temperature of 80°C, the flow rate increases from 1.4 l/min (BLUE-C13.5) to 1.68 l/min (BROWN-C24.5). Looking at the J90 journal, the flow rate does not change much with the increase of the clearance. For example, at a supply pressure of 10 bar and a supply temperature of 80°C, the flow rate increases from 1.2 l/min (BLUE- C13.5) to 1.22 l/min (BROWN- C25.8).

The main conclusion that can be drawn from these results is that the circumferential position of the supply hole has, as for the RS connecting rod, a very important influence on the flow rate and its variation with the other parameters.

Figure 3.17 shows the thermocouples location. For the particular case of ZX10 conrod 5 thermocouples are installed. Three of them (T0, T1 and T2) are measuring the back-bearing shell temperature at median plane, while other two (T3 and T4) measures the temperature of the exiting flow bulk in the shank region on both sides.

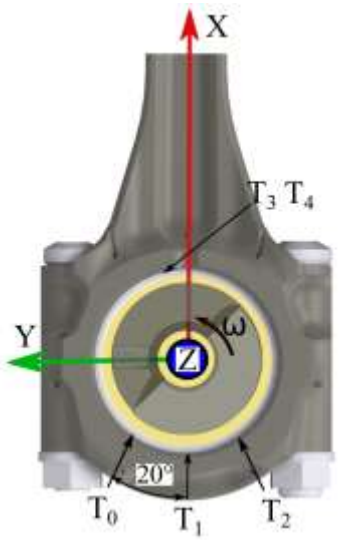

Figure 3.17 Kawasaki ZX10 Thermocouples location

The next lines analyse the influence of the oil pressure supply, clearance and oil hole angle on the bearing temperature, presented in the Figure 3.18 and Table 3.9. To begin with, a local thermal analysis is performed based on the thermocouple location around the bearing. It can be seen that depending on the location of the thermocouples, inside the connecting rod (T0, T1 and T3) or outside (T3 and T4), the thermal levels are considerably different. For example, the temperature measured by the T0, T1, and T2, which are located inside the connecting rod cap and measures the back-bearing shell temperature are about 10°C to 20°C higher than the temperatures measured by T3 and T4, which measures the temperature of the oil bulk exiting the bearing. The difference between T3 and T4 is argued by the fact that T3 is located between the two connecting rods, while T4 faces the rotating shaft which may bring thermal perturbations.

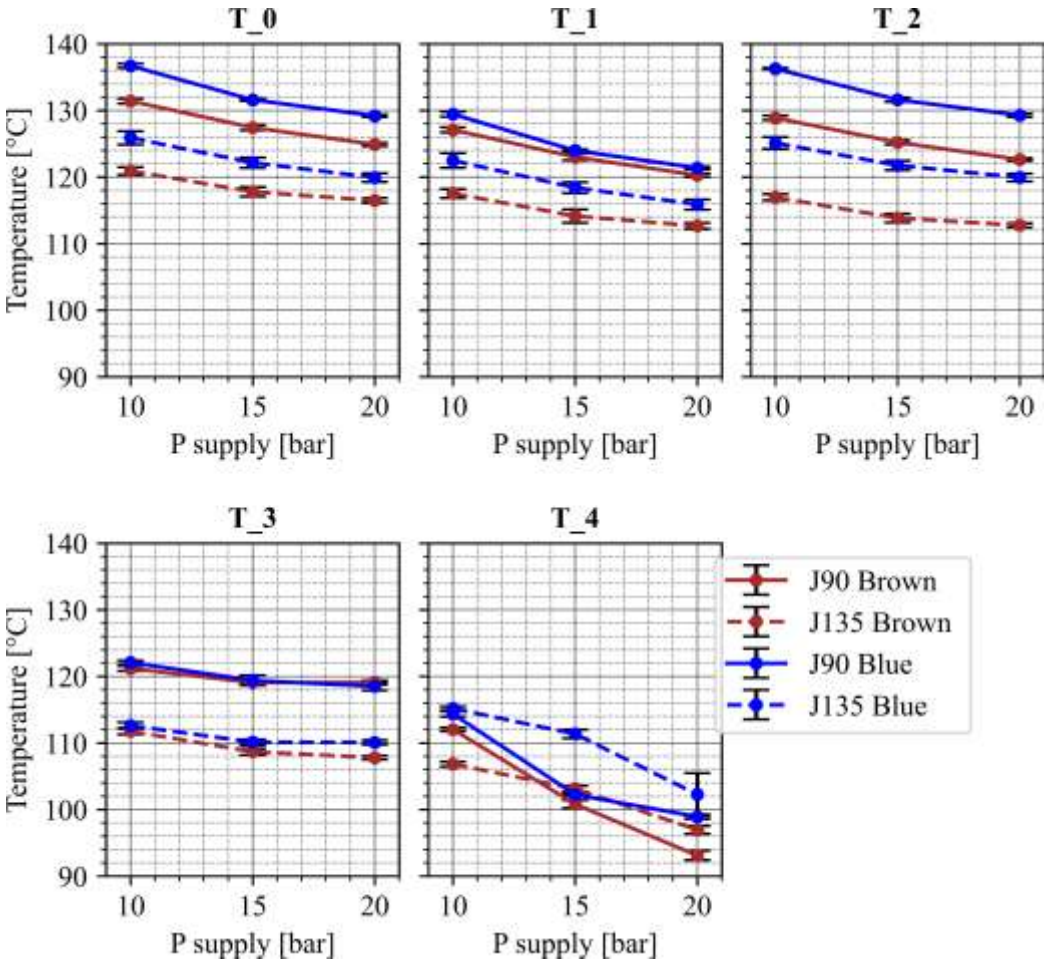

Figure 3.18 Kawasaki ZX10 Bearing temperature at 80°C oil supply

Table 3.9 Mean back-bearing temperature at 80°C oil supply temperature

		Mean Bearing Temperature [°C]		
	Pressure supply [bar]	**10**	**15**	**20**
J90 Journal	**BLUE- C14.9**	133	129	126
	BROWN- C25.9	129	125	122
J135 Journal	**BLUE- C13.5**	124	120	118
	BROWN- C24.4	116	109	106

By performing a global thermal analysis based on the cap side temperatures depicted in Table 3.9, it can be seen that the J135 journal results in a decrease in average temperature of about 10°C compared to the J90 journal for the same clearance. Again, the circumferential position of the supply hole has a strong influence on the bearing temperature.

Furthermore, it is noticed that for the J135 journal, the mean bearing temperature decreases by 4°C from a clearance of BLUE-C21.7 to BROWN-C32.64. Meanwhile, the J90 journal mean bearing temperature decreases by 8°C for the same clearance increase. The cooling effect generated by the increase in clearance can be argued by the increase of the supply flowrate. Thus, the thermal energy is carried out of the bearing through the oil bulk exiting the fluid domain.

For all the tested conditions, the increase in pressure supply decreases the bearing temperature. This is mainly due to the increase of the flow entering the bearing as show in the oil supply flow rate analysis plot (Figure 3.16). As expected, a lower flow rate results in a higher average bearing temperature. Thus, overall, the decrease in supply pressure and mean clearance leads to a higher operating temperature.

Figure 3.19 shows the variation of the bearing temperature for a supply temperature of 100°C. Overall, the same trends as for a supply temperature of 80° are observed. The only difference is the temperatures mean level, which increases by about 15°C.

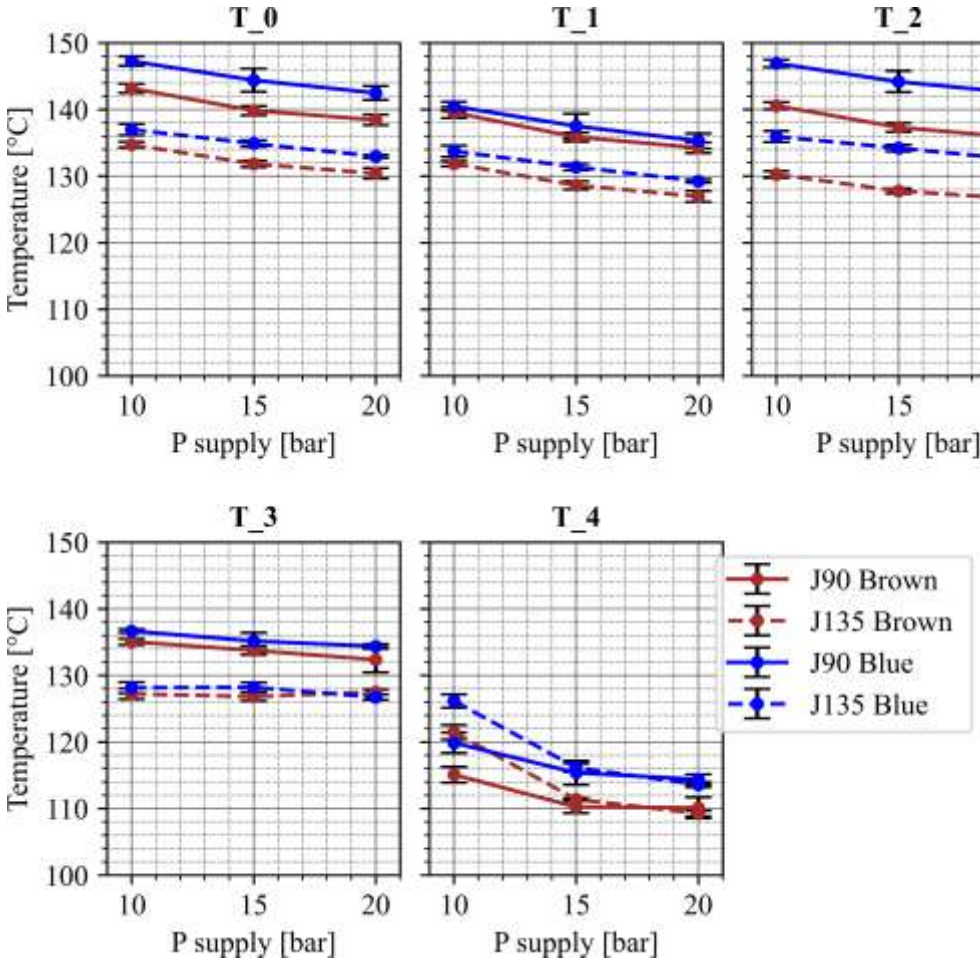

Figure 3.19 Kawasaki ZX10 Bearing temperature at 100°C oil supply

Table 3.10 Mean back-bearing temperature at 100°C oil supply temperature

		Mean Bearing Temperature [°C]		
	Pressure supply [bar]	**10**	**15**	**20**
J90 Journal	**BLUE-C14.9**	145	142	140
	BROWN-C25.9	136	133	132
J135 Journal	**BLUE-C13.5**	141	138	136
	BROWN-C24.4	132	129	128

3.2.3.3 Investigation of the evolution of the clearance space

During the test campaigns, the evolution of the bearing shape for the test rod was also monitored. Table 3.11 shows the operating times of the connecting rods. At each change of eccentric, the metrology of the connecting rod is redone. For example, for the BLUE bearing, a first measurement is taken after the bearing has been mounted (measurement C1), a second one after the end of the test with the eccentric J90 (measurement C2) and a third one at the end of the test with the eccentric J135 (measurement C3). For the BROWN connecting rod, the C2 measurement is made after having been used with the eccentric J135 and the C3 measurement is made at the end of the tests. Once the tests are completed, the connecting rod is disassembled and the two bearing shells are weighed. This measurement is then compared with the measurements of the bearing shell weights taken before the assembly on the connecting rod.

Table 3.11 Bearing testing Time and Sliding Distance

	Time[h]			**Sliding Distance[m]**		
	J90	**J135**	**Total**	**J90**	**J135**	**Total**
BLUE	5.4	3.7	9.14	2.45E+08	1.86E+08	4.3E+08
	J135	**J90**	**Total**	**J90**	**J135**	**Total**
BROWN	2.95	3.7	6.65	1.71E+08	2.20E+08	3.92E+08

These weighing results are represented in Table 3.12. The measurements are made with a precision weighing scale (0.1 mg). Before each measurement, the bearing shells are cleaned in an ultrasonic bath and weighed. This is done at least three times until the mass stabilizes, ensuring that no contaminants remain on the bearing shells.

Table 3.12 Kawasaki ZX10 Bearing mass measurement

	New		Used		Weigh Loss		
Bearing	**Upper[g]**	**Lower[g]**	**Upper [g]**	**Lower [g]**	**Upper [g]**	**Lower [g]**	**Total[g]**
BLUE	10.5202	10.5348	10.5196	10.5291	0.0006	0.0057	0.0063
BOWN	10.4899	10.4991	10.4887	10.4964	0.0012	0.0027	0.0039

Figure 3.20 represents the investigation of the clearance evolution for the BLUE and BROWN bearings. The left plots represent the clearance profile over the bearing height. On the right side is represented the difference between the clearances. Comparing the first measurement (C1) with the other two (C2 and C3) and for both bearings, it can be observed a significant change in profile in the regions where the clearance is low (at the shank plane: C_U_c and C_L_c in Figure 3.3). This leads to an increase of about 7 µm in radial clearance in these regions. The differences between the C2 and C3 measurements remain very small.

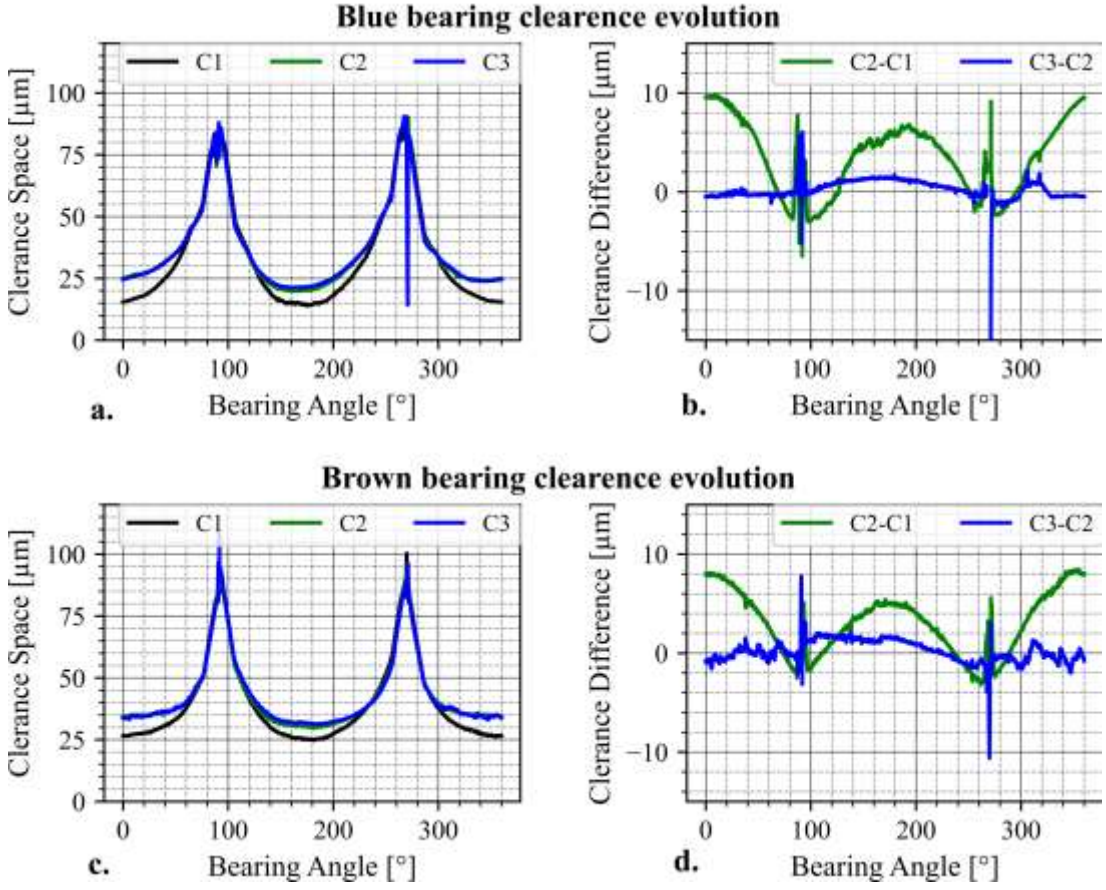

Figure 3.20 Bearing quenching investigation

Table 3.13 Radial clearance evolution between testing sets

Bearing	BLUE			BROWN		
Measurement	**C1**	**C2**	**C3**	**C1**	**C2**	**C3**
J90	14.95	22.76	23.15	25.85	32.28	32.64
J135	13.45	21.22	21.70	24.35	30.78	31.10

Based on the fact that the mass of the bearings hardly evolves between the beginning and the end of the tests (as seen in Table 3.12, which shows an evolution of the mass lower than 0.06% of the initial bearing shells mass) it can be concluded that the evolution of the shape of the bearing shells is mainly generated by the creep of the soften layer of the bearing in the high-pressure zones.

In order to reinforce this hypothesis, a first comparison with the numerical results is shown in Figure 3.21 which represents the profiles of the connecting rod clearance in cylindrical coordinates as well as the maximum pressure per cycle numerically predicted with ACCEL. It is interesting to note that the change in radial clearance occurs in areas where the connecting rod shell is subject to high hydrodynamic pressure (larger than 60 MPa).

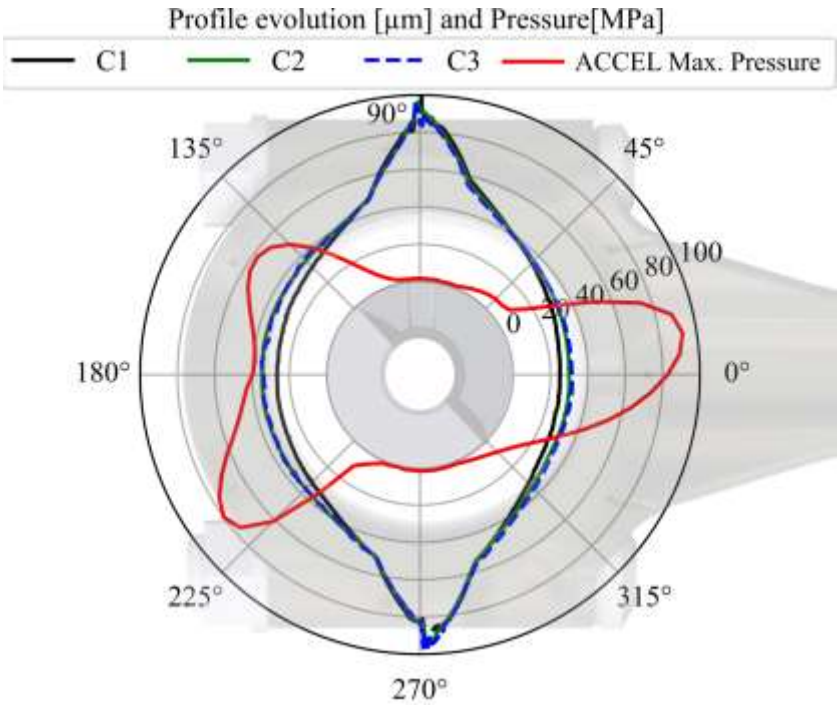

Figure 3.21 Bearing quenching and computed pressure history

The evolution of the shape of the bearing is also accompanied by an evolution of the surface roughness. Measurements were carried out with an optical profilometer before and after the tests (these measurements require the dismantling of the connecting rod and therefore, it is not possible to have an intermediate follow-up of the roughness). The measurements are performed along the traction - compression direction of the bearing shell. A number of 21 measurements are taken along this direction, each having a dimension of 1x1mm (see Figure 3.22). All the 21 measurements are stitched together. Before calculating the topology parameters, a shape correction is applied to the surface. This process is needed due the concave shape of the bearing. Figure 3.23 and Figure 3.24 show the two surface textures and a comparison between two profiles measured before and after the use of the bearing shell.

Figure 3.22 Roughness Measurement locations

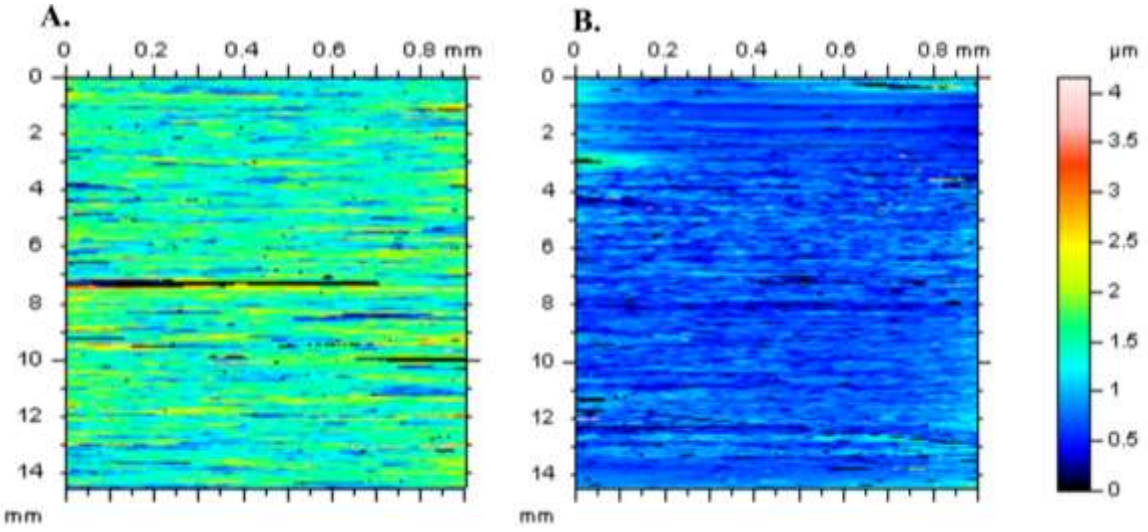

Figure 3.23 Bearing shell roughness surfaces: A. New; B. Used

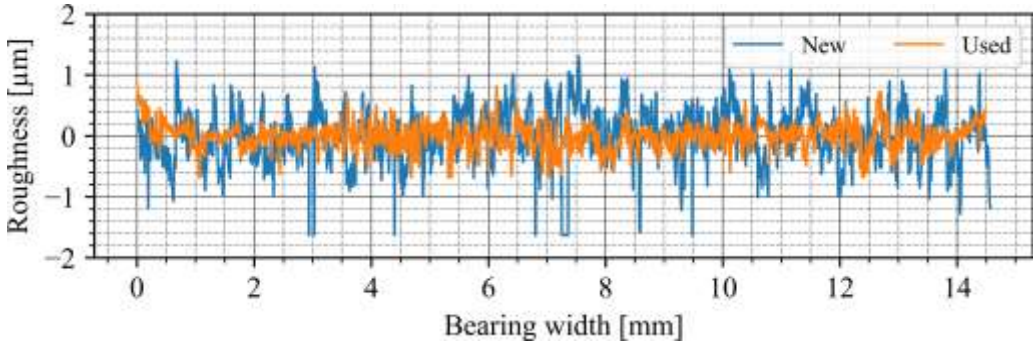

Figure 3.24 Extracted roughness profiles

Table 3.14 summarises the roughness of the bearing taken along the axis shown in Figure 3.22, before and after operation. The parameters are as follows: Sq - root mean square height; Ssk- Skewness; Sku-Kurtosis, defined in ISO 25178-2:2012. The conclusion to be drawn here is that the surface roughness decreases even if no contact occurs. This is an indicator that the overlay surface is modified by the hydrodynamic pressure, as explained above.

Table 3.14 New and used Bearing surface parameters

Parameter	**Sq [µm]**		**SSk**		**Sku**	
Bearing state	**New**	**Used**	**New**	**Used**	**New**	**Used**
Values	0.505	0.259	-0.0667	1.65	5.26	21.9

Another surface topology change phenomenon observed during the Kawasaki ZX10 testing is presented in Figure 3.25. The wear marks resemble to a tree branch shape and are located on the lower bearing shell (cap side) at an angle of 100° to 130°. This type of wear has been visually remarked that it grows with the time testing.

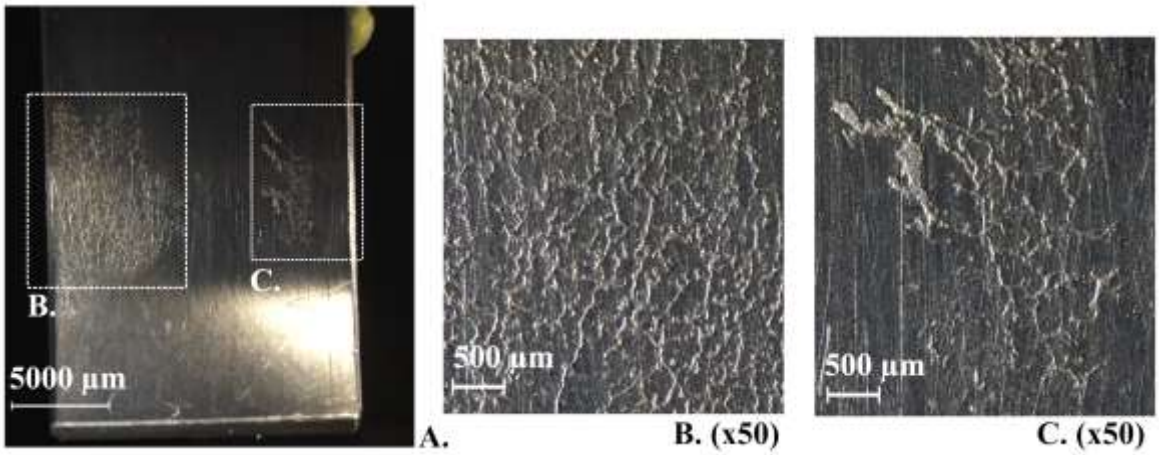

Figure 3.25 Fatigue wear on lower bearing shell. BLUE bearing. Zeiss microscope

For example, the most affected bearing is the BLUE one, which has been in used for the longest time (see Table 3.11). The same type of wear was found in reference [97]. The authors explain that this phenomenon is specific to high-speed engine, where the minimal film thinness may have the same order as the roughness (mixed lubrication regime), therefore direct contact may occur. However, this is not the case here. Yet, as the intensity and the frequency of the contacts is high due to the high speed, the fatigue wear is favourited to appear. Another key factor described by the authors is the stiffness distribution of the bearing housing affects the fatigue resistance.

3.2.3.4 Interpretation and comparison with numerical results for oil supply flow rate

This paragraph will be focused on the comparison between the experimental measurements and the numerical predictions for the Kawasaki connecting rod. The first comparisons concern the supply flow rate.

Because the measured flow rate is the total flow rate of both bearings and the load and clearance spaces are different from left to right connecting rods, it is necessary to numerically predict the oil supply flow rate for left and right connecting rods.

An important parameter in the prediction of the oil supply flow rate is the oil quantity in the vicinity of the bearing. A certain amount of oil can be sucked inside the bearing at its edges due to possible sub-ambient pressure and this is dependent on the amount of oil present at the edges of the bearing. Therefore, in the following analysis two extreme cases are taken in consideration. The first one is when the bearing is fully submerged in oil (f_1 equation (3.4)) and the second is when no oil presence is around the bearing (f_0 in equation (3.4)).

$$\begin{cases} f_1 - bearing\ is\ fully\ submerged\ in\ oil \\ f_0 - no\ presence\ of\ lubricant\ at\ the\ bearing\ edge \end{cases} \tag{3.4}$$

The plots below (see Figure 3.27, Figure 3.29, Figure 3.31, Figure 3.33) represent comparison between the experimental oil supply flow rate (in BLUE) which are surrounded by the ACCEL results for no oil at the bearing edge (F_0 case - in green) and fully submerged (F_1 case - in red). The right hatch represents the right conrod, while the left hatch is the left one (half load). The flow rate values are marked on the bar plots along with the error in percentage between numerical and experimental.

All the calculations are performed at a speed of 11500 rpm. The numerical model is isothermal, the oil temperature input being the measured mean temperature of the bearing. The load is the experimental measured load on MEGAPASCALE for each individual point. The modelling carried out on the two connecting rods considers that the bearing operates without misalignment. This is not true for the left connecting rod, but the misalignment depends on the load applied and can only be predicted correctly by a model that takes into account the operation of both connecting rods in a coupled manner, taking into account the compliance of the journal.

Also, the bearing clearance is assumed to be the same as the measured clearance at ambient temperature and therefore not dependent on the variation of the mean temperature during operation. This assumption is justified by the fact that both connecting rod and journals are made of steel. However, we are not entirely certain that the coefficient of expansion of the two parts is exactly the same.

Another important factor is the clearance. As previously seen, it has been established that the bearing clearance increases after the first cycles due to the overlay crushing. Therefore, calculations are made with clearance values measured before and after each test campaign. From the following plots, it appears that, the comparisons are better if the calculations are carried out with the clearance measured after the tests (Figure 3.29 to Figure 3.33). This suggests that the evolution of the bearing shape appears relatively quickly, during the first few minutes of operation.

Despite all the uncertainties described here, the comparisons show, for several of the cases presented, an experimentally measured flow rate that lies between the two numerically predicted flow rate values. This shows that the numerical model is relevant.

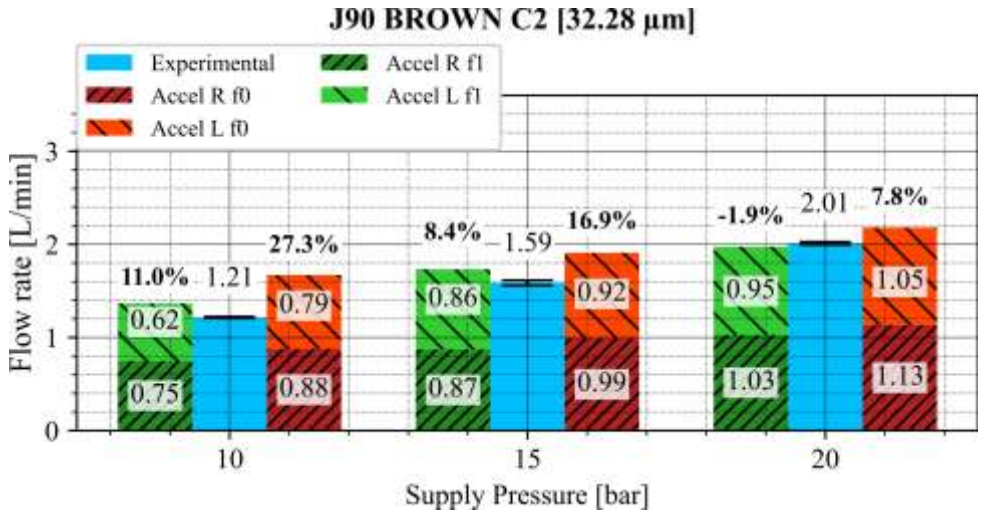

Figure 3.26 Oil supply flow rate vs Pressure supply for initial clearance BROWN-C2 [32.28µm] and J90 Journal

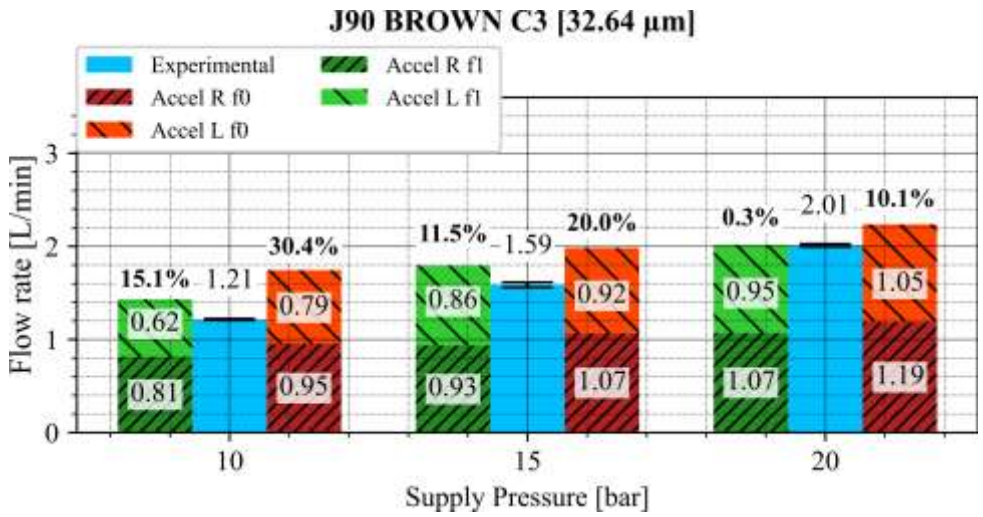

Figure 3.27 Oil supply flow rate vs Pressure supply for final clearance BROWN-C3 [32.64 µm] and J90 Journal

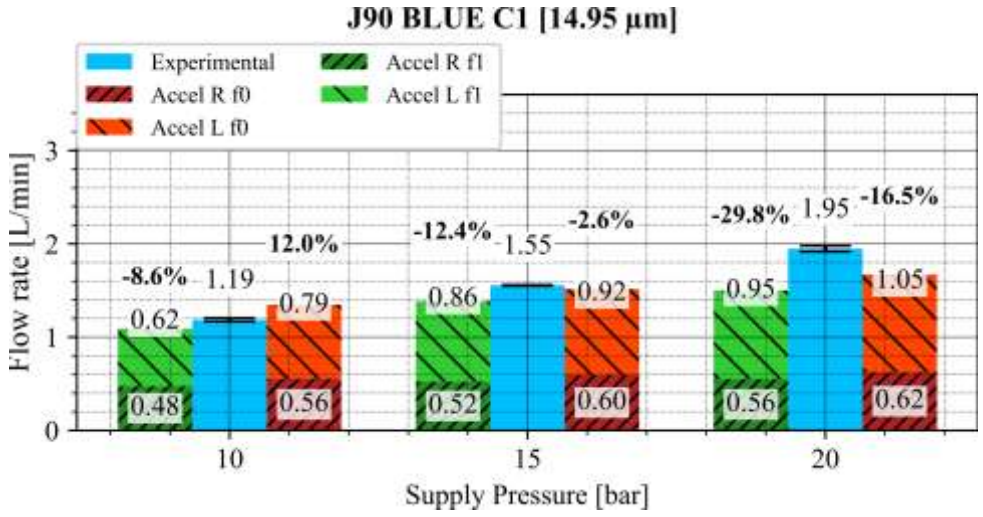

Figure 3.28 Oil supply flow rate vs Pressure supply for initial clearance BLUE-C1 [14.95 µm] and J90 journal

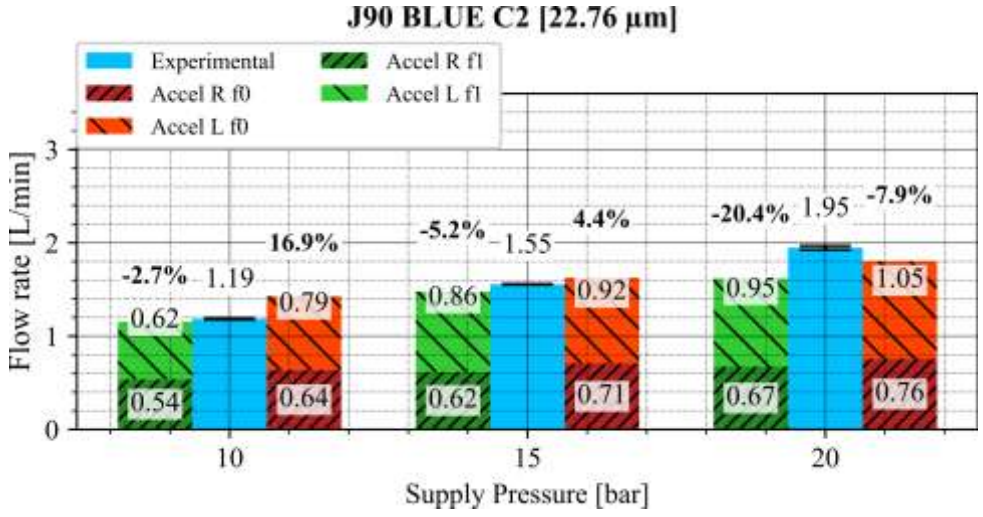

Figure 3.29 Oil flow rate supply vs Pressure supply for final clearance BLUE-C1 [22.76 µm] and J90 journal

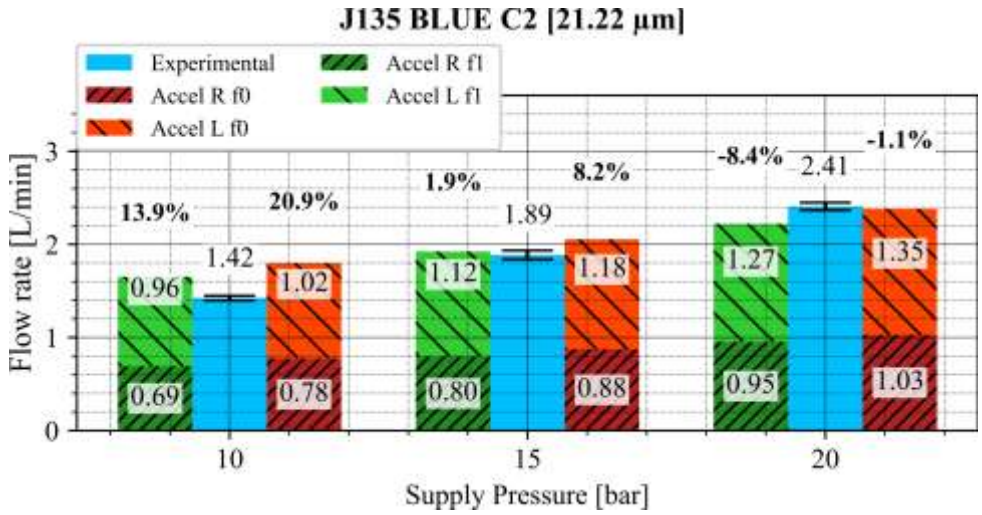

Figure 3.30 Oil flow rate supply vs Pressure supply for initial clearance BLUE-C2 [21.22 µm] and J135 journal

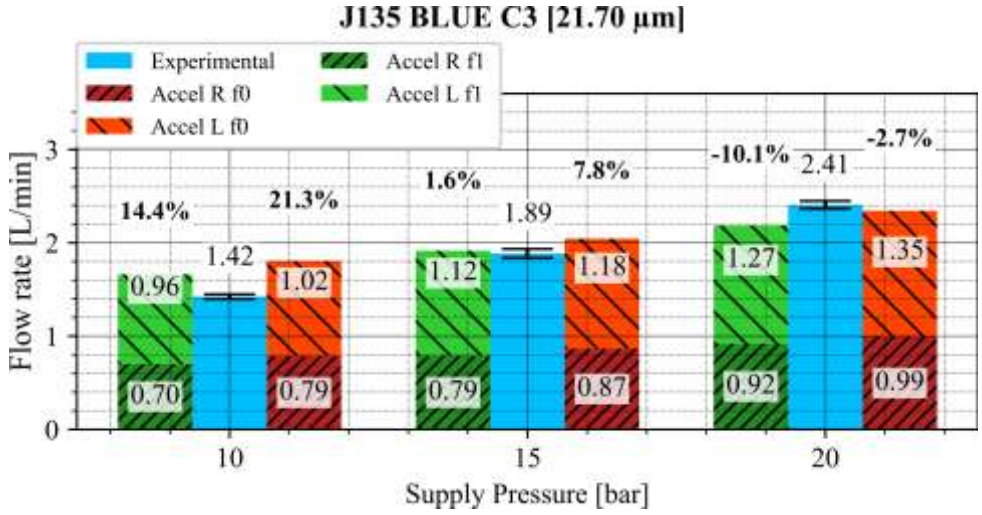

Figure 3.31 Oil flow rate supply vs Pressure supply for final clearance BLUE-C3 [21.70 µm] and J135 journal

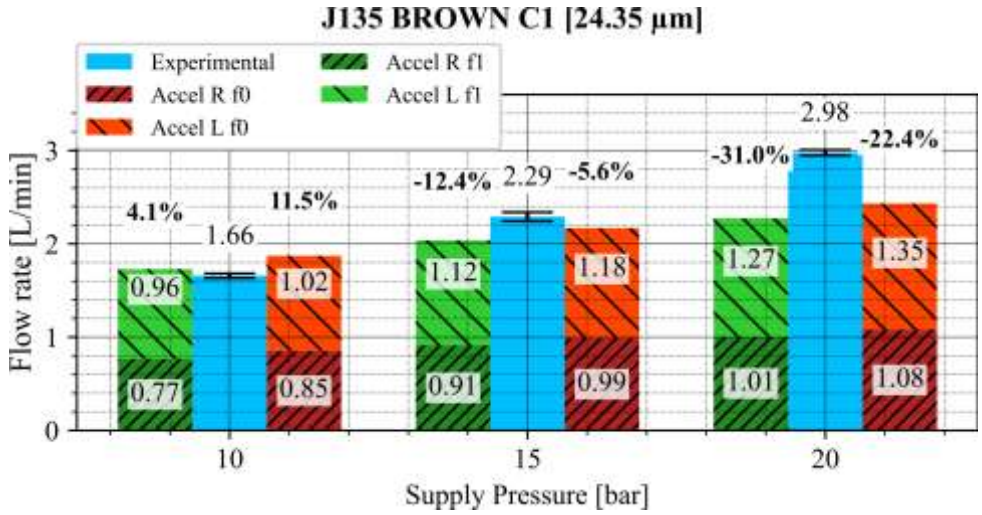

Figure 3.32 Oil flow rate supply vs Pressure supply for initial clearance BROWN-C1 [24.35 µm] and J135 journal

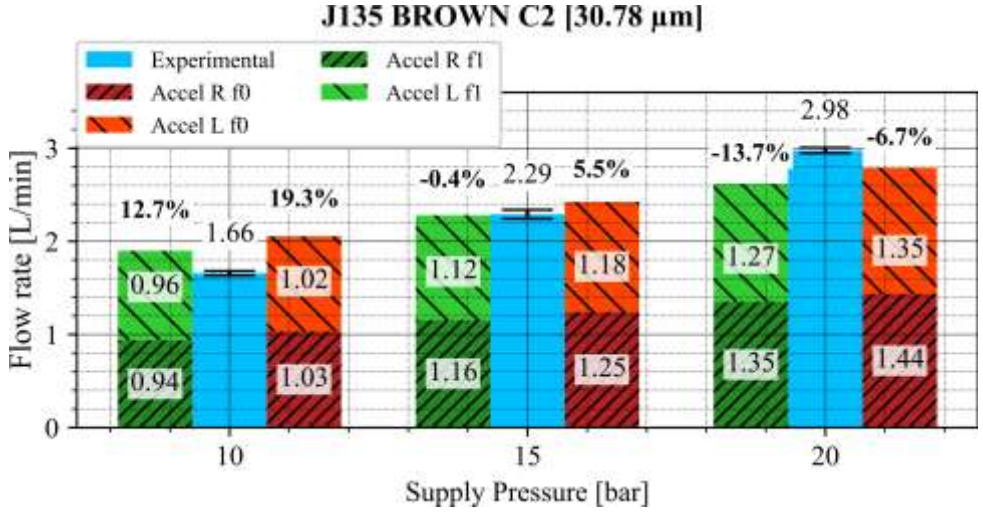

Figure 3.33 Oil flow rate supply vs Pressure supply for final clearance BROWN-C2 [30.78 µm] and J135 journal

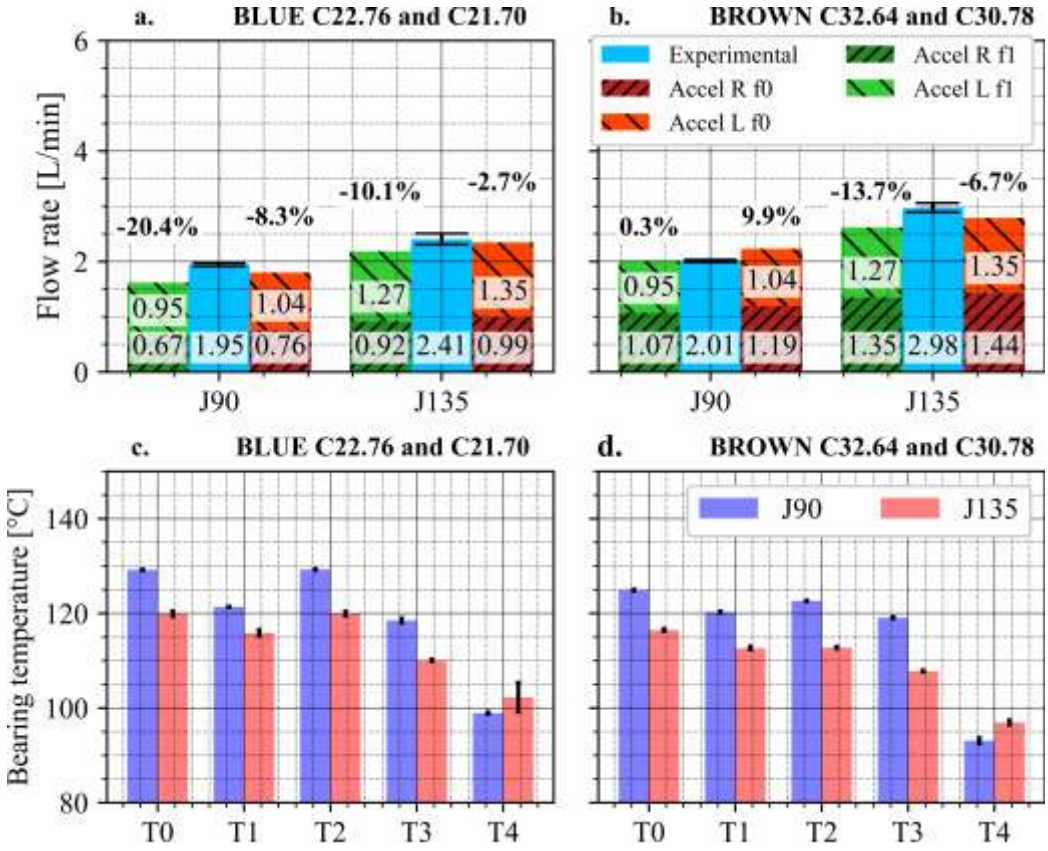

Figure 3.34 Oil supply flow rate and bearing temperature: a. Flow rate BLUE J90 and J135; b. Flow rate BROWN J90 and J135; c. Temperature BLUE J90 and J135; d. Temperature BROWN J90 and J135

It can be seen, from Figure 3.34 a. that, for a given clearance (BLUE C22.77 respectively C21.70) the J90 experimental flow rate is smaller by 23 % and the average temperature higher by 7 % than J135. In this case, the decrease in viscosity generated by a higher operating temperature in the case of J90, is not sufficient to generate a higher flow rate than that of J135.

If the radial clearance is increased by about 10 µm (Figure 3.34 b.), the flow rate increases from BLUE-C21.70 to BROWN-C30.78 by 19 % (from 2.41 l/min to 2.98 l/min). The J90 bearing is 8°C cooler than J135. However, for the case of J90, the flow rate does not change much with the increase of the clearance neither on experiment nor in the calculation results (about 2 %).

Concluding, concerning the flow rate, the majority of the performed simulations predict well the experimental flow rate tendencies. The experimental - numerical differences are considered satisfactory and can be explained by following factors. The numerical modelling is performed by imposing an average temperature of the bearings (average temperature measured experimentally). Moreover, the numerical model considers a pressure imposed at the level of the supply hole and this may be an erroneous boundary condition when the supply hole crosses the pressure field. Moreover, for the left connecting rod, the bearing is not perfectly aligned due to the deformation of the eccentric subjected to different loads (the load applied to the left connecting rod is twice as small as that applied to the right connecting rod). And this is not considered by the model.

3.2.4. Eddy current gap sensors

As presented in the Chapter 2, three eddy current gap sensor are installed around the Kawasaki ZX10 connecting rod big end. This paragraph will present the results obtained with this type of instrumentation. As it will be seen, the values indicated by the three sensors correspond to the displacement between each sensor and the journal. And this can also be predicted by numerical simulation, which will provide an indirect measure of the film thickness in the bearing.

3.2.4.1 Experimental results

The analysis begins by studying the influence of the oil hole angle on the measurements. Two journals with an oil hole angle at 90° and 135°, with the same bearing clearance (BROWN- C32.64 respectively BROWN-C30.78), at the same supply pressure (10 bars) and at the same supply temperature (80°C) are examined.

The second analysis is performed on the influence of clearance. Two bearings with different clearances (BROWN-C32.64 and BLUE-C22.76) are tested with the J90 journal at the same supply temperature of 80°C and at the same oil supply pressure of 10 bar.

The third analysis is performed on the influence of oil supply pressure on the measurements. Three oil supply pressures: 10, 15 and 20 bar are analysed at constant 80°C oil supply temperature for J90 journal, BROWN bearing.

The last analysis investigates the oil supply temperature influence. Two supply temperature of 80°C and 100°C are investigated, for a constant oil supply pressure of 10 bar and for the J90 BROWN bearing.

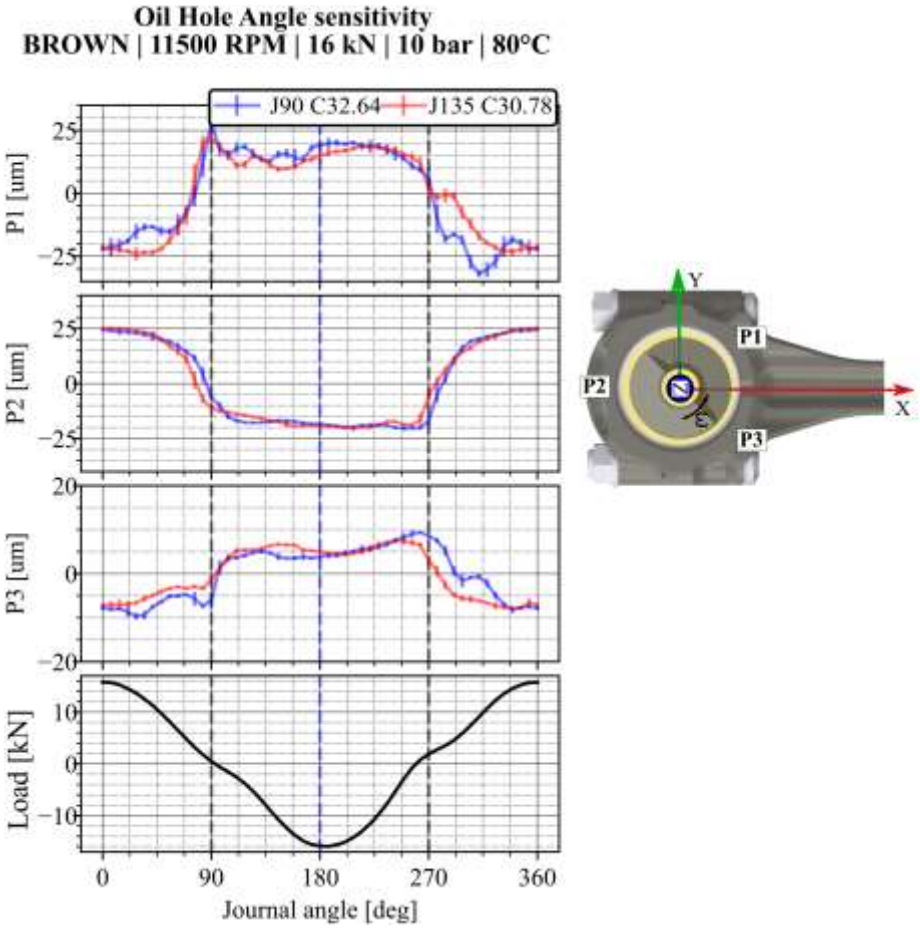

Figure 3.35 Eddy Current Gap Sensors Measurements: Oil hole angle influence

Figure 3.35 depicts oil hole angle influence on eddy current gap sensors measurements. The two different oil hole angles are represented by the J90 journal in blue colour line and J135 journal in red colour line. The tests are performed with the BROWN bearings shells having an initial average radial clearance of 25.8 µm and 24.3 µm and a final average clearance of

32.64 µm and 30.78 µm (even if the connecting rods are identical, differences in clearance appear because of the manufacturing tolerances of the eccentrics).

It is evident that both journals oscillate around zero due to the dynamic load at a frequency equal to the rotating speed. Each journal subjects the conrod to compression from 0º to 90º and 270º to 360º and traction from 90º to 270º.

The entire cycle can be brake in 4 stages: **stage I:** 0º to 90º compression unload, **stage II:** 90º to 180º traction load, **stage III:** 180º to 270º traction unload and **stage IV:** 270º to 360º compression load.

Stage I (compression unload): Eccentricity approaches zero (bearing centre), because compression force decreases and speed remains constant.

Stage II (traction load): This stage starts with a sudden equilibrium change. The journal is quickly pushed towards the bearing due to the load changing direction.

Following the evolution of P2, J90 linearly decreases directly down to the minimal position, while J135 enhances a saddle point around 95º and then, slowly decreases down to the minimum corresponding to the maximum load. This different behaviour is mainly due to the oil hole position that, in the case of J90, disturbs the hydrodynamic pressure field. Therefore, the bearing load capacity is reduced and the journal is pushed faster towards the bearing.

Following the evolution of P1, a dampened oscillation can be observed for both journals, but again, J90 enhancing bigger amplitudes. Basically, the fluid film is "regenerating" step by step being able to support the load as the oil hole turns away the hydrodynamic pressure field.

Stage III (traction unload): At this stage both journals encounter the same trajectory. The oil hole is far from the pressure field and therefore the load can be supported.

Stage IV (compression load): This stage is similar with the stage II. Again, the journal J90 is faster pushed towards the bearing by the applied load. This is explained by the fact that the oil hole is in the middle of the hydrodynamic field and this reduces the bearing load capacity.

Figure 3.36 depicts the clearance influence on the eddy current gap sensors measurements. Two different clearances are analysed: BLUE-C22.76 in BLUE line respectively BROWN-C32.64 in BROWN line. The tests are performed with the J90 journal at an oil supply pressure and temperature of 10 bars and 80°C, respectively. It can be noticed that the BROWN-C32.64 has a greater amplitude. This is due to a larger clearance space for the journal to move in the bearing.

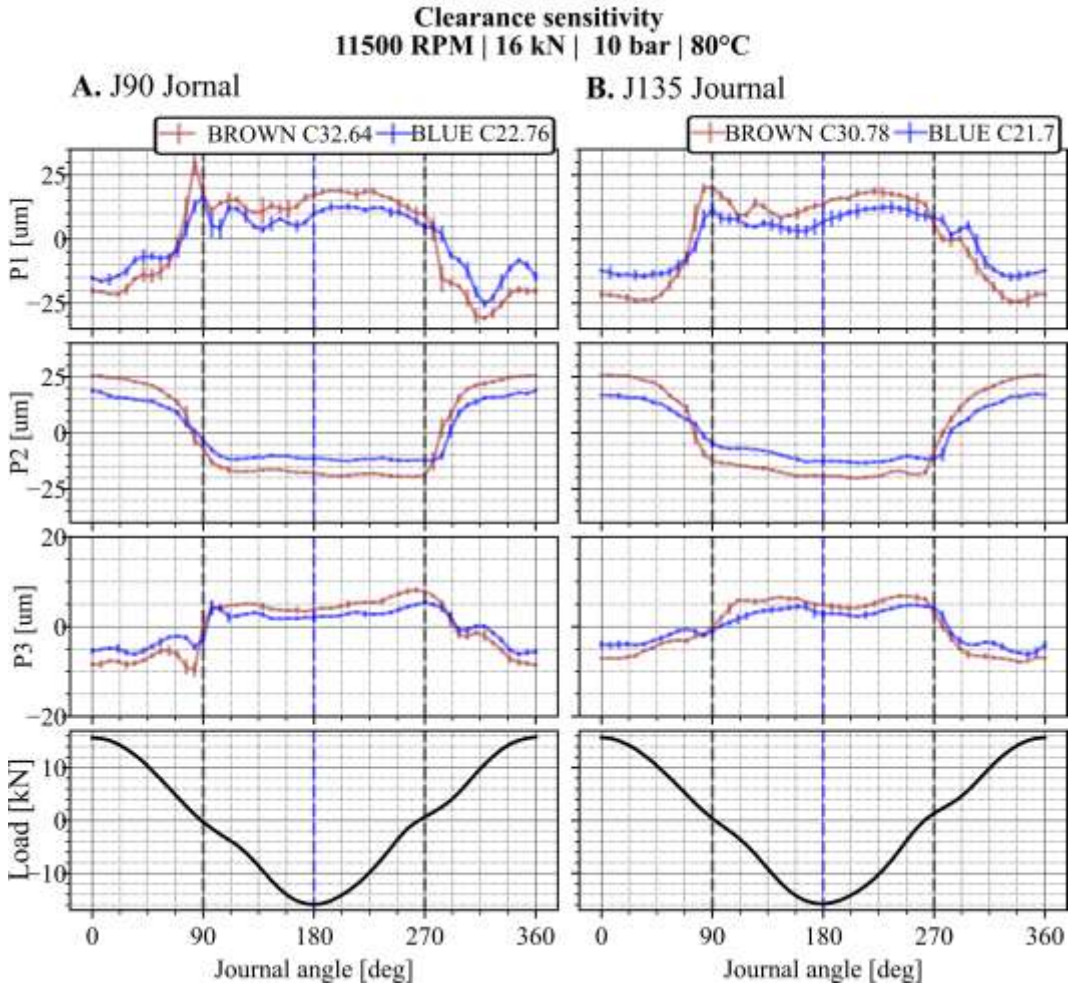

Figure 3.36 Eddy Current Gap Sensors Measurements: Clearance influence. a. J90 Journal; b. J135 journal

Figure 3.37 a. represents the oil supply temperature influence on eddy current gap sensors measurements, while Figure 3.37 b. represents the oil supply pressure influence on eddy current gap sensors measurements. As it can be seen from these figures, the pressure and temperature have little influence on the measured displacement of the shaft inside the bearing (small enough to be considered within the accuracy range of the sensors). This conclusion will be further confirmed by the voltage drop measurement, which is a second method to investigate the fluid film thickness evolution and also by the ACCEL calculations.

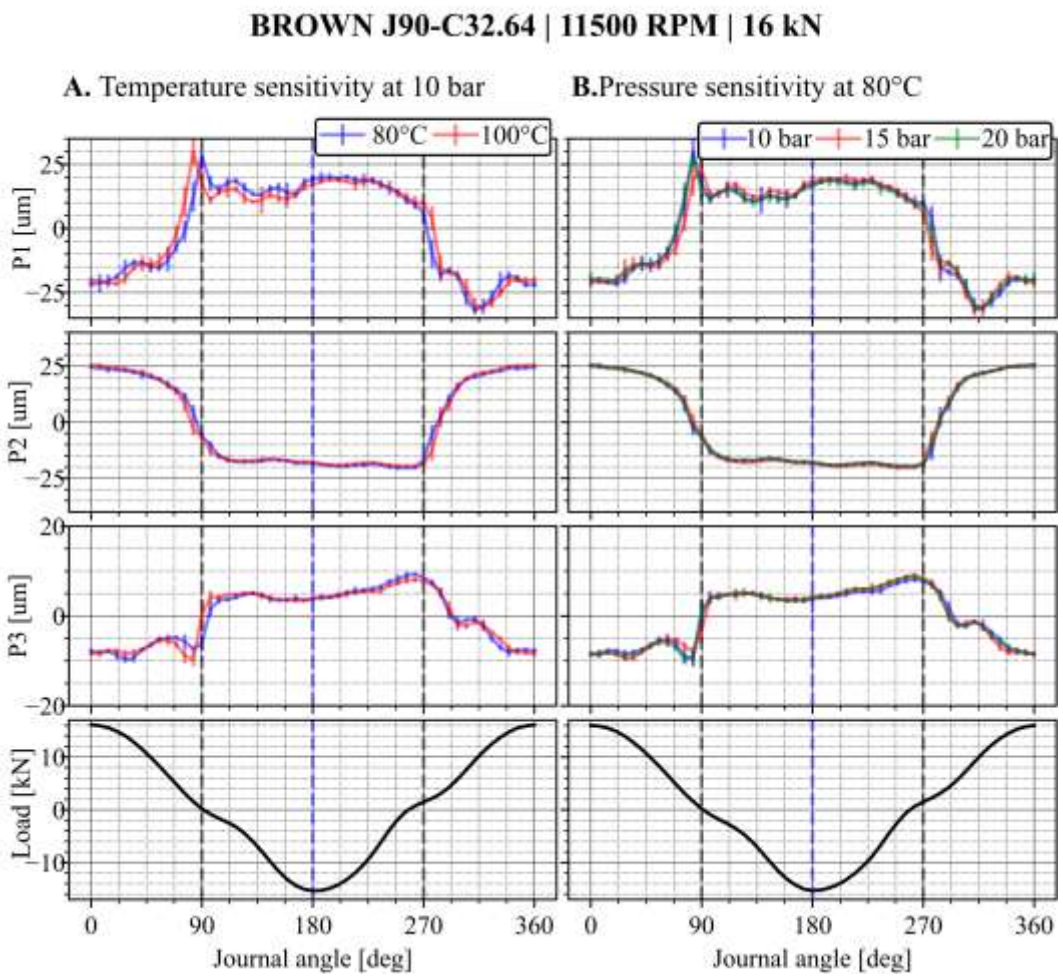

Figure 3.37 Eddy Current Gap Sensors Measurements for BROWN-C32.64 bearing and J90 journal: a. Oil Supply Pressure influence; b. Oil Supply Temperature influence

3.2.4.2 Interpretation and comparison with numerical results for eddy current gap sensors

This subsection treats the comparison between the eddy current gap sensors measurement and ACCEL computations.

The experiment and the simulation were both performed at the same conditions: 11500 rpm speed, 80ºC oil supply temperature, 20 bar oil supply pressure and 16 kN pick amplitude dynamic load (traction and compression). The oil hole position was the only variable and changed from 90° to 135 ° before the maximum load.

Figure 3.38 and Figure 3.39 depicts the comparison between the eddy current gap sensor measurements and ACCEL calculation for the BLUE, respectively BROWN bearings, each of

them tested with J90 and J135 journals. In Black line is represented the experimental data, while in red line is the ACCEL computation. The simulation results are the predicted displacements in the radial direction in front of each sensor.

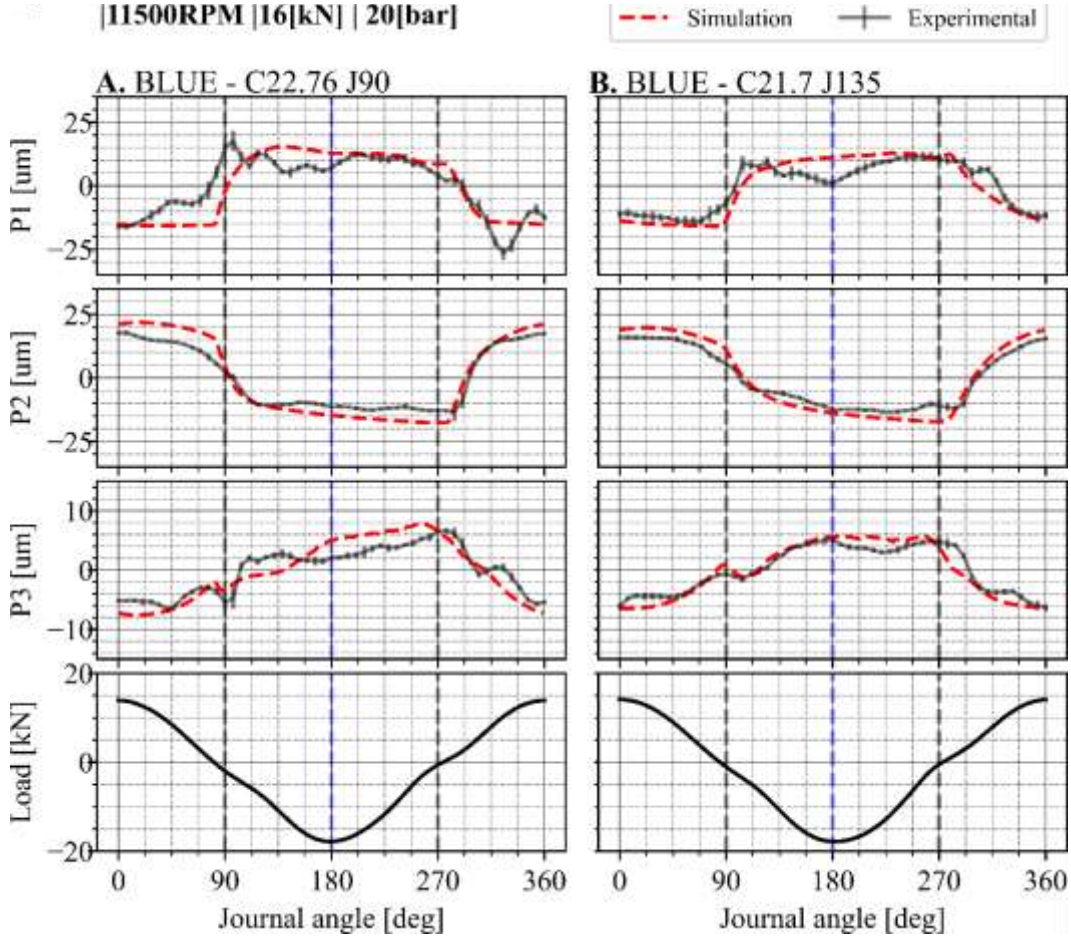

Figure 3.38 Comparison between experimental and simulation of bearing - journal gap for BLUE bearing: a. J90 journal; b. J135 Journal

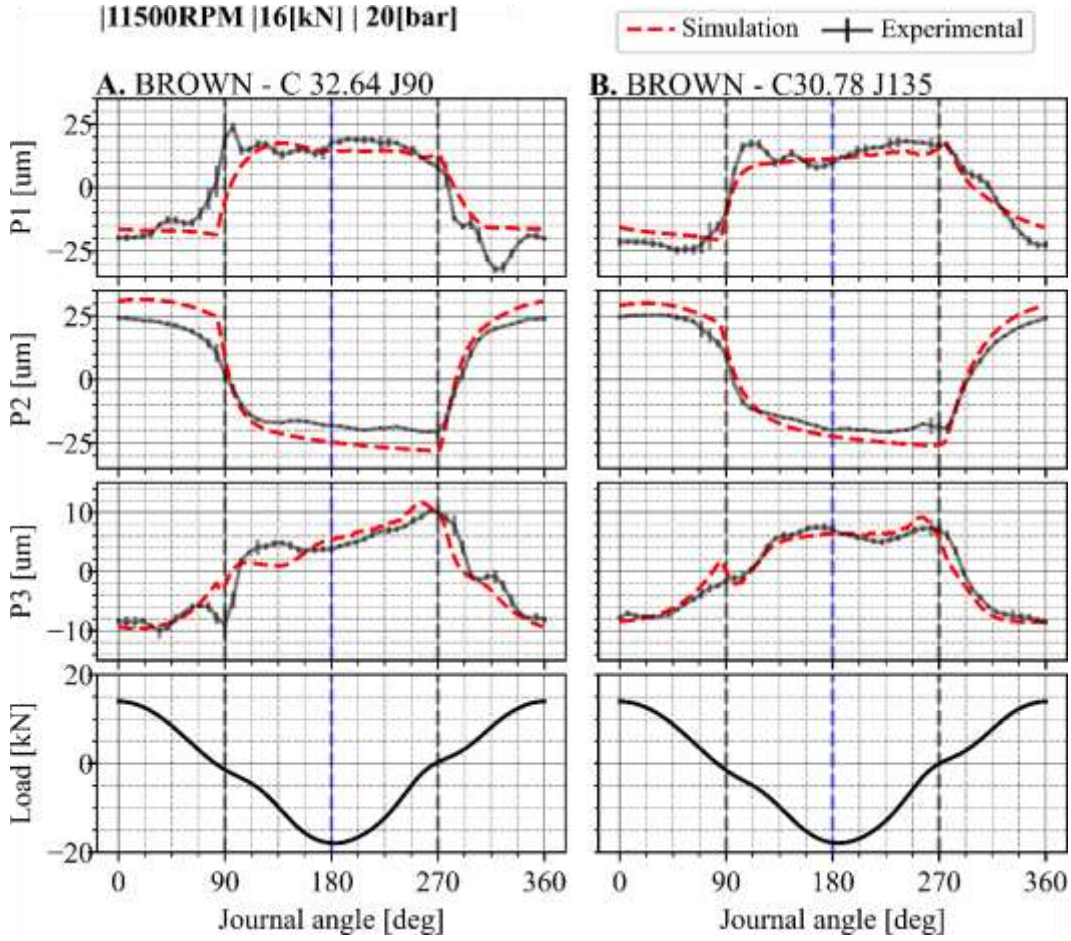

Figure 3.39 Comparison between experimental and simulation of bearing - journal gap for BROWN bearings: a. J90 journal; b. J135 Journal

Both data are represented in relative system. In order to compare the results, the mean value of the data has been removed from both numerical and experimental variations. This process is needed due to the uncertainty of the reference point in the experimental measurements. As a result, the data oscillates around zero, having both negative and positive values.

The conclusion to be withdrawn is that the simulation results follow very well the experimental signals. Not only the calculated trend of displacements in front of each sensor matches the experimental one, but also the relative amplitudes also match each other. Other results, leading to the same conclusions but obtained for lower rotation speeds, are presented in Appendix B.

As the comparisons presented above prove, the numerical predictions are in good agreement with the experimental measurements. Therefore, the numerical analysis will allow a better understanding of the bearing behaviour. To explain the influence of the circumferential position of the supply hole in relation to the loading magnitude, the orbit of the shaft will be represented in the reference frame of the bearing.

Figure 3.40 shows a schematic representation for five representative angles of the four stages described in the previous paragraph (3.2.4.1). The represented case is the (25µm radial clearance) BLUE bearing with J135 and J90 journals. The negative side of *x* axis points the conrod cap while on the positive side points the conrod shank. The journal is represented by a circle (dashed line J90, while the continuous line is J135), while the oil supply hole is represented by a line starting from the centre of the journal. The load amplitude and direction are represented by the black arrow. The yellow arrow represents the rotation direction of the journal.

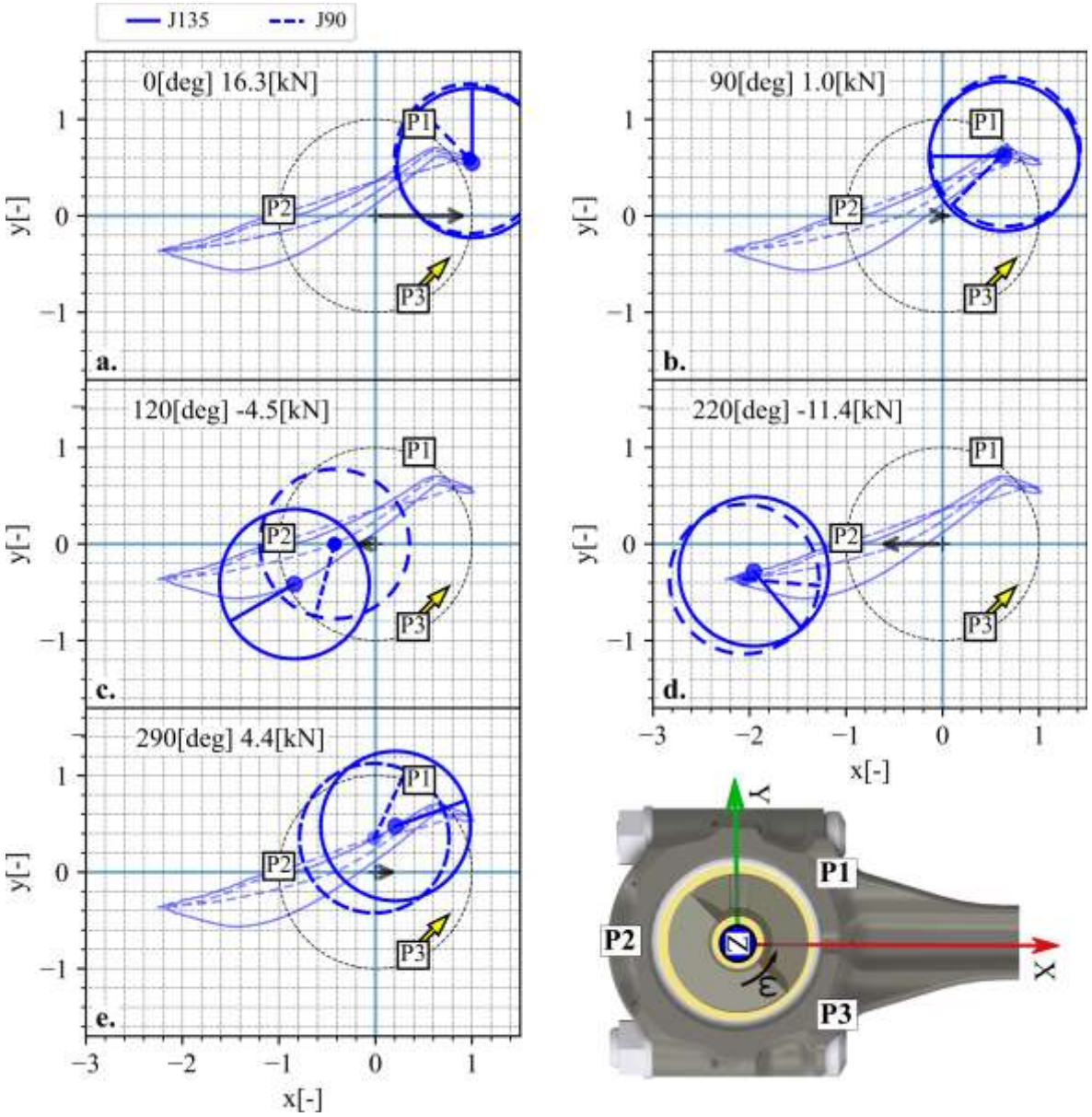

Figure 3.40 Snapshots of computed journals orbits for BLUE bearing J90 and J135 a. start stage I; b. end stage I; c. intermediate stage II, d. intermediate stage III, e. intermediate stage IV

It can clearly be seen form the Figure 3.40 b. c. and e. that in the case of J90 journal, oil supply hole points towards the region where the pressure field should be established. Therefore, the occurrence of pressure field penetration is explained.

Analogously to the orbit resulted from the experimental measurements, the hydrodynamic pressure and fluid film thickness fields are plotted in Figure 3.41. Both, J135 and J90 fields are represented at 120° crank angle. The fact that J90 is more prone to pressure field penetration confirms the orbit plots. Looking at the fields, it can be clearly seen that the oil hole supply enters in the pressure field. Complementary, the fluid film thickness fields show that, in the case of J90, at cycle angle 120°, the minimal fluid film thickness is 50% lower than J135 (10 µm respectively 20 µm). The same phenomenon happens during the stage IV (compression load).

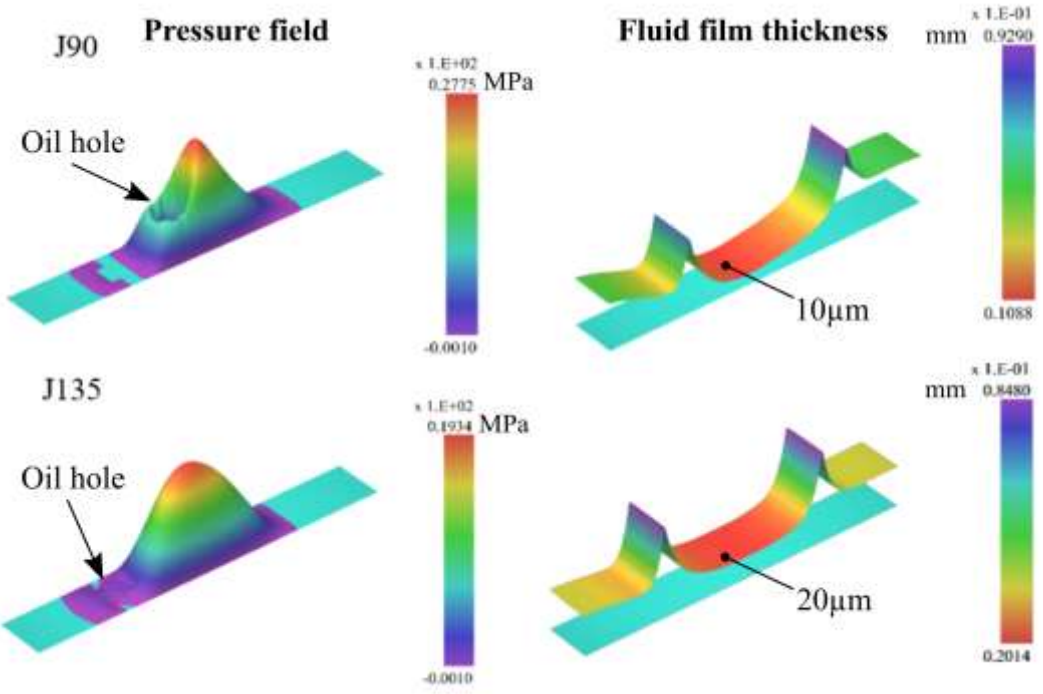

Figure 3.41 ACCEL pressure and film thickness fields for 120° crank angle for BLUE Bearing

To sum up, this subchapter focused on the eddy current gap sensor measurements and its correlation to simulation results provided through ACCEL computation. The simulation results are the predicted average displacements in the radial direction in front of each sensor. Four analyses are performed: oil hole angle, clearance, oil supply pressure and temperature.

Firstly, it is evident that both journal eccentricities oscillate around zero due to the dynamic load at a frequency equal to the rotating speed. Furthermore, four stages have been pointed out over the cycle which corresponds to the loading and unloading of the bearing. From all of those

the most important captured behaviour is the difference in trajectory between J90 and J135, which shows the impact of the oil hole hydrodynamic field penetration. Finally, it has been concluded that the eddy current gap sensor signal increases with the increase of clearance. No important sensitivity has been noticed in case of the temperature and pressure supply variation. Lastly, the comparison between experimental and simulation gave very good results.

3.2.5. Voltage drop measurement

This measurement is meant to express a qualitative interpretation and not a quantitative over the bearing-journal contact. A detailed description of the method has been developed in Chapter 2, section 2.6. As well-known from the literature (Suzuki [14], Dyson [92], Cameron [91]) the voltage drops over a fluid film remains proportional to the thickness of the film under certain conditions.

3.2.5.1 Experimental results

In this study we will use the voltage decent ratio method, used by Suzuki [14] in the case of a dynamically loaded bearing to interpret the voltage drop signal. The voltage decent ratio (RC) expressed in the equation (3.5) represents the cycle averaged voltage descend to perfect insulation. Where, V_0 is the voltage under insulation – which can be seen as the maximum voltage over the film thickness, and V_t is the measured voltage between the journal and bearing.

The result of this formula can take values inside the interval [0, 1] where 0 represents no contact, while 1 represents direct contact.

$$RC = \frac{\int_0^{360} (V_0 - V_t)\, d\theta_{cyc}}{360 V_0} \tag{3.5}$$

Figure 3.42 shows the raw contact measurement [CNT] for the two journals (J90 and J135), each of them tested with two different bearing clearances (BLUE and BOWN) at 80 ºC oil supply temperature and 10 bar oil supply pressure.

For each test, the measurement is plotted in black line, while the normalized histogram is plotted near. This histogram displays the frequency of the contact voltage drop over 0.1 s (19 cycles). 10 V is the voltage drop value, where the current supply saturates, since the film thickness is large enough to open the electrical circuit. Therefore, it is considered that the bearing is, at this point, in hydrodynamic regime. 0 V is the voltage drop value, when the journal is in direct contact with the bearing. Comparing J90 and J135 for the same clearance, it can clearly be seen that in the case of J135 bearing, about 80 % of the distribution represents the 10 V. In the case of J90 bearing, the distribution shifts towards 50 %.

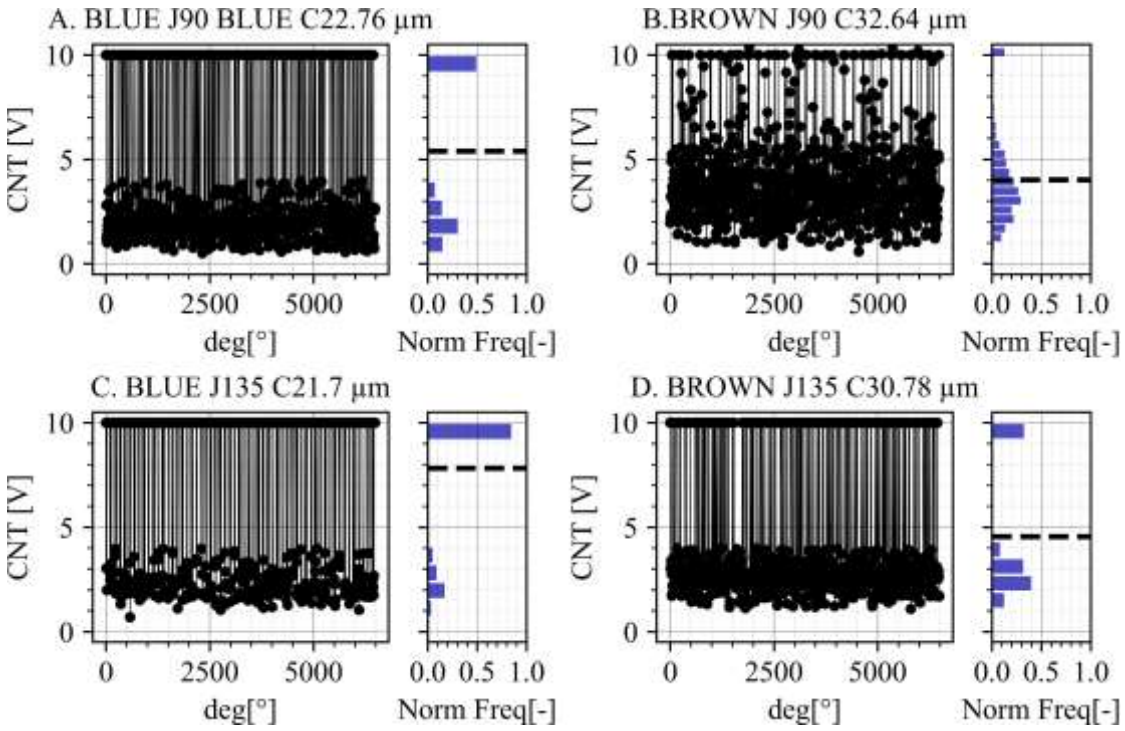

Figure 3.42 Voltage drop measurement

Figure 3.43 represents the sensitivity analysis of the RC in function of: oil supply pressure, oil supply temperature, oil hole angle and clearance. For a better visibility the *y* axis is limited to a maximum value of 0.45.

It can be seen that the RC is always lower for the J135 bearing which indicates a higher film thickness. This is consistent with the flow rate measurements (see Figure 3.16) which show a higher flow rate for J135 bearings. It is also interesting to note that increasing the oil supply pressure leads to a slight decrease in RC which, again, can be translated into an increase in film thickness. This is also consistent with the flow rate measurement which increases with increasing feed pressure. Analysing the results from the oil supply temperature point of view, no clear-cut conclusion can be withdrawn. Analysing the results from the clearance point of

view, it can be seen that the decrease in clearance leads to a decrease in RC, which can be interpreted as an increase in thickness and therefore an increase in supply rate.

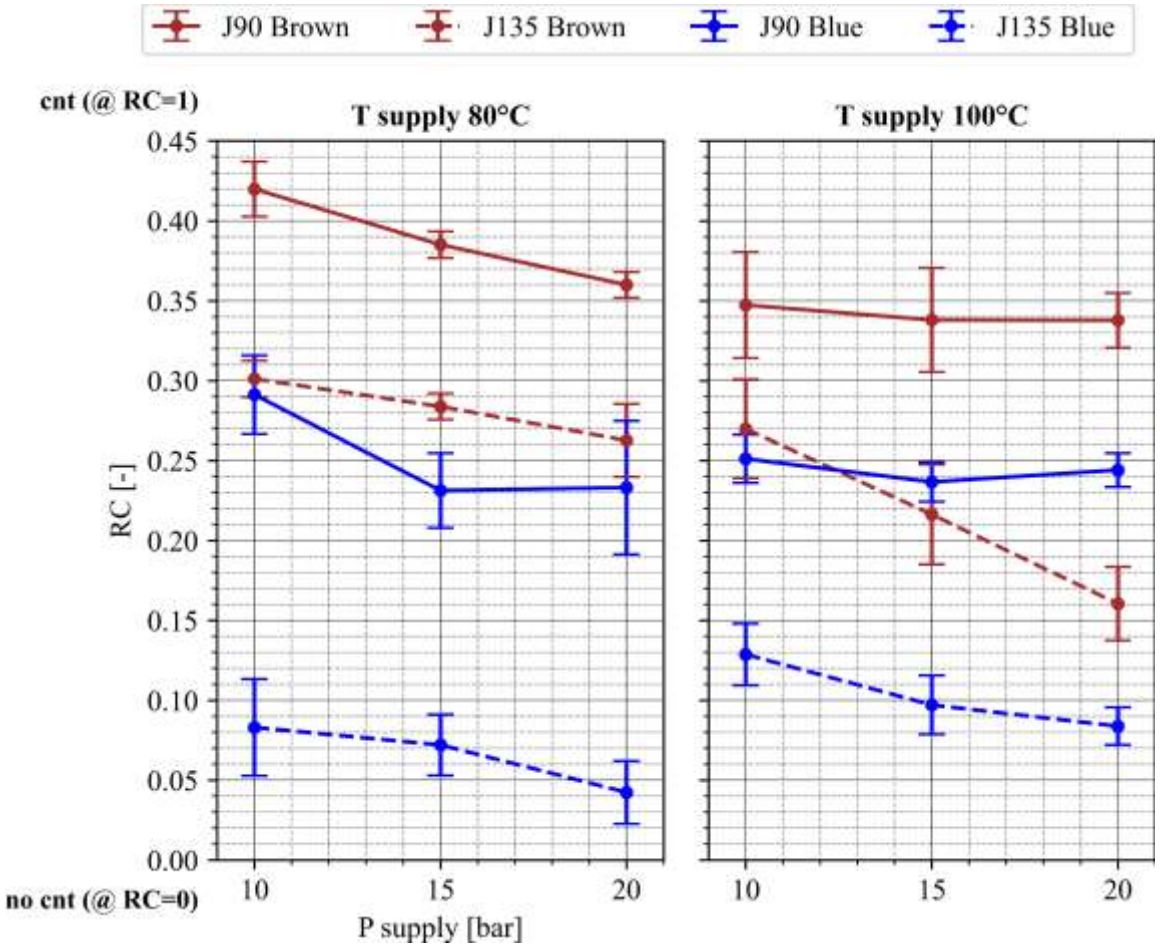

Figure 3.43 Voltage drop decent ratio variation for different supply pressures, temperatures and positions

Overall, the results presented here are fully consistent with the flow rate measurements as well as with the eddy current gap sensor measurements and their interpretation through numerical simulations. The link between flow rate, film thickness and RC measurements is, for example, reinforced by the Figure 3.44 depicting numerical predictions of the variation in minimum film thickness over a cycle obtained for the 25µm clearance bearing tested with J90 and J135 journals: for J90 journal, a lower film thickness is predicted which leads to a larger RC signal and a lower supply rate compared to J135 journal.

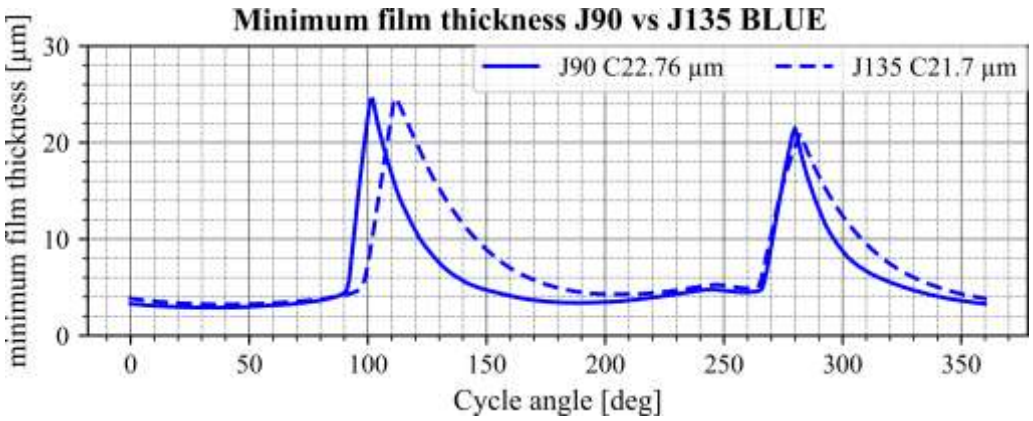

Figure 3.44 Minimum film thickness history. Comparison between J90 C22.76 µm and J135 C21.7 µm for BLUE bearing at 10 bar oil supply pressure, 80°C oil supply temperature

Further investigations were carried out by keeping the load constant (±16kN traction - compression) and decreasing the speed down to 5000 rpm. The used bearings are the BLUE ones, while the journal is the J90. Figure 3.45 depicts the voltage drop decent ratio (RC) variation with the speed. It can clearly be seen that the voltage drop ratio decreases with the speed which suggest the increase in film thickness. This is confirmed numerically by Figure 3.46 which shows the variation of the minimum film thickness with speed.

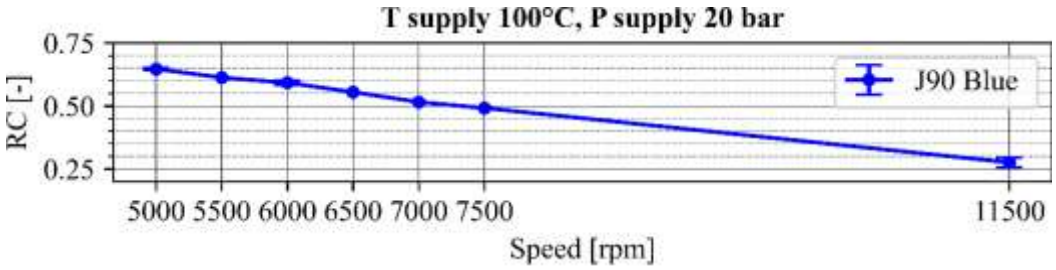

Figure 3.45 RC variation with speed: experimental results

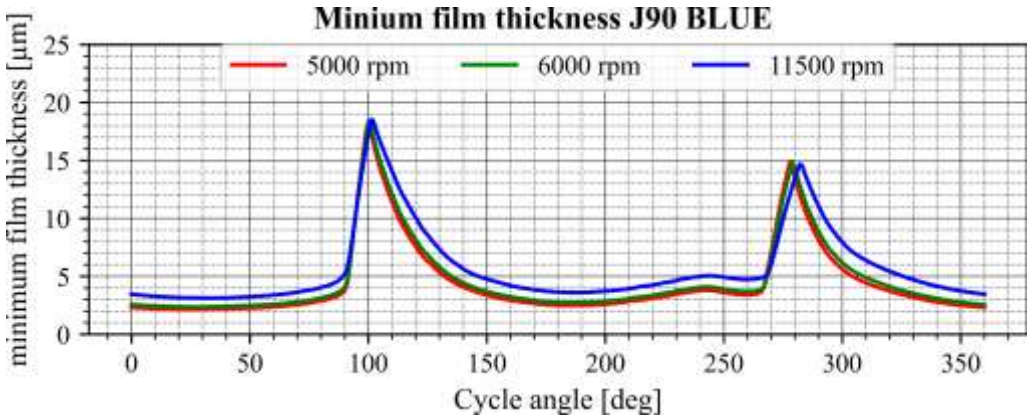

Figure 3.46 Minimum film thickness variation with cycle angle for different speeds: numerical predictions

The purpose of this measurements was to investigate through another experimental technique (different from the eddy current gap sensors) the state of the bearing. The main conclusion, in agreement with other users of this method (Suzuki [14], Dyson [92], Cameron [91]) is that the voltage drop measurement is a variable signal and not a binary one. It can be used to qualitatively compare the severity of the operating conditions. Further experimental investigations, accompanied by numerical simulations, may even lead to quantitative information (e.g. order of magnitude of the film thickness). However, this would require further experiments to determine the resistivity of the oil as a function of bearing clearance, speed, inactive zones in the gap, etc.

3.2.6. Conclusions on Kawasaki ZX10 testing campaign

This testing campaign, carried out in the second part of the thesis makes it possible to continue the studies begun with the Renault RS connecting rod. The availability of different bearing shell thicknesses allowed us to perform a clearance study. Similar to the the Renault connecting rods testing campaign, two different oil hole angles have been machined. One which corresponds to the real Kawasaki ZX10 crankshaft and another one which is better positioned in respect to the maximum load. Even more, for this testing campaign two additional measurements techniques were introduced. The first one was the eddy current gap sensors, which gave information about the position of the journal relative to the bearing shell. Those measurements showed a good agreement with the numerical predictions. The second technique was the voltage drop measurement which provided qualitative information on the operation of the bearing, consistent with that obtained by the other experimental techniques.

3.3. Conclusions

This chapter summarises the test campaigns carried out on two different connecting rods: the Renault RS connecting rod, operating at speeds up to 4000 rpm and the Kawasaki connecting rod, operating at speeds up to 11500 rpm. Numerical simulations allowed us, on the one hand, to validate the existing models (but also to identify weak points) and, on the other hand, to better understand some of the experimental measurements. Some measurement techniques (eddy current gap sensors and voltage drop measurements) previously used for investigations

of statically loaded bearings have been successfully implemented and used for highly compliant dynamically loaded bearings.

The most important results include the following:

- highlighting, both experimentally and numerically, the importance of the circumferential position of the feed hole on the flow rate as well as of the minimum film thickness;

- the rapid and significant evolution of the clearance of a connecting rod bearing, generated by a plastic flow rate of the anti-wear layer deposited on the bearing shells. This is, to our knowledge, a result that has not been reported before in the literature. In order to achieve this, it was necessary to develop a methodology for measuring bearing clearances with a very high degree of accuracy;

- the use of eddy current gap sensors to obtain information on film thickness in the context of highly compliant bearings subjected to dynamic loading. This technique has been previously widely used to characterise rigid bearings but very rarely for bearings whose elastic deformations exceed the initial clearance;

- proof of concept for the use of electrical measurements to obtain qualitative information on the degree of operating reliability of a bearing subjected to dynamic loading.

Overall, the objective of testing the ability of the ACCEL software to predict the characteristics of connecting rod bearings for a wide range of operating conditions has been achieved. Difficulties were noted in correctly predicting feed rates for cases where the feed hole passes through areas of thin film thickness: this is a point to be improved. However, comparisons with other measured parameters are in good agreement, which shows that ACCEL can successfully predict the important parameters of a connecting rod bearing.

(this page intentionally left blank)

CONCLUSIONS and PERSPECTIVES

This thesis is originated from the necessity of validating the ACCEL software. A software which predicts the tribological behaviour of a dynamically loaded bearing. The validation process has been achieved by comparing numerical results with experimental data obtained from a special test bench called MEGAPASCALE. The work took place between researchers at the Institut Pprime located in Angouleme, France and AKIRA, a French company which is in charge of race engine preparation for Kawasaki. Two different connecting rods have been tested. The first one being a Renault RS, operating at speeds up to 4000 rpm and the second one was a Kawasaki ZX10 connecting rod, operating at speeds up to 11500 rpm.

For the case or Renault RS connecting rod, the traction - compression load was fixed at 10 kN respectively 20 kN and a transversal charge of 2.8 kN pick to pick was also applied. Three different journals having different oil supply holes configurations were studied. The pressure supply was set at 20, 25 and 30 bar for a 70°C oil supply temperature, while the speed was varied from 2000 to 4000 rpm. The bearing was equipped with thermocouples which measured the temperature of the back of the bearing shell as well as the temperature of the axial oil bulk flow leaving the bearing. The supply oil flow rate was monitored as well.

The sensitivity analysis of the supply flow rate with the pressure supply showed a clear increase for the case of the journal with a feed hole circumferential position angle of 160° before the maximum load and 3 mm diameter (RS_J160_3). On the other hand, for the other two journals having an oil hole position angle of 60° (RS_J60_3, RS_J60_4), the variation of the oil flow rate with the pressure is negligible. The increase of speed leads to an increase of oil flow rate supply for the 160° oil hole angle, but no real influence is observed for a circumferential position at 60°. The comparison between the journals with the same supply angle position (60°) and with different diameters showed that, for the tested configuration, the oil flow rate slightly increases with the increase in diameter. The average bearing temperature analysis showed that the angular position of the supply hole has a more significant influence on the operating temperature than its diameter.

The comparison with the numerical simulations showed an acceptable agreement with the experimental data for the oil supply flow rate at a supply angle position of 160°. On the other hand, at a supply angle position of 60°, the simulation precision decreased significantly. This

is due to the oil hole penetrating the pressure field. This particular situation is not well modelled by the numerical model which imposes a constant supply pressure.

The second connecting rod tested is the KAWASAKI Z10, connected rod provided by AKIRA. For this testing campaign, new sensors and clearance measure techniques were employed. The testing speed was set at 11500 rpm and the load at 16kN, equal in traction and compression. The pressure supply was set at 10, 15 and 20 bars, while the supply temperature was kept constant at 80°C, respectively 100°C. Two different bearing clearances were tested, as well as two journals with a 135° respectively 90° oil hole angles positions and a 5mm hole diameter. Three eddy current gap sensors were installed on the outer edge of the connecting rod to dynamically measure the journal position in the bearing. The voltage drop technique was also used to monitor the bearing. Three thermocouples monitored the temperature of the back of the bearing shell.

An original calibration method for the eddy current gap sensors was performed. By this mean, the Talyrond RMM machine has been used to check the distance between the sensor and calibration target. A second original aspect is the concentric lobe calibration target, which increased the calibration precision. A third original approach, is the temperature calibration of the sensors. For this method, a stepper motor has been employed to rotate the target in an electric oven and for temperatures ranging from 50 to 110 °C. In such manner, the robustness of the measurements has been ensured.

In terms of clearance measurement, a special holding device based on Maxwell kinematics couplings was designed and built. Therefore, the precision of the measurements and the angular positioning of the connecting rod on the Talyrond turning table increased.

This methodology allowing a very high degree of metrological accuracy made it possible to measure a rapid and significant evolution of the clearance of a connecting rod bearing generated by a creep of the anti-wear layer. To our knowledge, this result, has not been previously reported in the literature.

Moreover, the use of eddy current gap sensors brought information about the oil film thickness for highly compliant bearings subjected to dynamically loading. This technique has been widely used for rigid bearings characterisation, but rarely for bearings where the elastic deformation exceeds the initial clearance. The eddy current gap sensor results showed a good agreement with the numerical predictions.

The experimental results of the voltage drop were analysed through a voltage decent ratio (RC). Overall, the RC results are fully consistent with the flow rate measurements as well as with the eddy current gap sensor measurements and their interpretation through numerical simulations.

Regarding the numerical calculations, it should be noted that the oil flow rate prediction is highly dependent on the clearance. Therefore, in addition to other work on MEGAPASCALE testing and ACCEL calculation, this thesis established a more precise clearance measurement. It has been proved that for oil holes which do not cross the pressure field, the oil flow rate prediction agrees with the experimental measurements. On the other hand, for oil holes which crosses the pressure field, the simulation precision decreases. The numerical model considers a pressure imposed at the level of the supply hole and this may be an erroneous boundary condition when the supply hole passes through the pressure field. Therefore, a new method for predicting the oil flow rate should be developed in order to better predictions in these situations.

During the thesis a telemetry system has been developed. The design process and the first test of the system has been presented in the Appendix A. The test confirmed the proof of concept of the telemetry system from an electronical point of view. Temperature signals have been sent during 10 minutes of testing. In order to improve the lifetime of the telemetry system and allow measurements for much longer periods of time, another attachment system is proposed: Either a metal cage, either gluing the module on the connecting rod only with Araldite® 2014-2 and not warping the board in Kapton scotch.

(this page intentionally left blank)

REFERENCES

[1] K. Holmberg, P. Andersson, and A. Erdemir, 'Global energy consumption due to friction in passenger cars', *Tribology International*, vol. 47, pp. 221–234, Mar. 2012

[2] B. J. Hamrock, S. R. Schmid, and B. O. Jacobson, *Fundamentals of fluid film lubrication*, 2nd ed. New York: Marcel Dekker, 2004.

[3] W. L. Cooke, 'Simulation of dynamically loaded bearings at NEL', *Tribology*, vol. 1, no. 2, pp. 102–103, Mar. 1968.

[4] G. C. Pratt, 'Materials for Plain Bearings', *International Metallurgical Reviews*, vol. 18, no. 2, 1973

[5] H. Xu, G. J. Jones, S. Aoyama, K. Ushijima, Y. Okamoto, and K. Kitahara, 'Simulation of Bearing Wear and Its Influence Upon Bearing Performance Based on Elastohydrodynamic Analysis', *SAE Technical Paper 1999-01-1522*, May 1999

[6] H. A. Tripp and A. Berker, 'Oil Film Thickness measurements in a Dynamically Loaded Journal Bearing—A Comparison of Measured and Calculated Minimum Oil Film Thickness with Newtonian Lubricating Oils', presented at the 1988 SAE International Fall Fuels and Lubricants Meeting and Exhibition, Oct. 1988

[7] P. K. Goenka, 'Dynamically Loaded Journal Bearings: Finite Element Method Analysis', *Journal of Tribology*, vol. 106, no. 4, pp. 429–437, Oct. 1984

[8] T. Kataoka, T. Kikuchi, and K. Ashihara, 'Measurement of Oil Film Thickness in the Main Bearings of an Operating Engine using Thin-Film Electrode', *SAE Int. J. Fuels Lubr.*, vol. 5, no. 1, pp. 425–433, Aug. 2011,

[9] D. E. Sander *et al.*, 'Impact of high pressure and shear thinning on journal bearing friction', *Tribology International*, vol. 81, pp. 29–37, Jan. 2015

[10] S.-C. Vladescu, N. Marx, L. Fernández, F. Barceló, and H. Spikes, 'Hydrodynamic Friction of Viscosity-Modified Oils in a Journal Bearing Machine', *Tribol Lett*, vol. 66, no. 4, pp. 127, Dec. 2018

[11] N. Marx, L. Fernández, F. Barceló, and H. Spikes, 'Shear Thinning and Hydrodynamic Friction of Viscosity Modifier-Containing Oils. Part I: Shear Thinning Behaviour', *Tribol Lett*, vol. 66, no. 3, pp. 92, Sep. 2018,

[12] N. Marx, L. Fernández, F. Barceló, and H. Spikes, 'Shear Thinning and Hydrodynamic Friction of Viscosity Modifier-Containing Oils. Part II: Impact of Shear Thinning on Journal Bearing Friction', *Tribol Lett*, vol. 66, no. 3, pp. 91, Sep. 2018

[13] K. Yasuda, R. C. Armstrong, and R. E. Cohen, 'Shear flow properties of concentrated solutions of linear and star branched polystyrenes', *Rheol Acta*, vol. 20, no. 2, pp. 163–178, Mar. 1981.

[14] S. Suzuki, T. Ozasa, T. Noda, and T. Konomi, 'Amalysis of Con-Rod Big-End Bearing Lubriciation on the Basis of Oil Supply Rate', *SAE Technical Paper 982439*, pp. 13, 1998

[15] C. Fang, X. Meng, Y. Xie, C. Wen, and R. Liu, 'An improved technique for measuring piston-assembly friction and comparative analysis with numerical simulations: Under motored condition', *Mechanical Systems and Signal Processing*, vol. 115, pp. 657–676, Jan. 2019

[16] H.-W. Lee, C.-H. Oh, S. K. Kauh, and K.-P. Ha, 'Development of a multipiston temperature telemetry system using Bluetooth networks', *Proceedings of the Institution of Mechanical Engineers, Part D: Journal of Automobile Engineering*, vol. 220, no. 2, pp. 127–138, Feb. 2006

[17] C. Wen *et al.*, 'Online measurement of piston-assembly friction with wireless IMEP method under fired conditions and comparison with numerical analysis', *Measurement*, vol. 174, Apr. 2021

[18] R. Isarai, M. Sugino, M. Moritsugu, N. Kato, and M. Nakamura, 'Strain and Motion Measurement for Piston, Piston Ring and Connecting Rod of High Speed Running Engines using New Digital Telemeter', presented at the SAE World Congress & Exhibition, Apr. 2008

[19] G. Goodwin and R. Holmes, 'On the Continuous Temperature Monitoring of an Engine Bearing', *Proceedings of the Institution of Mechanical Engineers*, vol. 191, no. 1, pp. 161–167, Jun. 1977

[20] T. Masuda, K. Ushijima, and K. Hamai, 'A Measurement of Oil Film Pressure Distribution in Connecting Rod Bearing With Test Rig', *Tribology Transactions*, vol. 35, no. 1, pp. 71–76, Jan. 1992

[21] T. Ozasa, M. Yamamoto, S. Suzuki, Y. Nozawa, and T. Konomi, 'Elastohydrodynamic Lubrication Model of Connecting Rod Big End Bearings; Comparison with Experiments by Diesel Engine', *SAE Transactions*, vol. 104, no. 4, Oct. 1995

[22] T. Ozasa, T. Noda, and T. Konomi, 'Elastohydrodynamic Lubrication Model of Connecting Rod Big-End Bearings: Application to Real Engines', *ASME. J. Tribol.*, vol. 119, no. 3, pp. 568–578, Jul. 1997

[23] M. J. Goodwin, C. Groves, J. Nikolajsen, and P. J. Ogrodnik, 'Experimental measurement of big-end bearing journal orbits', *Proceedings of the Institution of Mechanical Engineers, Part J: Journal of Engineering Tribology*, vol. 214, no. 3, pp. 219–228, Mar. 2000

[24] A. O. Mian, D. D. Parker, and B. Williams, 'Measured Crankshaft Bearing Oil Flow and Temperatures with a Full and Partial Groove Main Bearing', presented at the SAE 2000 World Congress, Mar. 2000, pp. 2000-01–1341.

[25] H. Moreau, P. Maspeyrot, D. Bonneau, and J. Frene, 'Comparison between experimental lm thickness measurements and elastohydrodynamic analysis in a connecting-rod bearing', *Proceedings of the Institution of Mechanical Engineers, Part J: Journal of Engineering Tribology*, vol. 216, pp. 14

[26] D. R. Merritt, O. Mian, and D. Wang, 'Connecting rod bearing EHD analysis including inertia effects due to the distributed rod mass', presented at the 8th International Conference on Engines for Automobiles, Sep. 2007, pp. 2007-24–0134.

[27] D. Wang, G. Jones, O. Mian, D. Merritt, and T. Simon, 'Oil Flow and Temperature Predictions for a Big-End Bearing', in *ASME/STLE 2007 International Joint Tribology Conference, Parts A and B*, San Diego, California, USA, Jan. 2007, pp. 415–417

[28] C. Fang, X. Meng, Y. Xie, C. Wen, and R. Liu, 'An improved technique for measuring piston-assembly friction and comparative analysis with numerical simulations: Under motored condition', *Mechanical Systems and Signal Processing*, vol. 115, pp. 657–676, Jan. 2019

[29] J. F. Booker, S. Boedo, and D. Bonneau, 'Conformal elastohydrodynamic lubrication analysis for engine bearing design: A brief review', *Proceedings of the Institution of*

Mechanical Engineers, Part C: Journal of Mechanical Engineering Science, vol. 224, no. 12, pp. 2648–2653, Dec. 2010

[30] H. Allmaier and G. Offner, 'Current Challenges and Frontiers for the EHD Simulation of Journal Bearings: a Review', *SAE Technical Paper 2016-01-1856*, Jun. 2016

[31] K. P. Oh and K. H. Huebner, 'Solution of the Elastohydrodynamic Finite Journal Bearing Problem', *Journal of Lubrication Technology*, vol. 95, no. 3, pp. 342–351, Jul. 1973

[32] H. Xu and E. H. Smith, 'A New Approach to the Solution of Elastohydrodynamic Lubrication of Crankshaft Bearings', *Proceedings of the Institution of Mechanical Engineers, Part C: Mechanical Engineering Science*, vol. 204, no. 3, pp. 187–197, May 1990

[33] F. A. Stefani and A. U. Rebora, 'A Nonlinear Structure Based Elastohydrodynamic Analysis Method for Connecting Rod Big End Bearings of High Performance Engines', *Journal of Tribology*, vol. 126, no. 4, pp. 664–671, Oct. 2004

[34] P. K. Goenka and K. P. Oh, 'An Optimum Connecting Rod Design Study—A Lubrication Viewpoint', *Journal of Tribology*, vol. 108, no. 3, pp. 487–493, Jul. 1986

[35] H. Moreau, P. Maspeyrot, D. Bonneau, and J. FreÁne, 'Comparison between experimental lm thickness measurements and elastohydrodynamic analysis in a connecting-rod bearing', *Part J*, vol. 216, p. 14, 2002.

[36] T. Illner, D. Bartel, and L. Deters, 'Determination of the transition speed in journal bearings under consideration of bearing deformation', *Tribology International*, vol. 82, pp. 58–67, Feb. 2015

[37] H. Moreau, P. Maspeyrot, A. M. Chomat-Delalex, D. Bonneau, and J. Frene, 'Dynamic behaviour of elastic engine main bearings: Theory and measurements', *Proceedings of the Institution of Mechanical Engineers, Part J: Journal of Engineering Tribology*, vol. 216, no. 4, pp. 179–194, Apr. 2002

[38] D. Bonneau, D. Guines, J. Freˆne, and J. Toplosky, 'EHD Analysis, Including Structural Inertia Effects and a Mass-Conserving Cavitation Model', *Journal of Tribology*, vol. 117, no. 3, pp. 540–547, Jul. 1995

[39] J. D. C. McIvor and D. N. Fenner, 'Finite Element Analysis of Dynamically Loaded Flexible Journal Bearings: A Fast Newton-Raphson Method', *Journal of Tribology*, vol. 111, no. 4, pp. 597–604, Oct. 1989

[40] W. K. Liu *et al.*, 'Finite element method for mixed elastohydrodynamic lubrication of journal-bearing systems', *Int. J. Numer. Meth. Engng.*, vol. 60, no. 10, pp. 1759–1790, Jul. 2004

[41] D. Bartel, L. Bobach, T. Illner, and L. Deters, 'Simulating transient wear characteristics of journal bearings subjected to mixed friction', *Proceedings of the Institution of Mechanical Engineers, Part J: Journal of Engineering Tribology*, vol. 226, no. 12, pp. 1095–1108, Dec. 2012

[42] K. P. Oh and P. K. Goenka, 'The Elastohydrodynamic Solution of Journal Bearings Under Dynamic Loading', *Journal of Tribology*, vol. 107, no. 3, pp. 389–394, Jul. 1985

[43] G. Knoll, J. Lang, and A. Riena¨cker, 'Transient EHD Connecting Rod Analysis: Full Dynamic Versus Quasi-Static Deformation', *Journal of Tribology*, vol. 118, no. 2, pp. 349–355, Apr. 1996

[44] G. Knoll, J. Lang, and A. Riena¨cker, ‘Transient EHD Connecting Rod Analysis: Full Dynamic Versus Quasi-Static Deformation’, *Journal of Tribology*, vol. 118, no. 2, pp. 349–355, Apr. 1996

[45] A. Francisco, ‘Using Design of Experiments to Analyze the Connecting Rod Big-End Bearing Behavior’, *Journal of Tribology*, p. 13, 2009.

[46] D. Bonneau, *Hydrodynamic bearings*. London, UK : Hoboken, NJ: ISTE Ltd ; John Wiley and Sons Inc, 2014.

[47] F. J. Profito, D. C. Zachariadis, and D. Dini, ‘Partitioned fluid-structure interaction techniques applied to the mixed-elastohydrodynamic solution of dynamically loaded connecting-rod big-end bearings’, *Tribology International*, vol. 140, Dec. 2019

[48] G. Offner and O. Knaus, ‘A Generic Friction Model for Radial Slider Bearing Simulation Considering Elastic and Plastic Deformation’, *Lubricants*, vol. 3, no. 3, pp. 522–538, Jun. 2015

[49] G. Offner, ‘Friction Power Loss Simulation of Internal Combustion Engines Considering Mixed Lubricated Radial Slider, Axial Slider and Piston to Liner Contacts’, *Tribology Transactions*, vol. 56, no. 3, pp. 503–515, May 2013

[50] G. Offner, ‘Modelling of condensed flexible bodies considering non-linear inertia effects resulting from gross motions’, *Proceedings of the IMechE*, vol. 225, no. 3, pp. 204–219, Sep. 2011

[51] N. Lorenz, G. Offner, and O. Knaus, ‘Fast thermo-elasto-hydrodynamic modeling approach for mixed lubricated journal bearings in internal combustion engines’, *Proceedings of the Institution of Mechanical Engineers, Part J: Journal of Engineering Tribology*, vol. 229, no. 8, pp. 962–976, Aug. 2015

[52] K. Holmberg, P. Andersson, N.-O. Nylund, K. Mäkelä, and A. Erdemir, ‘Global energy consumption due to friction in trucks and buses’, *Tribology International*, vol. 78, pp. 94–114, Oct. 2014

[53] M. J. Covitch, M. Brown, C. May, T. Selby, I. Goldmints, and D. George, ‘Extending SAE J300 to Viscosity Grades below SAE 20’, *SAE Int. J. Fuels Lubr.*, vol. 3, no. 2, pp. 1030–1040, Oct. 2010

[54] E. Zadorozhnaya, I. Levanov, and O. Oskina, ‘Study of HTHS Viscosity of Modern Motor Oils’, *Procedia Engineering*, vol. 150, pp. 602–606, 2016

[55] V. Macián, B. Tormos, S. Ruiz, and G. Miró, ‘Low viscosity engine oils: Study of wear effects and oil key parameters in a heavy duty engine fleet test’, *Tribology International*, vol. 94, pp. 240–248, Feb. 2016

[56] V. Macián, B. Tormos, V. Bermúdez, and L. Ramírez, ‘Assessment of the effect of low viscosity oils usage on a light duty diesel engine fuel consumption in stationary and transient conditions’, *Tribology International*, vol. 79, pp. 132–139, Nov. 2014

[57] S. Bair, ‘Measurements of real non-Newtonian response for liquid lubricants under moderate pressures’, *Proceedings of the Institution of Mechanical Engineers, Part J: Journal of Engineering Tribology*, vol. 215, no. 3, pp. 223–233, Mar. 2001

[58] S. Bair, ‘The shear rheology of thin compressed liquid films’, *Proceedings of the Institution of Mechanical Engineers, Part J: Journal of Engineering Tribology*, vol. 216, no. 1, pp. 1–17, Jan. 2002

[59] H. Vogel, ‘The law of the relation between the viscosity of liquids and the temperature’, *Phys. Z*, vol. 22, no. 1, pp. 645–646, 1921.

[60] C. Barus, ‘ART. X.–Isothermals, isopiestics and isometrics relative to viscosity’, *American Journal of Science (1880-1910)*, vol. 45, no. 266, p. 87, 1893.

[61] M. M. Cross, ‘Rheology of non-Newtonian fluids: A new flow equation for pseudoplastic systems’, *Journal of Colloid Science*, vol. 20, no. 5, pp. 417–437, Jun. 1965

[62] H. Allmaier, C. Priestner, C. Six, H. H. Priebsch, C. Forstner, and F. Novotny-Farkas, ‘Predicting friction reliably and accurately in journal bearings—A systematic validation of simulation results with experimental measurements’, *Tribology International*, vol. 44, no. 10, pp. 1151–1160, Sep. 2011

[63] S. Bukovnik, G. Offner, V. Čaika, H. H. Priebsch, and W. J. Bartz, ‘Thermo-elasto-hydrodynamic lubrication model for journal bearing including shear rate-dependent viscosity: TEHD with shear rate dependent viscosity’, *Lubrication Science*, vol. 19, no. 4, pp. 231–245, Oct. 2007

[64] D. E. Sander *et al.*, ‘Edge loading and running-in wear in dynamically loaded journal bearings’, *Tribology International*, vol. 92, pp. 395–403, Dec. 2015

[65] A. Fatu, M. Hajjam, and D. Bonneau, ‘Analysis of non-Newtonian and piezoviscous effects in dynamically loaded connecting-rod bearings’, *Proceedings of the Institution of Mechanical Engineers, Part J: Journal of Engineering Tribology*, vol. 219, no. 3, pp. 209–224, Mar. 2005.

[66] D. Dowson, ‘Fundamental aspects of cavitation in bearings’, in *Proc. of the 1st leeds-lyon symposium on tribology, 1974*, 1974.

[67] K. G. Murty and others, ‘Note on a Bard-type scheme for solving the complementarity problem’, *Opsearch*, vol. 11, no. 2–3, pp. 123–130, 1974.

[68] K. P. Oh, ‘The Numerical Solution of Dynamically Loaded Elastohydrodynamic Contact as a Nonlinear Complementarity Problem’, *Journal of Tribology*, vol. 106, no. 1, pp. 88–95, Jan. 1984

[69] B. Jakobsson, L. Floberg, and L. Floberg, ‘The finite journal bearing, considering vaporization: Report from the Institute of Machine Elements’, 1957.

[70] K.-O. Olsson, ‘Cavitation in dynamically loaded bearings’, *Transactions of Chalmers University of Technology*, vol. 308, 1965.

[71] H. G. Elrod, ‘A cavitation algorithm’,ASME J. Lubr. Technol. 0022-2305, 103(3), pp. 350–354 1981.

[72] D. Bonneau and M. Hajjam, ‘Modélisation de la rupture et de la reformation des films lubrifiants dans les contacts élastohydrodynamiques’, *Revue Européenne des Éléments Finis*, vol. 10, no. 6–7, pp. 679–704, Jan. 2001.

[73] G. Offner, ‘Modelling of condensed flexible bodies considering non-linear inertia effects resulting from gross motions’, *Proceedings of the Institution of Mechanical Engineers, Part K: Journal of Multi-body Dynamics*, vol. 225, no. 3, pp. 204–219, 2011

[74] G. Offner, ‘Friction Power Loss Simulation of Internal Combustion Engines Considering Mixed Lubricated Radial Slider, Axial Slider and Piston to Liner Contacts’, *Tribology Transactions*, vol. 56, no. 3, pp. 503–515, May 2013

[75] L. Smolík, Z. Rendlová, and M. Byrtus, ‘An Analysis of the Influence of the Titanium Compressor Wheel on the Dynamical Properties of the Particular Turbocharger Rotor’, *Manufacturing Technology*, vol. 15, no. 1, pp. 93–99, Feb. 2015

[76] F. J. Profito and D. C. Zachariadis, ‘Partitioned fluid-structure methods applied to the solution of elastohydrodynamic conformal contacts’, *Tribology International*, vol. 81, pp. 321–332, Jan. 2015

[77] N. Patir and H. S. Cheng, ‘Application of average flow model to lubrication between rough sliding surfaces’, *Journal of Lubrication Technology*, vol. 101, pp. 220–229, 1979.

[78] D. N. Fenner and J. D. C. Mclvor, ‘Finite Element Analysis of Dynamically Loaded Flexible Journal Bearings: A Fast Newton-Raphson Method’, *ASME J. Tribology*, vol. 111, p. 597, 1989.

[79] J. F. Booker, ‘Dynamically Loaded Journal Bearings: Mobility Method of Solution’, *ASME Journal of Basic Engineering*, pp. 537–546, 1965

[80] K. Kalogiannis, P. Desai, O. Mian, and R. Mainwaring, ‘Simulated Bearing Durability and Friction Reduction with Ultra-Low Viscosity Oils’, presented at the International Powertrains, Fuels & Lubricants Meeting, Sep. 2018, pp. 2018-01–1802

[81] S. A. Ferreyra, S. Uehara, M. dos Santos Ferreira, and O. Mian, ‘Engine Lubrication System for Oil Flow Reduction’, presented at the SAE Brasil 2011 Congress and Exhibit, Oct. 2011, pp. 2011-36–0205.

[82] D. Bonneau, *Internal combustion engine bearings lubrication in hydrodynamic bearings*. Hoboken, NJ: ISTE Ltd/John Wiley and Sons Inc, 2014.

[83] D. Bonneau, *Mixed lubrication in hydrodynamic bearings*. London, UK : Hoboken, NJ: ISTE Ltd ; John Wiley and Sons Inc, 2014.

[84] D. Bonneau, A. Fatu, and D. Souchet, *Thermo-Hydrodynamic Lubrication in Hydrodynamic Bearings: Bonneau/Thermo-Hydrodynamic Lubrication in Hydrodynamic Bearings*. Hoboken, NJ, USA: John Wiley & Sons, Inc., 2014.

[85] P. Michaud, A. Fatu, and B. Villechaise, ‘Development of an Experimental Device to Study Real Connecting-Rod Bearings Functioning in Severe Conditions’, *Journal of Tribology*, vol. 129, no. 3, pp. 647–654, Jul. 2007

[86] Kawasaki Heavy Industries, Ltd, *Motorcycle Service Manual Ninja ZX-10R*. 2005.

[87] C. P. Reeve, ‘The calibration of a roundness standard’, National Bureau of Standards, Gaithersburg, MD, NBS IR 79-1758, 1979.

[88] B. A. Evans, ‘Development of Kinematic Coupling Preload Guidelines through Design and Testing of an Adjustable Micromanufacturing Fixture’, Massachusetts Institute of Technology, 2014.

[89] M. Sieniło, J. Skrzeszewska, and M. Wiśniewska, ‘Software for visualization and analysis of signals from devices for measurement of shape deviations’, *Mechanik*, no. 11, pp. 1038–1040, Nov. 2017

[90] J. S. Chen and C. C. Ling, ‘Improving the machine accuracy through machine tool metrology and error correction’, *Int J Adv Manuf Technol*, vol. 11, no. 3, pp. 198–205, May 1996

[91] I. O. MacConochie and A. Cameron, ‘The Measurement of Oil-Film Thickness in Gear Teeth’, *ASME J. Basic Eng.*, vol. 82, no. 1, p. 6, 1960

[92] A. Dyson, ‘Investigation of the discharge-voltage method of measuring the thickness of oil films formed in a disc machine under conditions of elastohydrodynamic lubrication’, *Proceedings of the Institution of Mechanical Engineers*, vol. 181, no. 1, pp. 633–652, 1966.

[93] A. W. Crook, ‘Simulated gear-tooth contacts : some experiments upon their lubrication and subsurface deformations ’, pp. 33

[94] A.W. Crook, ‘The lubrication of rollers’, *Phil. Trans. R. Soc. Lond. A*, Jan. 1958.

[95] K. Irani, M. Pekkari, and H.-E. Ångström, ‘Oil film thickness measurement in the middle main bearing of a six-cylinder supercharged 9 litre diesel engine using capacitive transducers’, *Wear*, vol. 207, no. 1–2, pp. 29–33, Jun. 1997.

[96] D. Bonneau, A. Fatu, and D. Souchet, *Paliers hydrodynamiques. 1, 1,*. 2011.

[97] K. Ushijima, S. Aoyama, K. Kitahara, Y. Okamoto, G. Jones, and H. Xu, ‘A Study on Engine Bearing Wear and Fatigue Using EHL Analysis and Experimental Analysis’, presented at the International Fuels & Lubricants Meeting & Exposition, May 1999, pp. 1999-01–1514. doi: 10/fr3s3w.

[98] K. M. Ebrahimi, A. Lewalski, A. Pezouvanis, and B. Mason, ‘Piston Data Telemetry in Internal Combustion Engines’, *American Journal of Sensor Technology*, p. 6, 2014.

[99] IR Telemetrics, ‘Wireless measurement systems’. [Online]. Available: www.irtelemetrics.com

[100] IR Telemetrics, ‘Wireless Data Transfer’. [Online]. Available: www.irtelemetrics.com

[101] datatel-telemetry, ‘Advanced Telemetry Systems for Automotive Testing’, datatel-telemetry. [Online]. Available: www.datatel-telemetry.com

(this page intentionally left blank)

NOMENCLATURE

μ	Friction coefficient	[-]
$\boldsymbol{\eta}$	Dynamic viscosity	[Pa·s]
$\boldsymbol{\omega}$	Rotational speed	[RPS]
W	Normal load	[N]
$\dot{\boldsymbol{\gamma}}$	Shear rate	[s^{-1}]
$\boldsymbol{p}$	Pressure	[MPa]
$\boldsymbol{T}$	temperature	[°C]
U	Linear velocity	[m/s]
$\mathbf{e_R}$	Journal eccentricity right connecting rod	[mm]
$\mathbf{e_L}$	Journal eccentricity left connecting rod	[mm]
$\mathbf{K_c}$	Connecting rod stiffness	[N/m]
$\mathbf{K_f}$	Adjustable stiffens	[N/m]
$\vec{\Delta}$	Roundness deviation	[mm]
$\left\|\overrightarrow{O_1P^i}\right\| = \boldsymbol{R_{fit}}$	Radius of the reference circle	[mm]
α	Angular deviation of Reference circle from datum	[°]
$\boldsymbol{r} = \left\|\overrightarrow{OO_1}\right\|$	length deviation of Reference circle from datum	[mm]
$\boldsymbol{R_t} = \left\|\overrightarrow{OP}\right\|$	Workpiece trace	[mm]
$\overrightarrow{\boldsymbol{H_p}}$	Horizontal arm position	[mm]
$\overrightarrow{\boldsymbol{S_d}}$	Stylus deflection	[mm]
$\boldsymbol{\theta_i}$	is the instantaneous angle in the roundness profile	[°]
i	Index of a circumferential position	[-]
$\vec{\boldsymbol{S}}_{\boldsymbol{d\_PRF}}$	Stylus deflection for PRF file	[mm]

$\vec{\Delta}_{MDR}$	Roundness deviation from MDR file	[mm]
$\vec{R}_{fit\_MDR}$	Radius of the reference circle from MDR file	[mm]
$\vec{R}_{\_MDR}$	Roundness profile from MDR file	[mm]
$\vec{S}_{d\_MDR}$	Stylus deflection of the *.MDR	[mm]
x_{ecc}, y_{ecc}	Cartesian coordinates of the eccentricity (r)	[mm]
$x_{MDR(i)}, y_{MDR(i)}$	Cartesian coordinates of the Workpiece trace from MDR file	[mm]
h	Bearing height section plane	[mm]
P1, P2, P3	Eddy current gap sensors location	[-]
$\mathbf{R_a}$	mean roughness	[µm]
$\boldsymbol{v}$	Kinematic viscosity	
$\boldsymbol{m}$		
$\boldsymbol{n}$		
v_1, v_2	Kinematic viscosities for Mc Coull and Walther law	[cST]
T_{v_1}, T_{v_2}	Temperatures for Mc Coull and Walther law	[K]
a	Coull and Walther law coefficient	[cST]
C_U_l	Clearance Height Upper bearing Left	[µm]
C_U_c	Clearance Height Upper bearing Centre	[µm]
C_U_r	Clearance Height Upper bearing Right	[µm]
C_L_l	Clearance Height Lower bearing Left	[µm]
C_L_c	Clearance Height Lower bearing Centre	[µm]
C_L_r	Clearance Height Lower Bearing Right	[mm]
Cr_h_U_l	Crush Relief Height Upper Bearing Left	[mm]
Cr_h_U_r	Crush Relief Height Upper Bearing Right	[mm]
Cr_w_U_l	Crush Relief Width Upper Bearing Left	[mm]
Cr_w_U_r	Crush Relief Width Lower Bearing Right	[mm]

Cr_h_L_l	Crush Relief Height Lower Bearing Left	[mm]
Cr_h_L_r	Crush Relief Height Lower Bearing Right	[mm]
Cr_w_L_l	Crush Relief Width Lower Bearing Left	[mm]
Cr_w_L_r	Crush Relief Width Lower Bearing Right	[mm]
C	Radial clearance	[µm]
Sq	Root mean square height	[µm]
Ssk	Skewness	[µm]
Sku	Kurtosis	[µm]
$\boldsymbol{RC}$	voltage decent ratio	[-]
$\boldsymbol{V_0}$	voltage under insulation	[V]
$\boldsymbol{V_t}$	measured voltage	[V]
$\boldsymbol{\theta_{cyc}}$	Cycle angle	[°]

ACRONYMS

ICE	Internal Combustion Engines
TEHD	ThermoElastoHydroDynamic
HD	Hydrodynamic
EHD	Elastohydrodynamic
MOFT	Minimum oil film thickness
FE	Finite element
MBS	Multi body system commercial software
DAEs	Differential Algebraic Equation system
HTHS	High Temperature High Shear
DOF	Degree of freedom
ACCEL	L'Analyse et le Calcul des Contacts Elastique Lubrifies or the analyse and computation for lubricated elastic contacts
MEGAPASCALE	Machine d'Essais pour Guidage d'Arbre par PAliers Sous Charges ALternativées Elevees
CAE	Computer aided engineering
RMM	Roundness Measuring Machine
LSC	Least mean squares
RC	voltage drop decent ratio
ADC	Analogue-to-digital converters
SPI	Serial peripheral interface
PCB	Printed circuit board
BLE	BLUEtooth Low Energy
SPS	Samples per second

LIST OF FIGURES

LIST OF TABLES

Appendix A Development of a Telemetry System

A.1. Design constrains and motivation

The custom development of the telemetry system was driven by the need of real engine data acquisition. At the beginning of the thesis two types of experimental approaches have been purpose, the first one is through the special test rig called MEGAPASCALE which represents the core experimental data source for this thesis and have been intensively used to generate experimental data in the need of ACCEL validation. The second approach is the real engine test rig. It is widely known the difficulty of data logging inside an engine, especially for the data linked to the connecting rod.

Few publications are available on the literature on telemetry systems for engine [16]–[18], [28], [98] while commercial telemetry systems suited for connecting rods are hard to find on the market [99]–[101]. Most of the systems have been used for slow-engines, with large connection rods, where the available space for the circuits is large compared to the space available on the Kawasaki ZX10.

This section describes the development of a miniaturized telemetry system for high speed engines. As the high-speed engines connecting rods are small in term of dimensions, data logging became difficult to implement. The requirements for such a system are very high. First of all, the telemetry system circuitry dimensions are constrained by the connecting rod dimensions and secondly by the clearance between the connecting rod and piston, connecting rod and crankshaft balancing weights. The harsh chemical and thermal environment requires that the electronic circuitry be protected. Another important design feature is the data transmission, as the connecting rod is place inside the crankcase, the output of the radio signal become difficult to be achieve due to the tendency of faraday cage effect of the crankcase.

Another important design constrain is the added mass, as the engine operates at high speeds. For example, 11 500 rpm for the specific case of the Kawasaki ZX10 engine, the telemetry system mass must be as light as possible I order to limit the inertial effects.

This section focuses on the development of a telemetry system able to record the big-end bearing temperature while engine is running and transmit the data to an external PC. Another design feature to be considered is the attachment to the connecting rod.

A.2. Telemetry synopsis

Figure A.1 shows the telemetry module synopsis. The telemetry system is composed of two modules: connecting rod module and bench module. Both of them are based on two identical microchips produced by Nordic Semiconductors nRF52840. Both of them functions as transmitter and receiver. At left of the diagram is the connecting rod module which is composed of two layers. The first one, here called c-microchip layer, is a I-SYST dongle, a crowd founded component based on the nRF5240. Its function is firstly to send the data received from the signal conditioning layer to the bench module. The signal conditioning layer is based on two 16-bit two channel delta-sigma analogue-to-digital converters (ADC) from Texas Instruments ADS1018. The ADC has an integrated thermistor and cold junction compensation for thermocouples measurements and adjustable gain. The communication between the signal conditioning and the c-microchip layer is performed through Serial Peripheral Interface (SPI) communication protocol. The entire module is powered by a 3V, 48mAh BR1225 Panasonic coin battery. The data transition between the connecting rod module and the bench module is performed through Bluetooth Low Energy (BLE) communication protocol. The acquired data by the connecting rod module is sent to the bench module through an antenna mounted inside the crank case. In such manner, the faraday cage effect of the crankcase is avoided. The bench module is composed of an nRF52840 dev kit which is connected to the PC via an USB cable. The data is acquired and logged inside the PC through serial connection.

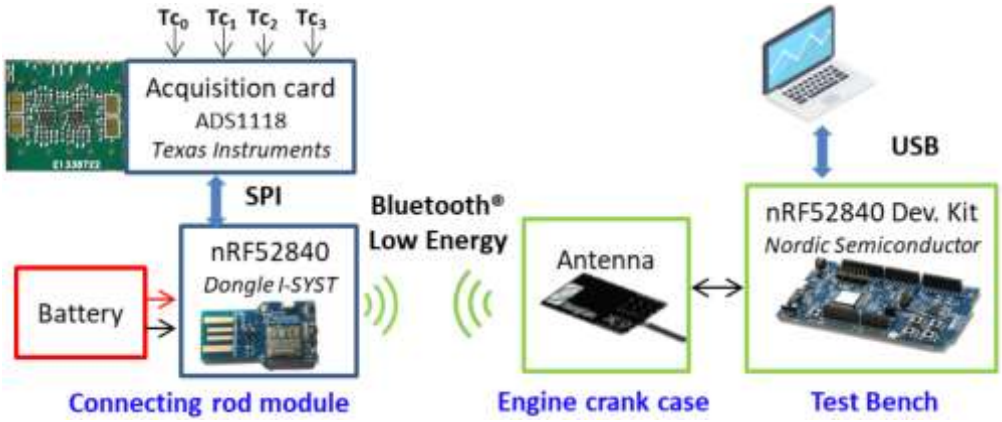

Figure A.1 Telemetry module synopsis

A.3. Signal Conditioning layer

The signal conditioning is based on two 16-bit ADC converter: ADS1018 Texas Instruments. An input multiplexer allows two differential or four single ended inputs. For this particular case, two differential thermocouples are used per ADC. The ADC conversions data rates are up to 3300 samples per second (SPS). The ADC operate in 2 modes, continuous-conversion mode or single-shot mode which reduces significantly the power consumption. The data are transferred through serial peripheral interface (SPI). In order to connect the I-SYST dongle nRF5240 to the signal conditioning, a printed circuit board (PCB) was design. Figure A.2 depicts the electrical diagram of the PCB. I-SYST dongle nRF5240 connection bloc represents the input/output pins needed for current supply and SPI communication. For each thermocouple, a filtering and protection circuit has been used.

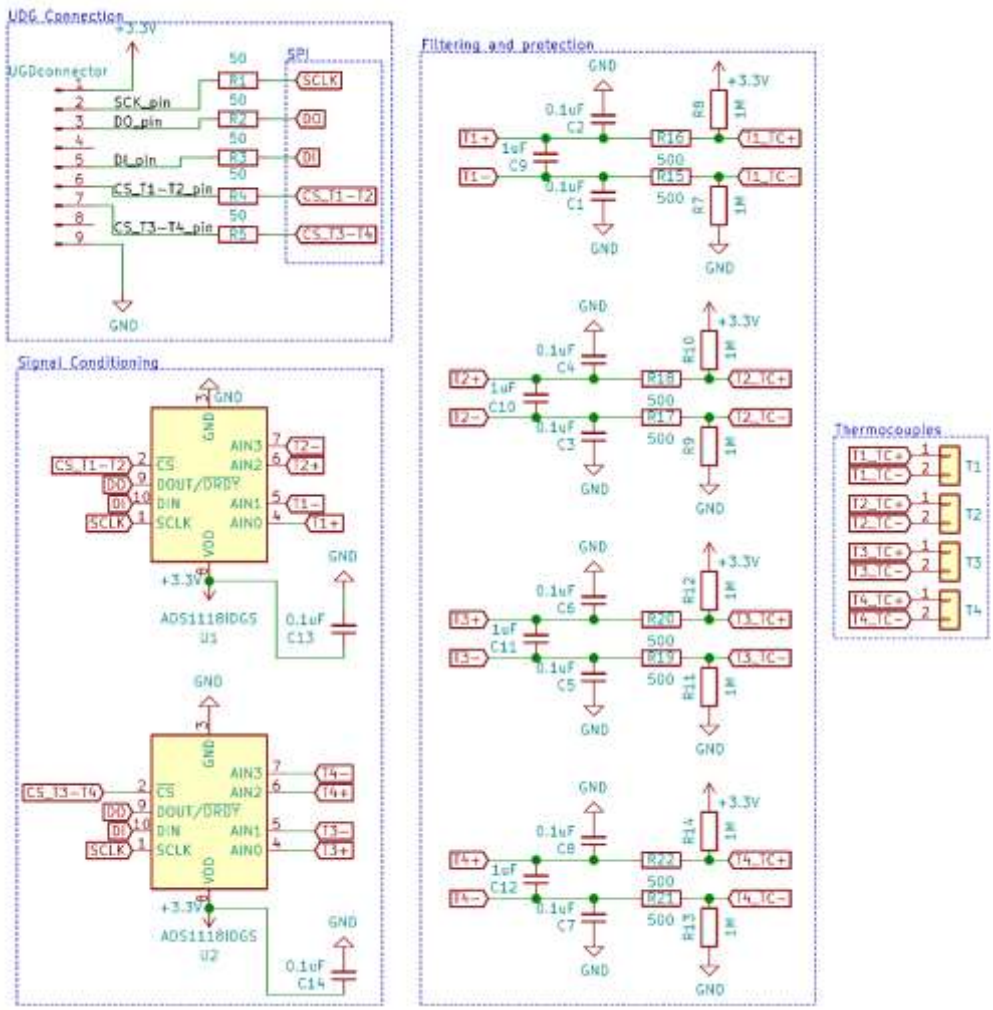

Figure A.2 Signal Conditioning e Electronic Circuit schema

A.4. Power Management Design

One of the biggest constrains of this telemetry system are the available dimensions. In terms of power supply, the only available battery on the market which is small enough to fit is a Panasonic coin battery BR1225 with a capacity of 48mAh. Therefore, the telemetry design must be worked around this capacity values in order to fulfil the testing time request.

Due to the fact that after assembling the instrumented connecting rod inside the engine no physical reach is possible to turn on or off the telemetry system, the battery must supply electrical power at least for the connecting rod module assembly (8h), engine assembly (around 8h) and testing, which makes a total of 24h. Of course, rechargeable battery and a charge module during testing can be implemented and it has been considered by testing induction coils charging modules, but because the time constrain and simplicity of the system, the coin battery has been finally chosen.

The relative high-power consumption (1.4 mA) of the SPI transition in comparison to the used battery capacity and the required time for assembly, a power management has been implemented.

The power management disables the SPI communication if the module is not connected to the bench module, but still advertise the BLE connection. In this mode the power consumption is 0.06 mA. When the BLE connection is established, which means the test begun, the SPI connection is enabled and the thermocouple signal is read and send to the bench module. Table A.1 depicts the measured consumption current for both, stand by and running modes.

Table A.1 Power Consumption

Parameters	Stand By	Running
Power consumption [mA]	0.6	1.4
Battery capacity [mAh] @ 60°C	38	
Battery life time [h]	63	27
Assembly time [h]	24	

A.5. Firmware

As previously mentioned, the connecting rod module system is based on two components, which communicate between them. The fits layer is the ADS1018 (signals conditioning), which transforms the analogue thermocouple measurements to digital values; the second one is the c-microchip layer (nrf52) which: (1) retrieves the converted data from the signal conditioning through SPI communication protocol, (2) sends the retrieved data to the bench module through BLE communication protocol and (3) control the power management. The firmware handling all the functionalities is written in C language and flashed on the microchip using Seeger Embedded Studio which features a real time debugging process.

In order to established the SPI communication between the ADC and microchip layer a library was written. Figure A.3 shows the pseudocode for the ADC conversion function. The conversion is performed in 16-bit single-shot mode accordingly to the ADS1018 datasheet. A register (temp_reg) is sent in 8-bit sequences. The first one represents the most significant bit: m_tx_MBS and the second one is the last significant bit: m_tx_LBS. In order to initiate the data conversion, the chip select pin (CS) is set low. Thren, the SPI transfer function is called to perform the transaction, the CS pin is set high after the transaction and the received data is composed in a single 16-bit variable, which will further be transformed from binary to decimal values. The transmitted register contains information about the multiplexer MUX to be read, the gain values and the conversion speed (Table A.2).

Table A.2 Example of configuration register (temp_reg)

SS	MUX	PGA	MODE	DR	TS_MODE	PULL Up	NOP	RESERVED
1	0 0 0	1 1 1	1	0 0 0	0	1	0 1	0

```
int16_t get_ADC_Result(uint16_t temp_reg,uint8_t CS_Pin)
{
	// 16-Bit data transmition cycle
	uint16_t ads_conv;
	//Initialise the SPI transmiter buffer
	m_tx_MSB[0] = (uint8_t)(temp_reg >> 8);
	m_tx_LSB[1] = (uint8_t)(temp_reg);
	// Set CS pin LOW - start data transmmission
	nrf_gpio_pin_clear(NRF_GPIO_PIN_MAP(CS_Pin_i,CS_Pin));
	//SPI transmfer function
	APP_ERROR_CHECK(nrf_drv_spi_transfer(&spi, m_tx_buf, 2, m_rx_buf, 2));
	// Set CS pin HIGH - end data transmition
	nrf_gpio_pin_set(NRF_GPIO_PIN_MAP(CS_Pin_i,CS_Pin));
	nrf_delay_us(10);
	//Read out the data from SPI reciever buffer
	ads_conv = (uint16_t)((m_rx_buf[0] << 8) | m_rx_buf[1]);
	return ads_conv;
}
```

Figure A.3 Function for reading the ADC conversion data

The data acquisition from the ADC and transition through Bluetooth is handled by the function called transmit (see Figure A.4). The function firstly initialises the default register the ADC. Then the register is modified to read one of the two thermocouples of each ADC through the function ADC_setMux. Then, the ADC conversion function is called. The conversion result is then transformed from binary to decimal and sent through BLE to the bench module by the ble_temperature_send. The process is repeated for all 4 thermocouples.

Figure A.5 depicts the main function of the connecting rod module firmware. The first section initialises the Bluetooth function as well the SPI and the chip select pins for the ADCs. Then, the power management loop checks if the connecting rod module is connected to the bench module. If not, the “idle_state_handle” function puts the microcontroller in standby mode. If the BLE-connect is satisfied, the SPI communication is enabled and the data transfer between the signal conditioning module and the bench module begin.

```
void transmit()
{
	float tempC = 0.0;
	float tempCJ = 0.0;
	// initialise the ADC register
	uint16_t temp_reg_def = ADC_DEFAULTCONFIG;
	// Read Thermistor----------------------------------------------
	//set gonfig register to read the thermistor
	uint16_t temp_reg_CJ = ADC_setMux(temp_reg_def, ADS_TEMPSENSING_MODE);
	//Start data convertion
	uint16_t ADC_conv_TCJ = get_ADC_Result(temp_reg_CJ, CS_ADC1);
	//Convert Temparature
	tempCJ = ADC_convertTemperature_CJ(ADC_conv_TCJ);
	// Termocouple1
	// set up config register for reading thermocpuple 1
	uint16_t temp_reg_Th1 = ADC_setMux(temp_reg_def, ADS_AIN0P_AIN1N);
	//Start data transmition
	uint16_t ADC_conv_1 = get_ADC_Result(temp_reg_Th1, CS_ADC1);
	//Convert Temparature
	tempC = ADC_convertTemperature(ADC_conv_1);
	//Compensate for Cold junction
	temperature = tempC + tempCJ;
	// Send temperature trough bluetooth
	ble_temperature_send(&m_tmp, temperature);
	// Termocouple2 ----
	uint16_t temp_reg_Th2 = ADC_setMux(temp_reg_def, ADS_AIN2P_AIN3N);
	uint16_t ADC_conv_2 = get_ADC_Result(temp_reg_Th2, CS_ADC1);
	tempC = ADC_convertTemperature(ADC_conv_2);
	temperature = tempC + tempCJ;
	ble_temperature_send(&m_tmp, temperature);
	// Termocouple3 ----
	uint16_t temp_reg_Th3 = ADC_setMux(temp_reg_def, ADS_AIN0P_AIN1N);
	uint16_t ADC_conv_3 = get_ADC_Result(temp_reg_Th3, CS_ADC2);
	tempC = ADC_convertTemperature(ADC_conv_3);
	ble_temperature_send(&m_tmp, temperature);
	// Termocouple4 ----
	uint16_t temp_reg_Th4 = ads_setMux(temp_reg_def, ADS_AIN2P_AIN3N);
	uint16_t ADC_conv_4 = get_ADC_Result(temp_reg_Th4, CS_ADC2);
	tempC = ADC_convertTemperature(ADC_conv_4);
	temperature = tempC + tempCJ;
	ble_temperature_send(&m_tmp, temperature);
}
```

Figure A.4 Function a quiring and transmitting data

```
int main(void)
{
    // Initialize libraries.
    log_init();
    timers_init();
    power_management_init();
    ble_stack_init();
    gap_params_init();
    gatt_init();
    advertising_init();
    services_init();
    sensor_simulator_init();
    conn_params_init();
    peer_manager_init();
    // Start execution.
    application_timers_start();
    advertising_start(erase_bonds);
    // initialize the chip select (CS) pins for ADC
    nrf_gpio_cfg_output(CS_Th1_Th2);
    nrf_gpio_cfg_output(CS_Th3_Th4);
    // Power management loop.
    for (;;)
    {
      if(ble_connected)
      {
        // If connected, read ADC and send data.
         spi_setup_init();
         transmit(); // transition function
         disable_SPI();
      }
        // If not connected, Enter in sleep mode for power saving.
        idle_state_handle();

    }
}
```

Figure A.5 Main Loop

A.6. Test Preparation and fixture

There are several ways attaching the PCBs to the connecting rod. One of them is by machining a metal housing, which is quite time inefficient and cost expensive. Another way is by using glue. For this particular test, the second method has been employed due to time efficient. In order to ensure the integrity of the bond, a simple dynamic calculation was performed to obtain the shear force acting on the PCB during the most critical functioning regime, 12 000rpm. Table A.3 shows the results of the calculation.

Table A.3 Shear stress calculation

engine speed [rpm]	**max acceleration [m/s^2]**	**PCB mass [kg]**	**Force [N]**	**PCB area [mm^2]**	**Shear Stress [MPa]**
12000	45658.2516	0.005	228.291	256	0.892

The Shear Stress resulting from the calculation are compared with the Lap Shear Strength of the Araldite® 2014-2, the used glue, at different temperature. The Connecting rod shank temperature during functioning is estimated to be about 120°C.

Table A.4 shows the values of the safety factor for the Araldite® 2014-2 bond, values that ensures the integrity during the testing on the harshest conditions. According to the Araldite® 2014-2 datasheet the glue is not degraded by immersion in lubricant oil.

Table A.4 Araldite® 2014-2 Bond Safety Factor

Temperature[°C]	Lap shear strength [MPa]	Safety factor
140	5	5.6
120	7.5	8.4
100	10	11.2

The following subsection describes the preparation steps. The preparation process begun by assembling the PCBs (see Figure A.6 a.) together. The nine communication pins between the nRF and the Acquisition card are soldered (see Figure A.6 b.) and protected with Kapton tape. Next, the PCBs are prepared and installed on the connecting rod, along with the four thermocouples. In order to allow the connecting rod assembly on the crankshaft pin, the electrical jumpers were added on the thermocouple wires (see Figure A.6 c.).

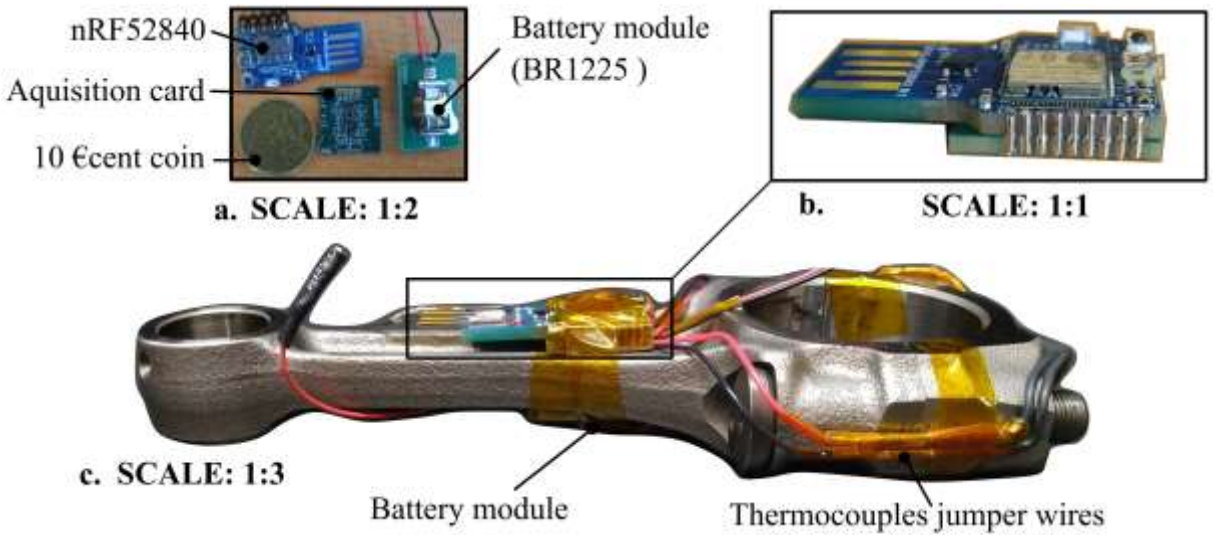

Figure A.6 PCBs assembly: a. the PCBs; b. Soldered connection of the nRF and signal conditioning PCB; c. MOCK-UP: connecting rod

The entire electrical circuit, along with the battery module and the thermocouples are covered in Araldite® 2014-2 and cured at 120°C for one hour. The final result of this step is sowed in Figure A.7.

Figure A.7 The connecting rod after curing the Araldite® 2014-2 glue

The clearance between the balancing weights and PCBs has been checked (see Figure A.8a). The antenna was installed inside the crankcase and glued with the same Araldite® 2014-2 (see Figure A.8 b).

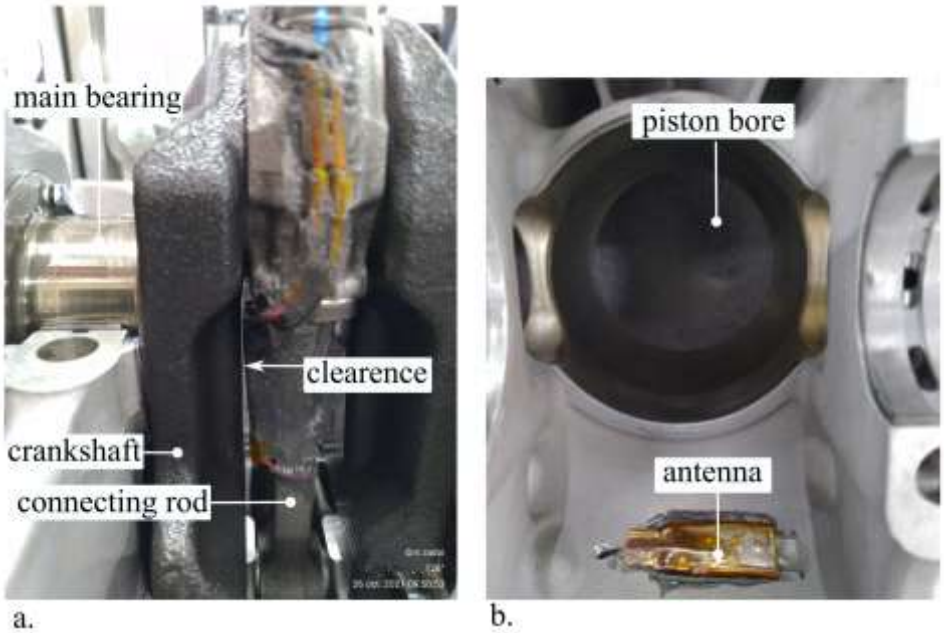

Figure A.8 Connecting rod assembly inside the engine: a. clearance check; b. antenna mount

Figure A.9 b. depicts the first telemetry system functioning testing after engine assembly.

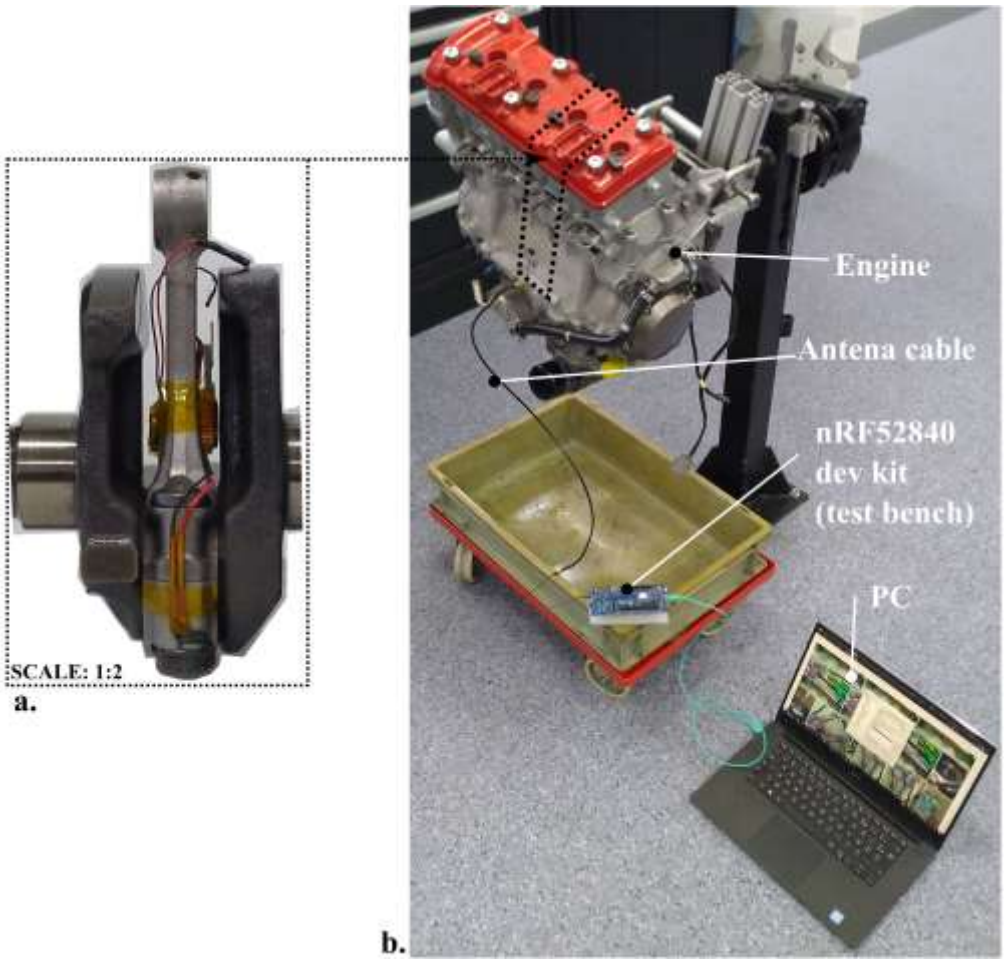

Figure A.9 a. Mook-up connecting rod, telemetry system and crankshaft; b. First connection test before installing the engine on the testbench

A.7. **Results**

The preliminary tests were performed at four speeds: 2500 rpm, 3000 rpm, 4000 rpm and 6000 rpm. Figure A.11 depicts the tests results, where the T0, T1, T2 and T3 are the thermocouples mounted on the connecting rod (see Figure A.10), while T4 is the board thermistor used for cold junction compensation. It can be seen that that the temperatures values are properly received. At the minute 8 the thermocouple 4 lost signal and at the minute 10 the hole communication was lost. Otherwise, the bearing temperature increases with time. Unfortunately, those result are not useful for reasonable ACCEL calculations because the thermal equilibrium of the engine and bearing was not reached. And is the reason why this work is presented here, in the appendix, and does not have a dedicated chapter by itself.

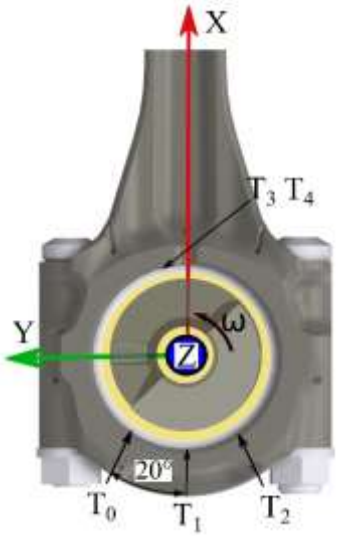

Figure A.10 Thermocouples location

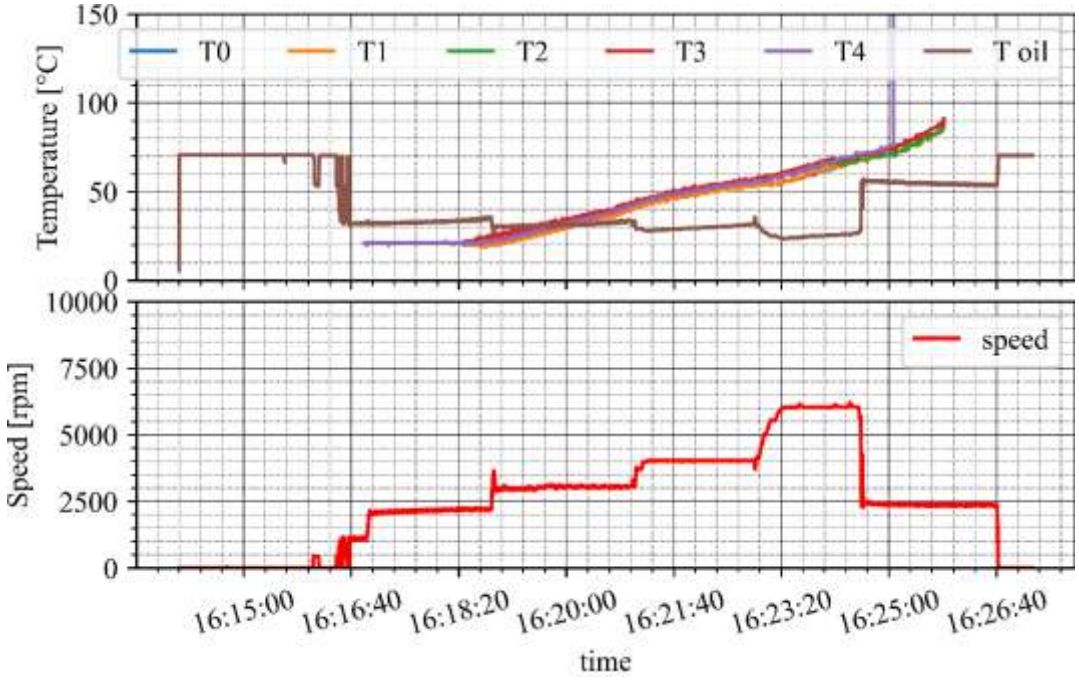

Figure A.11 Test results; T0, T1, T2, T3 - thermocouples T4 - thermistor

The tests have been stopped due to total signal loss after 10min of good functioning. After disassembling the engine, it has been found that the connecting rod module was detached from the connecting rod shank.

Two reasons are responsible to this failure. The firs one is the breakage/take off of one thermocouple which probably was caught between the connecting rod and crankshaft, after a while, the free wire was pinched again pulling out the module from its bound. Unfortunately, the thermocouple wire was wired behind the PCB. Therefore, it had enough leverage to pull out the circuit and brake the bond. The second reason is the Kapton-Araldite® 2014-2 bond. The

Kapton tape was used reasoning that it may bring thermal and electrical insulation. But in the other hand brought weak bond. Basically, the non-sticky face of a scotch tape is treated for non-stickiness because the tape should be rolled out to be used. Unfortunately for this test I learned this the hard way.

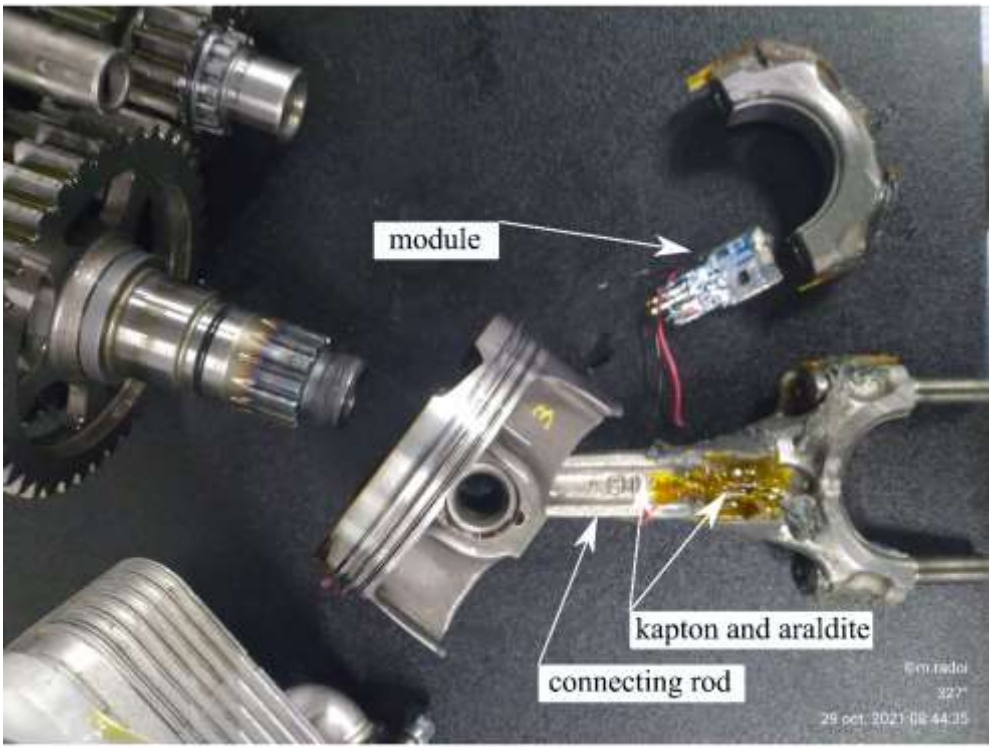

Figure A.12 PCB attachment failure due to Kapton-Araldite® 2014-2bond filature

Even though the attachment bond failed after 10min of testing, the hole process can be considered as a success from a proof-of-concept point of view. Concluding this section, it has been showed that is possible to build a functional and cheap telemetry system. The total cost of the system was 500 € from which 300 € were just for the PCB assembly process.

A.8. Further Development.

First of all, the most important issue to be treated is the Kapton - Araldite® 2014-2 bond. I suggest DO NOT USE Kapton. Due to the fact that the connecting rod module was warped in KAPTON with the purpose of oil and thermal isolation KAPTON the module was easily pulled out from its place. The reason is that the Kapton scotch has an anti-stick treatment on the back side, the bond is weakened.

Secondly are the routing of the thermocouple wires. This issue can be solved firstly by routing the wires in a way that they do not pull off the circuit if they are caught by the crankshaft, and if so, they should brake instead of ripping apart the module. Another solution is to manufacture custom thermocouples. This process was considered, but due to time constraints I used off commercially available k-type thermocouples, which I chopped to fit them on the connecting rod.

Thirdly, going into more fine tuning of the design, a further miniaturization of the module is possible. Instead of sandwiching two PCBs one over another, a single PCB containing nRf252 chip, the Bluetooth antenna and the signal conditioning is possible. This approach may shrink the total size by a factor or 3.

Fourthly, other sensors can be used, for example strain gauges and accelerometers, especially that during the last 3 years the MEMS accelerometer technology improved and are capable of measuring accelerations up to 5000g.

Fifthly, regarding the power system, the battery can be replaced by a wireless charging system.

Appendix B Comparison of Eddy current gap sensors measurements with ACCEL fluid film thickness at different speeds

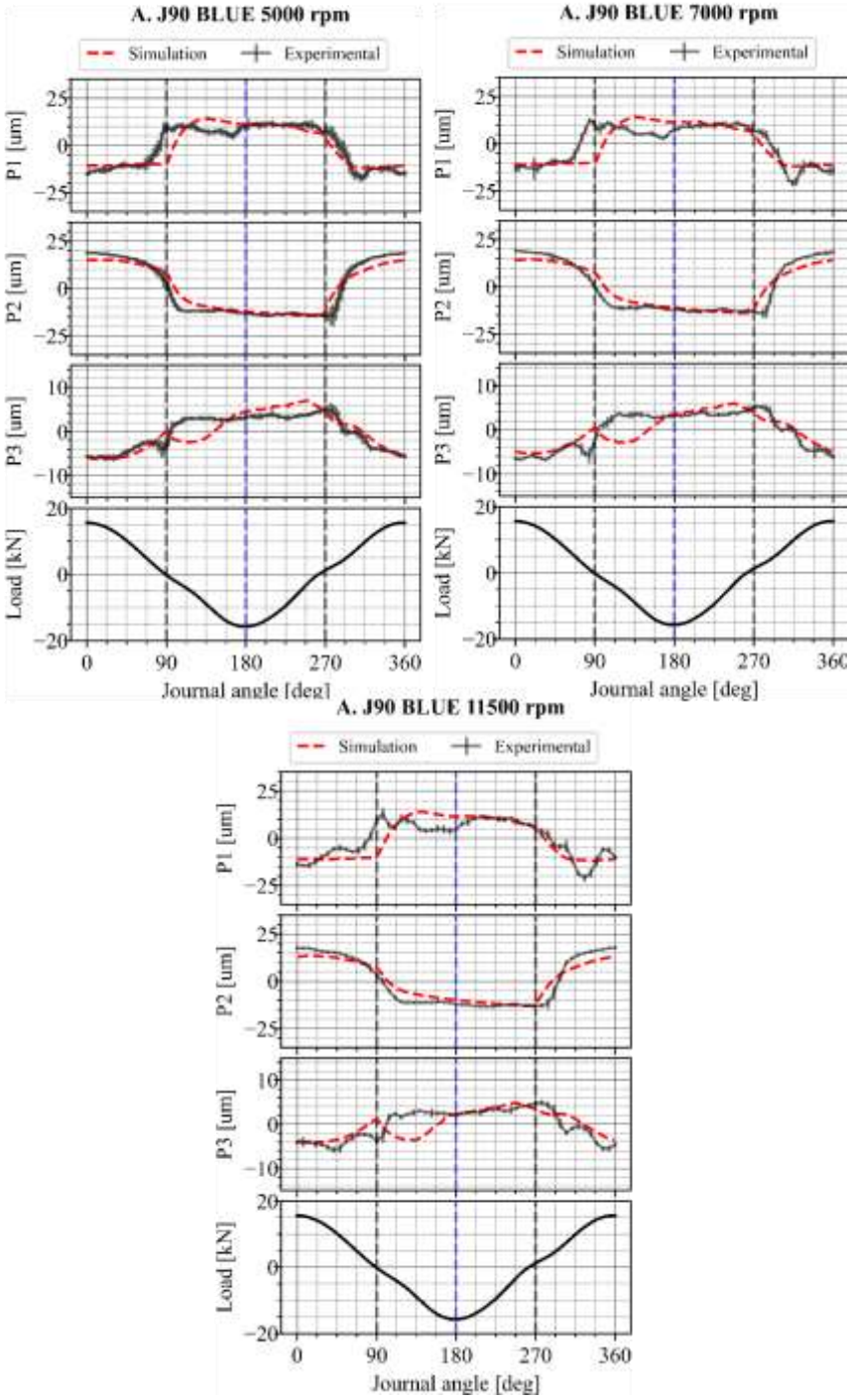

Figure B.1 Eddy current gap sensors comparison with ACCEL results for different speeds

Figure B.1 depicts the comparison between the eddy current gap sensors measurements and ACCEL results. As it can be seen the amplitudes for both, numerical and experimental results do not change much with speed. Form the point of view of experimental data, the reason is that the small variation of the oil film thickness with speed is lower than the sensor precision.

Appendix C Kinematic Viscosity

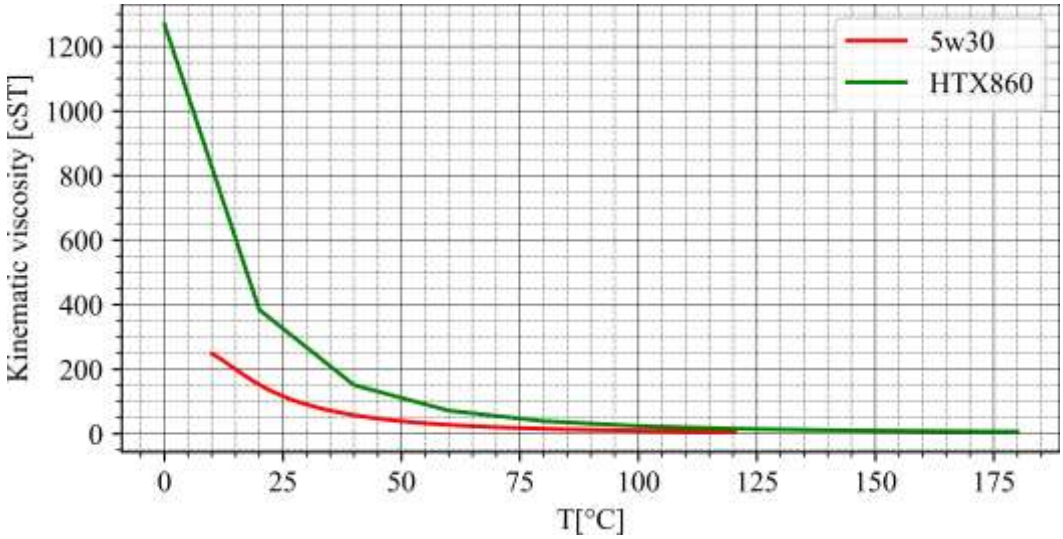

Figure C.1 Mc Coull and Walther law for the tested oils

Appendix D Drawings

Table D.1 Drawing tables for parts

Qnt.	Reference AKIRA	Nom
		MEGAPASCALE
1	PI0021-001	Excentrique KX10; 90 deg alimentation; 20kN traction 20kN compression
1	PI0021-002	Excentrique KX10; 135 deg alimentation; 20kN traction 20kN compression
2	PI0021-003	Axe pied bielle KX10
2	PI0021-004	Douille centrage KISTLER pour 9061A KX10
4	PI0021-005	Entretoise adaptation axe pied bielle KX10

1	PI0021-006	Entretoise extérieure-droite bielle KX10
1	PI0021-007	Entretoise extérieure-gauche bielle KX10
1	PI0021-008	Entretoise intérieure-droite bielle KX10
1	PI0021-009	Entretoise intérieure-gauche bielle KX10
	Support TALYROND + Capteurs Proxy	
1	PI0021-010	Base
1	PI0021-011	Cylindré Calibration
2	PI0021-012	Pied Lisse 3 mm
1	PI0021-013	Pied Lisse 5,5 mm
1	PI0021-014	Douille de centrage
1	PI0021-015	Pion pied

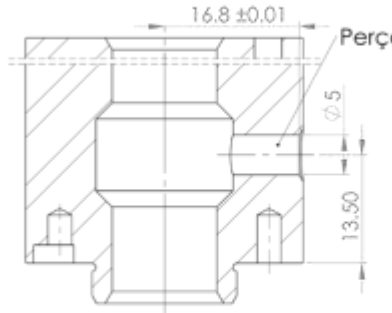

COUPE B-B
(back/0.250mm)

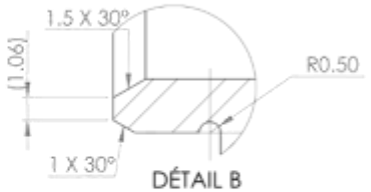

DÉTAIL B
ECHELLE 4 : 1

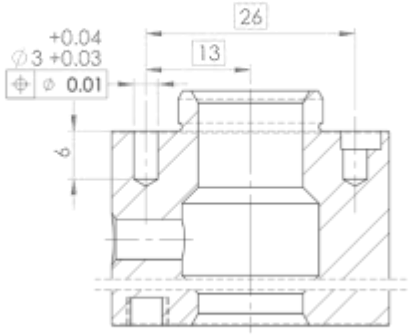

COUPE H-H (centrée)
ECHELLE 3 : 2

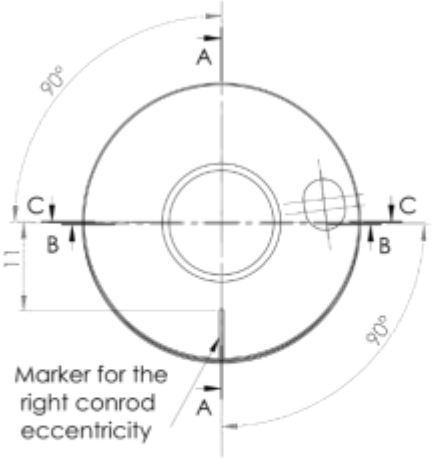

Les 2 excentricités sont dephasées de 180°

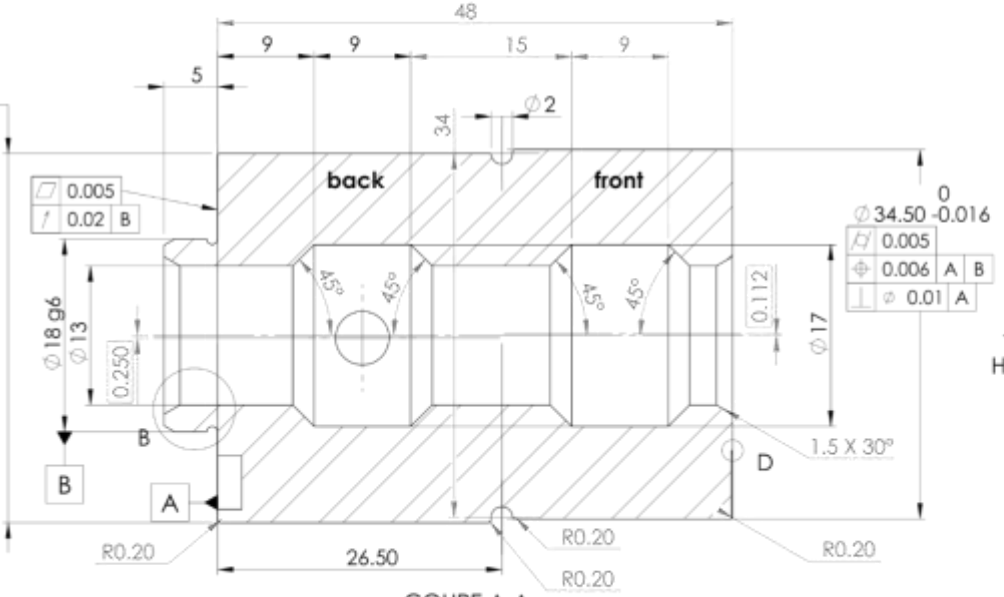

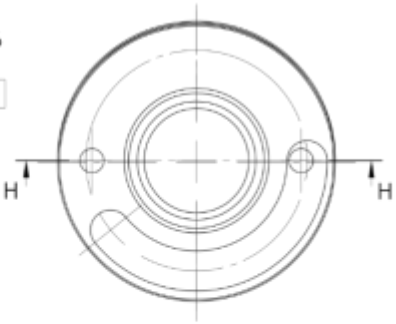

COUPE A-A
Echelle 2:1

Perçage à 90° de l'excentricité max

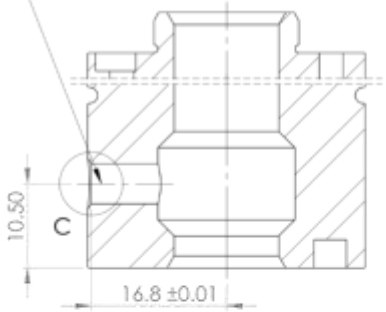

COUPE C-C
(front/0.112mm)

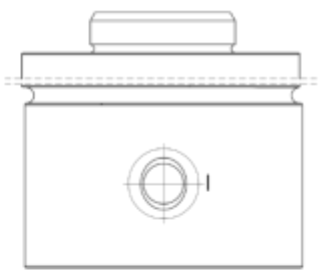

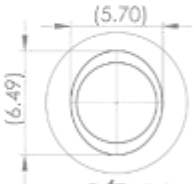

DÉTAIL I

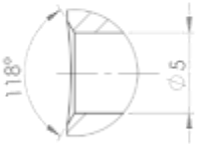

DÉTAIL C

DÉTAIL D

Date	Indice	Modification	Par
24/02/2020	B	Corrections	YH
10/02/2020	A	Création	MR

TOLERANCES GENERALES

Linéaires : +/- 0.1
Angulaires : +/- 0.25°
Rugosités : Ra 0.5 - 1
Ebavurage : casser les angles vifs par R0.2 - 0.4

Matières et traitements :

32CDV13 (Aubert et Duval GKHW)
Rm = 1250 à 1400MPa
Nituration gazeuse

Remplace la pièce référence :

Peut être obtenu à partir de :

Masse : * gr

Nbr 1

Ech. : 3:2

Désignation :

Excentrique KX10
- 20kN traction 20kN compression
- 90 deg alimentation

Dessiné le : 12/02/2020

Par : M.RADOI

Référence / Ind. PI0021-001

Pl. 1/2

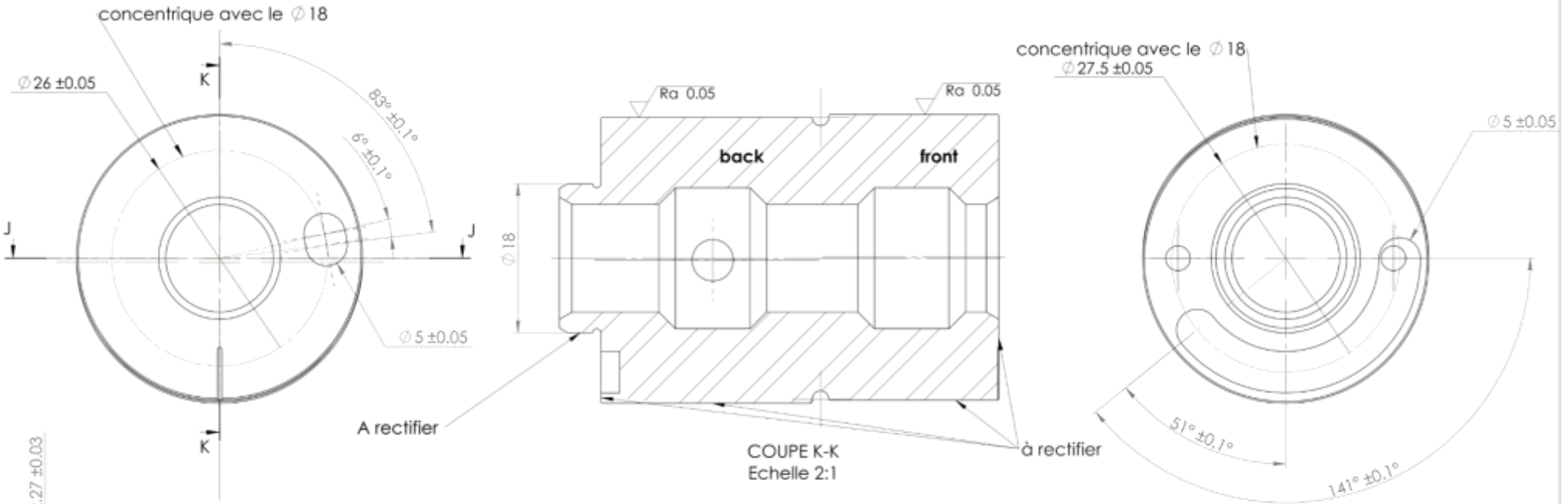

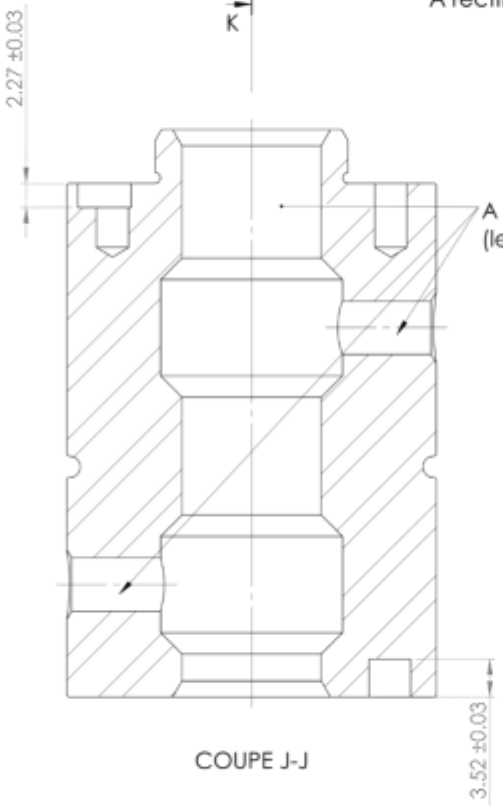

COUPE J-J

Diametre extèrieur
Dureté superficielle > 750 Hv
Profondeur niturée 0.3 à 0.4
Couche blanche supprimée

Date	Indice	Modification	Par
24/02/2020	B	Corrections	YH
10/02/2020	A	Création	MR

TOLERANCES GENERALES

Linéaires : +/- 0.1
Angulaires : +/- 0.25°
Rugosités : Ra 0.5 - 1
Ebavurage : casser les angles vifs par R0.2 - 0.4

Matières et traitements :

32CDV13 (Aubert et Duval GKHW)
Rm = 1250 à 1400MPa
Nituration gazeuse

Remplace la pièce référence :

Peut être obtenu à partir de :

Masse : 275.6 gr

Nbr 1

Ech. : 3:2

Désignation :

Excentrique KX10
- 20kN traction 20kN compression
- 135 deg alimentation

Dessiné le : 12/02/2020

Par : M.RADOI

Référence / Ind. PI0021-01

Pl. 2/2

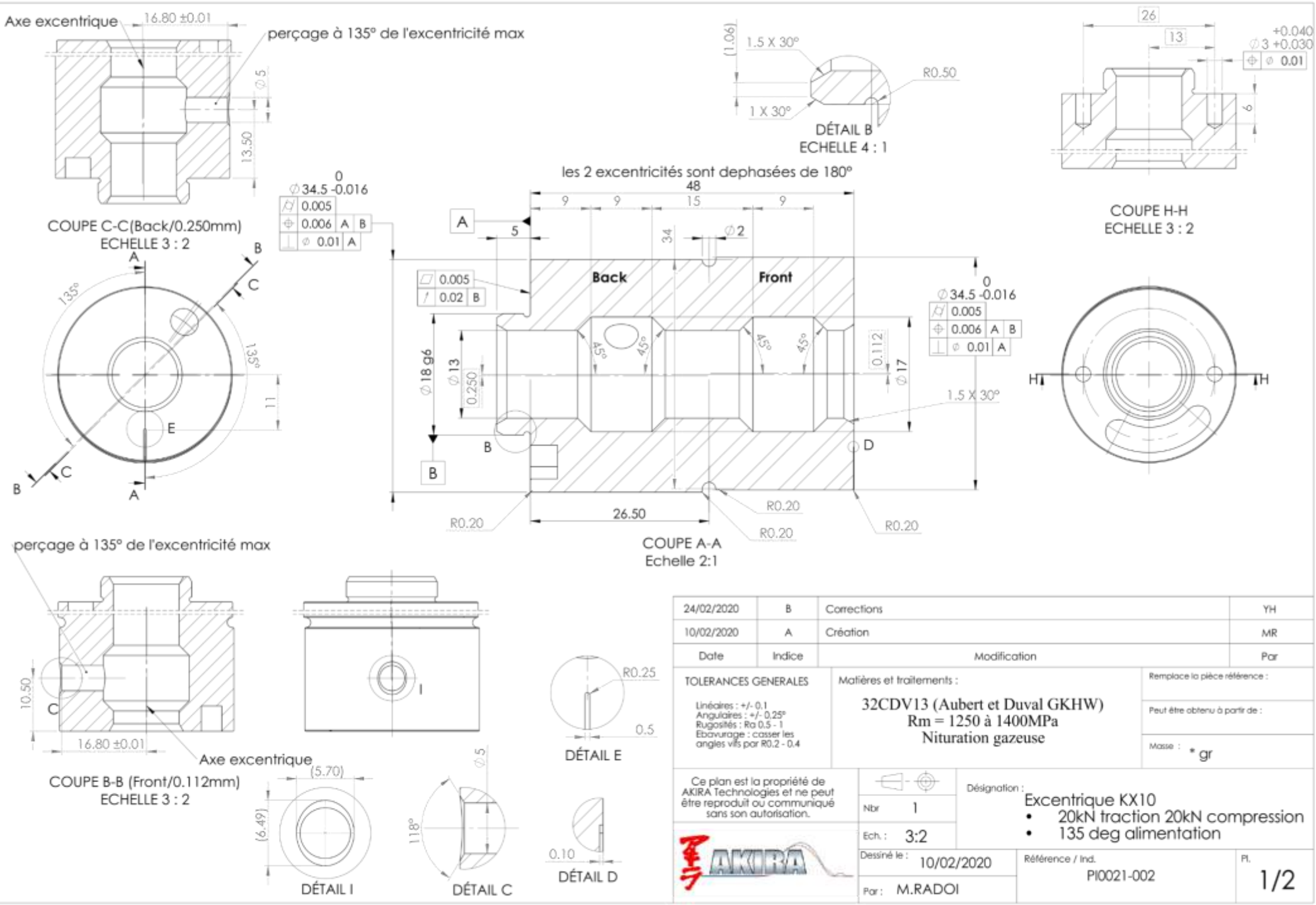

Date	Indice	Modification	Par
24/02/2020	B	Corrections	YH
10/02/2020	A	Création	MR

TOLERANCES GENERALES

Linéaires : +/- 0.1
Angulaires : +/- 0.25°
Rugosités : Ra 0.5 - 1
Ebavurage : casser les angles vifs par R0.2 - 0.4

Matières et traitements :

32CDV13 (Aubert et Duval GKHW)
Rm = 1250 à 1400MPa
Nituration gazeuse

Remplace la pièce référence :

Peut être obtenu à partir de :

Masse : * gr

Nbr 1

Ech. : 3:2

Désignation :

Excentrique KX10
- 20kN traction 20kN compression
- 135 deg alimentation

Dessiné le : 10/02/2020

Par : M.RADOI

Référence / Ind. PI0021-002

Pl. 1/2

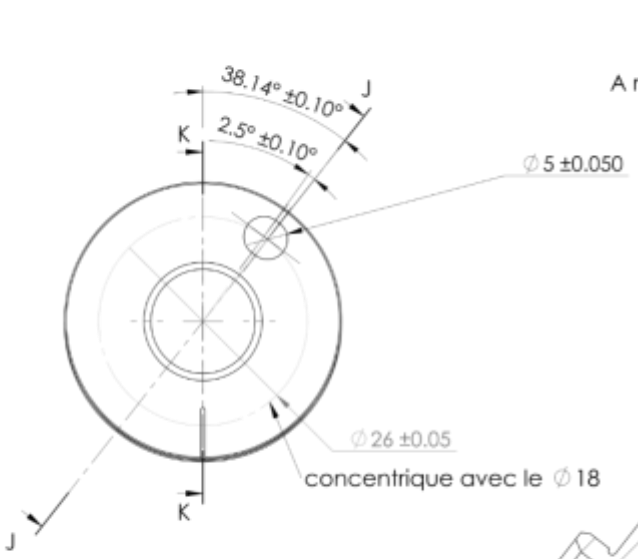

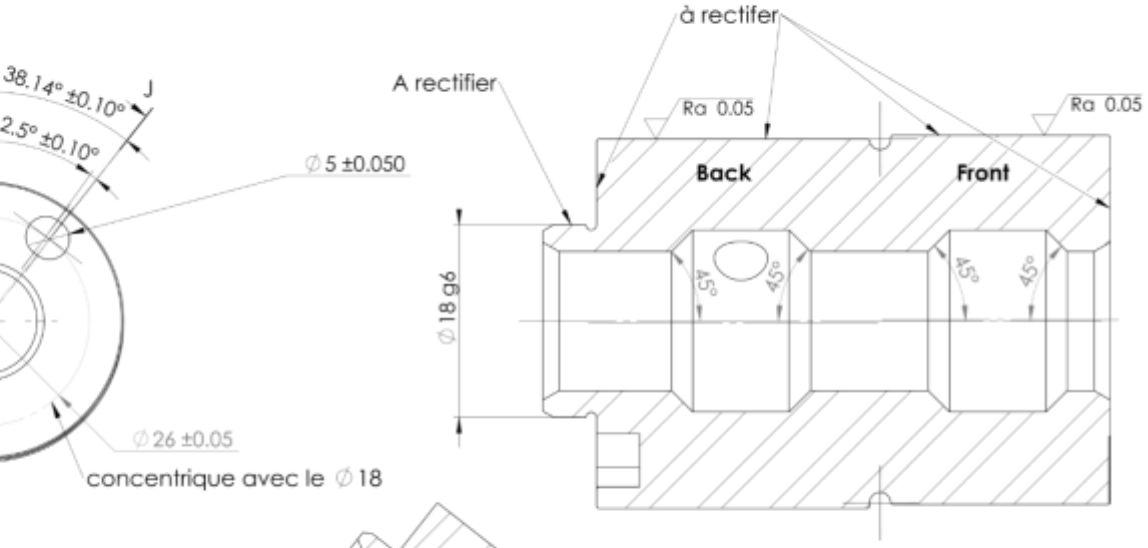

COUPE K-K
Echelle 2:1

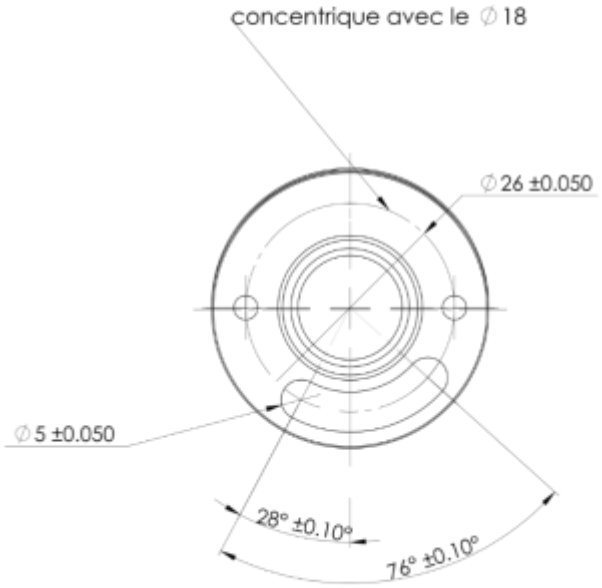

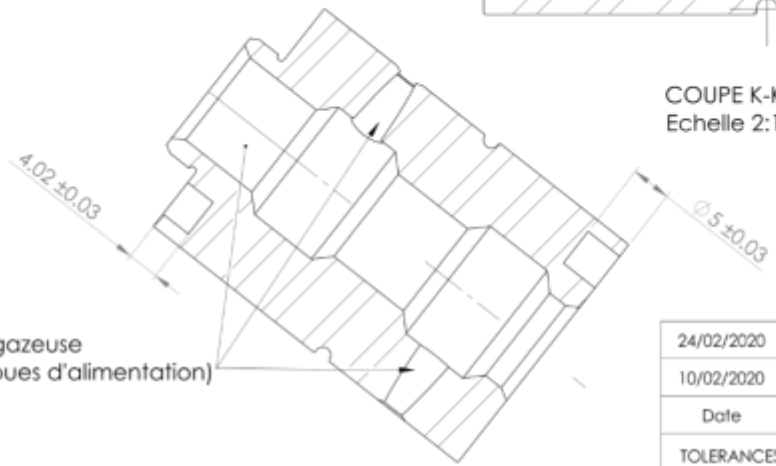

A proteger contre nituration gazeuse
(le diametre intérieur et les troues d'alimentation)

COUPE J-J
ECHELLE 3 : 2

Diametre extèrieur
Dureté superficielle > 750 Hv
Profondeur niturée 0.3 à 0.4
Couche blanche supprimée

Date	Indice	Modification	Par
24/02/2020	B	Corrections	YH
10/02/2020	A	Création	MR

TOLERANCES GENERALES

Linéaires : +/- 0.1
Angulaires : +/- 0.25°
Rugosités : Ra 0.5 - 1
Ebavurage : casser les angles vifs par R0.2 - 0.4

Matières et traitements :

32CDV13 (Aubert et Duval GKHW)
Rm = 1250 à 1400MPa
Niturations gazeuse

Remplace la pièce référence :

Peut être obtenu à partir de :

Masse : * gr

Nbr 1

Ech. : 3:2

Désignation :

Excentrique KX10
- 20kN traction 20kN compression
- 135 deg alimentation

Dessiné le : 10/02/2020

Par : M.RADOI

Référence / Ind. PI0021-02

Pl. 2/2

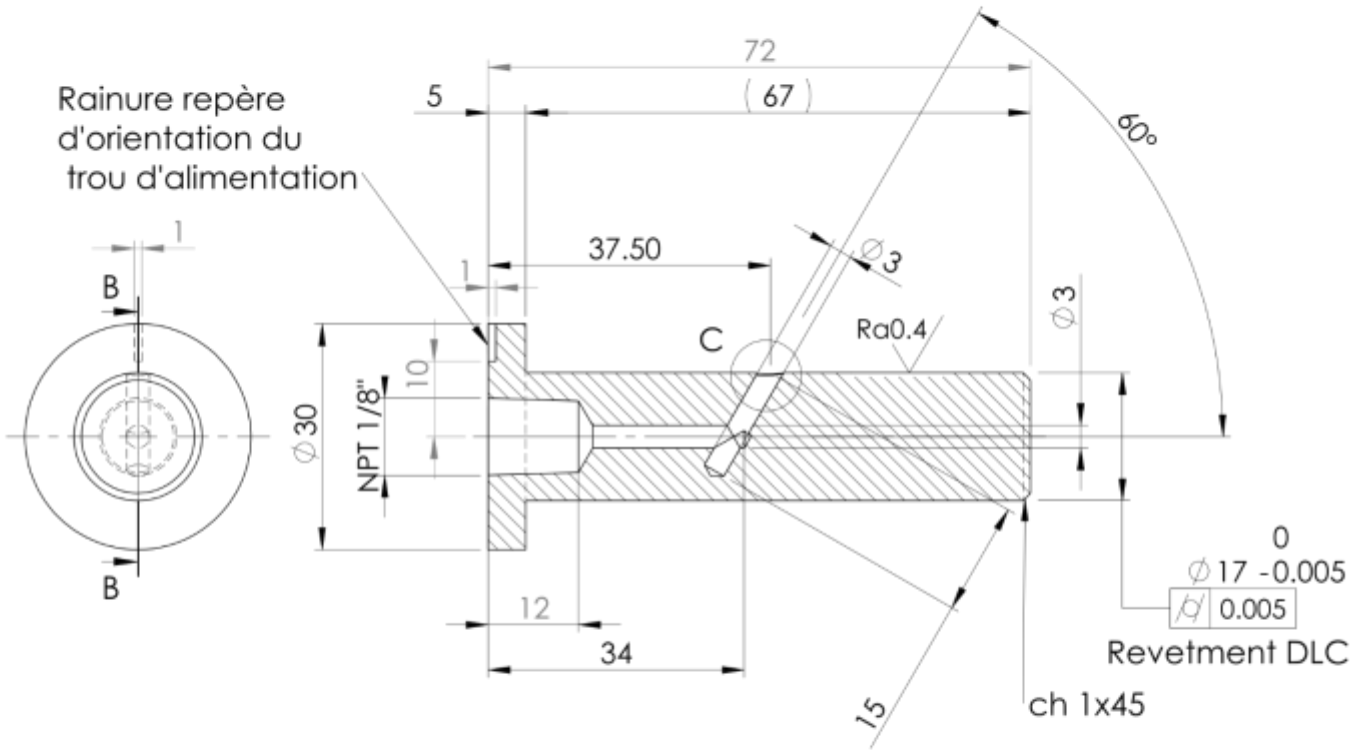

COUPE B-B

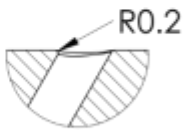

DÉTAIL C
ECHELLE 2 : 1

Date	Indice	Modification	Par
13/02/2020	B	corrections	YH
10/02/2020	A	Création	MR

TOLERANCES GENERALES

Linéaires : +/- 0.1
Angulaires : +/- 0.25°
Rugosités : Ra 1.8 - 3.2
Ebavurage : casser les angles vifs par R0.2 - 0.4

Matières et traitements :

FMDA Aubert et Duval (30 NCD 16)
Re 1250 MPa Rm 1750 MPa mini

Remplace la pièce référence :

Peut être obtenu à partir de :

Masse : gr

Nbr 2

Ech. : 1:1

Désignation : Axe pied bielle KX10

Dessiné le : 15/07/2002

Par : M.RADOI

Référence / Ind. PI0021-003

Pl. 1/1

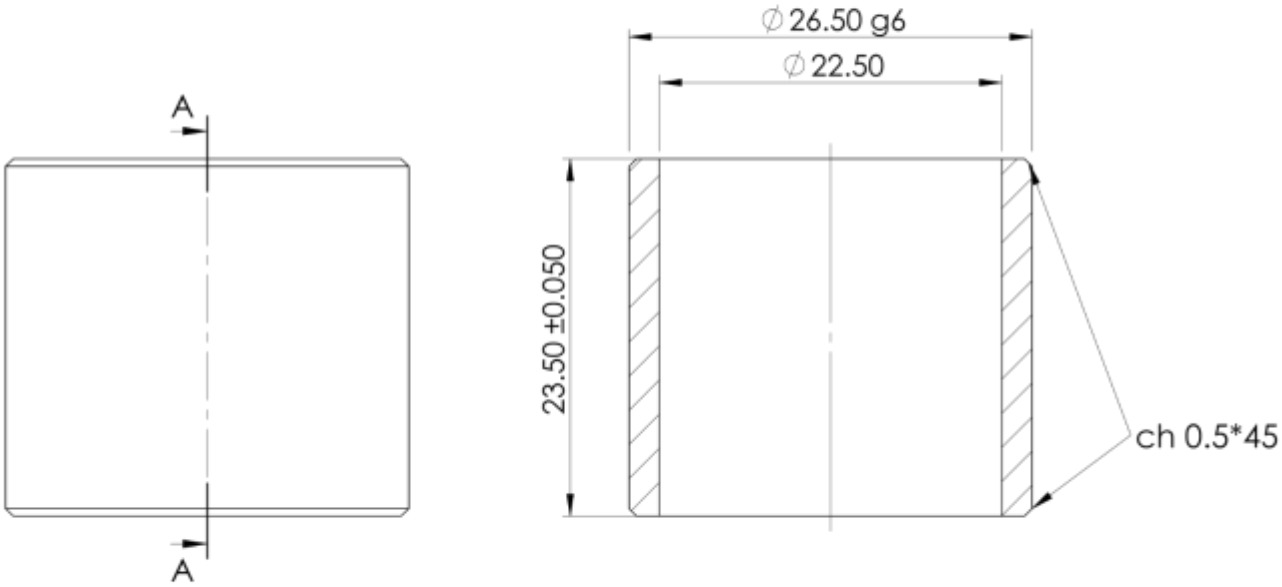

	A	Création	
Date	Indice	Modification	Par

TOLERANCES GENERALES Linéaires : +/- 0.1 Angulaires : +/- 0.25° Rugosités : Ra 1.8 - 3.2 Ebavurage : casser les angles vifs par R0.2 - 0.4	Matières et traitements : 30 Cr Ni Mo 8 THYSSEN (30 CND 8) pré-traité Re > 1050 MPa, Rm 1250-1450 MPa	Remplace la pièce référence : Peut être obtenu à partir de : Masse : *

	Nbr 2	Désignation : Douille centrage KISTLER pour 9061A KX10	
AKIRA	Ech. : 2:1		
	Dessiné le : 05/02/2020	Référence / Ind. PI0021-004	Pl. 1/1
	Par : M.RADOI		

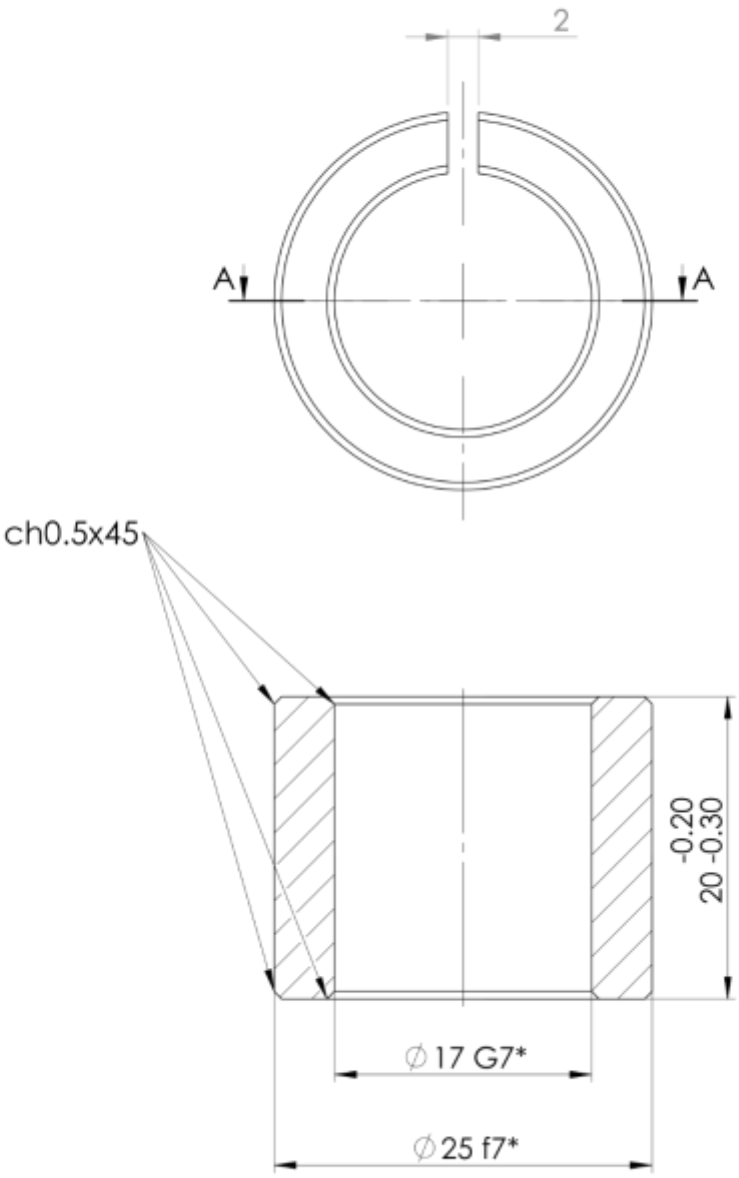

Date	Indice	Modification	Par
13/02/2020	B	Corrections	YH
10/02/2020	A	Création	MR

TOLERANCES GENERALES

Linéaires : +/- 0.1
Angulaires : +/- 0.25°
Rugosités : Ra 1.8 - 3.2
Ebavurage : casser les angles vifs par R0.2 - 0.4

Matières et traitements :

30 Cr Ni Mo 8 (30 CND 8)
pré-traité Re > 1050 MPa, Rm = 1250-1450 MPa

Remplace la pièce référence :

Peut être obtenu à partir de :

Masse : *

Nbr 4

Ech. : 2:1

Désignation :

Entretoise adaptation axe pied de bielle kx 10

Dessiné le : 05/02/2020

Par : M.RADOI

Référence / Ind. PI0021-005

Pl. 1/1

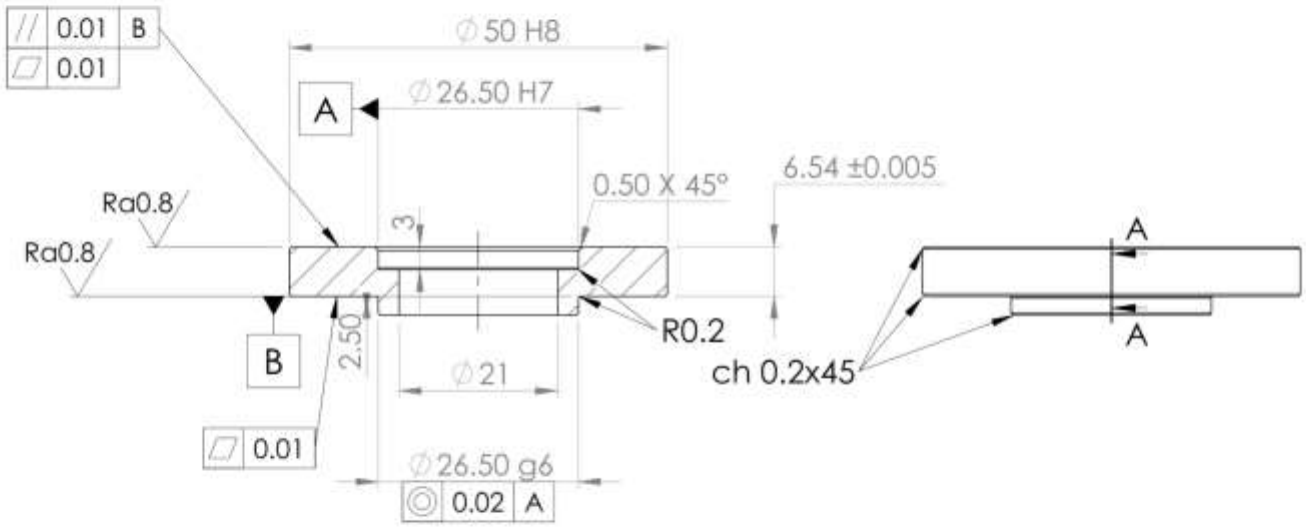

COUPE A-A

Date	Indice	Modification	Par
13/02/2020	B	Corrections	YH
10/02/2020	A	Création	MR

TOLERANCES GENERALES

Linéaires : +/- 0.1
Angulaires : +/- 0.25°
Rugosités : Ra 1 - 2
Ebavurage : casser les angles vifs par R0.2 - 0.4

Matières et traitements :

30 Cr Ni Mo 8 (30 CND 8)
pré-traité Re > 900 MPa, Rm = 1100-1300 MPa

Remplace la pièce référence :

Peut être obtenu à partir de :

Masse : *

Nbr 1

Ech. : 1:1

Désignation :

Entretoise extérieure-droite bielle KX10

Dessiné le : 05/02/2020

Par : M.RADOI

Référence / Ind. PI0021-006

Pl. 1/1

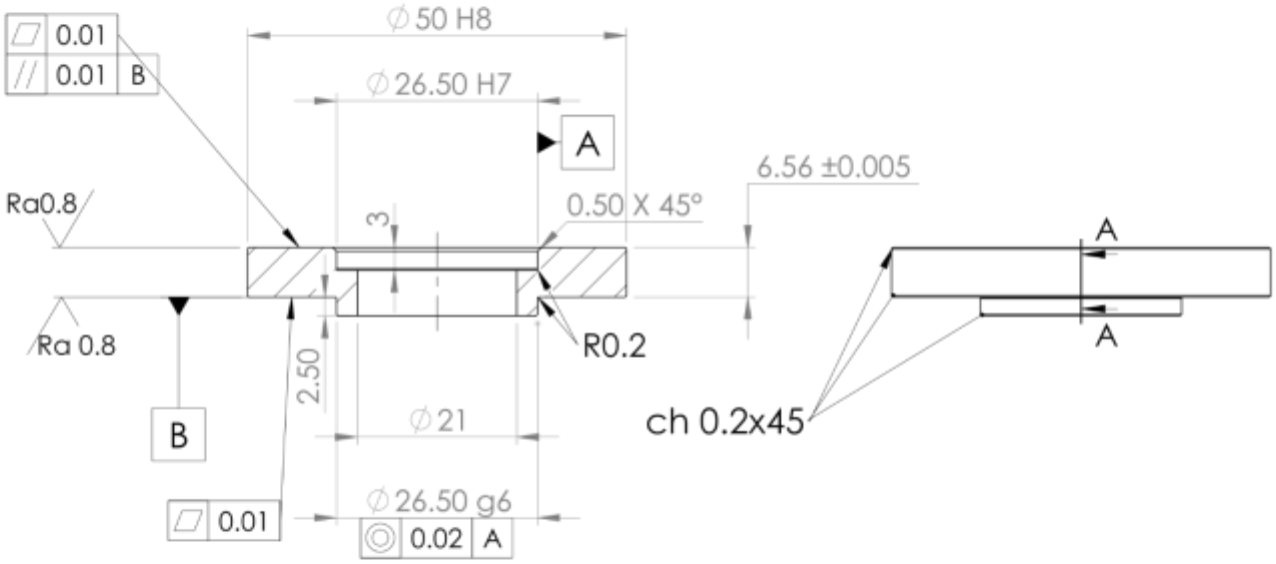

Date	Indice	Modification	Par
13/02/2020	B	Corrections	YH
05/02/20	A	Création	MR

TOLERANCES GENERALES

Linéaires : +/- 0.1
Angulaires : +/- 0,25°
Rugosités : Ra 1- 2
Ebavurage : casser les angles vifs par R0.2 - 0.4

Matières et traitements :

30 Cr Ni Mo 8 (30 CND 8)
pré-traité Re > 900 MPa, Rm = 1100-1300 MPa

Remplace la pièce référence :

Peut être obtenu à partir de :

Masse : *

Nbr 1

Ech. : 1:1

Désignation :
Entretoise extérieure-gauche bielle KX10

Dessiné le : 05/02/2020

Par : M.RADOI

Référence / Ind. PI0021-007

Pl. 1/1

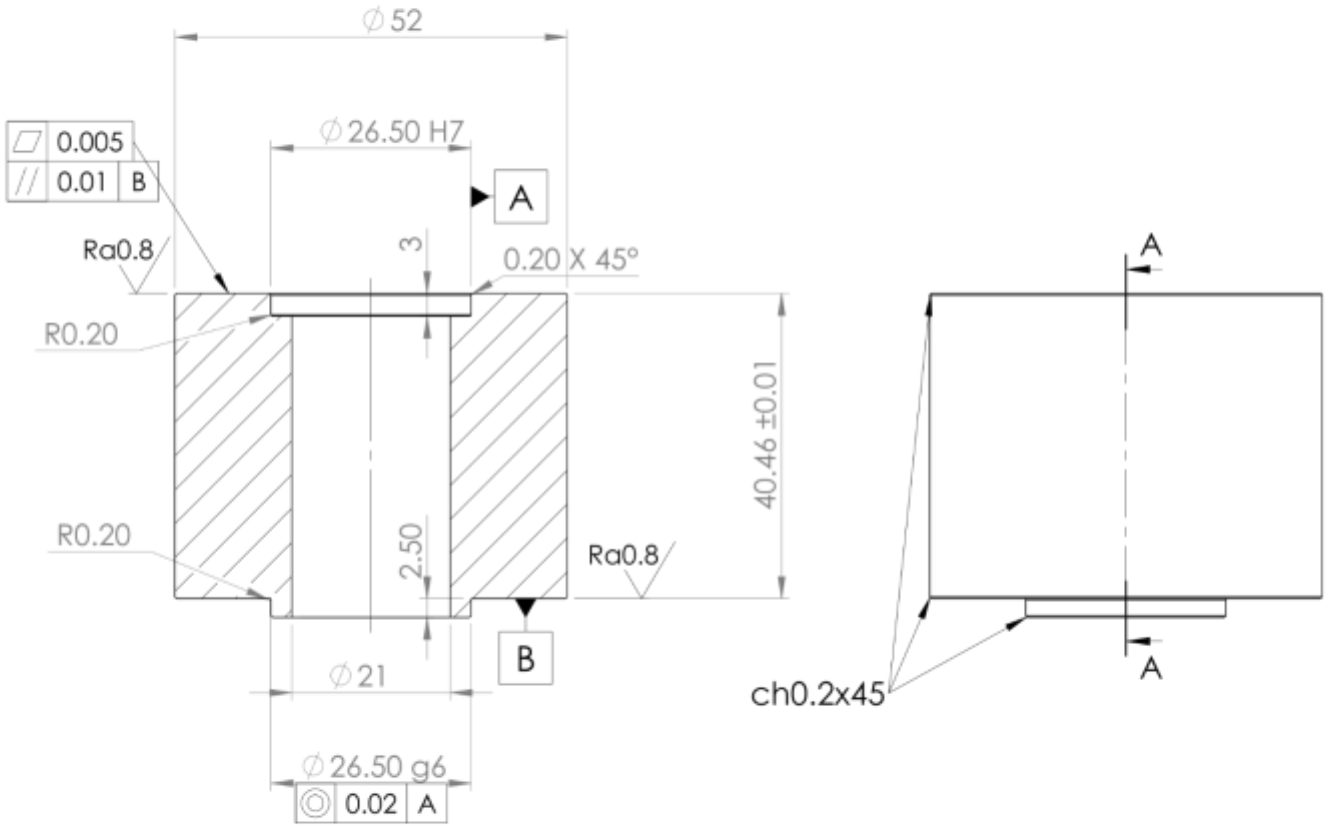

Date	Indice	Modification	Par
13/02/2020	B	Corrections	YH
10/02/2020	A	Création	MR

TOLERANCES GENERALES

Linéaires : +/- 0.1
Angulaires : +/- 0.25°
Rugosités : Ra 1.8 - 3.2
Ebavurage : casser les angles vifs par R0.2 - 0.4

Matières et traitements :

30 Cr Ni Mo 8 (30 CND 8)
pré-traité Re > 900 MPa, Rm = 1100-1300 MPa

Remplace la pièce référence :

Peut être obtenu à partir de :

Masse : *

Nbr 1

Ech. : 1:1

Désignation :

Entretoise intérieure-droite bielle KX10

Dessiné le : 05/02/2020

Par : M.RADOI

Référence / Ind. PI0021-008

Pl. 1/1

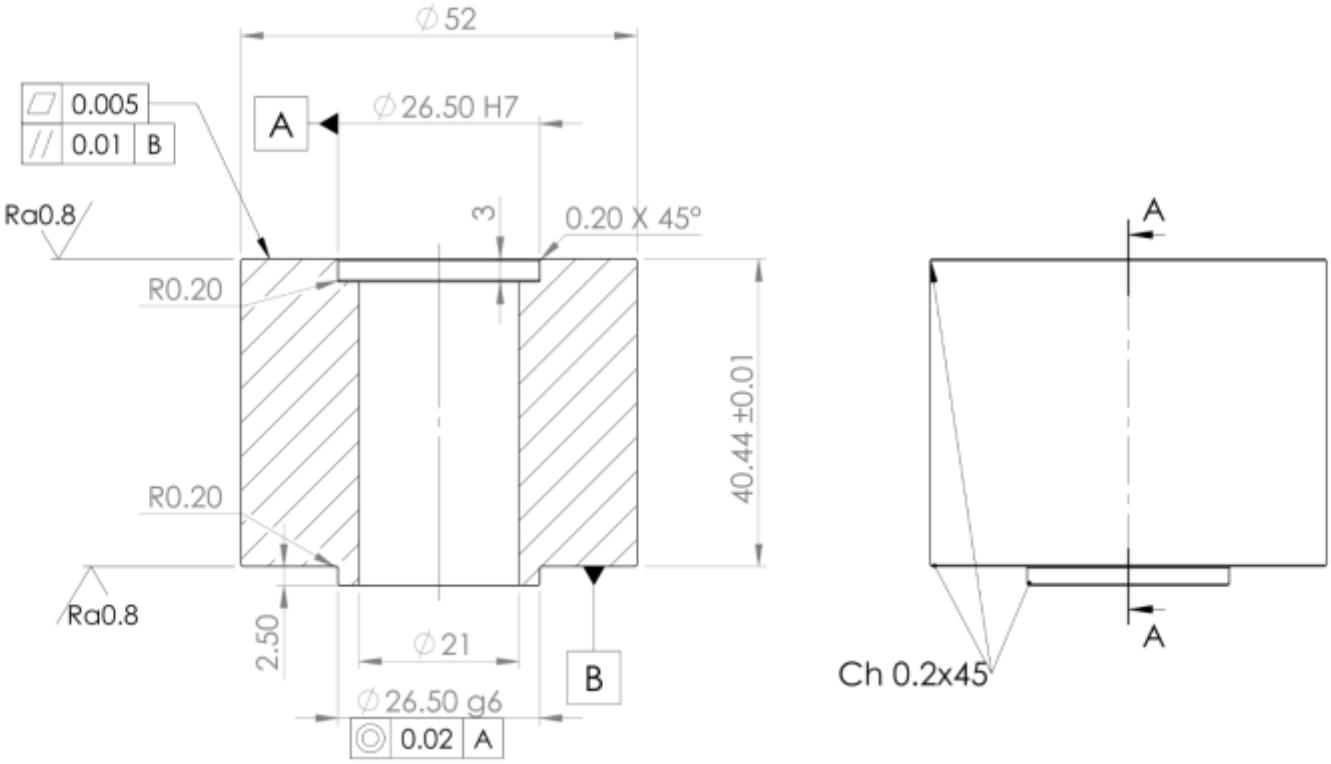

Date	Indice	Modification	Par
13/02/2020	B	Corrections	YH
05/02/2020	A	Création	MR

TOLERANCES GENERALES

Linéaires : +/- 0.1
Angulaires : +/- 0.25°
Rugosités : Ra 1.8 - 2
Ebavurage : casser les angles vifs par R0.2 - 0.4

Matières et traitements :

30 Cr Ni Mo 8 (30 CND 8)
pré-traité Re > 900 MPa, Rm = 1100-1300 MPa

Remplace la pièce référence :

Peut être obtenu à partir de :

Masse : * gr

Nbr 1

Ech. : 1:1

Désignation :

Entretoise intérieure-gauche bielle KX10

Dessiné le : 05/02/2020

Par : M.RADOI

Référence / Ind. PI0021-009

Pl. 1/1

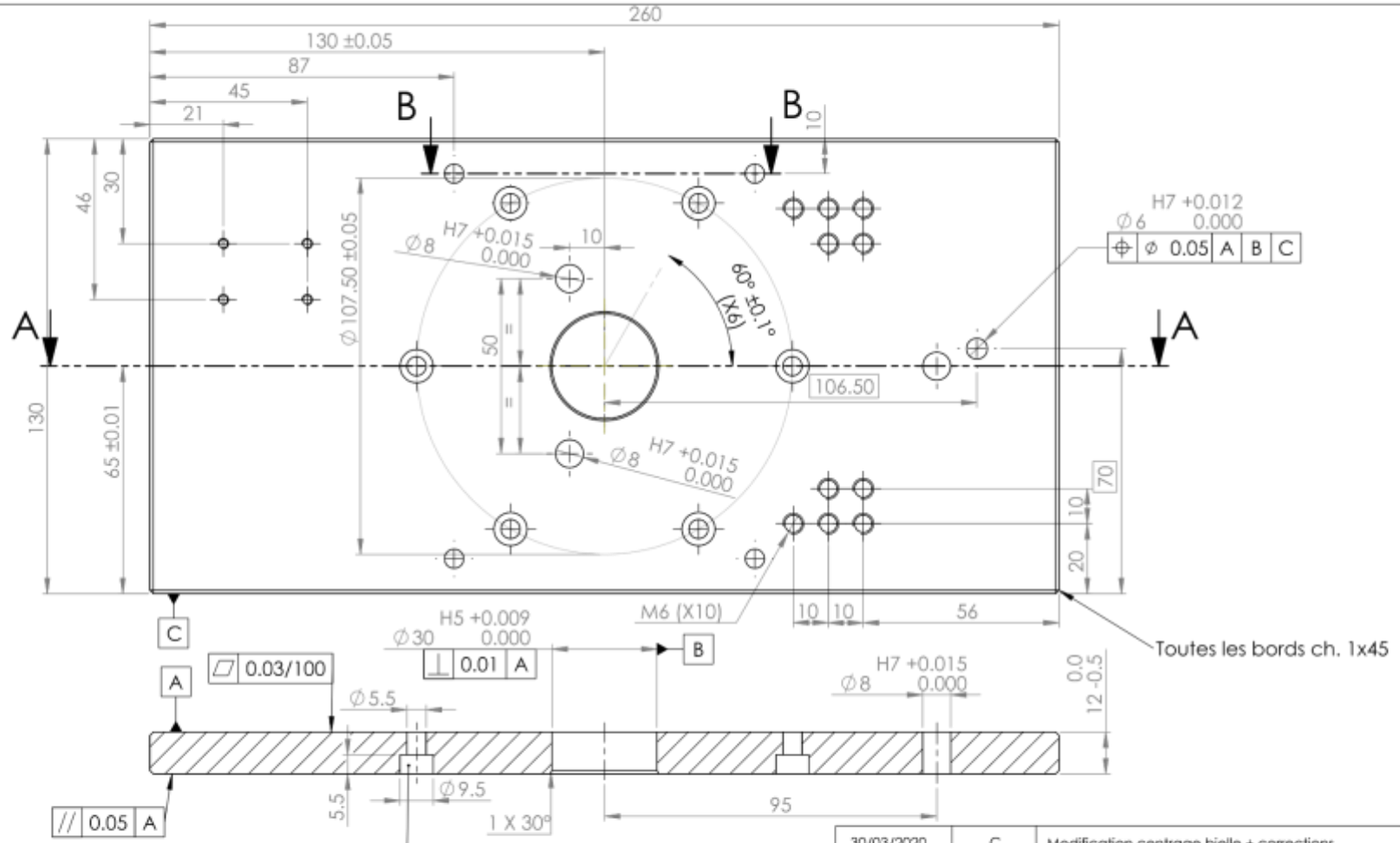

COUPE A-A

ECHELLE 3 : 4

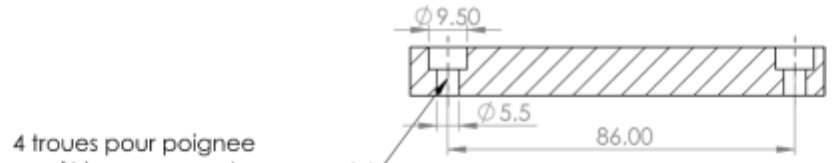

COUPE B-B

ECHELLE 3 : 4

Date	Indice	Modification	Par
30/03/2020	C	Modification centrage bielle + corrections	YH
11/03/2020	A	Création	MR

TOLERANCES GENERALES

Linéaires : +/- 0.1
Angulaires : +/- 0.25°
Rugosités : Ra 0.5 - 1
Ebavurage : casser les angles vifs par R0.2 - 0.4

Matières et traitements :
35CD4 ou 35NCD8 ou 30CMD8
trempé et revenu pour 900N/mm2 <Rm<1100N/mm2
!!! pas d'acier à isinabilité amelioréé!!!

Brunissage

Remplace la pièce référence :

Peut être obtenu à partir de :

Masse : * gr

Nbr 1

Ech. : 3:4

Désignation : BASE

Dessiné le : 12/02/2020

Par : M.RADOI

Référence / Ind. PI0021-010

PL 1/1

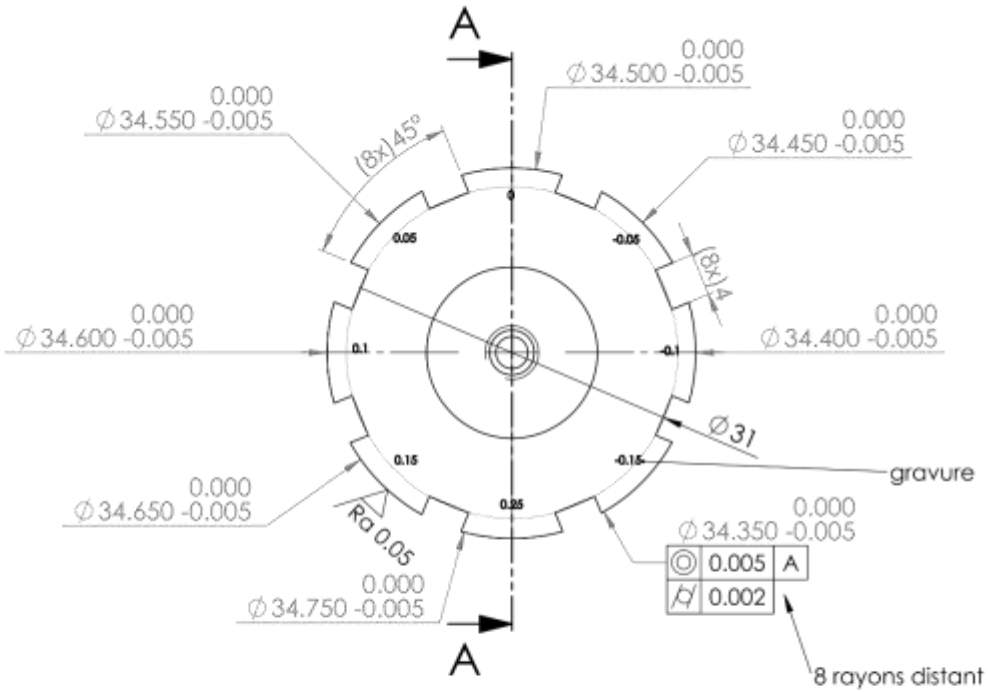

8 rayons distant de 45 deg

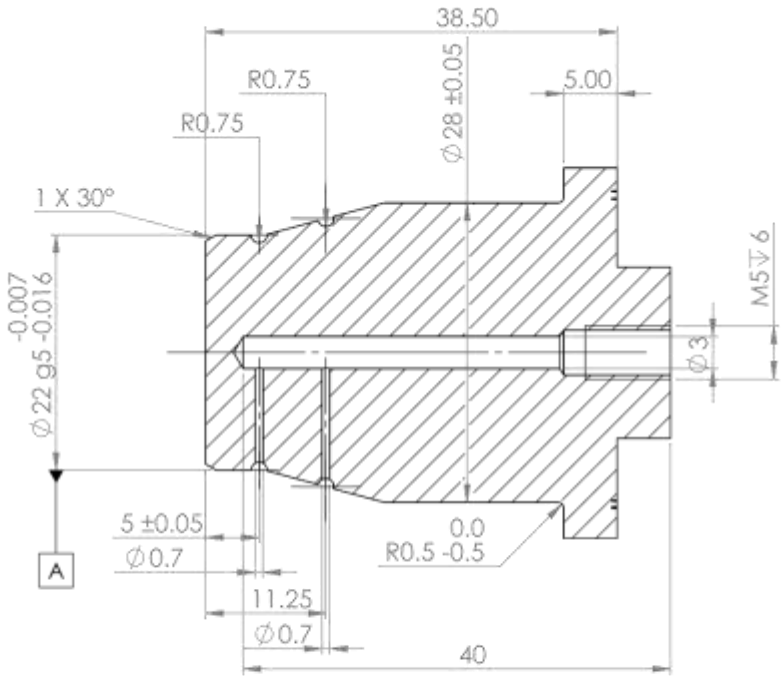

cone ajusté avec PI021-014 "douille de centrage " par rodage

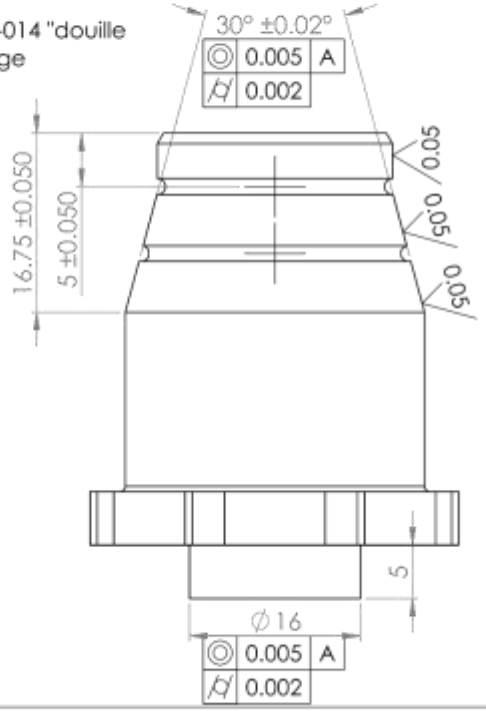

- état de surface pour chaque secteur: 0.05
- tolérance géométrique appliquée pour les 8 rayons

Dureté superficielle > 750 Hv
Profondeur niturée 0.3 à 0.4
Couche blanche supprimée

COUPE A-A
3:4

Date	Indice	Modification	Par
30/03/2020	C	centrage sur cone	YH
10/02/2020			MR

TOLERANCES GENERALES
Linéaires : +/- 0.1
Angulaires : +/- 0.25°
Rugosités : Ra 0.5 - 1
Ebavurage : casser les angles vifs par R0.2 - 0.4

Matières et traitements :
32CDV13 (Aubert et Duval GKHW)
Rm = 1250 à 1400MPa
Nituration gazeuse
(identique au maneton du vilebrequin)

Remplace la pièce référence :
Peut être obtenu à partir de :
Masse : * gr

Nbr 1
Ech. : 3:2
Désignation : Cylindre Calibration
Dessiné le : 12/02/2020
Par : M.RADOI
Référence / Ind. PI0021-011
Pl. 1/1

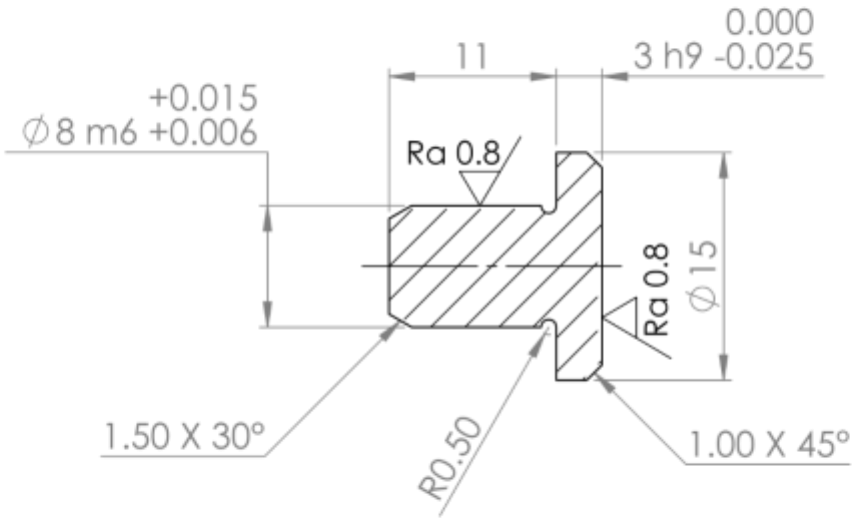

COUPE B-B
2:1

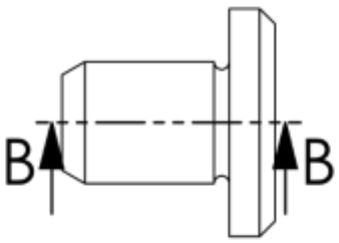

Date	Indice	Modification	Par
12/03/2020	B	Validé	YH
11/03/2020	A	Création	MR

TOLERANCES GENERALES

Linéaires : +/- 0.1
Angulaires : +/- 0.25°
Rugosités : Ra 1.8 - 3.2
Ebavurage : casser les angles vifs par R0.2 - 0.4

Matières et traitements :

35CD4 ou 35NCD8 ou 30CMD8
trempé et revenu pour 900N/mm2<Rm<1100N/mm2
!!! pas d'acier à isinabilité ameliorée!!!

Brunissage

Remplace la pièce référence :

Peut être obtenu à partir de :

Masse : gr

Nbr 2

Ech. : 2:1

Désignation : Pied Lisse 3 mm

Dessiné le : 10/03/2020

Par : M.RADOI

Référence / Ind. PI0021-012

Pl. 1/1

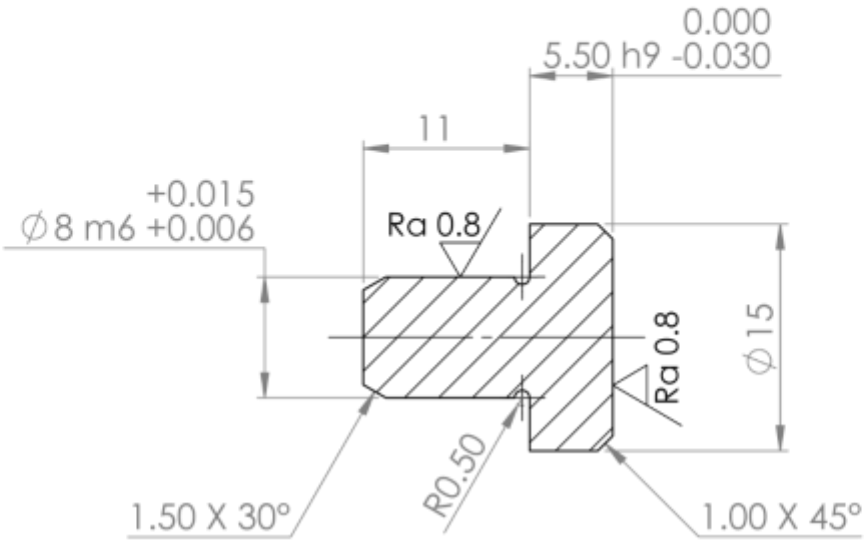

COUPE A-A
2:1

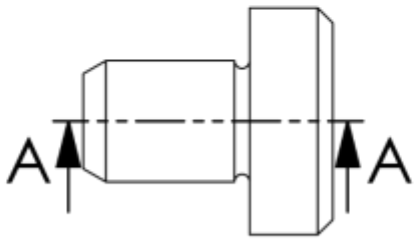

Date	Indice	Modification	Par
12/03/2020	B	Validé	YH
11/03/2020	A	Création	MR

TOLERANCES GENERALES

Linéaires : +/- 0.1
Angulaires : +/- 0.25°
Rugosités : Ra 1.8 - 3.2
Ebavurage : casser les angles vifs par R0.2 - 0.4

Matières et traitements :
35CD4 ou 35NCD8 ou 30CMD8
trempé et revenu pour 900N/mm2<Rm<1100N/mm2
!!! pas d'acier à isinabilité ameliorée!!!

Brunissage

Remplace la pièce référence :

Peut être obtenu à partir de :

Masse : gr

Nbr 1

Ech. : 2:1

Désignation :
Pied Lisse 5,5 mm

Dessiné le : 10/03/2020

Par : M.RADOI

Référence / Ind. PI0021-013

Pl. 1/1

- cone ajusté avec PI021-011 "cylindre calibration" par rodage
- montage avec dilatation thermique avec la piece PI021-010 (alésage chauffé à 60°C)

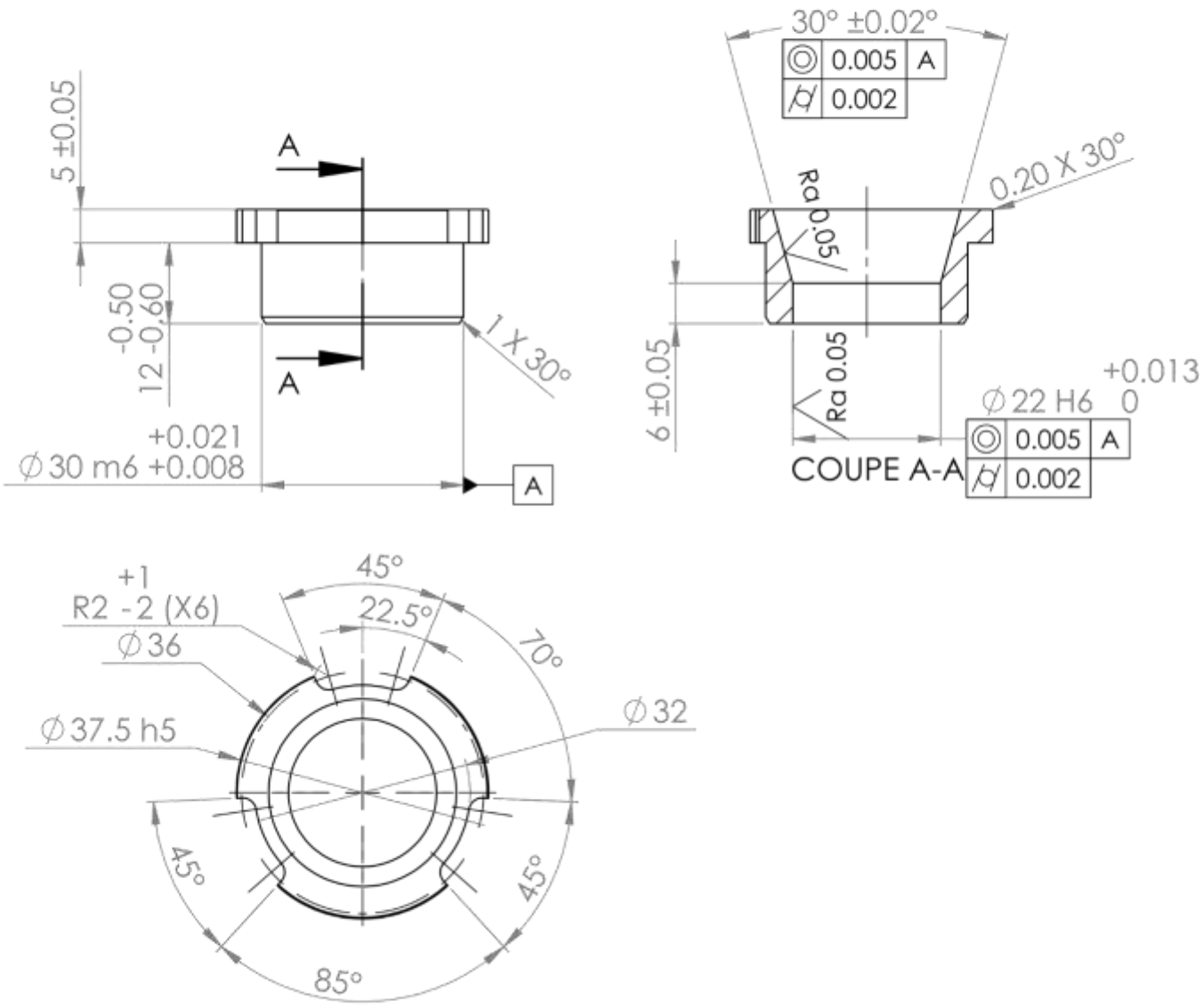

30/03/2020	A	Création pour relecture	YH
Date	Indice	Modification	Par

TOLERANCES GENERALES Linéaires : +/- 0.1 Angulaires : +/- 0.25° Rugosités : Ra 1.8 - 3.2 Ebavurage : casser les angles vifs par R0.2 - 0.4	Matières et traitements : 35CD4 ou 35NCD8 ou 30CMD8 trempé et revenu pour 900N/mm2<Rm<1100N/mm2 !!! pas d'acier à isinabilité ameliorée!!!	Remplace la pièce référence : Peut être obtenu à partir de : Masse : gr

	Nbr 1	Désignation : douille de centrage
AKIRA	Ech. : 1:1	
	Dessiné le : 30/03/2020 Par : Y.HENRY	Référence / Ind. PI0021-14
		Pl. 1/1

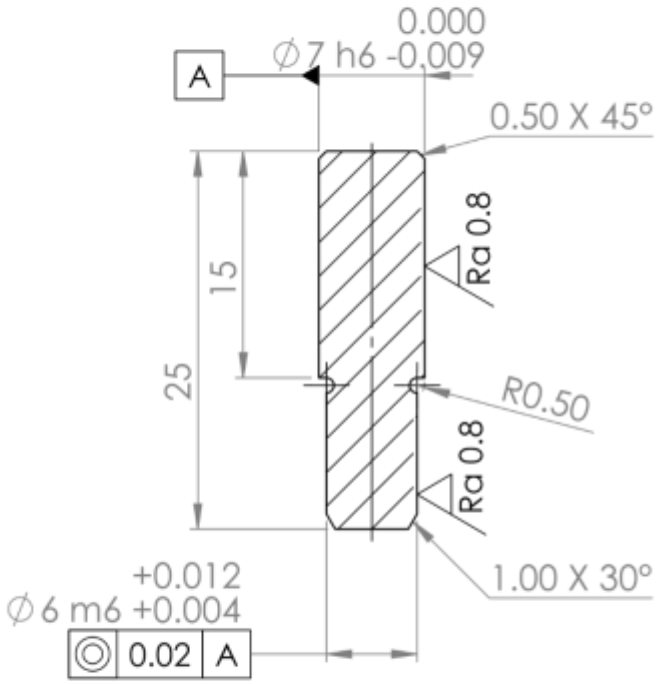

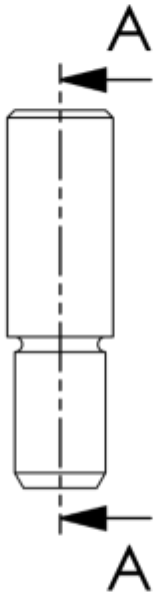

COUPE A-A

ECHELLE 2 : 1

Date	Indice	Modification	Par
12/03/2020	B	Validé	YH
11/03/2020	A	Création	MR

TOLERANCES GENERALES

Linéaires : +/- 0.1
Angulaires : +/- 0.25°
Rugosités : Ra 1.8 - 3.2
Ebavurage : casser les angles vifs par R0.2 - 0.4

Matières et traitements :

35CD4 ou 35NCD8 ou 30CMD8
trempé et revenu pour 900N/mm2<Rm<1100N/mm2
!!! pas d'acier à isinabilité ameliorée!!!

Brunissage

Remplace la pièce référence :

Peut être obtenu à partir de :

Masse : gr

Nbr 1

Ech. : 2:1

Désignation : Pion pied

Dessiné le : 10/03/2020

Par : M.RADOI

Référence / Ind. PI0021-015

Pl. 1/1

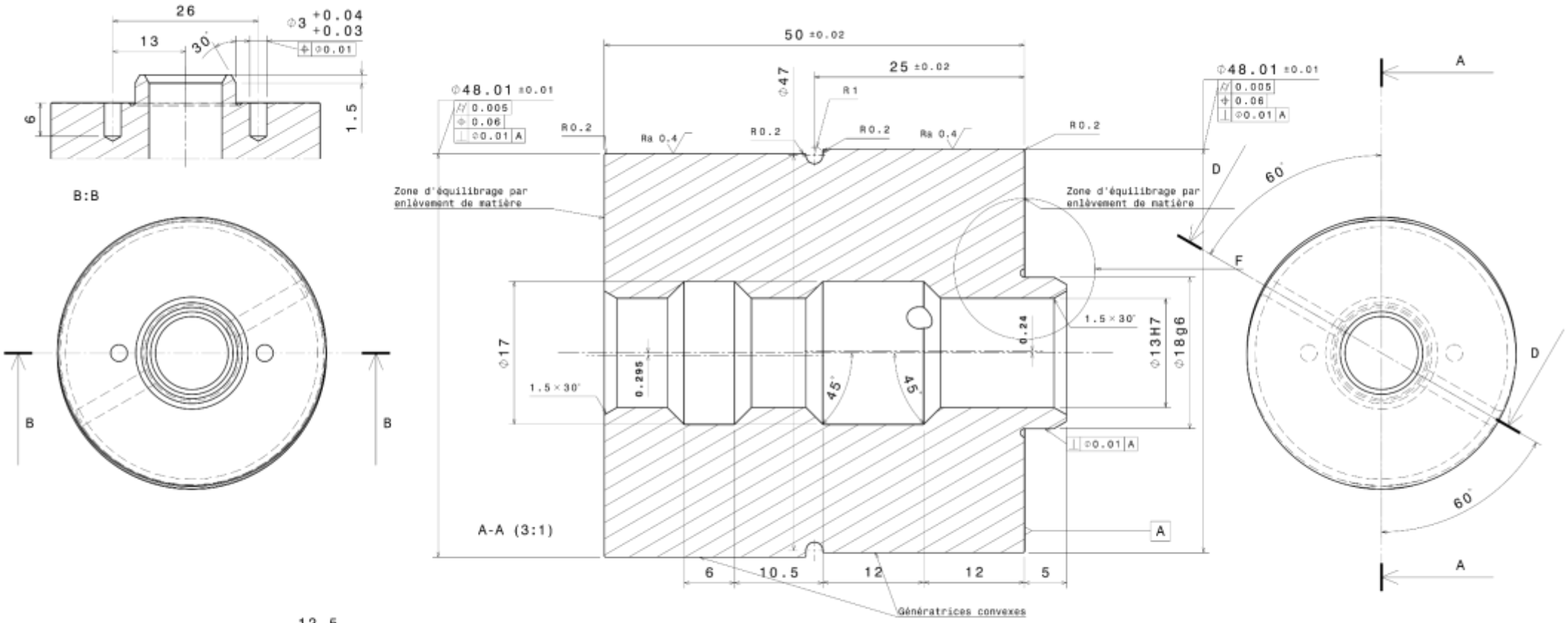

DESIGNED BY: Aurelian FATU DATE: 24/02/2014	Spécifications particulières Matière : FONA Ausbert et Duval (30NCD16) Re 1250MPa Rm 1750MPa mini Equilibrage : G1 Indice de rugosité : Ra 1.6 Tolérences générales ISO 2768 - fH	I H G F E D C B A
CHECKED BY: Pascal Jolly DATE: XXX		
SIZE: A2	Excentrique / Institut PPRIME	
SCALE: 2:1 WEIGHT (kg): XXX	8523-01-DP-S62-D01-M3 Pos. 60° ; Diam. 3mm ; Ray. 1mm	SHEET: 1/1

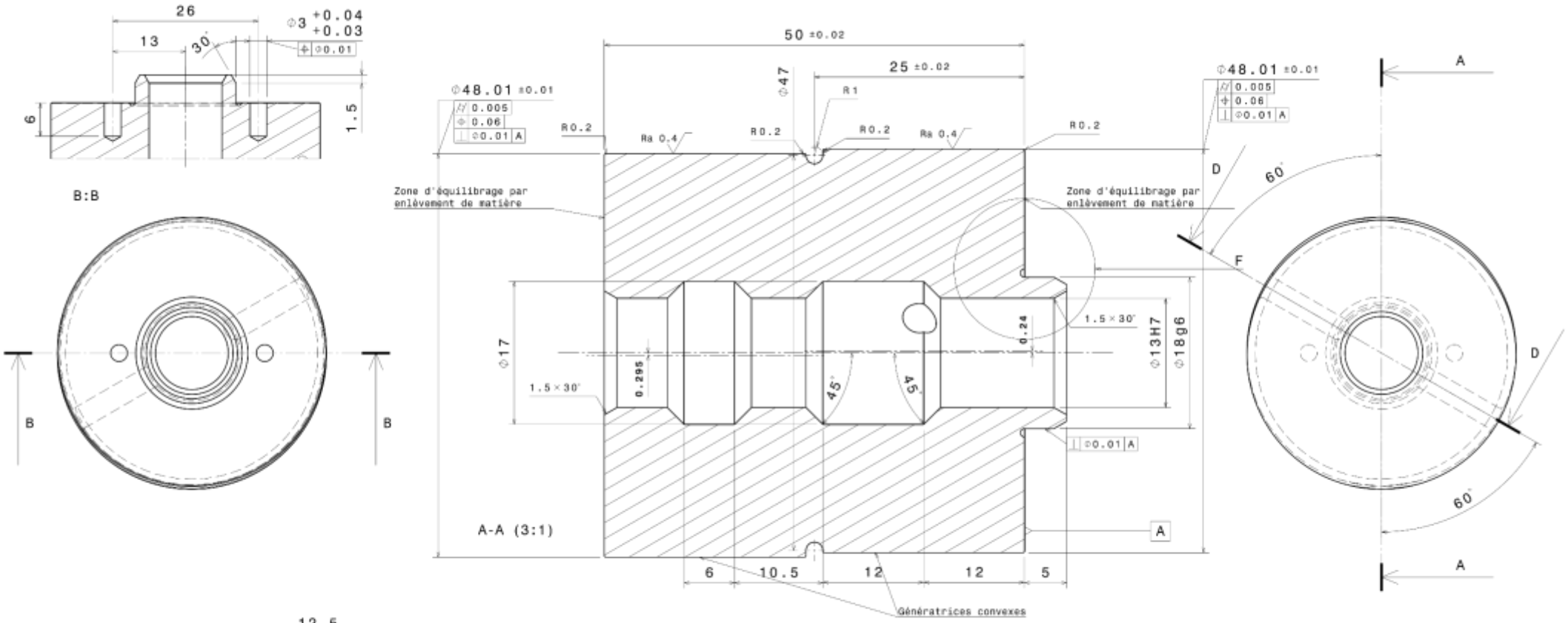

Designed by: Aurelian FATU Date: 24/02/2014	Spécifications particulières Matière : FORA Aubert et Duval (30NCD16) Re 1250MPa Rm 1750MPa mini Equilibrage : G1 Indice de rugosité : Ra 1.6 Tolérences générales ISO 2768 - fH	I …
Checked by: Pascal Jolly Date: XXX		H …
		G …
		F …
		E …
Size: A2	Excentrique / Institut PPRIME	D …
		C …
Scale: 2:1 Weight (kg): XXX	8523-01-DP-S62-D01-M4 Pos. 60° ; Diam. 4mm ; Ray. 1mm	Sheet: 1/1
		B …
		A …